FINE SCALE PHENOMENA IN REACTING SYSTEMS: IDENTIFICATION AND ANALYSIS FOR THEIR REDUCTION

A Dissertation

Submitted to the Graduate School
of the University of Notre Dame
in Partial Fulfillment of the Requirements
for the Degree of

Doctor of Philosophy

by

Ashraf Nadim Saleh Al-Khateeb

Joseph M. Powers, Director

Graduate Program in Aerospace and Mechanical Engineering
Notre Dame, Indiana
February 2010

FINE SCALE PHENOMENA IN REACTING SYSTEMS:
IDENTIFICATION AND ANALYSIS FOR THEIR REDUCTION

Abstract

by

Ashraf Nadim Saleh Al-Khateeb

A robust method for rational reduction of chemically reacting models is developed using a rigorous scale analysis. All the physical scales, spatial and temporal, inherent in reacting systems are accurately identified via eigenvalue analysis. The required temporal scales to assure accuracy in modeling reactive systems and the required spatial discretization to formally capture all detailed continuum physics in the reaction zone are calculated. The interplay between chemistry and transport is addressed via conducting a spectral analysis of reactive flow structure, and the relation between closed reactive systems' dynamics and notions from equilibrium/non-equilibrium thermodynamics is investigated. It revealed that reacting systems' physical scales are coupled, and their dynamics cannot be deduced from classical thermodynamics. The slow invariant manifolds of dynamical systems arising from modeling closed reacting mixtures are constructed. These manifolds describe accurately the reactive systems' slow dynamics. The hydrogen–air reactive mixture described by detailed mass-action kinetics is employed as a paradigm in this work.

To my lovely wife, Muna.

TABLE OF CONTENTS

LIST OF FIGURES

LIST OF TABLES

ACKNOWLEDGMENTS

I would like to thank my advisor Prof. Joseph M. Powers for his extraordinary support, continuous guidance, teaching, and valuable insight throughout my graduate work. He has been extremely helpful in improving my writing and communication skills. His contributions towards my education are gratefully acknowledged, and all the words are unable to describe my sincere gratitude to him.

I am also grateful to Profs. Samuel Paolucci, Andrew J. Sommese, and Meng Wang for serving on my committee. I would like to thank Prof. Samuel Paolucci for his contribution to my research work, and his valuable advice. Also, I acknowledge my research group from the Mathematics Department, Prof. Andrew J. Sommese, Dr. Jeffery A. Diller, and Dr. Jonathan D. Hauenstein, for collaborating with me in the construction of the slow invariant manifolds. I acknowledge my colleague Mr. Joshua D. Mengers for collaborating with me in the investigation of the relation between thermodynamics and reactive systems dynamics as well as Dr. Michael J. Davis from Argonne National Laboratories for useful discussions regarding laminar flame theory. I am thankful for the friendship of many graduate students who shared the 300 and 321 Cushing offices with me, especially Dr. John Kamel, Dr. Weiming Li, Mr. Jason Mayes, Mr. Gianluca Puliti, and Dr. Damrongsak Wirasaet.

I thank all the faculty and staff of the Department of Aerospace and Mechani-

cal Engineering at the University of Notre Dame, and I would like to acknowledge the financial support of the National Science Foundation (NSF), the Center for Applied Mathematics at the University of Notre Dame (CAM), and Argonne National Laboratories.

Finally and most importantly, I thank my parents for their dedication and unlimited love and support.

NOMENCLATURE

Roman Letters

A	Helmholtz free energy, erg.
$\mathcal{A}$	Collision frequency factor, $(mol/cm^3)^{1-\sum_{i=1}^{N}\nu'_{ij}}/(s\ K^{\beta})$.
a	Random number.
a, b	Scaling coefficients.
C, c	Constants.
c_p	Specific heat at constant pressure, $erg/(g\ K)$.
D	A constant diffusion coefficient, cm^2/s.
D^T	Thermal diffusion coefficient, $g/(cm\ s)$.
$\mathfrak{D}$	Multicomponent diffusion coefficient matrix, cm^2/s.
$\mathfrak{D}$	The species projection matrix.
d	Molecular collision cross-section diameter, cm.
E, e	Total and specific internal energy, $erg, erg/g$.
F, f	Non-linear functions.
g	General algebraic function.
G, g	Total and specific Gibbs free energy, $erg, erg/g$.
$\mathbf{H}$	Hessian matrix.
H, h	Total and specific enthalpy, $erg, erg/g$.
$\mathbf{I}$	The identity matrix.

$I, \overline{I}$	An equilibrium located at infinity and its antipodal counterpoint.
$\mathbf{J}$	Jacobian matrix.
J	Total number of reactions.
j^m	Element mass flux, $g/(cm^2\ s)$.
J^m	Diffusive mass flux, $g/(cm^2\ s)$.
J^q	Energy flux, $erg/(cm^2\ s)$.
K	Boltzman's constant; $1.381 \times 10^{-16}\ erg/K$.
K^c	Equilibrium constant, $(mol/cm^3)^{\sum_{i=1}^{N} \nu_{ij}}$.
k	Thermal conductivity, $erg/(cm\ K\ s)$.
k	Arrhenius kinetic rate, $(mol/cm^3)^{1-\sum_{i=1}^{N} \nu'_{ij}}\ /s$.
L	Total number of atomic elements.
$\mathbf{L}$	A lower triangular matrix.
L	Spatial length, cm.
M	The Mach number.
M	The third body symbol.
m, m	Mass, g.
N	Total number of molecular species.
$\mathcal{N}$	Avogadro's number; $6.022 \times 10^{23}\ 1/mol$.
$\mathcal{N}$	Number of spatial grid points.
n, n	Number of moles, mol.
$\mathfrak{n}$	An eigenfunction's number of zero crossings.
P	A homogeneous term in a polynomial.
p	Pressure, $atm = 1.01325 \times 10^6\ dyne/cm^2$.
Q	Heat transfer, erg.

$\mathfrak{q}$	Polynomial maximum degree.
q	Fourier's heat flux, $erg/(cm^2\ s)$.
R	The dimension of the reduced composition space.
r	Reaction rate, $mol/(cm^3\ s)$.
S, s	Total and specific entropy, $erg/K, erg/(g\ K)$.
S_L	Flame speed, cm/s.
$\mathcal{S}$	Stiffness.
S	Composition space contraction factor.
$\mathcal{S}$	Poincaré sphere.
$\mathbb{S}$	The physically accessible domain.
T	Temperature, K.
T	A free parameter.
t	Time, s.
$\mathfrak{t}$	Homotopy index.
$\mathfrak{t}$	The projective space independent variable, $s(g/mol)^{\mathfrak{q}-1}$.
$\mathbf{U}$	An upper triangular matrix.
$\mathcal{U}$	Dependent variable in Poincaré sphere.
u	Velocity, cm/s.
V	Volume, cm^3.
W	Work, erg.
$\dot{w}$	Molar production rate per unit volume in the reduced composition space, $mol/(g\ s)$.
X	Mole fraction.
x	Spatial coordinate, cm.
Y	Molecular mass fraction.

y	Element mass fraction.
Z	Projective space dependent variable.
z	Dependent variable.

Greek Letters

α	Coefficient of the third body collision efficiency.
β	Temperature-dependency exponent.
Γ	Scaled polynomials.
δ_{ij}	Kronecker delta.
ϵ	A small number.
ζ	Scaled dependent variable.
η	Viscosity coefficient, $g/(cm\ s)$.
κ	Wavenumber, $1/cm$.
θ	An angle, rad.
$\Lambda, \widehat{\Lambda}$	Regular and modified wavelength, cm.
λ	Eigenvalue.
$\bar{\mu}$	The chemical potential, erg/mol.
ν	Net stoichiometric coefficient.
ν', ν''	Stoichiometric coefficient of a reactant and product.
ξ	The relaxation collision number.
ρ	Density, g/cm^3.
σ	Irreversibility production rate, $erg/(K\ s)$.
ς	Lennard-Jones collision diameter, cm
$\boldsymbol{\tau}$	The viscous stress tensor, $dyne/cm^2$.
τ	Time scale, s.

υ Eigenvector.

Φ The equivalence ratio.

ϕ Element index matrix.

χ Chemical symbol.

Ω Collision integral.

$\dot{\omega}$ Molar production rates per unit volume, $mol/(cm^3\ s)$.

Symbols

$\mathscr{A}, \mathscr{B}, \mathscr{C}$ Collision integral ratios.

$\mathscr{D}$ Binary diffusion coefficient, cm^2/s.

$\bar{\mathcal{E}}$ Activation energy, $cal/mol = 4.1868 \times 10^7\ erg/mol$

$\mathscr{F}$ A functional.

$\mathcal{G}$ Poincaré sphere's equator equation.

$\mathcal{H}$ Homotopy mapping.

$\mathtt{i}$ The imaginary number; $\sqrt{-1}$.

$\mathcal{L}$ Linear operator.

ℓ Length scale, cm.

$\mathcal{O}()$ Order of ( ).

$\mathcal{P}$ Projective space mapping.

Re The real part.

$\bar{\Re}$ The universal gas constant; $8.314 \times 10^7\ erg/(mol\ K)$.

∇ The spatial gradient operator, $1/cm$.

Superscripts

B Backward elementary reaction.

F	Forward elementary reaction.
T	Transpose.
e	Property at equilibrium state.
f	Formation.
o	Reference property or property at reference conditions.
$*$	Property at initial condition.
$-$	Property on a molar basis.
$\sim$	Property in Eulerian frame.
$'$	Perturbed quantity.

Subscripts

f	Specified quantity.
i, j, k, l	Indices.
t	Temporal.
x	Spatial.
u	Property at unburned state.
$*$	Arbitrarily selected quantity.

CHAPTER 1

INTRODUCTION

In recent years, there have been orders of magnitude enhancements in computational capabilities, enabled by improvement in both hardware and software, which have spurred the scientific and engineering community to employ mathematical models to solve challenging physical problems. Some of the most difficult of these are of multiscale nature; such problems are characterized by physics that evolve over a wide range of scales. Typical examples are found in combustion [1, 2], biochemistry [3, 4], oceanography [5], and atmospheric chemistry [6], where a number of physical and chemical processes that occur at different scales exist.

In simulating multiscale problems, the presence of a broad range of scales incurs a large computational cost [7]. In addition, to have confidence in the computational results, and to guarantee that they can be repeated by other researchers with their own particular algorithms, predictions should be accompanied by evidence that all physical scales inherent in the mathematical model have been captured.

It is well understood that in any mathematically based scientific theory, associated computations should have fidelity with the underlying mathematics, and the underlying mathematical model has to represent the observed physics. The first issue is demonstrated by comparing computational results with another known solution and/or performing a formal grid convergence study, while the second issue is demonstrated by comparing the computational predictions with experimental

data. Addressing these two issues, in this order, is a necessity in any computational study to build confidence in both the simulation strategy and the underlying mathematical model.

The exercise of demonstrating the harmony of the discrete solution with the foundational mathematics is known as verification [8]. For multiscale problems, verification is difficult due to the range of the scales, which may span many orders of magnitude. As the range of scales widens, solution verification becomes increasingly difficult. In this kind of problem, usually modeled by nonlinear equations, significant coupling across the scales can occur, so that errors at small scales can rapidly cascade to the large scales. Moreover, the strength of the coupling across the scales is not known *a priori*. So, all the physical scales of the mathematical model have to be captured in order to have full confidence that predictions are repeatable, grid-independent, and thus verifiable. Subsequently, in the validation step one can choose what physical phenomena and to what accuracy one wants to reproduce experiments.

Chemically reactive flow simulation involves solving a large set of partial differential equations (PDEs) which represent chemical species evolution coupled with the conservation axioms of mass, momentum, and energy. In addition, reactive systems contain a broad range of spatial and temporal scales. As the scales' range widens, more stringent demands arise to assure the numerical stability of the solution algorithm, and the accuracy of the results. The computational cost for such simulations increases with the scales' range, the number of species, and the number of reactions. For combustion problems, which are inherently unsteady and spatially inhomogeneous, the dynamics are often crucial, and proper numerical resolution of all time and spatial scales can be critical to draw correct conclusions.

Subsequently, it is a priority to determine the physical, spatial and temporal, scales inherent in such problems. Furthermore, combustion processes are events in which reaction, advection, and diffusion scales are fully coupled. Thus, for accurate modeling, the interplay between chemistry and transport needs to be captured.

In the combustion literature, there is some ambiguity about what constitutes a resolved solution. Most consider a calculation to be resolved if certain global or derived quantities are insensitive to grid size. Indeed, these are necessary conditions. However, as discussed by Roache [9], convergence of global quantities only is not a sufficient indicator of a fully resolved solution, and taken alone can lead to incorrect conclusions. While a derived quantity may be a function of the dependent variables, it may be insensitive to errors in some of them. Which variables they are insensitive to is problem-dependent, and impossible to determine *a priori*. Thus, following Roache, we adopt the more rigorous characterization of a resolved solution as one in which *all dependent variables* throughout the spatio-temporal domain are insensitive to changes in spatio-temporal discretization size is needed. This more demanding characterization is fully consistent with standard notions found in the broader mathematical and scientific computing literature, *cf.* [10–14].

1.1 Motivation and objective

For spatially inhomogeneous reactive systems, the employed models need to adequately describe all the involved physical processes in order to obtain fidelity with experiment. Thus, it became a necessity to employ a detailed kinetics model to describe the reaction process [2], and a detailed multicomponent model to describe the transport processes [15, 16]. Obtaining resolved solutions of such

model problems is a challenge that requires a prohibitive computational resources; *e.g.* Wang and Trouvé [17] report that to perform a single simulation for 6.4×10^{-2} s to simulate the flame-wall interactions, the total computational cost was 39100 processor hours using 256 processors on two super-computers. Since, in most cases, this difficulty is induced by the reaction term, the majority of the developed algorithms to make the calculation of combustion processes feasible focus on reducing the computational cost imposed by the use of detailed kinetics.

In detailed chemical kinetics models, the presence of a wide range of scales adds a large computational cost. A typical reaction mechanism for a real fuel involves more than 1000 molecular species; *e.g.* the detailed kinetics mechanism for the n-heptane contains 1034 species that react in 4326 reaction steps [18]. However, employing detailed chemical kinetics is essential in order to obtain accurate results and draw correct conclusions [2]. Hence, numerous methods based on several approaches have been proposed in the literature to reduce the computational cost of simulating reactive systems described by detailed kinetics [19–48]. The main challenge for these methods is to simplify the model equations without significant loss of accuracy.

For spatially homogeneous reactive systems, reaction dynamics are described by a set of non-linear coupled ordinary differential equations (ODEs) [49]. The solutions of this set of ODEs are represented by trajectories in the species composition space. Each trajectory represents the reactive system's evolution with time for a specific initial condition. After a short transient, the evolved trajectories seem to be attracted to a special trajectory and stay exponentially close to it until they reach equilibrium in infinite time [29]. The reactive system's slow modes are the only active ones on this special trajectory. This implies that these mani-

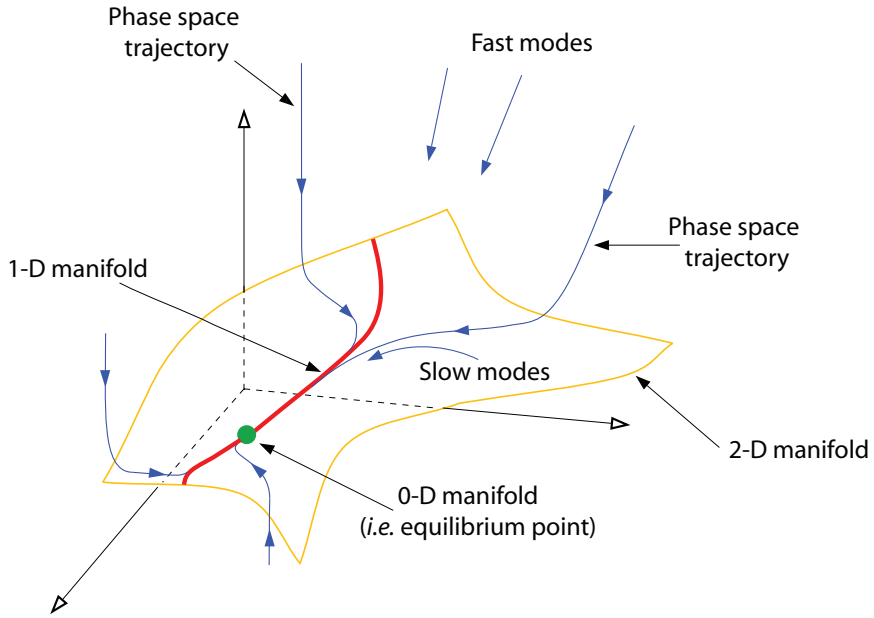

Figure 1.1. A lower dimensional manifolds in the composition phase space of a three-dimensional reaction system.

folds, which are of smaller dimension than the full composition space dimension; see Fig. 1.1, can describe the systems slow dynamics [45]. Thus, identifying this manifold for a reactive system makes it possible to reduce the computational cost by filtering the system's fast modes. Such an approach relies on identifying these manifolds within the species composition space which describes the slow dynamics of a reactive system [37, 39, 41, 50, 51].

The dimension reduction approach can significantly reduce the computational cost of modeling the detailed kinetics of a reactive system [37]. This approach is based on representing the chemistry of a reactive system's variables in terms of the chemistry of a reduced number of variables, such that the reduced variables retain only the original system's slow dynamics. So, by constructing the slow invariant manifold (SIM) for a reactive system, the asymptotic structure of the

invariant attracting reactive system's trajectories during their relaxation toward equilibrium is captured.

This dissertation will focus on the development of an accurate and rational algorithm to reduce the computational cost of simulating combustion processes modeled by detailed kinetics. Explicitly, the main intent of this work is to reduce the reacting system's model equations in a way that maintains fidelity with the underlying physics. To accomplish this aim, the scale spectrum over which a reactive flow problem evolves needs to be calculated, and the system's fine scales admitted by the physics have to be identified. Based on a rigorous analysis of these fine scales, an innovative method to describe the reacting system's slow dynamics is to be developed. A secondary set of goals of this research is to explore the fine scale coupling, and to investigate the non-equilibrium thermodynamics of the closed reacting system.

1.2 Literature review

Over the past decades, numerous methods have been developed to reduce the computational burden imposed by the use of detailed chemical kinetics in modeling reacting systems; some of them are reviewed by Refs. [1, 52]. These methods can be classified into several major groups, where each group relies upon a different approach. In this section, a summary of these methods is presented.

The first group of these methods employs several strategies to reduce the number of species and reaction steps in the employed reaction mechanism [19, 21, 22, 53–65]. These methods are employed to extract a skeletal mechanism from a detailed kinetics mechanism by the elimination of the inconsequential species and/or reaction based on a specific strategy. The first method in this group is based on

describing a detailed kinetics mechanism by one- or two-steps model [53–59]. This method employs a curve-fitting of the reaction rates to eliminate most of the intermediate species and steps in the reaction mechanism. Although this method might capture some of the detailed kinetics model's features, it has an *ad hoc* basis. However, it is a useful tool to investigate complex physical phenomena, *e.g.* flame instability [60, 61]. Employing sensitivity analysis [62–65] to eliminate inconsequential species and reaction steps is another method in this group. To accomplish such a task, a sensitivity parameter for each species in the reacting mixture is defined based on the molar production rates of all the other species. For each species, this parameter are assumed to sense the effect of changing its presence in the mixture on the reactive system's dynamics. The sensitivity parameters that do not meet a desired precision threshold, which is arbitrarily-assigned, imply that the corresponding species have negligible effects. Thus, these species and all the reaction steps in which they take part are eliminated from the reaction mechanism. Furthermore, following comparable procedure, redundant reaction steps, which have weak contribution, are eliminated from the original detailed mechanism. Here, the results for minor species are significantly deviated [52], and the thermodynamic state of the mixture is flawed. Several strategies to perform sensitivity analysis in chemical kinetic modeling are discussed by Kramer *et al.* [66]. Another method in this group employs optimization approaches [19, 20] to reduce the kinetic mechanism in terms of reaction steps and species. By formulating and solving a discrete constrained optimization problem, for a user-specified number of species or reactions, the optimal number of reaction steps is found. However, the optimization problem is non-linear, and solving it is not a straightforward task. The directed relation graph method [21, 22] is another method in this group

which employs the simple digraph technique. In this method, only the species that exist in the reaction steps that are significant to the production of specific, user-specified, species are included in the skeletal mechanism. Moreover, these user-specified species need to be experimentally measured. Although these methods significantly reduce the number of reaction steps and/or the number of species in the reaction mechanism, no significant computational saving is gained; these methods do not reduce the reactive system's stiffness.

The second group of methods have been developed to reduce the stiffness associated with modeling spatially homogeneous reactive systems. One of these methods is the lumping technique [23–26], which employs a transformation to represent the original reactive species by a subset of them. Such transformations depend on *a priori* knowledge of the reaction chemistry, and they might be linear [23, 24] or non-linear [25, 26]. The main challenge of this method is to identify the lumping transformation function, and its inverse, that retain accurate representation of the original reaction mechanism. Another widely used method in this group, which has been described in Warnatz *et al.* [67], is the quasi steady-state assumption (QSSA) [68, 69]. In this method, species that react at fast time scales, in comparison to other species in the mixture, are assumed to be in a pseudo-steady state. Consequently, the evolution of these species is described by a set of algebraic constraints instead of ODEs; the reactive system becomes modeled by a set of differential algebraic equations (DAEs). Although QSSA captures some of the reactive system's dynamics, it is based on an *ad hoc* analysis of the temporal scales, requires an extensive knowledge of the reaction's chemistry, and its accuracy remains questionable [70].

The third group of methods relies upon the dimension reduction approach [27–

48]. Within this approach, two major techniques exist. The first set of methods employs local linear time scale analysis to separate the system's modes into fast and slow, such as intrinsic low-dimensional manifolds (ILDM) [27], computational singular perturbation (CSP) [29–31], the global quasi-linearization (GQL) [28], and the G-Scheme [32]. In these methods, the dynamics are segregated using chemical bases. These bases are generated *a priori* in the ILDM, while in CSP and the G-Scheme they are estimated locally. Although ILDM is the more efficient than the G-Scheme and the CSP, it is less accurate than CSP [71]. Furthermore, the calculated manifolds using ILDM and GQL are not invariant [72]. Detailed description of CSP and ILDM methods are provided by Singh [73].

The second set of methods, some of which will be discussed in detail later on in this work, employs a geometrical approach to describe the multiscale kinetics. Examples include the iterative algorithms [43–46], the minimal entropy production trajectory (MEPT) method [41, 42], the method of invariant manifold (MIM) [39, 40], the rate-controlled constrained equilibrium (RCCE) method [33–35], and the invariant constrained equilibrium edge preimage curve method (ICE-PIC) [37, 38].

The iterative algorithms are the most accurate among these approaches [47]. They are based on constructing the attractive invariant manifold from the system trajectories by solving an algebraic functional equation, *i.e.* invariance equation, iteratively, and constructing the attractive invariant manifold from the system trajectories. The functional equation is obtained from the underlying system of differential equations within a composition phase space formulation. Although these methods have a rapid rate of convergence, they require a sufficiently accurate initial guess to converge [45]. Also, these methods have been used only for small model systems.

The RCCE method is based on describing the dynamical evolution of the reactive system via the kinetics of the species associated with the slower time scales. The remaining species are calculated via a constrained extremization of the appropriate classical thermodynamics quantity, *e.g.* Gibbs free energy, Helmhoiltz free energy, or entropy. It assumes that the reactive system evolves through a series of pseudo-equilibrium states, which are determined by the local constraints posed from the system's thermodynamic state. Thus, the resulting manifold from RCCE is composed of compositions in constrained chemical equilibrium, *i.e.* it depends solely on classical thermodynamics. Although this method is computationally efficient, the generated manifolds are not invariant [37].

The MIM method employ an arbitrary thermodynamic projector to construct the reactive system's SIM. It is based on formulating an equation to account for the condition of invariance, and by solving this equation iteratively, an invariant manifold is identified.

The MEPT is based on the optimization of trajectories subject to given constraints. The resulting trajectories are supposed to be maximally relaxed with respect to an optimization criterion; which is the minimal entropy production rate. Thus, the MEPT approach relies on the concept of minimum entropy production [74]. The validity of this principle has been called into question in other fields, *e.g.* heat diffusion [75]. Moreover, this approach assures that at least an approximation of slow attracting manifolds is found even in regions where there is no SIM [76].

The ICE-PIC method is developed based on the RCCE strategy to construct a constrained equilibrium manifold (CEM); by locally minimizing the appropriate thermodynamics variable, a subspace within the composition phase space is iden-

tified. But this method is computationally expensive, and it is not more accurate than the ILDM.

In general, MEPT, MIM, RCCE, and ICE-PIC methods employ classical thermodynamics far from the equilibrium state to construct the attractive manifolds. Such a speculation to elucidate the reactive systems' slow dynamics has been shown to have inherent flaws [76]. Moreover, while results from these methods may seem intuitive, a comparisons of two of them with the actual SIMs show that they are inaccurate in describing the reactive systems' slow dynamics.

Also, within this group, the Davis and Skodje method [45, 46], which is based on a global composition space analysis of the full dynamics of a reactive system, was able to construct the actual SIMs. However, such construction has been done only for small model systems. With the exceptions of the iterative algorithms and the technique presented by Davis and Skodje, all previously discussed methods, and any other method based on them, only approximate the reactive systems' actual SIMs or parts of them.

For completeness, most of the chemically reacting systems are spatially inhomogeneous. Several strategies have been developed to reduce the computational cost of modeling such systems. The majority of these reduction techniques are based on extending one of the previous methods, which approximate the SIM, to include the diffusion effect [28, 72, 77–90]. Some of these methods identify the reaction-based manifolds, and then project the transport processes onto it [37, 77–79]. Such an approach cannot account for the coupling between transport and chemistry. The second approach relies on incorporating the transport when the manifold is constructed [72, 81–83, 85–90], to retain the coupling between chemistry and transport.

On the other hand, fewer approaches have been developed to reduce the computational cost associated with transport. Most of them rely on adopting simple diffusion forms based on Fick's law [90, 91]. Mathematically, employing Fick's law causes the mixture mass not to be conserved [92]. To solve this issue, an equal diffusivity is used which may produce a significant error [93], or a correction term is added which is a first order approximation [94]. Another new approach is based on grouping species with similar diffusivity, such as species bundling [95]. Although this approach causes relatively small error, the computational time is not affected.

The effect of adopting simplified transport models has been clarified in the literature [15, 96–98]. Neglecting the thermal diffusion terms causes a significant change in the structure of two-dimensional flames [96]. Also, it leads to a large error in the calculation of flame speed [98]. Utilizing detailed heat flux description is a necessity in simulating confined flames [97], and simplifying mass fluxes is inaccurate [98]. So, to obtain accurate predictions it is important to employ the multicomponent transport model [15].

In general, with current computational capabilities, calculating the diffusion components is computationally inexpensive, but to draw a correct conclusion based on our expected predictions, the full multicomponent model will be employed, wherever it applicable, in this work.

1.3 Outline

This dissertation is organized as follows. In Chapter 2, the required mathematical foundation and the complete system of equations in a general form are presented for an unsteady spatially inhomogeneous reactive flow problem modeled

by detailed mass-action kinetics and multicomponent transport. This is followed by a reduction of the general mathematical form of the complete system into a simple mathematical form that describes a one–dimensional unsteady spatially inhomogeneous reactive flow problem under the low-Mach number limit. In Chapter 3, the reactive flow problems scales are identified. First, the time evolution of the spatially homogeneous version of the reactive system is obtained, and the time scale spectrum over which the system evolves is calculated. Then, a robust method to rigorously calculate the finest length scale for a steady laminar premixed flame propagating freely in a mixture of calorically imperfect ideal gases is developed. This followed by a fine scale analysis of the laminar premixed flame, and the coupling between temporal and spatial scales is investigated. Chapter 4 offers the first construction of a SIM for a realistic detailed kinetics system. First, the proposed method to construct the actual SIM for a closed, isothermal, spatially homogenous reacting system is presented in a geometric frame. Then, several model cases are introduced, and their actual SIMs are constructed. In Chapter 5, the relation between the isothermal reactive systems slow dynamics and notions from the thermodynamics, equilibrium and non-equilibrium, is addressed and revealed. Finally, specific conclusions and suggestions of promising areas for future research are stated in Chapter 6.

CHAPTER 2

MATHEMATICAL BACKGROUND

A complete exposition of the fundamental definitions, axioms, relations, and constraints that will be used throughout this dissertation are given in this chapter. The superscripts $(^o)$ and $(^f)$ denote evaluation at reference conditions and at formation, respectively, and quantities with an overbar $(^{-})$ denote the evaluation of quantities on a molar basis.

2.1 Preliminary analysis

Consider a volume V in which a reactive mixture consisting of N molecular species composed of L atomic elements is contained. The chemical interaction between the species within V is described by a reaction mechanism which consists of J reversible reaction steps. A compact notation of a reaction mechanism is given by

$$\sum_{i=1}^{N} \nu'_{ij} \chi_i \rightleftharpoons \sum_{i=1}^{N} \nu''_{ij} \chi_i, \quad j = 1, \ldots, J. \tag{2.1}$$

Here, χ_i is the chemical symbol of the i^{th} species, and for the j^{th} reaction, ν'_{ij} and ν''_{ij} are the stoichiometric coefficients of species i, denoting the number of moles of reactants and products, respectively.

2.1.1 Element constraints

Each molecular species is composed of at most L atomic elements, and each element has an elemental mass $\bar{\mathsf{m}}_l$. Thus, the molecular mass of the i^{th} species, $\bar{m}_i$, is given by

$$\bar{m}_i = \sum_{l=1}^{L} \bar{\mathsf{m}}_l \phi_{li}, \quad i = 1, \ldots, N. \tag{2.2a}$$

Here, ϕ_{li} is the element index matrix which provides the number of moles of element l in the i^{th} species. The total number of moles of the l^{th} element in the mixture n_l is given by

$$\mathsf{n}_l = \sum_{i=1}^{N} \phi_{li} n_i, \quad l = 1, \ldots, L. \tag{2.2b}$$

Here, n_i is the number of moles of species i in the mixture. Subsequently, the molecular mass of each species m_i is given by

$$m_i = n_i \bar{m}_i, \quad i = 1, \ldots, N. \tag{2.2c}$$

Throughout any chemical reaction process, in the absence of nuclear reactions, the number of moles of each element in each reaction is a conserved quantity. This molar balance is enforced by the following stoichiometric constraint on element l in reaction j,

$$\sum_{i=1}^{N} \phi_{li} \nu_{ij} = 0, \quad l = 1, \ldots, L, \quad j = 1, \ldots, J. \tag{2.3}$$

Here, $\nu_{ij} = \nu''_{ij} - \nu'_{ij}$ is the stoichiometric matrix, which gives the net stoichiometric coefficient for species i in reaction j. Equation (2.3) demands that ν_{ij} lie in the right null space of ϕ_{li}, and physically means that the mass and number of moles of each element are conserved in each reaction. In general, ϕ_{li} and ν_{ij} are non-square

matrices of dimensions $L \times N$ and $N \times J$, respectively. However, ϕ_{li} is of full rank, while ν_{ij} is of rank $R \leq (N - L)$. This implies that the chemical interaction between the N species can be described using R species.

2.1.2 Thermodynamic properties

Attention will be restricted to mixtures of calorically imperfect ideal gases obeying Dalton's model for ideal mixtures. This implies that the thermal equation of state is given by [99]

$$p = \sum_{i=1}^{N} p_i = \frac{\bar{\Re} T}{V} \sum_{i=1}^{N} n_i, \tag{2.4}$$

where p is the mixture pressure, p_i is the partial pressure of species i, T is the mixture temperature, and $\bar{\Re} = 8.314 \times 10^7 \; erg/mol/K$ is the universal gas constant. Also, for the i^{th} species, the mass-based specific internal energy e_i, enthalpy h_i, and entropy s_i are given, respectively, by the following constitutive relations,

$$e_i\left(T\right) = h_i\left(T\right) - \frac{\bar{\Re} T}{\bar{m}_i}, \quad i = 1, \ldots, N, \tag{2.5a}$$

$$h_i\left(T\right) = h_i^o\left(T\right) = h_i^f + \int_{T^o}^{T} c_{pi}(\hat{T}) \; d\hat{T}, \quad i = 1, \ldots, N, \tag{2.5b}$$

$$s_i\left(T, p_i\right) = \underbrace{s_i^f + \int_{T^o}^{T} \frac{c_{pi}(\hat{T})}{\hat{T}} \; d\hat{T}}_{s_i^o(T)} - \frac{\bar{\Re}}{\bar{m}_i} \ln\left(\frac{p_i}{p^o}\right), \quad i = 1, \ldots, N. \tag{2.5c}$$

In Eqs. (2.5), $T^o = 298 \; K$ is the reference state temperature, $p^o = 1 \; atm$ is the reference pressure, and for the i^{th} species, h_i^f, s_i^f, and c_{pi} are the mass-based specific enthalpy of formation, entropy of formation, and specific heat at constant pressure, respectively. These thermodynamic properties in molar-based units can be obtained by multiplying Eqs. (2.5) with the species molecular mass; $\bar{e}_i = e_i \bar{m}_i, \bar{h}_i = h_i \bar{m}_i, \bar{s}_i = s_i \bar{m}_i$. Moreover, the molar-based chemical potential $\bar{\mu}_i$

of species i is given by

$$\bar{\mu}_i\left(T, p_i\right) = \bar{g}_i\left(T, p, n_i\right) = \bar{\mu}_i^o\left(T\right) + \bar{\Re} T \ln\left(\frac{p_i}{p^o}\right), \quad i = 1, \ldots, N, \tag{2.6a}$$

$$\bar{\mu}_i^o\left(T\right) = \bar{h}_i^o\left(T\right) - T\bar{s}_i^o\left(T\right), \quad i = 1, \ldots, N, \tag{2.6b}$$

where for the i^{th} species $\bar{\mu}_i^o$ and $\bar{g}_i = g_i \bar{m}_i$ are the molar-based chemical potential at the reference pressure and specific Gibbs free energy, respectively.

2.1.3 Gas mixture properties

Now, we denote the total mass of the mixture as $m = \sum_{i=1}^{N} m_i$, and the total number of moles in the mixture as $n = \sum_{i=1}^{N} n_i$. So, $\bar{m} = m/n$ is the mixture molecular mass, and $\rho = m/V$ is the mixture mass density. Subsequently, the i^{th} species in the mixture can be characterized by any of these variables: mass fraction $Y_i = m_i/m$, mole fraction $X_i = n_i/n$, or molar density $\bar{\rho}_i = n_i/V$, *i.e.* concentration. The relation between these variables is

$$\frac{Y_i}{\bar{m}_i} = \frac{\bar{\rho}_i}{\rho} = \frac{X_i}{\bar{m}}, \quad i = 1, \ldots, N, \tag{2.7}$$

where it is clear from their definitions that

$$\sum_{i=1}^{N} Y_i = 1, \tag{2.8a}$$

$$\sum_{i=1}^{N} X_i = 1, \tag{2.8b}$$

$$\sum_{i=1}^{N} \bar{\rho}_i = \frac{p}{\bar{\Re} T}. \tag{2.8c}$$

The mass-based mixture-average specific heat at constant pressure c_p, internal energy e, enthalpy h, entropy s, and Gibbs free energy g are given by

$$c_p = \sum_{i=1}^{N} Y_i c_{pi}. \tag{2.9a}$$

$$e = \sum_{i=1}^{N} Y_i e_i, \tag{2.9b}$$

$$h = \sum_{i=1}^{N} Y_i h_i, \tag{2.9c}$$

$$s = \sum_{i=1}^{N} Y_i s_i, \tag{2.9d}$$

$$g = \sum_{i=1}^{N} Y_i g_i, \tag{2.9e}$$

and the mixture total internal energy E, enthalpy H, entropy S, and Gibbs free energy G are given by

$$E = me = \sum_{i=1}^{N} m_i e_i = \sum_{i=1}^{N} n_i \bar{e}_i, \tag{2.10a}$$

$$H = mh = \sum_{i=1}^{N} m_i h_i = \sum_{i=1}^{N} n_i \bar{h}_i, \tag{2.10b}$$

$$S = ms = \sum_{i=1}^{N} m_i s_i = \sum_{i=1}^{N} n_i \bar{s}_i, \tag{2.10c}$$

$$G = mg = \sum_{i=1}^{N} m_i g_i = \sum_{i=1}^{N} n_i \bar{g}_i = \sum_{i=1}^{N} n_i \bar{\mu}_i. \tag{2.10d}$$

2.1.4 Chemical kinetic relations

Each of the reversible reaction steps in the mechanism described by Eq. (2.1) consists of two irreversible reaction steps; the forward reaction step and the backward reaction step. The molar rate of formation per unit volume of species i as a result of the reaction mechanism is given by the following widely recognized formula, *cf.* [99–103],

$$\dot{\omega}_i = \sum_{j=1}^{J} \nu_{ij} r_j, \quad i = 1, \ldots, N, \tag{2.11}$$

where

$$r_j = \mathsf{k}_j \left(\prod_{i=1}^{N} \bar{\rho}_i{}^{\nu'_{ij}} - \frac{1}{K_j^c} \prod_{i=1}^{N} \bar{\rho}_i{}^{\nu''_{ij}} \right), \quad j = 1, \ldots, J, \tag{2.12}$$

is the reaction rate given by the law of mass action. Here, for the j^{th} reaction, k_j and K_j^c are, respectively, the Arrhenius kinetic rates given by

$$\mathsf{k}_j = \mathcal{A}_j \; T^{\beta_j} \; \exp\left(\frac{-\bar{\mathcal{E}}_j}{\bar{\Re} T} \right), \quad j = 1, \ldots, J, \tag{2.13a}$$

and the equilibrium constants given by

$$K_j^c = \left(\frac{p^o}{\bar{\Re} T} \right)^{\sum_{i=1}^{N} \nu_{ij}} \exp\left(- \frac{\sum_{i=1}^{N} \bar{\mu}_i^o \nu_{ij}}{\bar{\Re} T} \right), \quad j = 1, \ldots, J. \tag{2.13b}$$

For each reaction in Eqs. (2.13), the quantities $\mathcal{A}_j, \beta_j$, and $\bar{\mathcal{E}}_j$ represent the collision frequency factor, the temperature-dependency exponent, and the activation energy, respectively.

In the case of third body M dependency, its concentration in the j^{th} reaction is given by [67]

$$\bar{\rho}_{\mathsf{M}j} = \sum_{i=1}^{N} \alpha_{ji} \bar{\rho}_i, \quad j = 1, \ldots, J, \tag{2.14}$$

where α_{ji} are the coefficients of the collision efficiency of the i^{th} species with the third body, and these coefficients play a role only in the reactions that require a third body. For the j^{th} reaction, $\alpha_{ji} = 1, i = 1 \ldots, N$, if all the species have the same efficiency as third bodies. Otherwise, α_{ji} values differ from unity and vary between species for reaction j.

2.2 Reactive flow axioms

2.2.1 General mathematical model

The governing PDEs for a premixed reactive mixture of N gas phase molecular species which undergo J reversible reactions are taken to be the unsteady reactive Navier-Stokes equations. In conservative form, with no body force present, these $N + 4$ equations are:

$$\frac{\partial \rho}{\partial t} = -\nabla \cdot (\rho \mathbf{u}), \tag{2.15a}$$

$$\frac{\partial}{\partial t}(\rho \mathbf{u}) = -\nabla \cdot (\rho \mathbf{u}\mathbf{u} + p\mathbf{I} - \boldsymbol{\tau}), \tag{2.15b}$$

$$\frac{\partial}{\partial t}\left(\rho\left(e + \frac{\mathbf{u}\cdot\mathbf{u}}{2}\right)\right) = -\nabla \cdot \left(\rho \mathbf{u}\left(e + \frac{\mathbf{u}\cdot\mathbf{u}}{2}\right) + \mathbf{J}^q + (p\mathbf{I} - \boldsymbol{\tau}) \cdot \mathbf{u}\right), \tag{2.15c}$$

$$\frac{\partial}{\partial t}(\rho y_l) = -\nabla \cdot (\rho \mathbf{u} y_l + \mathbf{j}_l^m), \qquad l = 1, \ldots, L-1, \tag{2.15d}$$

$$\frac{\partial}{\partial t}(\rho Y_i) = -\nabla \cdot (\rho \mathbf{u} Y_i + \mathbf{J}_i^m) + \dot{\omega}_i \bar{m}_i, \qquad i = 1, \ldots, N-L, \tag{2.15e}$$

where $\nabla \equiv \{\frac{\partial}{\partial x_1}, \frac{\partial}{\partial x_2}, \frac{\partial}{\partial x_3}\}$ is the spatial gradient operator, and the independent variables are the time t and the spatial coordinates $\boldsymbol{x}$. Here, $\mathbf{u}$ is the mixture's velocity vector, $\mathbf{I}$ is the identity matrix, $\boldsymbol{\tau}$ is the viscous stress tensor, $\mathbf{J}^q$ is the energy flux vector, $\mathbf{J}_i^m$ is the diffusive mass flux vector of the i^{th} species, and for the l^{th} element, y_l and $\mathbf{j}_l^m$ are, respectively, the element mass fraction and the

element mass flux vector, which are defined as

$$y_l = \bar{\mathsf{m}}_l \sum_{i=1}^{N} \frac{\phi_{li} Y_i}{\bar{m}_i}, \quad l = 1, \ldots, L, \tag{2.16a}$$

$$\mathbf{j}_l^m = \bar{\mathsf{m}}_l \sum_{i=1}^{N} \frac{\phi_{li} \mathbf{J}_i^m}{\bar{m}_i}, \quad l = 1, \ldots, L. \tag{2.16b}$$

Equations (2.15a)–(2.15c) describe the conservation of mass, linear momentum, and energy. Together Eqs. (2.15a) and (2.15d) describe the conservation of the L atomic elements, and in conjunction with Eq. (2.15e) they describe the evolution of the N species in time.

Equation (2.15d) can be obtained by multiplying the evolution of species, Eq. (2.15e), with $\bar{\mathsf{m}}_l \phi_{li} / \bar{m}_i$ and summing from $i = 1$ to N to get

$$\frac{\partial}{\partial t}\left(\rho \sum_{i=1}^{N} \frac{\bar{\mathsf{m}}_l \phi_{li} Y_i}{\bar{m}_i}\right) = -\nabla \cdot \left(\rho \mathbf{u} \sum_{i=1}^{N} \frac{\bar{\mathsf{m}}_l \phi_{li} Y_i}{\bar{m}_i} + \sum_{i=1}^{N} \frac{\bar{\mathsf{m}}_l \phi_{li} \mathbf{J}_i^m}{\bar{m}_i}\right) + \sum_{i=1}^{N} \bar{\mathsf{m}}_l \phi_{li} \dot{\omega}_i,$$

which, by employing Eqs. (2.16a), (2.16b), and (2.11), can be rewritten as

$$\frac{\partial}{\partial t}(\rho y_l) = -\nabla \cdot (\rho \mathbf{u} y_l + \mathbf{j}_i^m) + \bar{\mathsf{m}}_l \sum_{j=1}^{J} r_j \sum_{i=1}^{N} \phi_{li} \nu_{ij}.$$

Now, using Eq. (2.3) to eliminate the second term in the right hand side, one recovers Eq. (2.15d).

Similarly, the conservation of mass, Eq. (2.15a), can be obtained by either one of these two procedures: 1) summing the evolution of species, Eq. (2.15e), from $i = 1$ to N, employing Eqs. (2.11) and (2.3), and insisting that the species mass

fluxes be constrained by [100, 104]

$$0 = \sum_{i=1}^{N} \mathbf{J}_i^m, \tag{2.17a}$$

2) summing the conservation of elements, Eq. (2.15d), from $l = 1$ to L and insisting that the element mass fluxes be constrained by

$$0 = \sum_{l=1}^{L} \mathbf{j}_l^m. \tag{2.17b}$$

Now to describe the diffusive transport of momentum, mass, and energy within a mixture, the fundamental equations for such processes are included. The following relations for $\boldsymbol{\tau}$, $\mathbf{J}_i^m$, and $\mathbf{J}^q$ are adopted [105]:

$$\boldsymbol{\tau} = \eta\left(\nabla\mathbf{u} + (\nabla\mathbf{u})^T - \frac{2}{3}(\nabla\cdot\mathbf{u})\,\mathbf{I}\right), \tag{2.18a}$$

$$\mathbf{J}_i^m = \sum_{\substack{j=1\\ j\neq i}}^{N} \frac{\rho\bar{m}_i\mathfrak{D}_{ij}Y_j}{\bar{m}}\left(\frac{\nabla X_j}{X_j} + \left(1 - \frac{\bar{m}_j}{\bar{m}}\right)\frac{\nabla p}{p}\right) - D_i^T\frac{\nabla T}{T}, \quad i = 1,\ldots,N, \tag{2.18b}$$

$$\mathbf{J}^q = \mathrm{q} + \sum_{i=1}^{N}\mathbf{J}_i^m h_i - \bar{\Re}T\sum_{i=1}^{N}\frac{D_i^T}{\bar{m}_i}\left(\frac{\nabla X_i}{X_i} + \left(1 - \frac{\bar{m}_i}{\bar{m}}\right)\frac{\nabla p}{p}\right), \tag{2.18c}$$

where

$$\mathrm{q} = -k\nabla T, \tag{2.18d}$$

In Eqs. (2.18), η is the mixture viscosity coefficient, q is the Fourier heat flux, and the variables $\mathfrak{D}_{ij}, k,$ and D_i^T are the diffusion coefficients between species i and species j, the mixture isotropic thermal conductivity, and the thermal diffusion coefficient of specie i, respectively. The last three variables, $\mathfrak{D}_{ij}, k,$ and D_i^T, are functions of thermodynamic state and molecular composition, and they are

computed from the solution of a linear system known as the detailed L-matrix system [104, 106]. Further details about this system and the calculation of these transport properties are presented in Appendix A.

Equation (2.18a) is the definition of the viscous stress tensor for a Newtonian fluid that satisfies Stokes' assumption. Equation (2.18b) states that the matter of the i^{th} species diffuses due to the existence of three driving forces. These driving forces are the mole fraction gradient, the pressure gradient, and the temperature gradient. Consequently, the first term in Eq. (2.18b) is called the material diffusion, the second term is called the pressure diffusion, and the third term is called the thermal diffusion; commonly known as Soret's effect or thermophoresis. Similarly, in Eq. (2.18c) the first term is Fourier's law which represents the heat flux due to heat diffusion, the second term is the heat flux due to mass diffusion, and the the third term is Dufour's effect which represents the heat flux due to pressure and matter gradients [100].

The presented system of PDEs, Eqs. (2.15), in addition to Eqs. (2.4)–(2.14) and Eqs. (2.16)–(2.18), as a constitutive relations, represent a complete system. This system is a general mathematical model for simulating reactive flows.

2.2.2 Simple mathematical form

Here, a simplified version of the complete system is derived by adopting several assumptions. The derived system of equations in this section will serve as the governing equations throughout this dissertation unless otherwise specified.

As a first assumption, we consider only the one-dimensional version of Eqs. (2.15)–(2.18). Then, we employ Eqs. (2.5a), (2.7), and (2.9b)–(2.9c) to rewrite the conservation of energy, Eq. (2.15c), in terms of the mixture-average spe-

cific enthalpy h. After that, by performing standard manipulations, multiplying Eq. (2.15b) with mixture velocity and subtracting the resulting equation and Eq. (2.15a) from Eq. (2.15c), the following set of equations is obtained:

$$\frac{\partial \rho}{\partial t} + \frac{\partial}{\partial x}(\rho u) = 0, \tag{2.19a}$$

$$\frac{\partial}{\partial t}(\rho u) + \frac{\partial}{\partial x}\left(\rho u^2 + p - \tau\right) = 0, \tag{2.19b}$$

$$\frac{\partial}{\partial t}(\rho h) + \frac{\partial}{\partial x}(\rho u h + \mathrm{J}^q) = \frac{\partial p}{\partial t} + u\frac{\partial p}{\partial x} + \tau\frac{\partial u}{\partial x}, \tag{2.19c}$$

$$\frac{\partial}{\partial t}(\rho y_l) + \frac{\partial}{\partial x}(\rho u y_l + \mathrm{j}_l^m) = 0, \quad l = 1, \ldots, L-1. \tag{2.19d}$$

$$\frac{\partial}{\partial t}(\rho Y_i) + \frac{\partial}{\partial x}(\rho u Y_i + \mathrm{J}_i^m) = \dot{\omega}_i \bar{m}_i, \quad i = 1, \ldots, N-L. \tag{2.19e}$$

To simplify these equations, the low-Mach number M assumption [107], which is reasonable for laminar premixed flame, *i.e.* deflagration wave, is adopted [108]. For that, a perturbation analysis with $1/M^2$ as a perturbation parameter is performed. Subsequently, Eq. (2.19b) can be reduced at leading order to $dp/dx = 0$ [107]. Furthermore, for a spatially open system, one can assume that p is time-independent [91, 109, 110], which has the consequence of rendering the thermodynamic pressure constant. Subsequently, all the thermodynamic properties are evaluated at the surrounding thermodynamic pressure. As a result of adopting this assumption, the momentum equation no longer need be considered, and the viscous dissipation $\tau\partial u/\partial x$ and the advection of pressure $u\partial p/\partial x$ in Eq. (2.19c) are

suppressed. Thus, the governing equations, in a non-conservative form, become

$$\frac{\partial \rho}{\partial t} + \frac{\partial}{\partial x}(\rho u) = 0, \tag{2.20a}$$

$$\rho \frac{\partial h}{\partial t} + \rho u \frac{\partial h}{\partial x} + \frac{\partial \mathrm{J}^q}{\partial x} = 0, \tag{2.20b}$$

$$\rho \frac{\partial y_l}{\partial t} + \rho u \frac{\partial y_l}{\partial x} + \frac{\partial \mathrm{j}_l^m}{\partial x} = 0, \quad i = 1, \ldots, L-1. \tag{2.20c}$$

$$\rho \frac{\partial Y_i}{\partial t} + \rho u \frac{\partial Y_i}{\partial x} + \frac{\partial \mathrm{J}_i^m}{\partial x} = \dot{\omega}_i \bar{m}_i, \quad i = 1, \ldots, N-L. \tag{2.20d}$$

Moreover, as a third assumption, the constitutive relations are simplified furthermore by neglecting the thermal diffusion effects, Soret's effect and Dufour's effect. So, Eqs. (2.18), after insisting that the species mass fluxes be constrained Eq. (2.17a), become

$$\mathrm{J}_i^m = \frac{\rho \bar{m}_i}{\bar{m}} \sum_{\substack{j=1 \\ j \neq i}}^{N} \frac{\mathfrak{D}_{ij} Y_j}{X_j} \frac{\partial X_j}{\partial x}, \quad i = 1, \ldots, N-1, \tag{2.21a}$$

$$\mathrm{J}^q = \mathrm{q} + \sum_{i=1}^{N} \mathrm{J}_i^m h_i, \tag{2.21b}$$

This system described by Eqs. (2.20)–(2.21) will serve as a mathematical model for this dissertation.

In a particular calculation in Sec. 3.3.5.1, for verification purposes, the Soret's effect in the mass flux model is considered to match the the model in Ref. [111]. So, in that particular calculation, the employed mass flux equation is given by

$$\mathrm{J}_i^m = \frac{\rho \bar{m}_i}{\bar{m}} \sum_{\substack{j=1 \\ j \neq i}}^{N} \frac{\mathfrak{D}_{ij} Y_j}{X_j} \frac{\partial X_j}{\partial x} - D_i^T \frac{\nabla T}{T}, \quad i = 1, \ldots, N-1. \tag{2.22}$$

CHAPTER 3

REACTIVE FLOW SCALE ANALYSIS

Here, the temporal and the spatial scales of a reactive flow problem are investigated, and the lower bounds for time step and grid resolution are provided for scenarios in which accurate knowledge of the spatio-temporal distribution of detailed species concentrations is required. Then, to gain a better understanding of the interaction between transport and chemistry, the coupling between temporal and spatial scales is explored via conducting a spectral analysis of the reactive flow problem.

The system under consideration is a standard multiscale problem: the unsteady one-dimensional laminar premixed flame propagating freely in a mixture of calorically imperfect ideal gases described by detailed kinetics and multicomponent transport, see Fig. 3.1. Many researchers have simulated this problem over the past decades, *cf.* [91, 111–116]. This problem is widely recognized as challenging [117], and part of its complexity is due to the non-linearity posed by the reaction term. To accomplish this task, the problem is first split into two separate problems that are treated independently. The first problem represents an unsteady spatially homogeneous reactive system, and the second problem represents a steady spatially inhomogeneous reactive system.

For the first problem, we identify the time scale spectrum over which the system evoloves. Analogously, the length scale spectrum inherent in the second

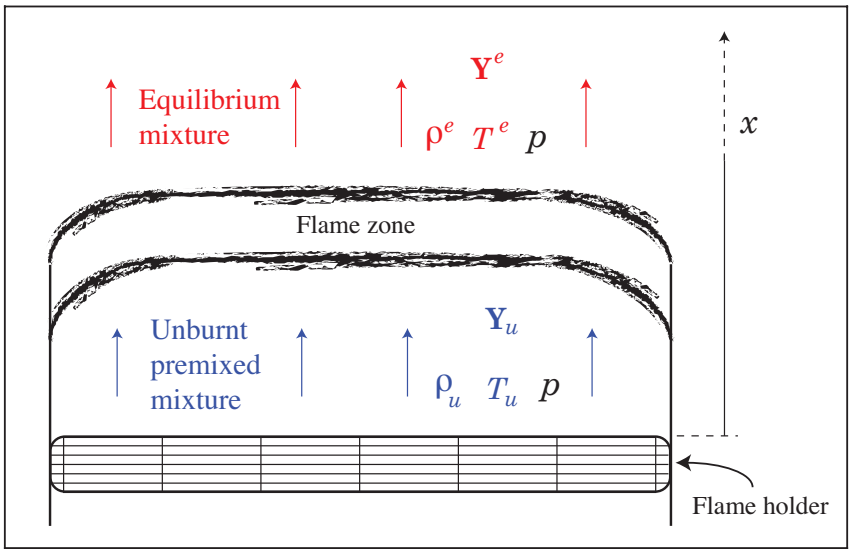

Figure 3.1. Illustration of a one-dimensional laminar premixed flame.

problem is identified. Finally, the time scales associated with each Fourier mode of varying wavelength for the full unsteady spatially inhomogeneous system are identified. We consider premixed mixtures of N calorically imperfect ideal gases that react and diffuse at N widely disparate rates; we specifically consider a model of hydrogen–air combustion.

In the first section of this chapter, a model problem is employed to present the basic idea of this chapter gradually. Then, the methodology to determine the temporal scales of the spatially homogeneous version of the governing equations is presented. This has been done briefly, since temporal scale analysis for spatially homogeneous reactive system is a well recognized and understood concept [27, 29, 67, 118]. Subsequently, this part will serve as an illustration of the concept of scale analysis. In the third section, the freely propagating steady laminar premixed flame is employed as a paradigm, and a robust method to rigorously determine the required spatial discretization to formally capture all detailed con-

tinuum physics in the reaction zone of a reactive flow is developed. This method has been used to assure that the reactive flow's structure is fully resolved. Finally, linear spectral analysis of the reactive flow problem is conducted, and the time scales associated with each Fourier mode of varying wavelength for the full unsteady spatially inhomogeneous reactive flow problem are identified.

3.1 Background

In order to acquire a better understanding of this chapter, a model problem is employed to illustrate the basic ideas.

Consider the following linear advection-diffusion-reaction problem:

$$\frac{\partial \psi(x,t)}{\partial t} + u\frac{\partial \psi(x,t)}{\partial x} = D\frac{\partial^2 \psi(x,t)}{\partial x^2} - a\psi(x,t), \tag{3.1a}$$

$$t = 0: \quad \psi(x) = \psi_u, \tag{3.1b}$$

$$x = 0: \quad \psi(t) = \psi_u, \tag{3.1c}$$

$$x \to \infty: \quad \frac{\partial \psi}{\partial x} \to 0, \tag{3.1d}$$

where the independent variables are $t > 0$ and $x \in (0, \infty)$. Here, $\psi(x,t)$ is a general scalar, $u > 0$ is a constant wave speed for a right running wave, $D > 0$ is a diffusion coefficient, and $a > 0$ is the consumption rate constant.

The spatially homogeneous version of Eqs. (3.1) is

$$\frac{d\psi_h(t)}{dt} = -a\psi_h(t), \qquad \psi_h|_{t=0} = \psi_u, \tag{3.2a}$$

which has the solution

$$\psi_h(t) = \psi_u \exp(-at). \tag{3.2b}$$

The time scale τ over which ψ_h evolves is $\tau = 1/a$. This time scale serve as an upper bound for the required time step to capture the dynamics in a numerical simulation. Since there is only one dependent variable in this problem, the temporal spectrum contains only one time scale. Consequently, this formulation of the system is not temporally stiff.

A simple means to determine an upper bound for the required grid resolution is to solve for the steady structure $\psi_s(x)$, which is governed by

$$u\frac{d\psi_s(x)}{dx} = D\frac{d^2\psi_s(x)}{dx^2} - a\psi_s(x), \qquad \psi_s|_{x=0} = \psi_u, \quad \left.\frac{d\psi_s}{dx}\right|_{x\to\infty} \to 0. \tag{3.3a}$$

The solution of Eq. (3.3a) is

$$\psi_s(x) = \psi_u \exp(\lambda x), \tag{3.3b}$$

where

$$\lambda = \frac{u}{2D}\left(1 - \sqrt{1 + \frac{4aD}{u^2}}\right). \tag{3.3c}$$

Here, there is one length scale in the system, $\ell \equiv 1/|\lambda|$; this formulation of the system is not spatially stiff. By examining Eq. (3.3c) in the limit $aD/u^2 \gg 1$, one finds that

$$\ell \approx \sqrt{\frac{D}{a}}. \tag{3.4}$$

So, this length scale ℓ reflects the inherent physics of coupled reaction-advection-diffusion.

Now, for Eqs. (3.1), it is possible to find a simple analytic expression for the continuous spectrum of time scales τ associated with a particular Fourier mode of wavenumber κ. A Fourier mode with wavenumber κ has wavelength $\Lambda = 2\pi/\kappa$.

Assume a solution of the form

$$\psi(x,t) = \Psi(t)\exp\left(\mathtt{i}\kappa x\right), \tag{3.5}$$

where $\Psi(t)$ is the time-dependent amplitude of the chosen Fourier mode. Substituting this into Eq. (3.1a) gives the following ODE:

$$\frac{d\Psi(t)}{dt} = -\left(\mathtt{i}\kappa u + D\kappa^2 + a\right)\Psi(t). \tag{3.6}$$

This has a solution of the form

$$\Psi(t) = c\exp\left(-(\mathtt{i}\kappa u + D\kappa^2 + a)\ t\right), \tag{3.7}$$

where c is an arbitrary constant. So, the continuous time scale spectrum is given by

$$\tau = \frac{1}{a\left(1 + \frac{\mathtt{i}u\kappa}{a} + \frac{D\kappa^2}{a}\right)}, \qquad 0 < \kappa \in \mathbb{R}. \tag{3.8}$$

From Eq. (3.8), it is clear that for $u\kappa/a \ll 1$ and $D\kappa^2/a \ll 1$, *i.e.* for sufficiently small wavenumbers or long wavelengths, the time scales will be dominated by reaction:

$$\lim_{\kappa\to 0}\tau = \frac{1}{a}. \tag{3.9a}$$

However, for $u\kappa/a \gg 1$ and $D\kappa^2/a \gg 1$, *i.e.* for sufficiently large wavenumbers or small wavelengths, the time scales are dominated by diffusion:

$$\lim_{\kappa\to\infty}\tau = \frac{1}{D\kappa^2} = \frac{1}{D}\left(\frac{\Lambda}{2\pi}\right)^2. \tag{3.9b}$$

It is clear that advection does not play a role in determining the limiting values

of the time scale spectrum; reaction and diffusion are the major players. Consequently, from Eq. (3.8), we see that a balance between reaction and diffusion exists for $\kappa = \sqrt{a/D}$. In terms of wavelength, and recalling Eq. (3.4), we see the balance at

$$\frac{\Lambda}{2\pi} = \sqrt{\frac{D}{a}} = \ell, \tag{3.10}$$

where $\ell = 1/\kappa$ is proportional to the wavelength.

Let us now study how the magnitude of τ varies with κ as predicted by Eq. (3.8); It can be easily checked that the magnitude of the complex τ is given by

$$|\tau| = \left[\left(a + D\kappa^2\right)^2 + (u\kappa)^2\right]^{-1/2}. \tag{3.11}$$

Additional insight is gained by examining how $|\tau|$ behaves in the short wavenumber, *i.e.* long wavelength, limit. Taylor expansion of Eq. (3.11) in this limit reveals that

$$|\tau| = \frac{1}{a}\left(1 - \frac{D\kappa^2}{a} - \frac{u^2\kappa^2}{2a^2}\right) + \mathcal{O}\left(\kappa^4\right). \tag{3.12}$$

So in the small κ limit, $|\tau|$ is dominated by reaction effects, and we see that advection and diffusion both decrease its magnitude.

We examine the behavior of the system quantitatively by choosing arbitrary numerical values of $a = 10^8\ 1/s$, $D = 10^1\ cm^2/s$, $u = 10^2\ cm/s$. For these values, we find the estimate from Eq. (3.4) for the length scale where reaction balances diffusion as $\ell = \Lambda/(2\pi) = 3.16228 \times 10^{-4}\ cm$. A plot of $|\tau|$ versus $\ell = \Lambda/(2\pi)$ from Eq. (3.11) is given in Fig. (3.2). For long wavelengths, the time scales are determined by reaction; for fine wavelengths, the time scale's falloff is dictated by diffusion, and our simple formula for the critical ℓ, illustrated as a dashed line, predicts the transition well. Lastly, for large κ, it is seen that a one decade

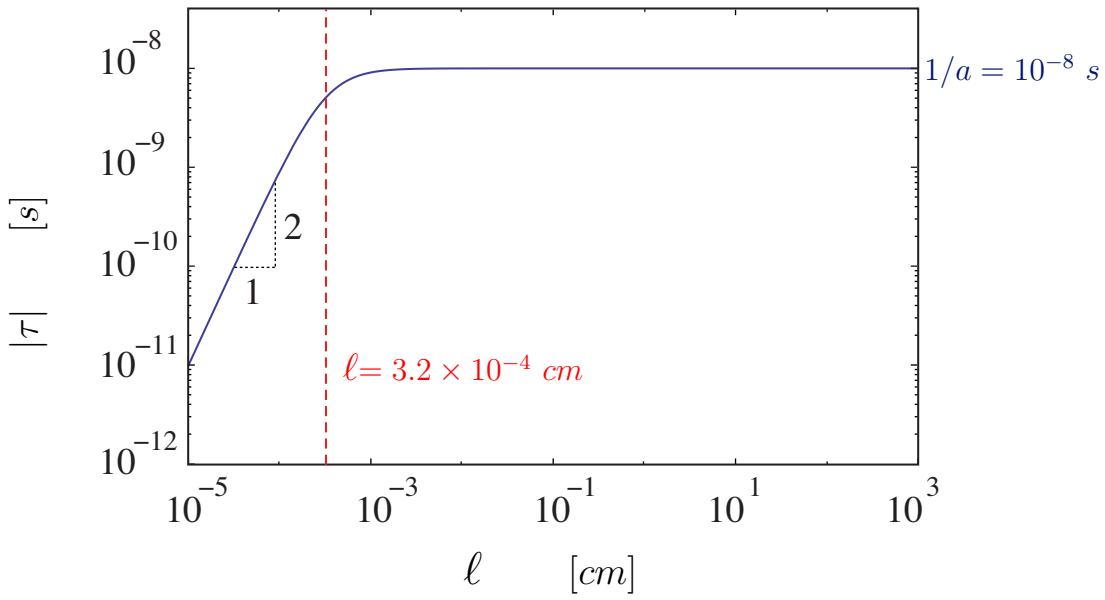

Figure 3.2. Time scale spectrum versus wavelength for the simple one species reaction-advection-diffusion system.

decrease in ℓ induces a two decade decrease in $|\tau|$, consistent with the prediction of Eq. (3.9b),

$$\lim_{\kappa \to \infty} (\ln \tau) \sim 2 \ln (\ell) - \ln (D) \,. \tag{3.13}$$

3.2 Temporal scales

Here, we confine our attention to unsteady spatially homogeneous mixtures of calorically imperfect ideal gases described by detailed kinetics. Thus, the govern-

ing equations (2.20) become

$$\frac{dh}{dt} = 0, \tag{3.14a}$$

$$\frac{dy_l}{dt} = 0, \qquad l = 1, \ldots, L, \tag{3.14b}$$

$$\frac{dY_i}{dt} = \frac{\dot{\omega}_i \bar{m}_i}{\rho}, \qquad i = 1, \ldots, N - L. \tag{3.14c}$$

Equation (3.14a) states that the mixture specific enthalpy is a conserved quantity, which implies that the system is adiabatic and isobaric, *i.e.* constant pressure. Moreover, Eq. (3.14b) implies that the L atomic elements are conserved; there are L dependent variables. For the $N - L$ dependent variables, *i.e.* species in the mixture, there are $N - L$ ODEs that describe the $N - L$ species evolution in time, Eqs. (3.14c). Further detail regards modeling spatially homogeneous reactive systems are provided in Appendix B.

In a detailed chemical kinetics model, the use of a reaction mechanism that contains several species and consists of several reaction steps will introduce a spectrum of time scales. Since each reaction has a rate given by Eq. (2.12), it will introduce its own time scale. The existence of a wide range of time scales is manifested in temporal stiffness in the governing equations. This presents a computational problem: to capture the dynamics and to assure numerical stability, the fastest time scale has to be captured. On the other hand, in approaching the equilibrium state, the slowest time scale must be achieved.

To obtain the time evolution of the spatially homogeneous reactive system, Eqs. (3.14) are integrated, starting from an initial condition, until the system comes to equilibrium. Equations (3.14) are a set of nonlinear autonomous ODEs which exhibit stiffness. The `DLSODE` [119] code is used for solving this set of ODEs.

In order to calculate the time scales over which Eqs. (3.14) evolve, a standard eigenvalue analysis is performed. Starting from the initial condition, the set of ODEs are lineraized at each time step about the local solution state, and the temporally local Jacobian matrix $\mathbf{J}$ is calculated. The local time scales τ_i over which the system evolves are given by the reciprocal of the real part of the local $\mathbf{J}$'s eigenvalues; $\tau_i = 1/\left|Re(\lambda_i)\right|$. Furthermore, the ratio between the largest and the smallest time scales, *i.e.* the slowest time scale and fastest time scale, identifies the system's temporal stiffness,

$$\mathcal{S}_t = \frac{\tau_{slowest}}{\tau_{fastest}}. \tag{3.15}$$

In general, the eigenvalues are complex, where the reciprocals of the real parts provide the scales of the amplitude growth, and the reciprocals of the imaginary parts represent the period of oscillations. Further details regarding the linearization technique are provided in Appendix C.

This work is focused on the hydrogen–air system described by the detailed kinetics mechanism extracted from Miller *et al.* [120]; it has been widely used in the literature [111, 121, 122]. This mechanism consists of $J = 19$ reversible reactions involving $N = 9$ species which are composed of $L = 3$ elements, see Table D.1. In this mechanism, the reactant species are $H_2, O_2, H, O, OH, HO_2, H_2O_2$, and H_2O. The inert diluent for the mixture is N_2. Here, a stoichiometric premixed mixture is considered, where the initial molar ratio is given by $2H_2 + O_2 + 3.76N_2$. The system was initially at $p = 1\ atm$ and $T^* = 800K$. Using `DLSODE`, the evolution of species mass fractions and temperature is presented in Fig. 3.3.

In Fig. 3.3 (a), a power law growth of the minor species is clearly noted for $t < 10^{-8}\ s$. For some minor species, this growth slightly modulates at $t \approx 10^{-8}\ s$,

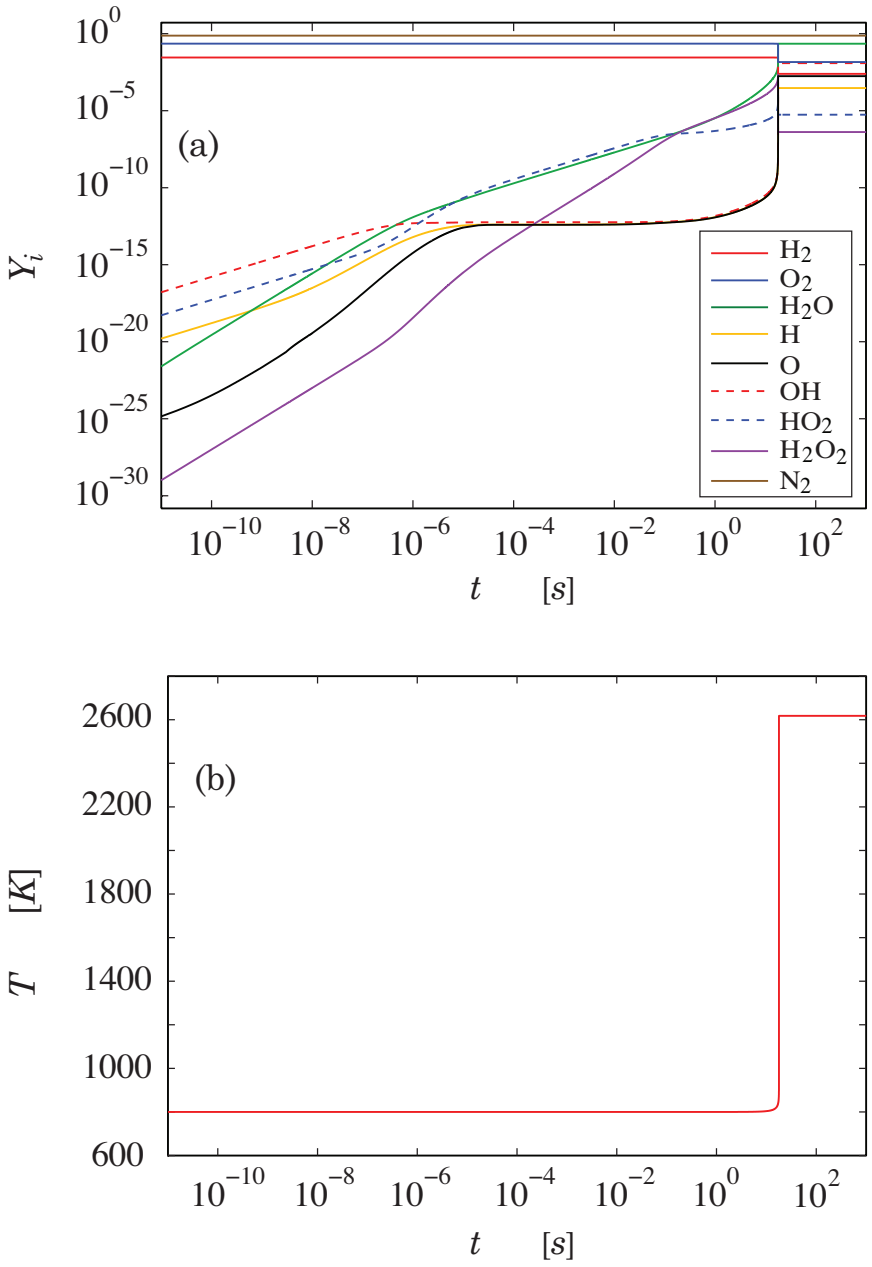

Figure 3.3. The time evolution of (a) species mass fractions, and (b) temperature for the stoichiometric hydrogen–air reactive system, $T^* = 800\ K$, $p = 1\ atm$.

which indicates that dissociation reactions are induced. At $t \approx 10^{-6}\ s$, the minor species growth rates change, which indicates that significant dissociation reactions are induced. For $10^{-6} < t < 10^{1}\ s$, the minor species continue to increase with disparate growth rates. On the other hand, the major species H_2, O_2, and N_2 have essentially constant concentrations. Just past $t \approx 10^{1}\ s$ all the species undergo significant change, and the radicals' mass fractions reach their maximum values. At $t \approx 2 \times 10^{1}\ s$, an exothermic recombination of radicals commences forming the predominant product H_2O, which continues up to $t \approx 4 \times 10^{1}\ s$, after which the system approaches the equilibrium state, which is confirmed by Fig. 3.3 (b) that shows the system's temperature evolution in time.

The time scales over which the system evolves are presented in Fig. 3.4. There are six time scales in the spectrum. This is because our reaction mechanism has $N = 9$ species with $L = 3$ elements being conserved. Thus, we find $N - L = 6$ independent modes. A conserved quantity is time-independent. Thus, it has a zero rate of change, *i.e.* an infinite time scale. The multiscale nature of this problem is clearly seen. Near equilibrium the slowest time scale is $1.85 \times 10^{-4}\ s$, and the fastest time scale is $1.03 \times 10^{-8}\ s$, giving rise to a stiffness of $\mathcal{S}_t \sim \mathcal{O}\left(10^4\right)$. The fastest time scale is consistent with the time scale over which minor species evolve. Thus, to capture the physical dynamics in a numerical simulation $\Delta t < \tau_{fastest} \approx 10^{-8}\ s$, needs to be employed.

In Table 3.1, precise values of various properties at the initial state and the equilibrium state are listed.

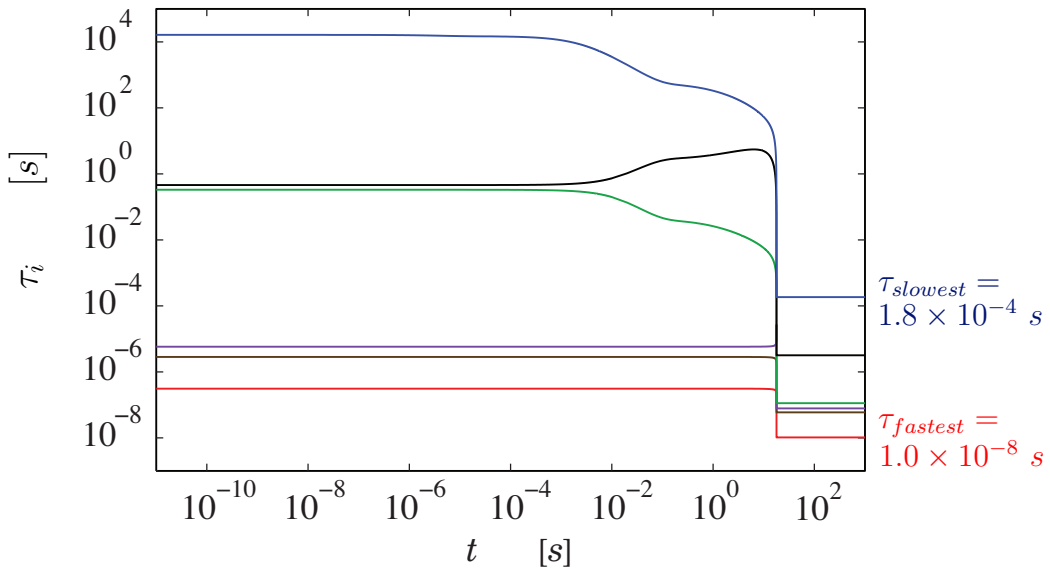

Figure 3.4. Time scales over which the stoichiometric hydrogen–air reactive system evolves, $T^* = 800\ K$, $p = 1\ atm$.

3.3 Spatial scales

Here, a robust method to calculate with great accuracy the length scales for gas phase laminar premixed flames, on a fundamental mathematical basis, is presented. The finest spatial scale which must be resolved in order for the mathematical model to be verified is thus determined. To this end, analysis is given to reduce the governing equations (2.20) to a highly refined, non-traditional system of differential algebraic equations (DAEs) which is most convenient for *a posteriori* determination of the length scales. Following this exposition, the more traditional equation set is presented, which is the system actually solved in the well known `PREMIX` [123] iterative technique to determine the reaction zone structure which is necessary for the subsequent length scale analysis.

TABLE 3.1

THERMOCHEMICAL AND DYNAMIC PROPERTIES FOR THE STOICHIOMETRIC HYDROGEN–AIR REACTIVE SYSTEM.

Property	Initial state	Equilibrium
$p \quad [dyne/cm^2]$	1.01325×10^{6}	1.01325×10^{6}
$T \quad [K]$	8.00000×10^{2}	2.61794×10^{3}
$\rho \quad [g/cm^3]$	3.18566×10^{-4}	1.11336×10^{-4}
Y_{H_2}	2.85219×10^{-2}	2.46789×10^{-3}
Y_{O_2}	2.26362×10^{-1}	1.44476×10^{-2}
Y_H	0.00000×10^{0}	2.96014×10^{-4}
Y_O	0.00000×10^{0}	1.74472×10^{-3}
Y_{OH}	0.00000×10^{0}	1.22014×10^{-2}
Y_{HO_2}	0.00000×10^{0}	5.49446×10^{-6}
$Y_{H_2O_2}$	0.00000×10^{0}	4.12847×10^{-7}
Y_{H_2O}	0.00000×10^{0}	2.23721×10^{-1}
Y_{N_2}	7.45116×10^{-1}	7.45116×10^{-1}
$\tau_{fastest} \quad [s]$	3.10804×10^{-7}	1.03309×10^{-8}
$\tau_{slowest} \quad [s]$	1.63257×10^{4}	1.84879×10^{-4}

3.3.1 Dynamical system form

First, Eqs. (2.20) are reduced into a system of ODEs by relaxing the time-dependent behavior of the system to a steadily propagating flame front moving to the left with constant, *albeit unknown*, flame speed S_L. A Galilean transformation is applied to the system with the frame speed equal to the flame speed,

$$\tilde{x} = x + S_L \tilde{t}, \tag{3.16a}$$

$$\tilde{t} = t, \tag{3.16b}$$

$$\tilde{u} = u + S_L. \tag{3.16c}$$

The spatial coordinate $\tilde{x}$ is a flame front-attached coordinate, and $\tilde{u}$ is the mixture velocity in the Galilean frame. Consequently, the equations that govern the structure of a steady flame are obtained,

$$\frac{d}{d\tilde{x}}\left(\rho\tilde{u}\right) = 0, \tag{3.17a}$$

$$\frac{d}{d\tilde{x}}\left(\rho\tilde{u}h + \mathrm{J}^q\right) = 0, \tag{3.17b}$$

$$\frac{d}{d\tilde{x}}\left(\rho\tilde{u}y_l + \mathrm{j}_l^m\right) = 0, \quad l = 1, \ldots, L-1, \tag{3.17c}$$

$$\frac{d}{d\tilde{x}}\left(\rho\tilde{u}Y_i + \mathrm{J}_i^m\right) = \dot{\omega}_i \bar{m}_i, \quad i = 1, \ldots, N-L. \tag{3.17d}$$

The system of ODEs that describes the steadily propagating laminar premixed flame consists of $2N+1$ equations. Only $N+1$ ODEs are listed explicitly in Eqs. (3.17); these equations are supplemented by the N ODEs, which represent the definition of J^q and J_i^m, $i = 1, \ldots, N-1$, Eqs. (2.21). So, $2N+1$ boundary

conditions are required. An appropriate set of boundary conditions is [55, 118]

$$\tilde{x} = 0: \qquad T = T_u, \quad Y_i + \frac{\mathrm{J}_i^m}{\rho_u S_L} = Y_{iu}, \quad i = 1, \ldots, N-1, \tag{3.18a}$$

$$\tilde{x} \to \infty: \qquad \frac{dT}{d\tilde{x}} \to 0, \quad \frac{dY_i}{d\tilde{x}} \to 0, \quad i = 1, \ldots, N-1, \tag{3.18b}$$

$$\tilde{x} = \tilde{x}_f: \qquad T = T_f, \tag{3.18c}$$

where $\tilde{x}_f$ is a specified spatial point, and T_f is the specified temperature at that location [118]. These are commonly used to study laminar premixed flames, though other formulations are possible. These boundary conditions are sufficient for freely propagating flames, where for this type of flame the mass flow rate, $\dot{m} = \rho\tilde{u}$, is unknown [124, 125], so the temperature at an interior spatial point has to be specified. The point $\tilde{x}_f$ and temperature T_f have to be selected such that all the gradients approach zero at the cold boundary, $x = 0$.

It will be useful to have additional values of variables at boundaries. Using Eqs. (2.4), (2.5b), (2.9c), and (2.16a) the following expressions are derived

$$\rho_u = \frac{p}{\bar{\Re} T_u \sum_{i=1}^{N} Y_{iu}/\bar{m}_i}, \tag{3.19a}$$

$$h_u = \sum_{i=1}^{N} Y_{iu} \left(h_i^f + \int_{T^o}^{T_u} c_{pi}(\hat{T}) d\hat{T} \right), \tag{3.19b}$$

$$y_{lu} = \bar{\mathsf{m}}_l \sum_{i=1}^{N} \frac{\phi_{li} Y_{iu}}{\bar{m}_i}, \quad l = 1, \ldots, L. \tag{3.19c}$$

By utilizing the boundary conditions (3.19), the homogeneous ODEs (3.17a)–

(3.17c) can be integrated exactly. So, the governing equations become

$$\rho\tilde{u} = \rho_u S_L, \tag{3.20a}$$

$$\rho\tilde{u}h + \mathrm{J}^q = \rho_u S_L h_u, \tag{3.20b}$$

$$\rho\tilde{u}y_l + \mathrm{j}_l^m = \rho_u S_L y_{lu}, \qquad l = 1, \ldots, L-1, \tag{3.20c}$$

$$\frac{d}{d\tilde{x}}\left(\rho\tilde{u}Y_i + \mathrm{J}_i^m\right) = \dot{\omega}_i \bar{m}_i, \qquad i = 1 \ldots, N-L. \tag{3.20d}$$

At this stage the variable S_L is considered a fixed parameter for a given calculation; an iterative technique is used to determine S_L so that all boundary conditions are satisfied. The equations are most conveniently posed as a set of $2N+2$ DAEs in terms of $2N+2$ state variables; species mass fraction $Y_i, (i = 1, \ldots, N)$, species mass flux $\mathrm{J}_i^m, (i = 1, \ldots, N)$, temperature T, and Fourier's heat flux q. This system, in a compact representation and after dropping $(\tilde{})$ for simplicity, is

$$\mathbf{A}\left(\mathbf{z}\right) \cdot \frac{d\mathbf{z}}{dx} = \mathbf{f}\left(\mathbf{z}\right). \tag{3.21}$$

Here,

$$\mathbf{A} = \begin{bmatrix} \boldsymbol{\mathcal{D}} & \mathbf{0} & \mathbf{0} \\ \dot{\boldsymbol{\mathcal{M}}} & \boldsymbol{\mathcal{I}} & \mathbf{0} \\ \mathbf{0} & \mathbf{0} & \boldsymbol{\mathcal{Q}} \end{bmatrix}, \ \mathbf{z} = \begin{bmatrix} Y_1 \\ \vdots \\ Y_N \\ \mathrm{J}_1^m \\ \vdots \\ \mathrm{J}_N^m \\ T \\ \mathrm{q} \end{bmatrix}, \ \mathbf{f} = \begin{bmatrix} \frac{\mathrm{J}_1^m \bar{m}}{\rho \ \bar{m}_1} \\ \vdots \\ \frac{\mathrm{J}_N^m \bar{m}}{\rho \ \bar{m}_N} \\ \dot{\omega}_1 \ \bar{m}_1 \\ \vdots \\ \dot{\omega}_{N-L} \ \bar{m}_{N-L} \\ \rho u y_1 + \mathrm{j}_1^m - (\rho_u S_L y_{1u}) \\ \vdots \\ \rho u y_L + \mathrm{j}_L^m - (\rho_u S_L y_{Lu}) \\ \rho u h + \mathrm{J}^q - (\rho_u S_L h_u) \\ \mathrm{q} \end{bmatrix}, \quad (3.22a)$$

where,

$$\mathcal{D}_{ik} = \mathfrak{D}_{ik} - \sum_{\substack{j=1 \\ j \neq i}}^{N} \frac{\mathfrak{D}_{ij} Y_j \bar{m}}{\bar{m}_k}, \qquad i = 1, \ldots, N, \quad k = 1, \ldots, N, \quad (3.22b)$$

$$\dot{\boldsymbol{\mathcal{M}}} = \left[\begin{array}{c:c} \rho_u S_L \mathbf{I}_{(N-L)\times(N-L)} & \mathbf{0}_{(N-L)\times L} \\ \hdashline \mathbf{0}_{L\times(N-L)} & \mathbf{0}_{L\times L} \end{array}\right], \quad (3.22c)$$

$$\boldsymbol{\mathcal{I}} = \left[\begin{array}{c:c} \mathbf{I}_{(N-L)\times(N-L)} & \mathbf{0}_{(N-L)\times L} \\ \hdashline \mathbf{0}_{L\times(N-L)} & \mathbf{0}_{L\times L} \end{array}\right], \quad (3.22d)$$

$$\boldsymbol{\mathcal{Q}} = \begin{bmatrix} 0 & 0 \\ -k & 0 \end{bmatrix}. \quad (3.22e)$$

$\mathbf{A}$ is a singular matrix of dimension $(2N+2) \times (2N+2)$, and its rank is $2N - L$,

$\mathbf{f}$ is a set of $(2N+2)\times 1$ non-linear functions of the state variables $\mathbf{z}$, also of dimension $(2N+2)\times 1$, and $\mathbf{I}$ is the identity matrix. Here, the dimensions of $\boldsymbol{\mathcal{D}}, \dot{\boldsymbol{\mathcal{M}}}$, and $\boldsymbol{\mathcal{I}}$ are $N \times N$, while the dimension of $\boldsymbol{\mathcal{Q}}$ is 2×2. In this system, the number of variables is $2N+2$, though the number of dependent variables is $2N-L$; there are $L+2$ conserved quantities. In Eqs. (3.21)–(3.22), $L+1$ of these quantities can be clearly seen, and they account for the conservation of L elements and the total energy. The additional conserved quantity in this system is due to the constraint on the species mass fluxes, Eq. (2.17a).

3.3.2 Standard form of model equations

The dynamical system (3.21) and the boundary conditions (3.18) are useful for length scale analysis. Direct solution of this system for the reaction zone structure is possible, in principle. However, the problem can be shown to be a high order shooting problem, rendering direct solution difficult.

Thus, to model stationary laminar premixed flames, the less refined, but more compact, form which commonly appears in the literature, *cf.* [118, 124, 125], is obtained. By including Eqs. (3.17c) into (3.17d), and substituting Eqs. (2.5b), (2.9c), and (2.21b) into Eq. (3.17b), following the same approach as [100], one arrives at, after dropping $(\tilde{\ })$,

$$\frac{d}{dx}(\rho u) = 0, \tag{3.23a}$$

$$\rho u c_p \frac{dT}{dx} + \frac{d\mathrm{q}}{dx} + \sum_{i=1}^{N}\left(\mathrm{J}_i^m \frac{dh_i}{dx} + \dot{\omega}_i \bar{m}_i h_i\right) = 0, \tag{3.23b}$$

$$\rho u \frac{dY_i}{dx} + \frac{d\mathrm{J}_i^m}{dx} = \dot{\omega}_i \bar{m}_i, \quad i = 1, \ldots, N-1. \tag{3.23c}$$

A solution for this boundary value problem, Eqs. (3.23) with the boundary

conditions Eqs. (3.18) can be obtained numerically. First, a finite spatial domain of length L is considered. Then, the system is spatially discretized using a difference scheme. The resulting algebraic system of equations are solved iteratively, where the solution iterate is brought into the convergence domain by using pseudo-time integration [118].

3.3.3 Length scale analysis

To accurately determine the length scales over which the system evolves, an eigenvalue analysis can be applied to Eq. (3.21). Since $\mathbf{A}$ is singular, the standard eigenvalue analysis is not applicable. Instead, the generalized eigenvalues of this dynamical system can be calculated [126]. Employing the generalized eigenvalue method on a singular system is a robust method to distinguish small physically based eigenvalues from those which are mathematically zero. Especially in multiscale problems, ordinary eigenvalue analysis often generates a set of eigenvalues for which the distinction is either difficult or impossible.

Assume first that $\mathbf{z} = \mathbf{z}_s(x)$ has been determined by some appropriate numerical method, as discussed in Sec. 3.3.2, so that $\mathbf{z}_s(x)$ satisfies Eqs. (3.18) and (3.21). Consider then an arbitrary spatial point $x = x_*$ at which the state variables are $\mathbf{z} = \mathbf{z}_s(x_*) = \mathbf{z}_*$. By defining the perturbation from $\mathbf{z}_s(x)$ as $\mathbf{z}'(x) = \mathbf{z}(x) - \mathbf{z}_s(x)$, then linearizing Eq. (3.21) about $x = x_*$, one finds

$$\left(\mathbf{A}_* + \mathbf{\Psi}_* \cdot \mathbf{z}'(x) + \mathcal{O}\left(\mathbf{z}'^2(x)\right) + \dots\right) \cdot \left(\left.\frac{d\mathbf{z}_s(x)}{dx}\right|_{x=x_*} + \frac{d\mathbf{z}'(x)}{dx}\right) = \left(\mathbf{f}_* + \mathbf{J}_* \cdot \mathbf{z}'(x) + \mathcal{O}\left(\mathbf{z}'^2(x)\right) + \dots\right), \tag{3.24}$$

where $\mathbf{A}_* = \mathbf{A}(\mathbf{z}_*)$ and $\mathbf{f}_* = \mathbf{f}(\mathbf{z}_*)$ are now locally constant, $\mathbf{J}_*$ and $\mathbf{\Psi}_*$ are,

respectively, the locally constant Jacobian and a third-order tensor evaluated as

$$J_{*ik} = \left.\frac{\partial f_i}{\partial z_k}\right|_{\mathbf{z}=\mathbf{z}_*}, \qquad i,k = 1,\ldots,2N+2, \tag{3.25a}$$

$$\Psi_{*ijk} = \left.\frac{\partial \mathrm{A}_{ij}}{\partial z_k}\right|_{\mathbf{z}=\mathbf{z}_*}, \qquad i,j,k = 1,\ldots,2N+2. \tag{3.25b}$$

By considering only linear terms in Eq. (3.24) and employing the fact that $\mathbf{A}_* \cdot d\mathbf{z}_s(x)/dx|_{x=x_*} = \mathbf{f}_*$, one can see that

$$\mathbf{A}_* \cdot \frac{d\mathbf{z}'(x)}{dx} = \mathbf{J}_* \cdot \mathbf{z}'(x) - \mathbf{\Psi}_* \cdot \mathbf{z}'(x) \cdot \left.\frac{d\mathbf{z}_s(x)}{dx}\right|_{x=x_*}, \tag{3.26}$$

which can be compactly written as

$$\mathbf{A}_* \cdot \frac{d\mathbf{z}'}{dx} = \mathbf{B}_* \cdot \mathbf{z}', \tag{3.27a}$$

where

$$B_{*ik} = \left(J_{*ik} - \Psi_{*ijk} \left.\frac{dz_{sj}}{dx}\right|_{x=x^*}\right), \quad i,k = 1,\ldots,2N+2. \tag{3.27b}$$

Next, adopt the standard assumption that

$$\mathbf{z}' = \boldsymbol{\upsilon} \exp(\lambda x), \tag{3.28}$$

where λ is in general a complex number denoting the generalized eigenvalue, and $\boldsymbol{\upsilon}$ is the corresponding generalized eigenvector. Substitution of Eq. (3.28) into Eq. (3.27a) yields the generalized eigenvalue problem

$$\lambda \mathbf{A}_* \cdot \boldsymbol{\upsilon} = \mathbf{B}_* \cdot \boldsymbol{\upsilon}. \tag{3.29}$$

Solving for $\lambda_i,\ i = 1, \ldots, 2N - L$, then using Eq. (3.28), it is easily seen that the length scales ℓ_i over which the dependent variables evolve are given by the reciprocal of the real part of these eigenvalues,

$$\ell_i = \frac{1}{|Re\,(\lambda_i)|}, \quad i = 1, \ldots, 2N - L. \tag{3.30}$$

By evaluating the eigenvalues at each spatial point, the length scales over which the system evolves through the reaction zone are determined. As a result, the minimum size of discretization to capture the finest scale of the system can be determined. In general, the eigenvalues are complex, where the reciprocals of the real parts provide the length scales of the amplitude growth, and the reciprocals of the imaginary parts represent the oscillatory length scale. Furthermore, the ratio of the largest to the smallest length scale identify the spatial stiffness,

$$\mathcal{S}_x = \frac{\ell_{coarsest}}{\ell_{finest}}. \tag{3.31}$$

As an alternative approach, it is possible to overcome the singularity of $\mathbf{A}$ by removing linear dependencies, and then differentiating the non-linear algebraic constraints (3.20b)–(3.20c), and recover a non-singular system of ODEs in the standard form. Then, the method described in Ref. [122] can be used to estimate the standard eigenvalues, where L of them are zeros, *albeit* corrupted by numerical roundoff error. These two approaches, the ordinary and the generalized eigenvalue methods, both accurately estimate the finest length scale. Nevertheless, since it has been constructed based on a $(L + 1)$-degrees lower dimensional space, the generalized eigenvalue method is more refined than the standard eigenvalue method.

3.3.4 Computational method

A double precision `FORTRAN-77` code has been developed and linked with the International Mathematical and Statistical Libraries (IMSL) routines `DFDJAC` for Jacobian evaluation, `DEVLRG` for eigenvalues estimation, `DGVLRG` for generalized eigenvalues estimation, and a double precision version of the public domain edition of the `CHEMKIN` package [127, 128] to obtain kinetic rates and thermodynamics properties, a double precision version of the public domain edition of the `TRANSPORT` package [129] to calculate multicomponent transport properties of species, and a double precision version of the public domain edition of the `PREMIX` algorithm [123] to obtain the steady structure of the adiabatic laminar premixed flames.

A second order central difference scheme has been employed to discretize all the spatial derivatives in (3.23). The mass and heat fluxes have been estimated at intermediate grid points to maintain second order accuracy. The resulting algebraic system of equations are solved using a damped modified Newton's method [123]. In all cases studied in this section, the relative and absolute error tolerances for iterative convergence are 10^{-9} and 10^{-14}, respectively. These values are five orders of magnitude more stringent than the default values; moreover, the absolute tolerance is approaching the machine precision error. All the calculations presented in this section were performed on a single processor 3.2 GHz Hewlett–Packard workstation, and typical calculations were completed within one minute.

3.3.5 Model problem

An adiabatic steady one-dimensional laminar premixed flame freely propagating in a stoichiometric hydrogen–air mixture at $p = 1\ atm$ has been considered.

The utilized kinetic model is identical to that of Sec. 3.2, see Table D.1. In this section, except for the systematic grid convergence studies in Sec. 3.3.5.1, all results are obtained on a grid that has been adaptively refined to control the error and capture regions of steep gradient; the minimum utilized grid sizes are listed in Table 3.2. The adaptive refinement algortithm is seen to demand that the finest grid sizes range from 1×10^{-6} to 9×10^{-4} cm, depending on p and mixture composition.

3.3.5.1 Verification and validation

Before presenting our predictions, we need to verify our computations. Two types of verification are performed: 1) we compare our results to those previously reported in a previous study, and 2) we conduct a formal grid convergence study.

For the first verification, a calculation is performed to reproduce the temperature and species profiles of a stoichiometric, atmospheric-pressure hydrogen–air flame found in Smooke *et al.* [111]. Equations (3.23) with the boundary conditions (3.18) are solved, where this mathematical model is identical to the one described in Ref. [111]. The specified spatial point is $x_f = 5 \times 10^{-2}$ cm, the specified temperature is $T_f = 400$ K, and the temperature of the unburned mixture is $T_u = 298$ K. In this particular calculation, the Dufour's effect in the heat flux model is neglected, while the Soret's effect in the mass flux model is considered to match the model in Ref. [111]; the mass flux is modeled by Eq. (2.22) instead of Eq. (2.21a). Although considering one of these terms and neglecting the other violates Onsager's reciprocity [104, 105], this is done here for verification purposes only. The results are illustrated in Fig. 3.5; visual inspection shows that the stationary flame structure is identical to that of Ref. [111].

TABLE 3.2

THE MINIMUM GRID SIZE EMPLOYED FOR LAMINAR PREMIXED FLAMES.

$p \quad [atm]$	$\Delta x \quad [cm]$	
	$H_2 - air$	$C_xH_y - air$
1×10^{-1}	9×10^{-4}	-
2×10^{-1}	6×10^{-4}	-
5×10^{-1}	2×10^{-4}	2×10^{-5}
1×10^{0}	6×10^{-5}	1×10^{-5}
2×10^{0}	5×10^{-5}	8×10^{-6}
5×10^{0}	3×10^{-5}	3×10^{-6}
1×10^{1}	1×10^{-5}	1×10^{-6}

However, modeling atmospheric-pressure laminar premixed flame at such unburned mixture's temperature, $T_u = 298\ K$, cause some of the reactive species mass fractions near the cold boundary, 1) artificially converge to negative values, and 2) show oscillations. Nevertheless, the behavior away from the neighborhood of the cold boundary has no obvious errors. This computational phenomenon is known as the cold-boundary difficulty [108]; a physical description for this problem is given in Ref. [55]. Consequently, to overcome this difficulty, the unburned mixture's temperature is raised up to $T_u = 800\ K$; the specified temperature is assigned $T_f = 900\ K$ at $x_f = 2.30\ cm$.

For the second more rigorous verification, the stationary structures of one-dimensional, stoichiometric, adiabatic, $2H_2+O_2+3.76N_2$ laminar premixed flames

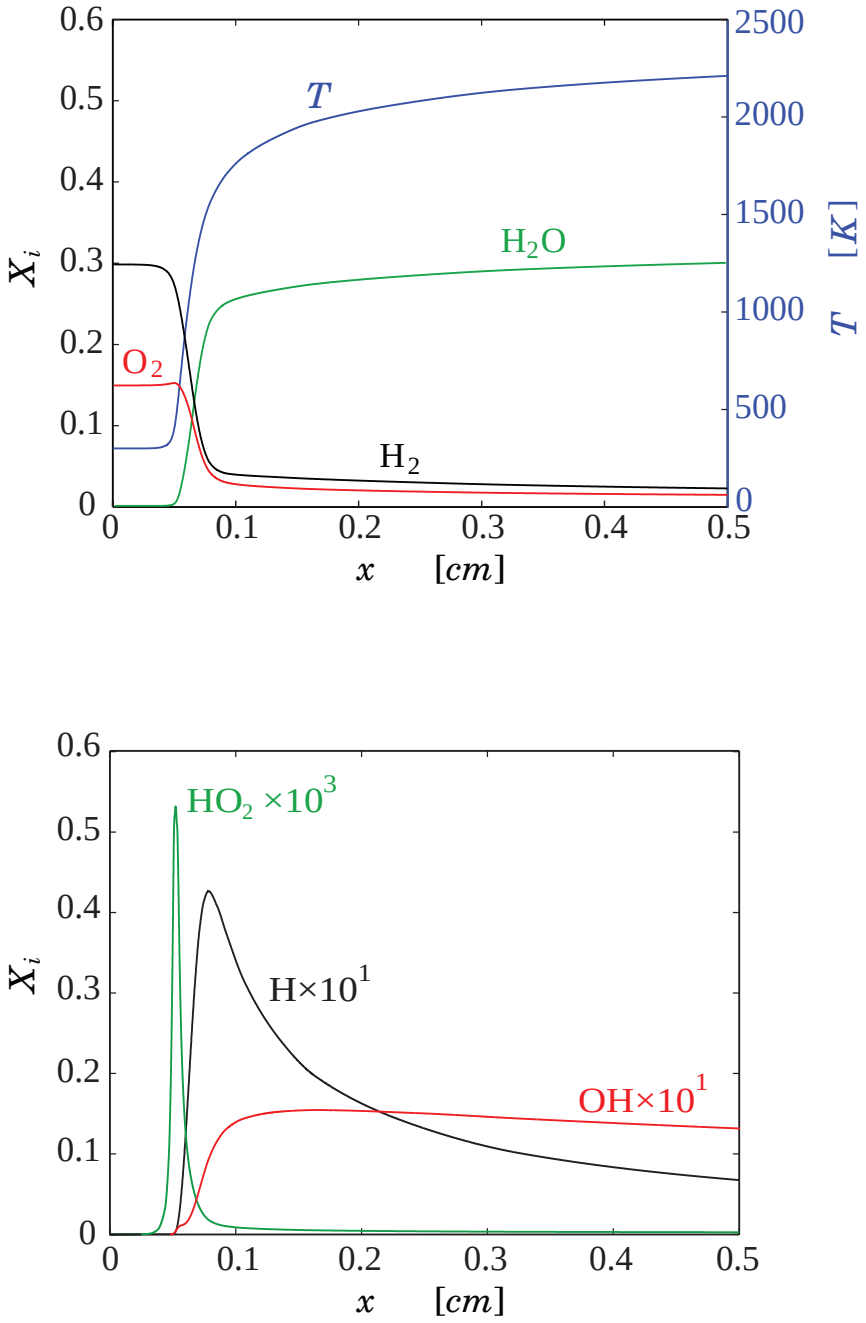

Figure 3.5. Temperature and species profiles versus distance in the stoichiometric hydrogen–air flame for numerical verification, equivalent to predictions of Smooke *et al.* $T_u = 298\ K$ and $p = 1\ atm$.

at $p = 1\ atm$ and $T_u = 800\ K$ are obtained over a wide range of uniform grid sizes: $3 \times 10^{-2} \leq \Delta x \leq 6.25 \times 10^{-5}\ cm$. Thus, the error-control mechanism in the adaptive refinement algorithm of `PREMIX` has been suppressed for this case to enable this standard calculation.

In this formal grid convergence study, for all dependent variables $\mathbf{z}$, the relative errors throughout the entire domain, $\boldsymbol{E}_\infty$, are calculated by using the following formula:

$$\boldsymbol{E}_\infty = max_{x_u \leq x \leq x_b} \left| \frac{\mathbf{z}^{exact}(x) - \mathbf{z}(x)}{\mathbf{z}^{exact}(x)} \right|. \tag{3.32}$$

The result for one dependent variable, the mass fraction of species OH, is presented in Fig. 3.6. Results for all other variables bear remarkable similarity to that for Y_{OH}. Solutions are obtained on eight different uniform grids. The "exact" solution is estimated using Richardson's extrapolation from the three finest grids [9]. In computing the error via Eq. (3.32), points with species mass fraction below 10^{-10} were excluded because of potential roundoff corruption in the double precision calculations.

Figure 3.6 shows that to obtain a desirable $E_{\infty\ OH} < 0.1$ in this problem, a spatial resolution of $\Delta x \leq 2 \times 10^{-4}\ cm$ has to be utilized. Larger discretization sizes can induce unacceptably large relative errors; *e.g.* for $\Delta x = 10^{-2}\ cm$ the relative error in Y_{OH} is 40, (4000%). In addition, it is found that the error at the finest two spatial discretizations is converging towards the exact solution at a rate of $\mathcal{O}(\Delta x^{1.64})$. It appears in Fig. 3.6 that the rate of convergence is increasing as Δx decreases. Finite computational resources prevented the use of finer grids; it is expected that on even finer grids, a convergence rate of $\mathcal{O}(\Delta x^2)$, consistent with the truncation error of the finite difference discretization, would have been achieved.

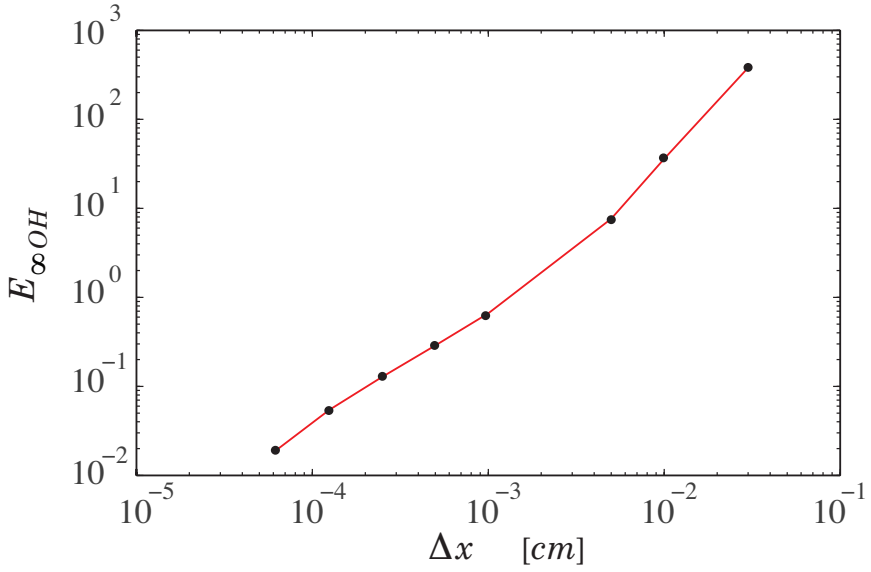

Figure 3.6. Relative error of Y_{OH} versus the discretization size for the hydrogen–air flame simulation with $T_u = 800\ K$ and $p = 1\ atm$.

In contrast, for this problem, the relative errors in laminar flame speed are not as sensitive. Figure 3.7 shows the relative error in laminar flame speed,

$$E_{S_L} = \left| \frac{S_L - S_L^{exact}}{S_L^{exact}} \right|,$$

as a function of Δx. To keep the relative error in S_L below 0.1, one need only employ a $\Delta x \sim 2 \times 10^{-3}\ cm$. For $\Delta x = 10^{-2}\ cm$, the relative error in S_L is around 0.3, much lower than that for species mass fractions. This result is in agreement with our adopted characterization of a resolved solution.

Consideration of the spatial distributions of two minor species' mass fractions, Y_{OH} and Y_{HO_2}, at four different grid resolutions, shown in Figs. 3.8–3.9, provides additional insight. Here, attention is focused on a region at the onset of flame ignition. In Fig. 3.8, clearly one sees that for $\Delta x = 3 \times 10^{-2}\ cm$ and $1 \times 10^{-2}\ cm$,

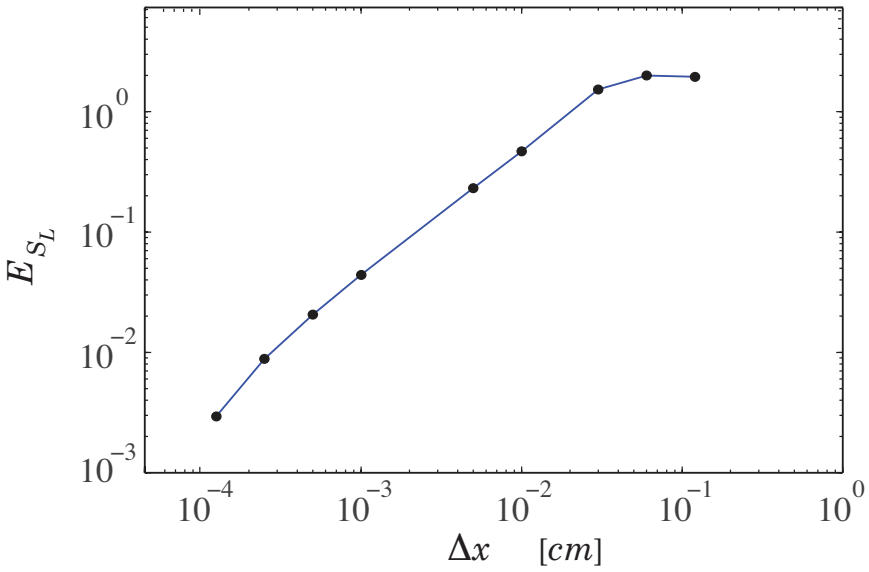

Figure 3.7. Convergence of the relative error in laminar flame speed with grid size Δx for the hydrogen–air flame simulation with $T_u = 800\ K$ and $p = 1\ atm$.

relative to calculations on a finer grid, there are orders of magnitude difference in the predictions of Y_{OH}. Only for the finer grid resolution is Y_{OH} seen to be converging to have a small relative error. Figure 3.9 shows a close view of how the HO_2 mass fraction profile varies with the grid resolution. The accurate capture of the peak values of species which are highly active only in the flame zone poses a computational challenge. Clearly the peak, and the behavior near the peak, is under-resolved for $\Delta x \geq 10^{-2}\ cm$. Most of the structure near the peak is well resolved for $\Delta x = 10^{-3}\ cm$; for $\Delta x = 1.25 \times 10^{-4}\ cm$, the error is very small. The peak values of Y_{HO_2} and the error in these values as a function of Δx are listed in Table 3.3. Assuming the value obtained on the finest grid to be "exact" allows calculation of E_{HO_2}; here the calculation of E is restricted to peak values. Figures 3.8–3.9 do not display the results for $\Delta x = 6.25 \times 10^{-5}\ cm$ as on this scale they

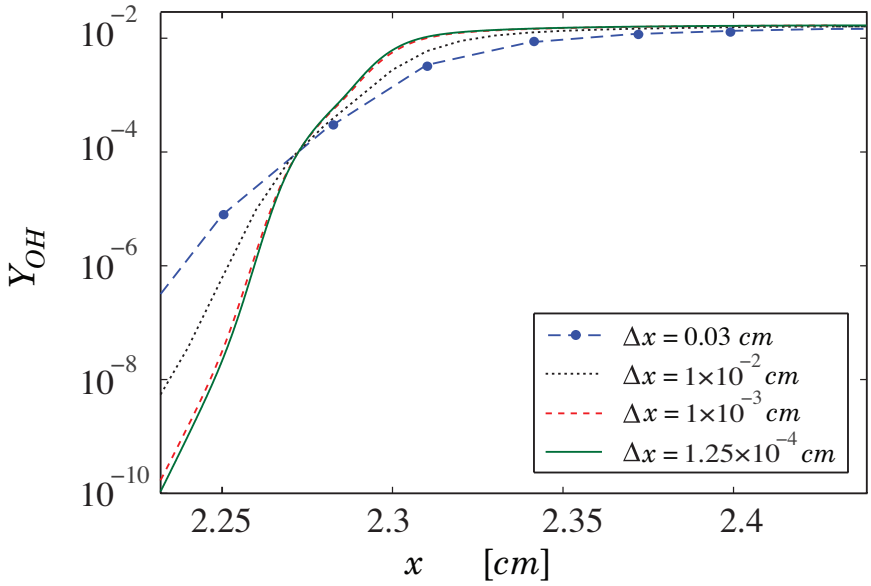

Figure 3.8. Spatial distribution of Y_{OH} at various discretization sizes for the hydrogen–air flame simulation with $T_u = 800\ K$ and $p = 1\ atm$.

are indistinguishable from those found for $\Delta x = 1.25 \times 10^{-4}\ cm$.

Next, a comparison with the experimental results addresses the question as to whether the model well represents the observable physics. For validation purposes, a series of calculations is performed on an atmospheric-pressure hydrogen–air laminar premixed flame initially at $T_u = 298\ K$. For different equivalence ratios Φ, the flame speed is determined; see Table 3.4. A comparison between the calculated flame speeds and a set of experimental data [130–138] is given in Fig. 3.10. It is clear that the computational predictions lie within the scatter of the experimental data, and they are as good as have been found by others [111, 139].

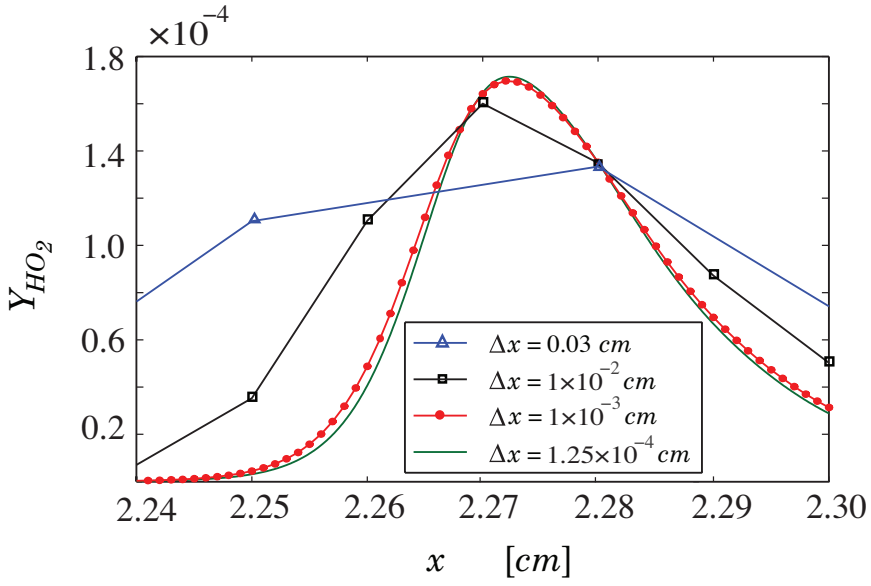

Figure 3.9. Spatial distribution of Y_{HO2} at various discretization sizes for the hydrogen–air flame simulation with $T_u = 800\ K$ and $p = 1\ atm$.

TABLE 3.3

PEAK VALUE OF Y_{HO_2} AND RELATIVE ERROR AS FUNCTION OF Δx FOR THE HYDROGEN–AIR FLAME SIMULATION WITH $T_u = 800\ K$ AND $p = 1\ atm$.

Δx $[cm]$	Peak of Y_{HO_2}	E_{HO_2}
3.0×10^{-2}	1.33366×10^{-4}	2.23×10^{-1}
1.0×10^{-2}	1.60060×10^{-4}	6.71×10^{-2}
1.0×10^{-3}	1.69659×10^{-4}	1.11×10^{-2}
1.25×10^{-4}	1.71143×10^{-4}	2.47×10^{-3}
6.25×10^{-5}	1.71566×10^{-4}	-

TABLE 3.4

THE COMPUTED FLAME SPEEDS OF LAMINAR PREMIXED HYDROGEN–AIR FLAMES FOR DIFFERENT EQUIVALENCE RATIOS, $T_u = 298\ K, p = 1\ atm.$

Φ	0.595	0.793	1.000	1.282	1.587
$S_L \quad [cm/s]$	101.12	170.26	238.40	275.62	286.90
Φ	1.947	2.380	2.909	3.570	4.420
$S_L \quad [cm/s]$	274.47	246.76	201.45	156.14	105.29

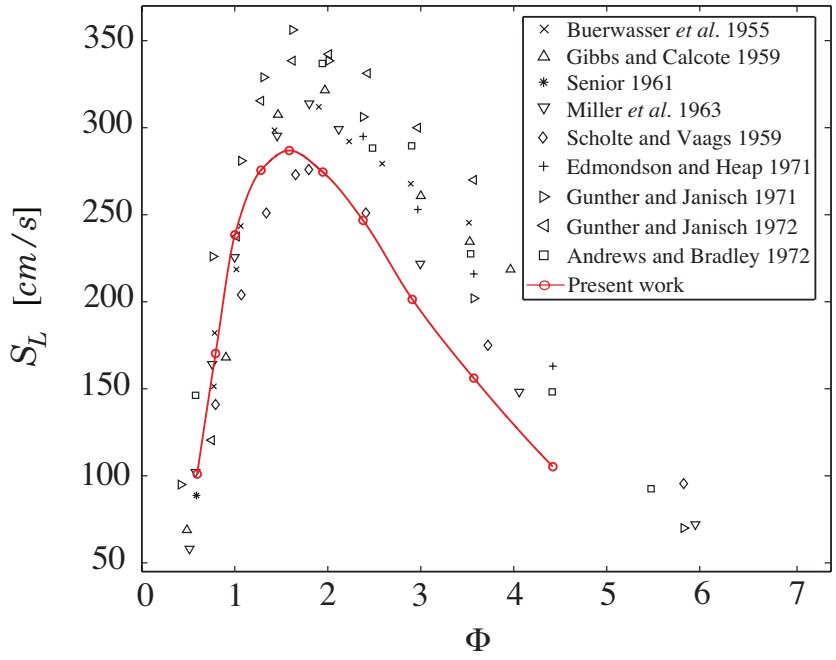

Figure 3.10. Comparison of predictions of flame speed versus the equivalence ratio with the experimental data, $T_u = 298\ K, p = 1\ atm.$

3.3.5.2 Resolved structure

The fully resolved steady species and temperature profiles are shown in Figs. 3.11–3.12. Although linear scales are usually used in the literature, here log–log and semi–log scales have been employed to better illustrate the disparate scales.

Figure 3.11 shows the spatial distribution of species mass fractions throughout the entire flame zone. At $x \approx 10^{-4}\ cm$, the minor species growth rates change slightly, which reveals that significant dissociation reactions at this scale are induced. Another increase in the minor species mass fraction growth rates is noted at $x \approx 10^{-2}\ cm$, which indicates the occurrence of more vigorous chemical interaction of the minor species. For $10^{-2} < x < 2.30 \times 10^{0}\ cm$, the minor species mass fractions continue to increase rapidly with different growth rates. On the other hand, the major species H_2, O_2, and N_2 have essentially constant mass fractions. Just past $x = 2.20 \times 10^{0}\ cm$, which is near the end of the preheat zone, all the species mass fractions undergo significant change, and the radicals' mass fractions reach their maximum values. At $x = 2.40 \times 10^{0}\ cm$, exothermic recombination of radicals commences forming the predominant product H_2O. This zone extends up to $x = 1.39 \times 10^{1}\ cm$; after that, the system comes to its chemical equilibrium state where all the spatial gradients vanish. To confirm this, the spatial domain was extended to $x = 1.00 \times 10^{2}\ cm$, but no further changes were noted.

In Fig. 3.12, the temperature profile is presented. At $x \approx 2.20 \times 10^{0}\ cm$, the reaction undergoes a particularly vigorous stage in which the change in the temperature is significant. Thus, the ignition point can be assigned; it is defined as the point where the temperature gradient dT/dx reaches a maximum value. Also, this particular point defines the end of the preheat zone and the beginning of the reaction zone. For this case the ignition point is assigned at $x = 2.315 \times 10^{0}\ cm$.

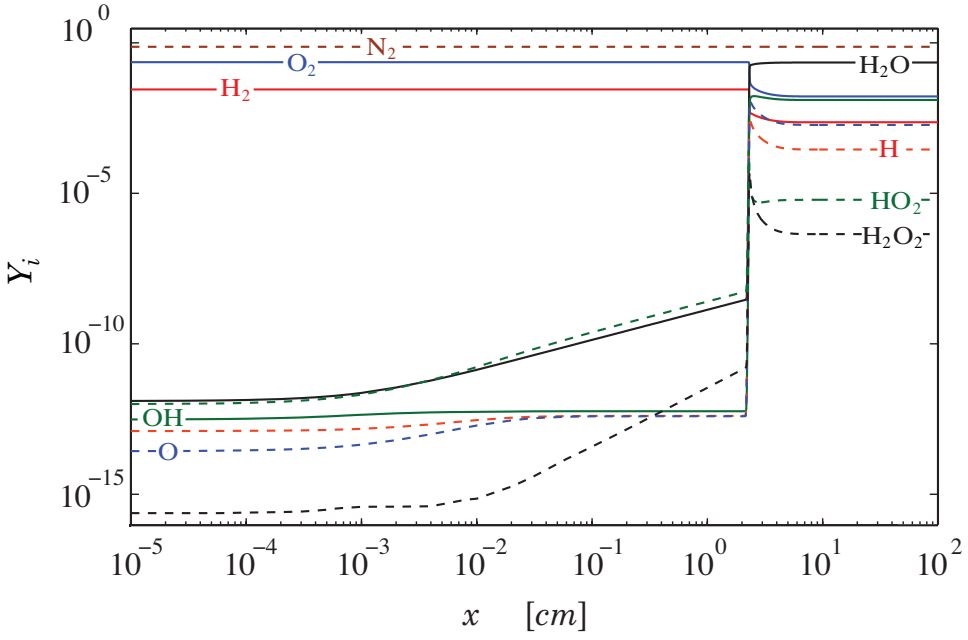

Figure 3.11. Species mass fraction versus distance for the stoichiometric hydrogen–air flame, $T_u = 800\ K, p = 1\ atm$.

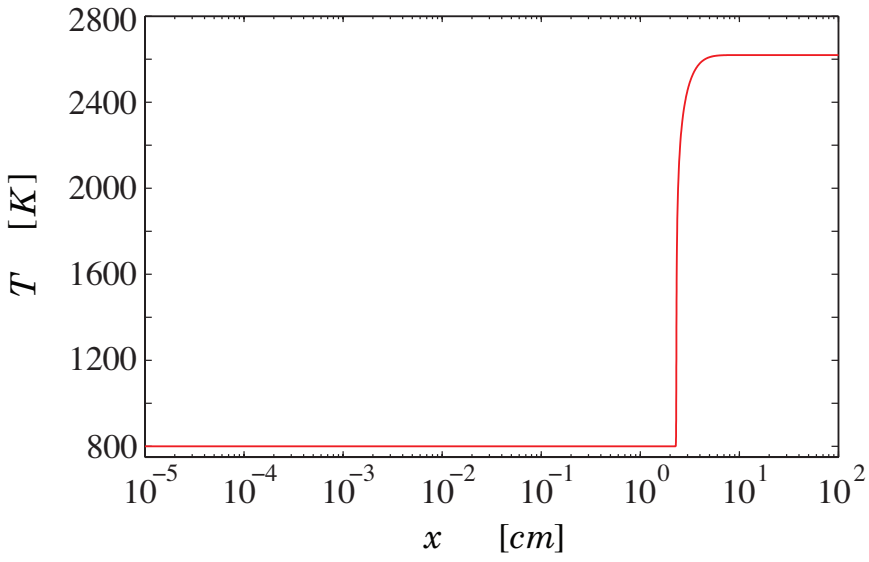

Figure 3.12. Temperature versus distance for the stoichiometric hydrogen–air flame, $T_u = 800\ K, p = 1\ atm$.

We adopt the simple estimate for the characteristic reaction length scale, *i.e.* flame thickness, given by Williams [108]:

$$\ell_{reaction} = \frac{k}{\rho_o c_p S_L}, \tag{3.33}$$

where for this case $\ell_{reaction} = 1.60 \times 10^{-3}\ cm$.

3.3.5.3 Length scale spectrum

Having the fully resolved structure in hand, the local Jacobian and the spatial generalized eigenvalues are calculated throughout the entire domain. As a result, the local length scales ℓ_i are predicted throughout the domain, Fig. 3.13. The multiscale nature of the problem and the length scales over which the species evolve are clearly shown; the system exhibits a spatial stiffness. Because the reaction mechanism has $N = 9$ species with $L = 3$ elements being conserved, there are $2N - L = 15$ length scales in the spectrum. Thus, there are 15 independent modes. This almost twice the number of time scales for the spatially homogeneous version. It would be exactly twice if element conservation were not a feature of this system. The finest length scale and the largest length scale for this system vary from $7.60 \times 10^{-4}\ cm$ and $1.62 \times 10^{7}\ cm$ in the preheat zone to $2.41 \times 10^{-4}\ cm$ and $2.62 \times 10^{0}\ cm$ in the hot far-field region, respectively. Thus, the spatial stiffness in the hot region is $\mathcal{S}_x \sim \mathcal{O}(10^4)$.

In addition to the values reported in Fig. 3.13, the eigenvalues were checked by calculation with other standard algorithms. All algorithms returned equivalent eigenvalues corresponding to fine length scales. However, numerical errors induced some discrepancies in the less important coarse length scale estimates. The least numerical error in the physical eigenvalues was noted in the direct calculation

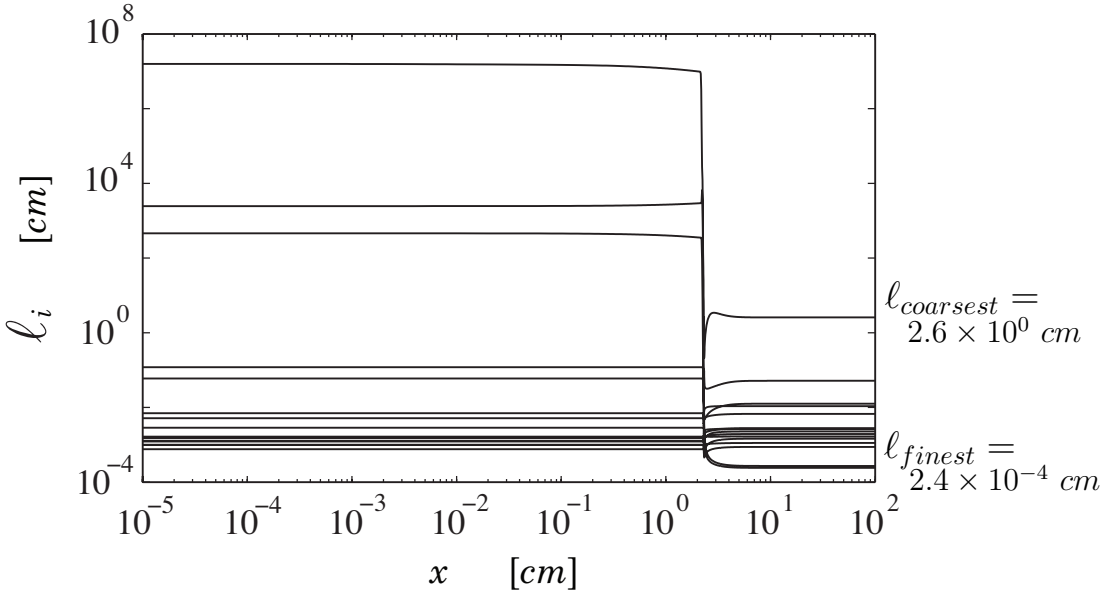

Figure 3.13. Predicted length scales over which the stoichiometric hydrogen–air flame evolves versus distance, $T_u = 800\ K, p = 1\ atm$.

of the eigenvalues; however, this algorithm returned $L = 3$ spurious eigenvalues, which were overruled by the more robust generalized eigenvalue method.

The evolution of a particular species is not associated with a particular length scale, since the species mass fractions depend on local linear combinations of all eigenmodes. So, the species mass fractions vary on these scales through the entire domain. The important finest scale is $\ell_{finest} = 2.41 \times 10^{-4}\ cm$, which occurs at the system's chemical equilibrium. The predicted finest length scale and the smallest scale over which the species vary, $x = 10^{-4}\ cm$, are nearly identical. Moreover, the finest length scale effect in the preheat zone can be observed in the variation of the minor species mass fractions, which ensures the consistency between the eigenvalue-determined finest length scale and the smallest scale over which the species vary. As the system approaches its equilibrium, all of the eigenvalues are

real: half are positive, and half are negative. Thus, the chemical equilibrium point for this advection-reaction-diffusion system is a saddle node.

As a summary of our results for the one-dimensional atmospheric-pressure freely propagating laminar premixed hydrogen–air flame, a precise list of several properties' values at the cold boundary, *i.e.* unburned mixture, and at the hot boundary, *i.e.* burned mixture, is given in Table 3.5.

A comparison between the predicted finest length scale ℓ_{finest} and the flame thickness $\ell_{reaction}$ over a wide range of pressures is presented in Fig. 3.14. It reveals that the finest length scale is well correlated with the flame thickness and that both of them decrease as pressure is increased. On the other hand, ℓ_{finest} is at least one order of magnitude smaller than $\ell_{reaction}$, which indicates the presence of scales smaller than the flame thickness.

3.3.5.4 Estimate from collision theory

We next explore the possibility that there may be a more fundamental underlying explanation for the finest length scales revealed by the eigenvalue analysis. We thus report an *ad hoc* but plausible analysis based on straightforward estimates from standard molecular collision theory. We find that a remarkably simple formula is able to accurately predict the length scales obtained by the preceding eigenvalue analysis. We believe this formula will be accurate for any collision-based kinetic model. However, an analytical proof of the connection between the eigenvalue prediction from detailed kinetics and the mean free path calculation is intractable.

In a totally independent calculation, the mean free path ℓ_{mfp} for the mixture

TABLE 3.5

THERMOCHEMICAL AND DYNAMIC PROPERTIES FOR THE ONE-DIMENSIONAL LAMINAR PREMIXED HYDROGEN–AIR FLAME.

Property	Cold boundary	Hot boundary
$p \quad [dyne/cm^2]$	1.01325×10^{6}	1.01325×10^{6}
$T \quad [K]$	8.00000×10^{2}	2.61940×10^{3}
$u \quad [cm/s]$	1.44081×10^{3}	4.11965×10^{3}
$\rho \quad [g/cm^3]$	3.18971×10^{-4}	1.11557×10^{-4}
$\bar{m} \quad [g/mol]$	2.09380×10^{1}	2.39769×10^{1}
Y_{H_2}	2.84030×10^{-2}	2.30040×10^{-3}
Y_{O_2}	2.27712×10^{-1}	1.66143×10^{-2}
Y_H	1.26367×10^{-13}	2.87103×10^{-4}
Y_O	2.70429×10^{-14}	1.88089×10^{-3}
Y_{OH}	3.04969×10^{-13}	1.26441×10^{-2}
Y_{HO_2}	9.89474×10^{-13}	6.10909×10^{-6}
$Y_{H_2O_2}$	2.37593×10^{-16}	4.42107×10^{-7}
Y_{H_2O}	1.25667×10^{-12}	2.22471×10^{-1}
Y_{N_2}	7.45116×10^{-1}	7.45116×10^{-1}
$\ell_{coarsest} \quad [cm]$	1.61618×10^{7}	2.62236×10^{0}
$\ell_{finest} \quad [cm]$	7.59517×10^{-4}	2.41237×10^{-4}

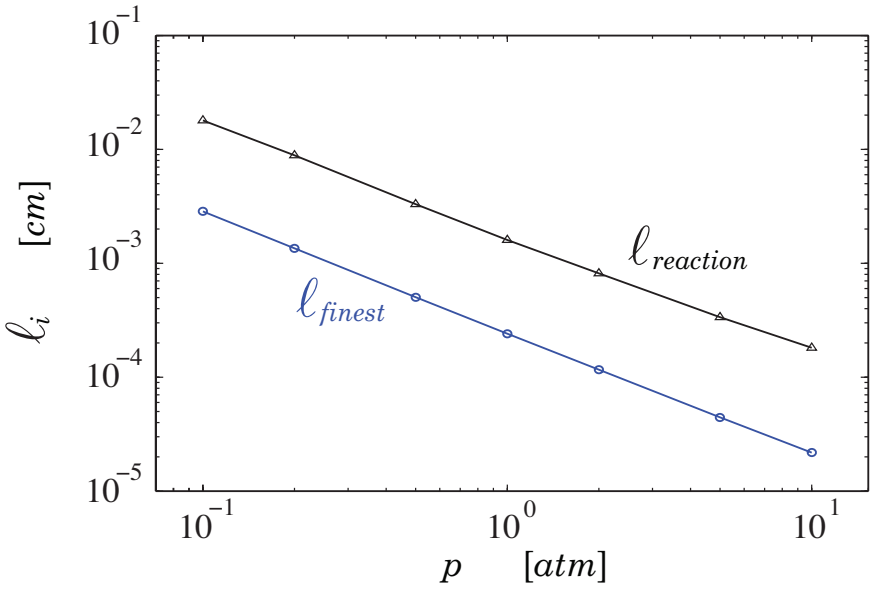

Figure 3.14. The flame thickness and the finest length scale predicted by eigenvalue analysis versus pressure for the stoichiometric hydrogen–air flame, $T_u = 800\ K$.

studied is estimated based on a simple relation given by Vincenti and Kruger [140]:

$$\ell_{mfp} = \frac{\bar{m}}{\sqrt{2}\pi d^2 \rho \mathcal{N}}, \tag{3.34}$$

where d is the molecular collision cross-section diameter, and $\mathcal{N} = 6.02250 \times 10^{23}\ mol^{-1}$ is Avogadro's number. For the calculation of ℓ_{mfp}, estimated at the equilibrium state, the estimate of $d = 3.70 \times 10^{-8}\ cm$ for air is adopted from Ref. [140]. This estimate of d is close in magnitude to the mixture average collision diameter $d_{mix} = 3.60778 \times 10^{-8}\ cm$, which can be calculated as the average of the species Lennard-Jones collision diameters, given by `TRANSPORT` [129],

$$d_{mix} = \frac{1}{N} \sum_{i=1}^{N} \varsigma_i. \tag{3.35}$$

Also, $\bar{m} = 23.98\ g/mol$ and $\rho = 1.12 \times 10^{-4}\ g/cm^3$ were obtained for the mixture from `PREMIX` calculations. The estimate (3.34) reveals that $\ell_{mfp} = 5.87 \times 10^{-5}\ cm$, which is roughly one order of magnitude smaller than the continuum-based ℓ_{finest}.

A comparison between ℓ_{finest} and ℓ_{mfp} over a wide range of pressures is presented in Fig. 3.15. Although this comparison should not be considered as formal proof of the existence of a relation between these scales, it is intriguing to note that ℓ_{finest} is always close to, and slightly above, ℓ_{mfp}. This is consistent with the fact that the parameters used in the constitutive models for the continuum theory have as their foundation a rational average of the more fundamental collision theory. Moreover, the same comparison between $\ell_{finest}, \ell_{reaction}$, and ℓ_{mfp} for the hydrogen–air mixture has been conducted for a wide range of Φ. The results are consistent with the previous one, and clearly show that the finest length scale is not a function of the fuel–air ratio, see Fig. 3.16.

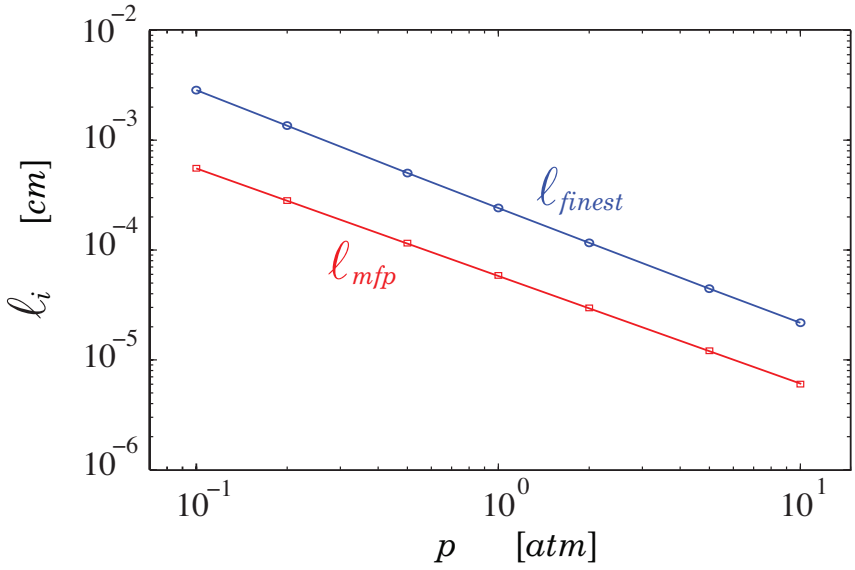

Figure 3.15. The mean free path and the finest length scale predicted by eigenvalue analysis versus pressure for a stoichiometric hydrogen–air flame, $T_u = 800\ K$.

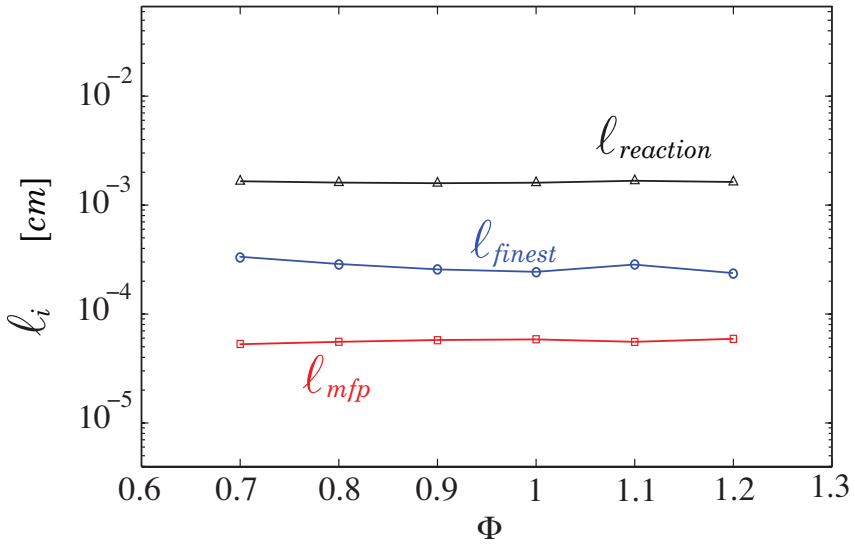

Figure 3.16. The flame thickness, the predicted finest length scale, and the mean free path versus the equivalence ratio for a hydrogen–air flame, $T_u = 800\ K, p = 1\ atm$.

3.3.6 Hydrocarbon–air mixtures

The approach presented in Sec. 3.3.5 is extended to several other stoichiometric reactive mixtures: 1) methane–air, 2) ethane–air, 3) propane–air, 4) ethylene–air, and 5) acetylene–air. The GRI-3.0 mechanism [141] with $L = 5$ elements, $N = 53$ species, and $J = 325$ reversible reactions has been adopted as a kinetic model. For each mixture, the pressure is $p = 1\ atm$, the mixture temperature at the cold boundary is $T_u = 298\ K$, the specified temperature location is assigned at $x_f = 2.30\ cm$, and the specified temperature is $T_f = 400\ K$.

The calculated ℓ_{finest}, $\ell_{reaction}$, and the estimated ℓ_{mfp} over a wide range of pressures are presented, Figs. 3.17–3.21. It is clearly shown that the predicted finest length scale is well correlated with the mean free path for all the calculations performed; in all cases ℓ_{finest} is slightly above ℓ_{mfp}, fully consistent with the continuum assumption. So, the finest length scale can be easily estimated *a priori* using Eq. (3.34). Moreover, it can be said with confidence that the finest scale is not a strong function of a particular mixture, a detailed kinetic mechanism, or a particular numerical method. It seems then that one may be able to claim that in order to accurately compute a reactive flow problem with bi- and tri-molecular collision-based detailed kinetic rates such as considered here, one has to resolve a spatial scale slightly above the mean free path scale.

However, it should be noted that there are other reaction mechanisms which are not collision-based and may involve uni-molecular decay attributable to some external source which excites vibrational frequencies [142]. Such scales may be faster or slower than collision-based scales. If, then, the reaction mechanism involves uni-molecular reactions, depending on the details of such reactions, resolution either above, at, or below the mean free path level may be required; if below,

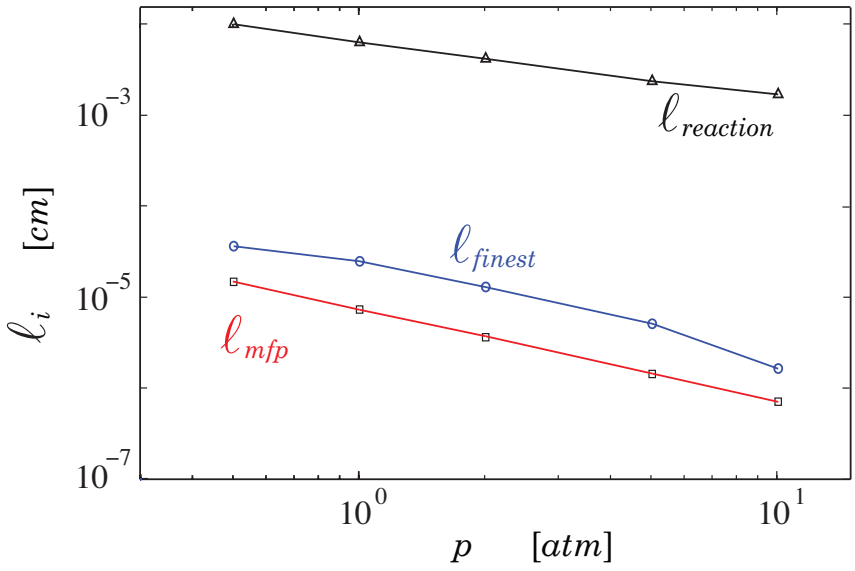

Figure 3.17. The flame thickness, the finest length scale predicted by eigenvalue analysis, and the mean free path versus pressure for a laminar premixed flame in a stoichiometric methane–air mixture, $T_u = 298\ K$.

the continuum model is certainly inappropriate!

Remarkably then, it seems to be possible to use ℓ_{mfp} as a simple *a priori* estimate for ℓ_{finest} predicted *a posteriori*. Such an estimate is useful in providing a lower bound for the computational grid resolution necessary to guarantee fully resolved continuum calculations. Further evidence on the existence of a relation between these scales are provided in Appendices E–F.

In Appendix E, the predicted finest length scale and the mean free path length scale in the reaction zone of a Chapman–Jouguet (CJ) detonation [143] have been calculated for several gas-phase mixtures over wide ranges of Φ and p. Similar to laminar premixed flames, a correlation between ℓ_{finest} and ℓ_{mfp} has been noted. In Appendix F, we were able to show analytically a connection between ℓ_{mfp} and ℓ_{finest} for a simpler kinetic scheme, the isothermal dissociation of diatomic oxygen.

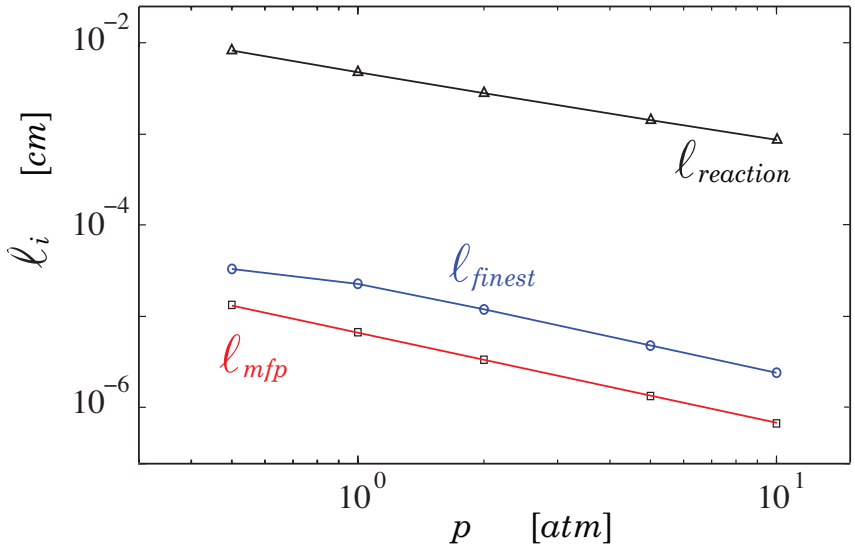

Figure 3.18. The flame thickness, the finest length scale predicted by eigenvalue analysis, and the mean free path versus pressure for a laminar premixed flame in a stoichiometric ethane–air mixture, $T_u = 298\ K$.

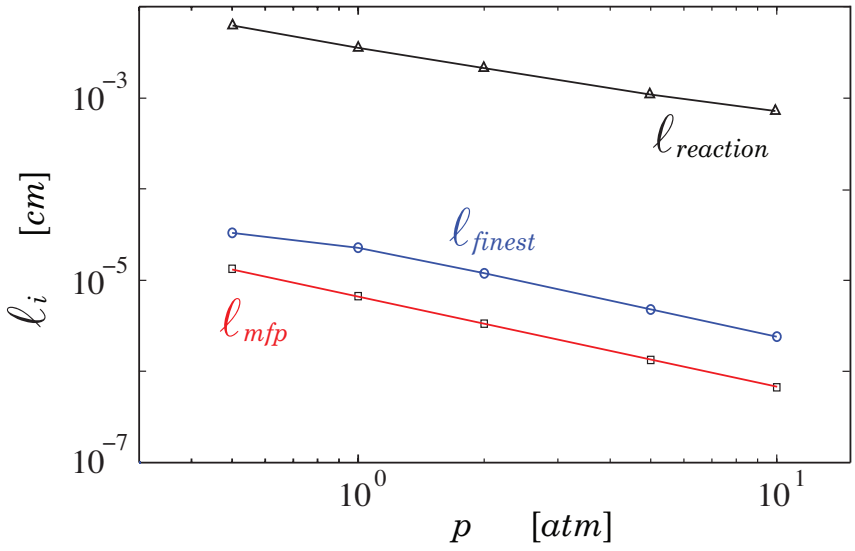

Figure 3.19. The flame thickness, the finest length scale predicted by eigenvalue analysis, and the mean free path versus pressure for a laminar premixed flame in a stoichiometric propane–air mixture, $T_u = 298\ K$.

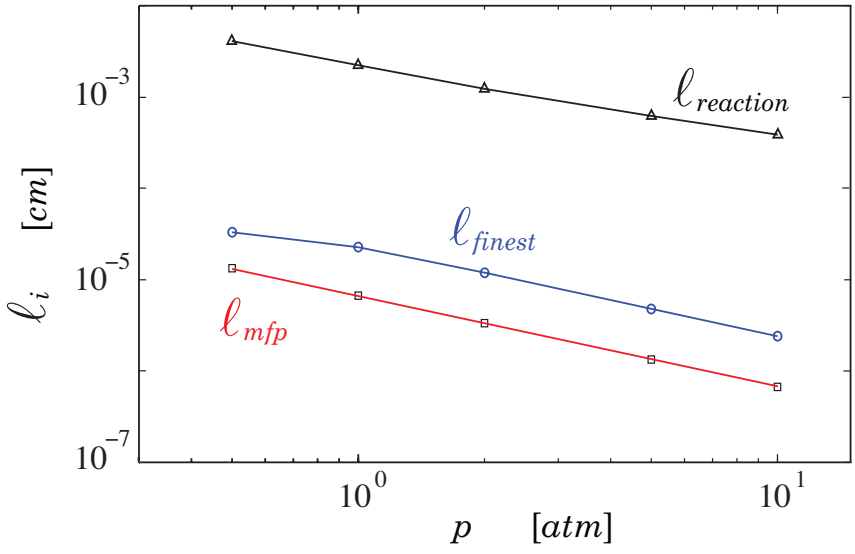

Figure 3.20. The flame thickness, the finest length scale predicted by eigenvalue analysis, and the mean free path versus pressure for a laminar premixed flame in a stoichiometric ethylene–air mixture, $T_u = 298\ K$.

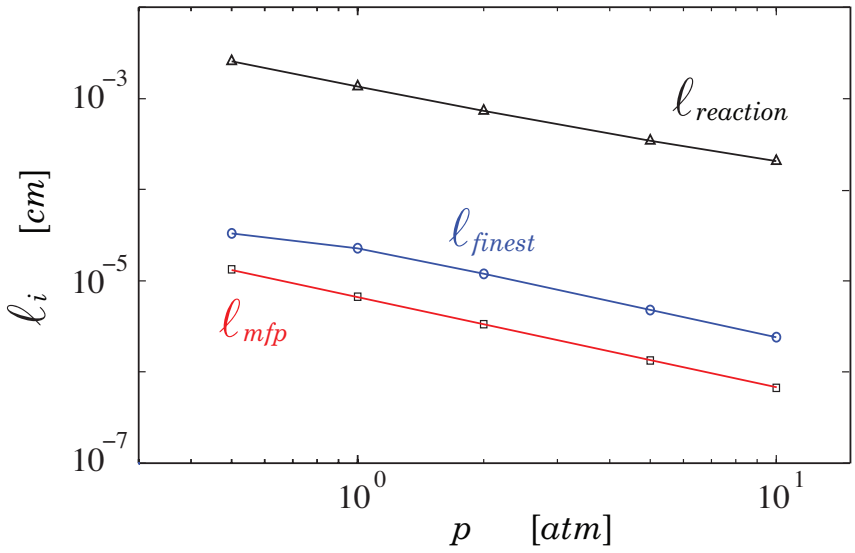

Figure 3.21. The flame thickness, the finest length scale predicted by eigenvalue analysis, and the mean free path versus pressure for a laminar premixed flame in a stoichiometric acetylene–air mixture, $T_u = 298\ K$.

3.3.7 Comparison with previously published results

Here, a comparison between the predicted finest length scale and the utilized discretization in some of the best calculations of flames in hydrogen–air and methane–air mixtures is presented. The results of these calculations are summarized in Table 3.6, which is organized such that for each study initial mixture molar ratio, temperature, pressure, flame thickness $\ell_{reaction}$, estimated mean free path length ℓ_{mfp}, finest length scale ℓ_{finest} predicted by the generalized eigenvalue analysis, and employed grid resolution Δx are listed, respectively. In all cases, the predicted ℓ_{finest} are at the micron-level, and they are well correlated with the associated cutoff length scales admitted by the continuum theory.

Katta and Roquemore [144] investigated the structure of an axi-symmetric premixed hydrogen–air jet flame using a time-dependent two-dimensional algorithm. The utilized discretization was nonuniform, and the minimum grid size in the axial direction was 2.50×10^{-2} cm. The detailed kinetics model consisted of $N = 11$ species and $J = 20$ reversible reactions. It has a typographical error in reaction $5 - 6$ which is unbalanced. This error is corrected by returning to the work of Westbrook [145] and adopting the corresponding reactions.

Thiele *et al.* [146] used a time-dependent two-dimensional model to simulate the spark-ignition in a quiescent hydrogen–air mixture described by a detailed kinetics. The reaction mechanism consists of $N = 9$ species and $J = 38$ irreversible reactions, adopted from the work of Warnatz *et al.* [67]. Although the grid discretization in this study is not mentioned, the predicted required length scale, 7.56×10^{-4} cm, to fully resolve such a system was beyond the existing computational capabilities.

Patnaik and Kailasanath [147] used a detailed kinetics model extracted from

the work of Burks and Oran [148] to simulate a two-dimensional burner stabilized hydrogen–air flame [118]. The extracted model consists of $J = 48$ elementary reactions involving $N = 9$ species, but the original model has typographical errors in reactions 4 and 12, which were unbalanced. These errors are corrected by returning to the work of Baulch *et al.* [149] and Hampson *et al.* [150] and adopting the corresponding reactions. The spatial resolution in this study was nonuniform, though the average grid size was $\Delta x = 3.54 \times 10^{-2}\ cm$.

Knio and Najm [151] and Najm and Wyckoff [152] investigated the interaction of a premixed methane–air flame with a two-dimensional vortex pair using an operator–splitting technique. In the first study, the detailed GRI-1.2 mechanism [153] is used with $N = 32$ species and $J = 177$ reversible reactions. And the utilized discretization was uniform with a grid size $1.5625 \times 10^{-3}\ cm$. In the second study, the chemical mechanism is a skeletal C_1-reaction set consisting of $N = 16$ species and $J = 27$ reversible reactions, such mechanisms are obtained by removing all the species that contain more than one carbon atom and eliminating the associated reaction steps from the detailed mechanism. Here, the utilized discretization is not clear, but the computational domain is $0.4\ cm \times 1.6\ cm$, which makes it beyond the existing computational capabilities to be fully resolved with $\ell_{finest} = 6.12 \times 10^{-4}\ cm$.

Katta *et al.* [154] used a detailed kinetics model from the work of Katta and Roquemore [155] to simulate a two-dimensional partially-premixed methane–air flame inside an idealized boiler. The kinetic model consists of $J = 81$ elementary reactions involving $N = 24$ species. Two different uniform spatial resolutions are used in this study. For the finest one, the grid size was $\Delta x = 5.00 \times 10^{-3}\ cm$.

TABLE 3.6

COMPARISON OF LENGTH SCALES AMONG VARIOUS MODELS THAT USE DETAILED KINETICS TO DESCRIBE A LAMINAR PREMIXED HYDROGEN–AIR FLAME.

Ref.	Mixture molar ratio	$T_u\ [K]$	$p\ [atm]$	$\ell_{reaction}\ [cm]$	$\ell_{mfp}\ [cm]$	$\ell_{finest}\ [cm]$	$\Delta x\ [cm]$
[144]	$1.26H_2 + O_2 + 3.76N_2$	4×10^2	1×10^0	2.93×10^{-3}	4.33×10^{-5}	8.05×10^{-4}	2.50×10^{-2}
[146]	$1.19H_2 + O_2 + 3.76N_2$	3.05×10^2	9.87×10^{-1}	4.83×10^{-3}	3.99×10^{-5}	7.56×10^{-4}	—
[147]	$0.59H_2 + O_2 + 3.76N_2$	3.50×10^2	1×10^0	7.24×10^{-2}	7.84×10^{-6}	4.35×10^{-5}	3.54×10^{-2}
[151]	$CH_4 + 2O_2 + 10N_2$	2.98×10^2	1×10^0	1.16×10^{-2}	6.68×10^{-6}	2.89×10^{-5}	1.56×10^{-3}
[152]	$CH_4 + 2O_2 + 10N_2$	2.98×10^2	1×10^0	2.45×10^{-2}	4.33×10^{-5}	6.12×10^{-4}	—
[154]	$CH_4 + 2O_2 + 7.52N_2$	2.98×10^2	1×10^0	3.48×10^{-3}	6.68×10^{-6}	5.21×10^{-5}	5.00×10^{-3}

The main result from Table 3.6 is that none of these studies have utilized a grid resolution Δx that is less than or equal to the finest length scale ℓ_{finest} which is required to have unambiguously resolved detailed species concentration predictions for a steady one-dimensional laminar premixed flame in comparable mixture under the same conditions. Moreover, the utilized grid resolution Δx is at least two orders of magnitude greater than ℓ_{finest}. In each study, different physical phenomena are simulated, and the mathematical models that are used vary, but the commonality in all studies is the usage of a detailed kinetics model to simulates flame in a reactive mixture.

3.4 Spatio-temporal spectrum

We next study the time spectrum of the full reacting flow system governed by Eqs (2.20). In principle, we would perturb the steady laminar flame structure of Sec. 3.3.5.2, and calculate the system's eigenvalue spectrum. However, this presents overwhelming computational demands in solving for eigenvalues of very large matrices.

As a useful alternative, we instead find the time scale spectrum associated with a system initially near a spatially homogeneous chemical equilibrium state. This is certainly relevant for laminar flame structure, as it represents the hot end. A spatially homogeneous system at chemical equilibrium is subjected to a spatially inhomogeneous perturbation, and its spatio-temporal response is predicted. To achieve this, the governing equations are most conveniently posed as a set of $2N+2$ partial differential algebraic equations (PDAEs) in terms of $2N+2$ state variables $\mathbf{z}$, composed of species mass fraction Y_i, species mass flux J_i^m, mixture specific

enthalpy h, and Fourier heat flux q. This system, in a compact representation, is

$$\mathbf{A}(\mathbf{z}) \cdot \frac{\partial \mathbf{z}}{\partial t} + \mathbf{B}(\mathbf{z}) \cdot \frac{\partial \mathbf{z}}{\partial x} = \mathbf{f}(\mathbf{z}). \tag{3.36}$$

When $\mathbf{z} = \mathbf{z}^e$, a constant vector, the system is in its equilibrium state, such that $\mathbf{f}(\mathbf{z}^e) = \mathbf{0}$. At this state, $\mathbf{A}(\mathbf{z})$, $\mathbf{B}(\mathbf{z})$ take on constant values, $\mathbf{A}(\mathbf{z}^e) \equiv \mathbf{A}^e$, $\mathbf{B}(\mathbf{z}^e) \equiv \mathbf{B}^e$. We next define perturbations from the equilibrium state as $\mathbf{z}' \equiv \mathbf{z} - \mathbf{z}^e$. We next eliminate $\mathbf{z}$ in favor of $\mathbf{z}'$ and linearize $\mathbf{f}$ about $\mathbf{z}^e$ in Eq. (3.36) to obtain

$$\mathbf{A}^e \cdot \frac{\partial \mathbf{z}'}{\partial t} + \mathbf{B}^e \cdot \frac{\partial \mathbf{z}'}{\partial x} = \mathbf{J}^e \cdot \mathbf{z}'. \tag{3.37}$$

Now, we address the problem via spatial discretization of the spatial derivative operators. Equation (3.37) is spatially discretized using a second order finite difference approximation on a spatially uniform grid. Then, the resulting equations are cast as a standard dynamical system of the form

$$\boldsymbol{\mathcal{A}}^e \cdot \frac{d\boldsymbol{\mathcal{Z}}}{dt} = (\boldsymbol{\mathcal{J}}^e - \boldsymbol{\mathcal{B}}^e) \cdot \boldsymbol{\mathcal{Z}}, \qquad \boldsymbol{\mathcal{Z}} \in \mathbb{R}^{2\mathcal{N}(N+1)} \tag{3.38}$$

where $\boldsymbol{\mathcal{A}}^e$ and $\boldsymbol{\mathcal{J}}^e - \boldsymbol{\mathcal{B}}^e$ are singular matrices of dimensions $2\mathcal{N}(N+1) \times 2\mathcal{N}(N+1)$, $\boldsymbol{\mathcal{Z}}$ is the set of state variables, and $\mathcal{N} = \dfrac{\mathtt{L}}{\Delta x} + 1 > 3$ is the total number of spatial points. Since $\boldsymbol{\mathcal{A}}^e$ is singular, standard eigenvalue analysis is not applicable. Instead, the generalized eigenvalues are calculated [126]; the system's time scales are the reciprocals of its generalized eigenvlaues. Moreover, each time scale is associated with a particular Fourier mode of wavenumber κ, which has a wavelength $\Lambda = 2\pi/\kappa$. Simultaneously, the associated generalized eigenvectors, *i.e.* discrete approximations of the continuous eigenfunctions which are normal modes of this dynamical system, are calculated. Figure 3.22 illustrates a portion of the first five

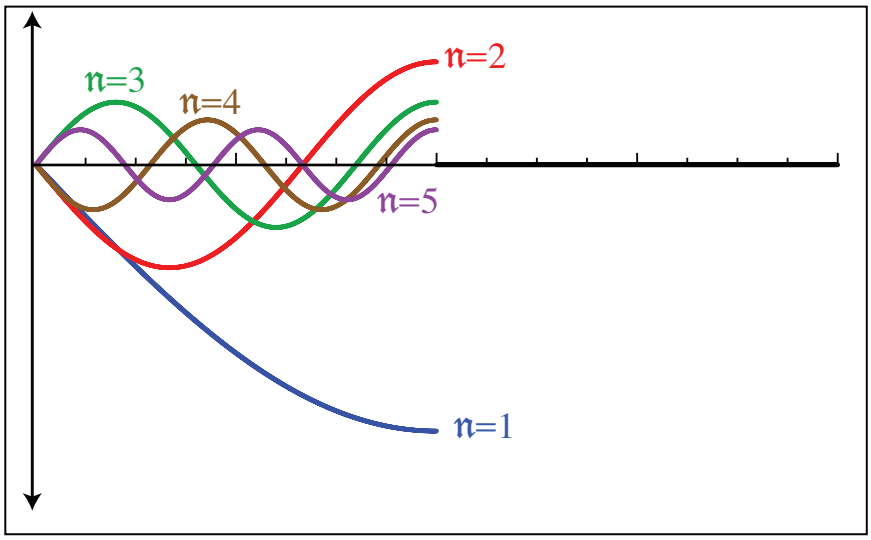

Figure 3.22. Portion of the first five discrete approximations of the continuous eigenfunctions for the hydrogen–air reaction-diffusion system.

generalized eigenvectors, since for each generalized eigenvector, the same pattern shown in Fig. 3.22 appears $N+1$ times.

For the system resulting from perturbing the chemical equilibrium state of the one-dimensional laminar premixed hydrogen–air flame, the time scale spectrum is presented in Fig. 3.23. Here, for the numerical results, the modified wavelength $\widehat{\Lambda}$ has been defined based on the number of zero crossings $\mathfrak{n}$, *i.e.* normal mode nodes, such that

$$\widehat{\Lambda} = \frac{4\mathrm{L}}{2\mathfrak{n}-1}, \qquad \mathfrak{n} = 1, 2, 3, \ldots \tag{3.39}$$

The unperturbed state is identical to the equilibrium state of Sec. 3.2; $T^e = 2617.95\ K$, $p = 1\ atm$, and $Y_i^e = [2.47\times10^{-3}, 1.44\times10^{-2}, 2.96\times10^{-5}, 1.74\times10^{-3}, 1.22\times10^{-2}, 5.49\times10^{-6}, 4.13\times10^{-7}, 2.24\times10^{-1}, 7.45\times10^{-1}]^T$, where $i = \{1, \ldots, 9\}$ corresponds to the species $\{H_2, O_2, H, O, OH, HO_2, H_2O_2, H_2O, N_2\}$, respectively.

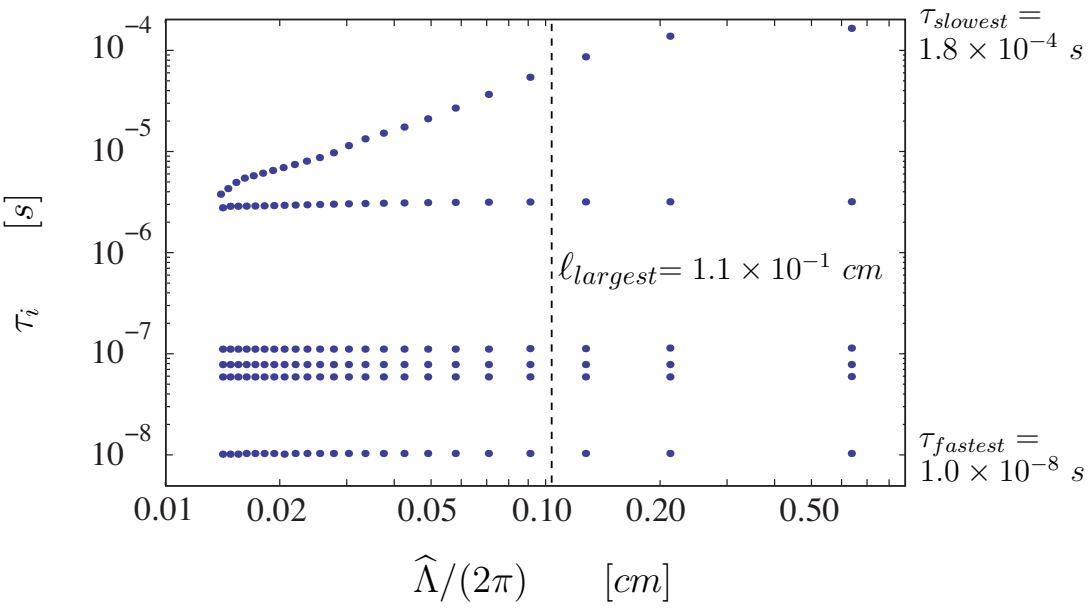

Figure 3.23. Time scale spectrum for the hydrogen–air reaction-advection-diffusion system versus the modified wavelength, $\mathtt{L} = 10^0\ cm$.

Because of the difficulty in calculating the generalized eigenvalues and eigenvectors of large systems, we were unable to present a window that contains more than one decade wavelength of the system's Fourier modes. Figure 3.23 clearly shows that the time scales associated with long wavelength modes match with the chemical time scales at the equilibrium state shown in Fig. 3.4; they are dictated by reaction. Moreover, the diffusion effect starts to appear through the slowest time scales associated with small wavelength modes.

By focusing on the fundamental mode and varying $\mathtt{L}$, a better understanding can be realized. In Fig. 3.24, the system's times scales associated with the fundamental modes, *i.e.* eigenfunctions with $\mathfrak{n} = 1$, are tracked as we vary the system's length. Because for $\mathfrak{n} = 1$, $\widehat{\Lambda} = 4\mathtt{L}$ from Eq. (3.39), we have $\widehat{\Lambda}/(2\pi) = 2\mathtt{L}/\pi$, and we use this for the abscissa. For large $\mathtt{L}$, the reaction-advection-diffusion system's

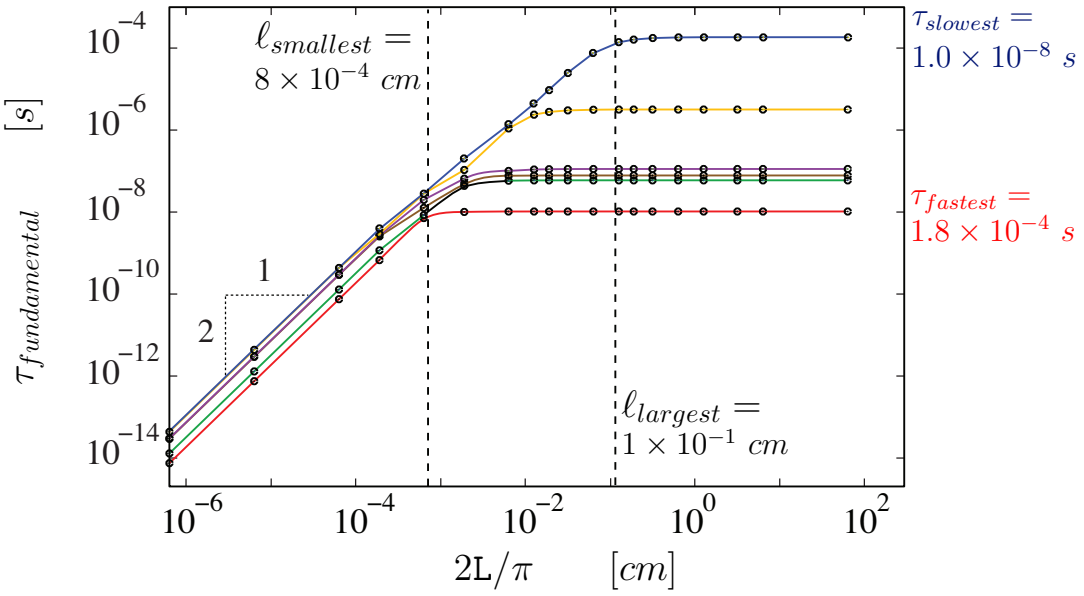

Figure 3.24. Time scales associated with the fundamental modes for the hydrogen–air reaction-advection-diffusion system versus the length $2\mathtt{L}/\pi$.

time scales and the reaction-only system's time scales at equilibrium are identical; compare Fig. 3.4 with Fig. 3.24 at large $\mathtt{L}$. However, for $2\mathtt{L}/\pi \sim 10^{-1}$ cm the effect of diffusion can be noted; it increases monotonically as $\mathtt{L}$ decreases. Also, the balance between reaction and diffusion is clear: short wavelength modes are dominated by diffusion, and large wavelength modes are dominated by reaction. Furthermore, the effect of adopting non-uniform diffusion coefficients, the multi-component diffusion coefficients $\mathfrak{D}_{ij}$ in Eqs. (2.21a), is noted in the time scale's falloff region, $\mathtt{L} \leq 10^{-4}$ cm. In this region where diffusion is dominant, one can note that the slope of each $\tau_{fundamental}$ is the same, but their intercepts are different. Also, it is obvious that in the diffusion-dominated region, there is a two decade drop in τ for every one decade drop in $\mathtt{L}$. Thus, one would expect that in this region $\tau \sim \mathtt{L}^2/\mathfrak{D}_{ij}$, which is consistent with our observations.

It is clear from Figs. 3.23–3.24 that the branch associated with the slowest chemical time scales starts to become influenced by diffusion before branches associated with the faster chemical time scales; the turning point for the fastest chemical time scale branch is $2\mathtt{L}/\pi \sim 10^{-3}\ cm$ and for the slowest chemical time scale branch is $2\mathtt{L}/\pi \sim 10^{-1}\ cm$. These turning points represent the length scale where diffusion starts to balance reaction.

Now we can also try to independently predict the turning points by employing an *ad hoc* formula to estimate the length scales,

$$\ell_{smallest} = \sqrt{D_{mix}\tau_{fastest}}, \tag{3.40a}$$

$$\ell_{largest} = \sqrt{D_{mix}\tau_{slowest}}, \tag{3.40b}$$

where $\tau_{fastest}, \tau_{slowest}$ are, respectively, the slowest and fastest time scales of the unsteady spatially homogeneous version of the problem, and D_{mix} is the mixture average diffusion coefficient. This is subject to greater error because we actually have a multicomponent diffusion process, coupled with diffusion of energy as well. Let us estimate the mixture average diffusion coefficient D_{mix} and take it to be the average of the species mass diffusion coefficients,

$$D_{mix} = \frac{1}{N^2}\sum_{i=1}^{N}\sum_{j=1}^{N}\mathfrak{D}_{ij}. \tag{3.41}$$

Our computational prediction gives $D_{mix} \approx 61.25\ cm^2/s$. As a result, we estimate the turning points for fast and slow reactions to be

$$\ell_{smallest} = 7.94 \times 10^{-4}\ cm, \tag{3.42a}$$

$$\ell_{largest} = 1.06 \times 10^{-1}\ cm, \tag{3.42b}$$

where $\tau_{fastest} = 1.03 \times 10^{-8}\ s$ and $\tau_{slowest} = 1.85 \times 10^{-4}\ s$ are presented in Sec. 3.2. Both of these estimates, illustrated as dashed lines in Fig. 3.24, predict well the turning points.

For the more rigorous calculation of the system's finest length scale, presented in Sec. 3.3, it has been found that the finest length scale admitted by the steady spatially homogeneous version is $\ell_{finest} = 2.41 \times 10^{-4}\ cm$. Interestingly, the simple estimate, Eq. (3.42a), is close in magnitude to ℓ_{finest} obtained by spatial eigenvalue analysis. Subsequently, it is clear that the reactive systems' temporal and spatial scales are coupled, and for a resolved structure, Fourier modes of varying wavelength are associated with time scales which are dictated by a balance between transport and chemistry. Another realistic problem, the ozone decomposition, is given in Appendix G.

CHAPTER 4

SLOW INVARIANT MANIFOLDS FOR SPATIALLY HOMOGENEOUS REACTIVE SYSTEMS

In this chapter, one-dimensional (1-D) slow invariant manifolds (SIMs) for unsteady, closed, isothermal, spatially homogeneous, reactive systems described by detailed kinetics are calculated. Here, dimensionality refers to the dimension of the composition space and not to the ordinary spatial dimension, as the systems we consider have no spatial inhomogeneity. The SIM for a reactive system is a subset of the species composition space. It describes the asymptotic structure of the invariant attracting reactive system's trajectories during their relaxation toward equilibrium. Here, only the 1-D SIMs will be constructed, although for each reactive system, there are SIMs of different dimensions.

A heteroclinic orbit is defined as a trajectory that connects two critical points. A 1-D SIM is defined here as a heteroclinic orbit that is locally attractive along the complete trajectory. The method is based on global analysis of the composition space of the reactive system. The identification of all the reactive system's critical points plays a major role in calculating the system's SIM. The SIMs are constructed by connecting the systems' critical points with each other via trajectories. The method will be applied to several realistic and model reactive systems, including a detailed hydrogen–air kinetics model.

4.1 Model equations

By confining our attention to unsteady spatially homogeneous mixtures of calorically imperfect ideal gases described by detailed kinetics, the governing equations presented in Sec. 2.2.2 are reduced to

$$\frac{dY_i}{dt} = \frac{\dot{\omega}_i \bar{m}_i}{\rho}, \quad i = 1, \ldots, N. \tag{4.1}$$

Thus, using Eqs. (2.7) and (2.11), the change in the number of moles of species i with t due to chemical reaction is described by the following system [99]:

$$\frac{dn_i}{dt} = V \sum_{j=1}^{J} \nu_{ij} r_j, \qquad i = 1, \ldots, N, \tag{4.2a}$$

$$n_i|_{t=0} = n_i^*, \qquad i = 1, \ldots, N. \tag{4.2b}$$

This system defines an N-dimensional composition space $\mathbb{R}^N$. But, as described in Sec. 2.1.1, in any closed reactive system the total number of moles of each element is conserved. Moreover, additional constraints could arise as a result of considering special cases. So, by multiplying both sides of Eq. (4.2a) by ϕ_{li}, summing the result from $i = 1$ to N, one gets

$$\frac{d}{dt}\left(\sum_{i=1}^{N} \phi_{li} n_i\right) = V \sum_{j=1}^{J} r_j \sum_{i=1}^{N} \phi_{li} \nu_{ij}. \tag{4.3}$$

By employing Eq. (2.3) to set the right side to zero, integrating the resulting homogeneous differential equation, and applying the initial condition, Eq. (4.2b), one obtains

$$\sum_{i=1}^{N} \phi_{li} n_i = \sum_{i=1}^{N} \phi_{li} n_i^*, \quad l = 1, \ldots, L. \tag{4.4}$$

Generally, Eq. (4.4) is an underconstrained linear system of L equations for the N values of n_i [156]. This implies that it has solutions of the following form

$$n_i = n_i^* + m\left(\sum_{k=1}^{R} \mathcal{D}_{ik} z_k\right), \quad i = 1, \ldots, N. \tag{4.5}$$

Here,

$$z_k = \frac{n_k}{m}, \quad k = 1, \ldots, R, \tag{4.6}$$

is a reduced composition variable which physically represents the number of moles of species k per total mass, and

$$\mathcal{D}_{ik} \equiv \boldsymbol{\mathcal{D}} : \mathbb{R}^N \rightarrow \mathbb{R}^R, \tag{4.7}$$

is a dimensionless constant matrix of size $N \times R$ and has a full rank R. Each column vector of $\boldsymbol{\mathcal{D}}$ is linearly independent of the remaining column vectors, and span the same column space as ν_{ij}. This can be illustrated by the following relation

$$\sum_{i=1}^{N} \phi_{li} \mathcal{D}_{ik} = 0, \quad l = 1, \ldots, L, \quad k = 1, \ldots, R. \tag{4.8}$$

However, $\mathcal{D}_{ik}$ is not unique; it can be constructed in several ways. Further information is given in Appendix H.

Equation (4.5) allows the N species to be represented in terms of R dependent variables. First, take the time derivative of Eq. (4.5) to get

$$\frac{dn_i}{dt} = m\left(\sum_{k=1}^{R} \mathcal{D}_{ik} \frac{dz_k}{dt}\right), \quad i = 1, \ldots, N. \tag{4.9a}$$

Now, by substituting Eq. (4.2a) into Eq. (4.9a), one obtains

$$\underbrace{\frac{V}{m}\sum_{i=1}^{N}\nu_{ij}r_j}_{\frac{1}{\rho}\dot{\omega}_i} = \sum_{k=1}^{R}\mathcal{D}_{ik}\frac{dz_k}{dt}, \quad i = 1,\ldots,N. \tag{4.9b}$$

In Gibbs notation, Eq. (4.9b) is written as

$$\frac{1}{\rho}\dot{\boldsymbol{\omega}} = \boldsymbol{\mathcal{D}}\cdot\frac{d\mathbf{z}}{dt}, \quad \mathbf{z}\in\mathbb{R}^R, \quad \dot{\boldsymbol{\omega}}\in\mathbb{R}^N. \tag{4.9c}$$

We take the matrix product of both sides of Eq. (4.9c) with $\boldsymbol{\mathcal{D}}^T$ to obtain

$$\frac{1}{\rho}\boldsymbol{\mathcal{D}}^T\cdot\dot{\boldsymbol{\omega}} = \boldsymbol{\mathcal{D}}^T\cdot\boldsymbol{\mathcal{D}}\cdot\frac{d\mathbf{z}}{dt}, \quad \mathbf{z}\in\mathbb{R}^R, \quad \dot{\boldsymbol{\omega}}\in\mathbb{R}^N. \tag{4.9d}$$

Then, to remove $\boldsymbol{\mathcal{D}}$ from the right hand side of Eq. (4.9d), we take the matrix product of both sides by $\left(\boldsymbol{\mathcal{D}}^T\cdot\boldsymbol{\mathcal{D}}\right)^{-1}$,

$$\frac{1}{\rho}\left(\boldsymbol{\mathcal{D}}^T\cdot\boldsymbol{\mathcal{D}}\right)^{-1}\boldsymbol{\mathcal{D}}^T\cdot\dot{\boldsymbol{\omega}} = \underbrace{\left(\boldsymbol{\mathcal{D}}^T\cdot\boldsymbol{\mathcal{D}}\right)^{-1}\cdot\left(\boldsymbol{\mathcal{D}}^T\cdot\boldsymbol{\mathcal{D}}\right)}_{=\mathbf{I}}\cdot\frac{d\mathbf{z}}{dt}, \quad \mathbf{z}\in\mathbb{R}^R, \quad \dot{\boldsymbol{\omega}}\in\mathbb{R}^N, \tag{4.9e}$$

where $\mathbf{I}$ is the identity matrix.

Consequently, the rate of evolution of the species in the reactive mixture is governed by

$$\frac{dz_k}{dt} = \dot{w}_k, \qquad k = 1,\ldots,R, \tag{4.10a}$$

$$z_k|_{t=0} = z_k^*, \qquad k = 1,\ldots,R, \tag{4.10b}$$

where

$$\dot{w}_k = \frac{1}{\rho}\sum_{j=1}^{R}\left[\left(\sum_{i=1}^{N}\mathcal{D}_{ik}\mathcal{D}_{ij}\right)^{-1}\left(\sum_{i=1}^{N}\mathcal{D}_{ij}\ \dot{\omega}_i\right)\right], \quad k = 1,\ldots,R, \tag{4.11}$$

is the molar production rate of species k in the reduced composition space. So, the reactive system's solutions, represented as trajectories, move within the reduced composition space $\mathbb{R}^R$ where $\mathbb{R}^R \subset \mathbb{R}^N$.

From a geometric point of view, the species specific moles $\mathbf{z}$ correspond to a vector in the Euclidian composition space $\mathbb{R}^R$. This vector is given by the following relation

$$\mathbf{z} = \mathcal{L}(\mathbf{n}) \ \Big|\ \mathcal{L} : \left(\mathbb{R}^N \rightarrow \mathbb{R}^R\right), \tag{4.12}$$

where

$$\mathcal{L}(\mathbf{n}) = \frac{1}{m}\left(\mathbf{\mathcal{D}}^T \cdot \mathbf{\mathcal{D}}\right)^{-1} \cdot \mathbf{\mathcal{D}}^T \cdot (\mathbf{n} - \mathbf{n}^*), \tag{4.13}$$

is a linear operator that accounts for all the system's linear constraints. The evolution of $\mathbf{z}$ in time is described as an autonomous dynamical system of the standard form

$$\frac{d\mathbf{z}}{dt} = \mathbf{f}(\mathbf{z}), \quad \mathbf{z} \in \mathbb{R}^R, \quad \mathbf{f} : \mathbb{R}^R \rightarrow \mathbb{R}^R, \tag{4.14}$$

where $\mathbf{f}$ is a set of R non-linear coupled algebraic functions. For an isothermal system, these functions are polynomials of degree $\mathfrak{q}$ connected with a given reaction mechanism. Generally, the k^{th} polynomial is given by the following form

$$f_k(\mathbf{z}) = \sum_{i=1}^{\mathfrak{q}} P_{ki}(\mathbf{z}), \tag{4.15}$$

where $P_{ki}(\mathbf{z})$ are a homogeneous i^{th} degree term in the k^{th} polynomial, *e.g.* the

second degree term in the k^{th} polynomial is $P_{k2}(\mathbf{z}) \equiv \sum_{l=1}^{R} \sum_{j=l}^{R} a_{klj} z_j z_l$, where a_{klj} is a constant.

4.2 Methodology

The construction method of the SIM is based on identifying all the equilibria of the dynamical system that describes the species evolution, Eq. (4.14). In general, the set of equilibria $\mathbf{z}^e$ of such functions is complex;

$$\mathbf{z}^e \in \mathbb{C}^R \mid \mathbf{f}(\mathbf{z}^e) = \mathbf{0} \,. \tag{4.16}$$

Also, as demonstrated by Perko [157], the set of equilibria $\mathbf{z}^e$ contains finite equilibria and infinite equilibria; *i.e.* equilibria located at infinity. Both classes of equilibria will be of interest. Furthermore, the equilibria can be positive dimensional continua [158, 159]; *i.e.* high-dimensional equilibria. Such equilibria have dimension larger than zero; 0-D equilibria are points, 1-D equilibria are curves, 2-D equilibria are surfaces, 3-D equilibria are volumes, *etc.* Then, the equilibria are connected via heteroclinic orbits obtained by numerical integration of the species evolution equations using any computationally inexpensive scheme. Recall that a heteroclinic orbit is a trajectory that connects two critical points. Finally, the 1-D SIM that describes the asymptotic structure of the invariant attracting trajectories is identified.

4.2.1 Computational remarks

Here, all calculations have been performed to 100 significant digits. However, all the listed results have been rounded to six significant digits. Integer values indi-

cate that the reported numbers are exact. The fourth-order Runge-Kutta scheme has been used to construct all the heteroclinic orbits. The thermodynamic properties are obtained from the public domain edition of the `CHEMKIN` package [128]. Subsequently, the property values are treated as having infinite precision.

Identifying all of the equilibria is the major task of constructing the reactive system's SIM. So, `BERTINI` [160], which is a free software package designed to compute the equilibria of polynomial systems over the field of complex numbers $\mathbb{C}$ using homotopy continuation [158], is used to obtain the system's finite and infinite equilibria to any desired accuracy. However, polynomial systems that arise from reactive systems modeling are poorly scaled; the differences between the equations' coefficients are several orders of magnitude. This can lead to numerical difficulties when the equilibria are computed. Thus, prior to the use of `BERTINI`, the polynomial systems have to be rescaled to assure robust behavior of `BERTINI`. Brief descriptions of `BERTINI` and polynomial scaling are provided in Appendix I.

4.2.2 Finite equilibria

First, finite equilibria of Eq. (4.14) are obtained by finding all the $\mathbf{z}^e$ that satisfy $\mathbf{f}(\mathbf{z}^e) = \mathbf{0}$. One of these finite equilibria is the reactive system's physical equilibrium point, which is defined, for closed spatially homogeneous reactive systems, by the following relation [161]

$$\sum_{i=1}^{N} \nu_{ij} \bar{\mu}_i = 0, \quad j = 1, \ldots, J, \tag{4.17}$$

which can be derived from Eq. (2.13b), see Appendix J. Equation (4.17) implies that the equilibrium of a reactive system is defined as the thermodynamic state at which there is no change in the mixture chemical potential, *i.e.* the mixture

chemical potential is extremum. Also, Eq. (4.17) implies that all the reaction steps in a mechanism have to halt at the system's physical equilibrium point.

This critical point is of special interest; it is the only critical point located inside the physically accessible domain, $\mathbb{S}$ [156], which is defined as a subspace within the reduced composition space where all the species are positive semi-definite and finite;

$$\mathbb{S} \subset \mathbb{R}^R \subset \mathbb{R}^N \mid n_i \geq 0, \quad i = 1, \ldots, N. \tag{4.18}$$

The rest of the finite equilibria are located outside $\mathbb{S}$; they are non-physical since at least one of the species has negative numbers of moles, $n_i < 0, \quad i \in \{1, \ldots, N\}$. Moreover, $\mathbb{S}$ represents the minimum of the mixture associated thermodynamic potential function. This function is the Gibbs free energy G in the case of an isothermal-isobaric system, and Helmholtz free energy $A = E - TS$ in the case of an isothermal-isochoric system.

4.2.3 Infinite equilibria

Second, the dynamical system's infinite equilibria are calculated by using a projective geometry technique. Two of these techniques are employed in this work: 1) the Poincaré sphere technique [157, 162], and 2) the projective space technique [158, 163]. These techniques map the equilibria at infinity into the finite domain where they can be easily computed. However, as a constraint, to employ one of these techniques, all the polynomials $\mathbf{f}(\mathbf{z})$ in Eq. (4.14) must be of the same degree, $\mathtt{q}$.

4.2.3.1 Poincaré sphere technique

The Poincaré sphere is a central projection technique which maps the phase space onto the surface of a unit sphere $\mathcal{S}$, which is defined as

$$\mathcal{S} = \left\{ \boldsymbol{\mathcal{U}} \in \mathbb{R}^{R+1} \;\middle|\; \sum_{i=1}^{R+1} \mathcal{U}_i^2 = 1 \right\}. \tag{4.19a}$$

where

$$\mathcal{U}_i = \frac{z_i}{\sqrt{1 + \sum_{j=1}^{R} z_j^2}}, \quad i = 1, \ldots R, \tag{4.19b}$$

$$\mathcal{U}_{R+1} = \frac{1}{\sqrt{1 + \sum_{j=1}^{R} z_j^2}}. \tag{4.19c}$$

Figure 4.1 illustrates the Poincaré sphere technique for a 2-D system from a geometric point of view. To employ ths technique, the origin of the original phase space is placed at the north pole of $\mathcal{S}$, and every point in the $\mathbf{z}$ space is connected with the center of $\mathcal{S}$ by a line. The intersection of the line with the surface of $\mathcal{S}$ assigns the location of the point in the transformed space, $\boldsymbol{\mathcal{U}}$. However, as shown in Fig. 4.1, each point z_* in the $\mathbf{z}$ space will be represented on the surface of $\mathcal{S}$ as two points; the point $\mathcal{U}_*$ and the antipodal point $\overline{\mathcal{U}}_*$. The antipodal point, or image, appears as a consequence of not using a one-to-one mapping, and its dynamical behavior is equivalent to $\mathcal{U}_*$ with a reversed flow direction; *i.e.* if $\mathcal{U}_*$ is a sink, then $\overline{\mathcal{U}}_*$ is source.

As a result of this mapping, the equilibria at infinity are mapped onto the equator of $\mathcal{S}$, where they can identified as the roots of following $R-1$ equations,

$$\mathcal{G}_k \equiv \mathcal{U}_i P_{j\mathfrak{q}} - \mathcal{U}_j P_{i\mathfrak{q}} = 0, \quad i \neq j, \quad i, j = 1, \ldots, R, \quad k = 1, \ldots, R-1. \tag{4.20}$$

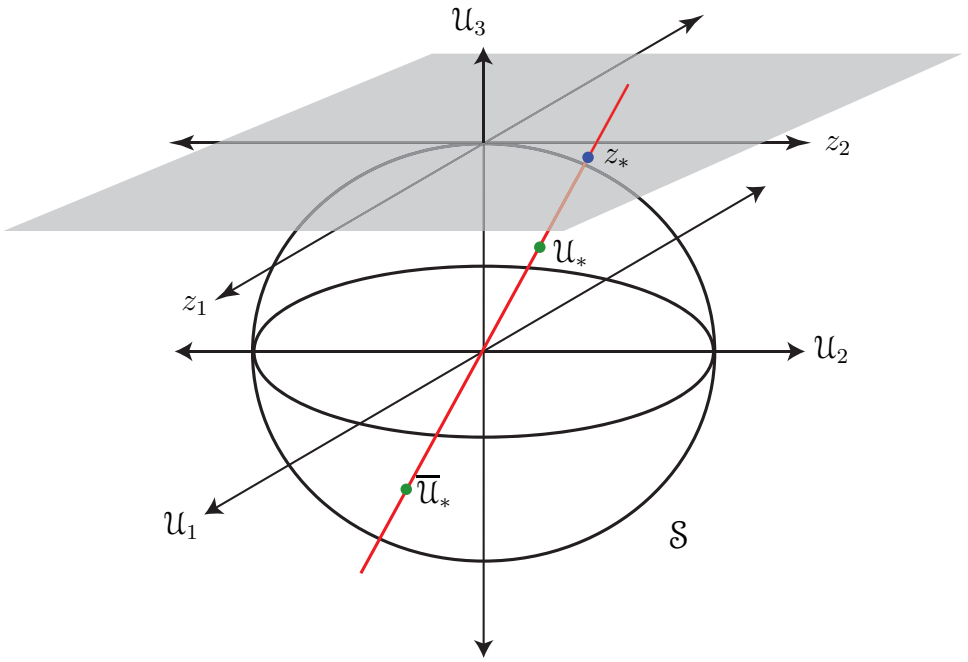

Figure 4.1. Sketch of the Poincaré sphere mapping. The point z_*, located in $\mathbf{z}$ space, is mapped onto the surface of $\mathcal{S}$, the $\boldsymbol{\mathcal{U}}$ space, as point $\mathcal{U}_*$ and as antipodal point $\overline{\mathcal{U}}_*$.

Recall that $P_{j\mathfrak{q}}$ is the highest degree terms in the j^{th} polynomial of the system $\mathbf{f}$. This technique has been used before in the literature to analyze the global dynamics of small, $N = 2$, reactive systems [45, 50]. The major disadvantages of this technique are: 1) it is not a one-to-one transformation, and 2) for high-dimensional systems, $N \geq 3$, it is computationally inefficient and algorithmically complex. But, it remains a useful tool for analyzing low dimensional systems; $N \leq 2$. Thus, in this work, use of this technique will be restricted to cases where better understanding of the low-dimensional reactive systems is needed.

4.2.3.2 Projective space technique

The projective space technique is a mapping approach to identify the equilibria located at infinity. It is defined as

$$\mathcal{P}\left(\mathbf{Z}\right) : \mathbb{R}^R \rightarrow \mathbb{R}^R, \tag{4.21}$$

Generally, it consists of the following two step one-to-one transformation:

$$Z_k = \frac{1}{\sum_{j=1}^{R} a_j z_j}, \qquad k \in \{1, \ldots, R\}, \tag{4.22a}$$

$$Z_i = \frac{z_i}{\sum_{j=1}^{R} a_j z_j}, \qquad i \neq k, \quad i = 1, \ldots, R, \tag{4.22b}$$

where $a_j \in [0, 1]$ is a set of random numbers such that $\sum_{j=1}^{R} a_j = 1$, $\mathbf{Z}$ are the state variables in the projective space, and Z_k is any arbitrarily selected new dependent variable. However, forms other than Eqs. (4.22) of this mapping exist. As a result of employing the projective space technique, the infinite equilibria are mapped onto the line $Z_k = 0$.

Here, to illustrate how the original dynamical system, Eq. (4.14), is recast in the projective space, the following simple form of the transformation, Eqs. (4.22), will be employed,

$$Z_k = \frac{1}{z_k}, \qquad k \in \{1, \ldots, R\}, \tag{4.23a}$$

$$Z_i = \frac{z_i}{z_k}, \qquad i \neq k, \quad i = 1, \ldots, R. \tag{4.23b}$$

where z_k is any arbitrarily selected dependent variable. Equations (4.23) are a

special form of Eqs. (4.22) that can be obtained by choosing a_j as,

$$a_j = \begin{cases} 0, & j \neq k, \\ 1, & j = k. \end{cases} \tag{4.24}$$

However, in certain cases there is a degeneracy in employing this simple form. Choosing certain dependent variables to serve as z_k in Eqs. (4.23) can cause one infinite equilibrium point to be missed. Explicitly, if there is an infinite equilibrium point located at $z_j = \infty, j \in \{1, \ldots, R\}$, the dependent variable z_k has to be selected such that $j = k$ to identify that particular equilibrium. In other words, that specific infinite equilibrium point is located at $Z_k = \infty$. Although the existence of such an equilibrium point is not known *a priori*, checking at least two projective spaces will overcome this issue.

We start the mapping process by rewriting the relation between the dependent variables in the original composition space $\mathbf{z}$, and the dependent variables in the transformed space $\mathbf{Z}$. From Eqs. (4.23), one gets

$$z_k = \frac{1}{Z_k}, \qquad k \in \{1, \ldots, R\}, \tag{4.25a}$$

$$z_i = \frac{Z_i}{Z_k}, \qquad i \neq k, \quad i = 1, \ldots, R. \tag{4.25b}$$

Thus, the original dynamical system, Eq. (4.14), becomes

$$\frac{d}{dt}\begin{pmatrix} Z_1/Z_k \\ \vdots \\ Z_{k-1}/Z_k \\ 1/Z_k \\ Z_{k+1}/Z_k \\ \vdots \\ Z_R/Z_k \end{pmatrix} = \begin{pmatrix} f_1\left(Z_1/Z_k, \ldots, Z_{k-1}/Z_k, 1/Z_k, Z_{k+1}/Z_k, \ldots, Z_R/Z_k\right) \\ \vdots \\ f_{k-1}\left(Z_1/Z_k, \ldots, Z_{k-1}/Z_k, 1/Z_k, Z_{k+1}/Z_k, \ldots, Z_R/Z_k\right) \\ f_k\left(Z_1/Z_k, \ldots, Z_{k-1}/Z_k, 1/Z_k, Z_{k+1}/Z_k, \ldots, Z_R/Z_k\right) \\ f_{k+1}\left(Z_1/Z_k, \ldots, Z_{k-1}/Z_k, 1/Z_k, Z_{k+1}/Z_k, \ldots, Z_R/Z_k\right) \\ \vdots \\ f_R\left(Z_1/Z_k, \ldots, Z_{k-1}/Z_k, 1/Z_k, Z_{k+1}/Z_k, \ldots, Z_R/Z_k\right) \end{pmatrix}. \tag{4.26a}$$

Using the chain rule, the left hand side of Eq. (4.26a) can be written as

$$\frac{d}{dt}\begin{pmatrix} Z_1/Z_k \\ \vdots \\ Z_{k-1}/Z_k \\ 1/Z_k \\ Z_{k+1}/Z_k \\ \vdots \\ Z_R/Z_k \end{pmatrix} \equiv \frac{1}{Z_k}\frac{d}{dt}\begin{pmatrix} Z_1 \\ \vdots \\ Z_{k-1} \\ 0 \\ Z_{k+1} \\ \vdots \\ Z_R \end{pmatrix} - \frac{1}{Z_k^2}\begin{pmatrix} Z_1 \\ \vdots \\ Z_{k-1} \\ 1 \\ Z_{k+1} \\ \vdots \\ Z_R \end{pmatrix}\frac{dZ_k}{dt}. \tag{4.26b}$$

By substituting Eq. (4.26b) in Eq. (4.26a), one gets

$$\frac{1}{Z_k}\frac{d}{dt}\begin{pmatrix} Z_1 \\ \vdots \\ Z_{k-1} \\ 0 \\ Z_{k+1} \\ \vdots \\ Z_R \end{pmatrix} - \frac{1}{Z_k^2}\begin{pmatrix} Z_1 \\ \vdots \\ Z_{k-1} \\ 1 \\ Z_{k+1} \\ \vdots \\ Z_R \end{pmatrix}\frac{dZ_k}{dt} = \begin{pmatrix} f_1\left(Z_1,\ldots,Z_k,\ldots,Z_R\right) \\ \vdots \\ f_{k-1}\left(Z_1,\ldots,Z_k,\ldots,Z_R\right) \\ f_k\left(Z_1,\ldots,Z_k,\ldots,Z_R\right) \\ f_{k+1}\left(Z_1,\ldots,Z_k,\ldots,Z_R\right) \\ \vdots \\ f_R\left(Z_1,\ldots,Z_k,\ldots,Z_R\right) \end{pmatrix}, \tag{4.26c}$$

where it is obvious that

$$f_i\left(\frac{Z_1}{Z_k},\ldots,\frac{Z_{k-1}}{Z_k},\frac{1}{Z_k},\frac{Z_{k+1}}{Z_k},\ldots,\frac{Z_R}{Z_k}\right) \equiv f_i\left(Z_1,\ldots,Z_k,\ldots,Z_R\right), \quad i=1,\ldots,R.$$

Here, the k^{th} row in Eq. (4.26c) states that

$$\frac{1}{Z_k^2}\frac{dZ_k}{dt} = -f_k\left(Z_1,\ldots,Z_R\right). \tag{4.26d}$$

Thus, Eq. (4.26a) can be rearranged, using Eqs. (4.26b) and (4.26d), to get

$$\frac{1}{Z_k}\frac{d}{dt}\begin{pmatrix} Z_1 \\ \vdots \\ Z_{k-1} \\ Z_k \\ Z_{k+1} \\ \vdots \\ Z_R \end{pmatrix} + f_k\left(Z_1,\ldots,Z_R\right)\begin{pmatrix} Z_1 \\ \vdots \\ Z_{k-1} \\ Z_k \\ Z_{k+1} \\ \vdots \\ Z_R \end{pmatrix} = \begin{pmatrix} f_1\left(Z_1,\ldots,Z_R\right) \\ \vdots \\ f_{k-1}\left(Z_1,\ldots,Z_R\right) \\ 0 \\ f_{k+1}\left(Z_1,\ldots,Z_R\right) \\ \vdots \\ f_R\left(Z_1,\ldots,Z_R\right) \end{pmatrix}. \tag{4.26e}$$

So, the original dynamical system, Eq. (4.14), is recast in the projective space, defined by Eqs. (4.25), in the following form:

$$\frac{d}{dt}\begin{pmatrix} Z_1 \\ \vdots \\ Z_{k-1} \\ Z_k \\ Z_{k+1} \\ \vdots \\ Z_R \end{pmatrix} = Z_k \begin{pmatrix} f_1\left(Z_1,\ldots,Z_R\right) - Z_1 f_k\left(Z_1,\ldots,Z_R\right) \\ \vdots \\ f_{k-1}\left(Z_1,\ldots,Z_R\right) - Z_{k-1} f_k\left(Z_1,\ldots,Z_R\right) \\ -Z_k f_k\left(Z_1,\ldots,Z_R\right) \\ f_{k+1}\left(Z_1,\ldots,Z_R\right) - Z_{k+1} f_k\left(Z_1,\ldots,Z_R\right) \\ \vdots \\ f_R\left(Z_1,\ldots,Z_R\right) - Z_R f_k\left(Z_1,\ldots,Z_R\right) \end{pmatrix}. \tag{4.26f}$$

In general, the projective space technique has the disadvantage of introducing a singularity in the dynamical system. By substituting $\mathbf{Z}$ in the polynomials $\mathbf{f}$, as described in the left hand side of Eq. (4.26f), and recalling Eqs. (4.15) and (4.25), it is clear that the highest degree terms in polynomials $\mathbf{f}$ have a $Z_k^{\mathfrak{q}}$ in their denominators. To overcome this difficulty, we define a transformed independent variable $\mathfrak{t}$ in the projective space which is related to t in the original space as follows:

$$\frac{dt}{d\mathfrak{t}} = \left(Z_k\right)^{\mathfrak{q}-1}, \tag{4.27}$$

where we recall that $\mathfrak{q}$ is the maximum degree of the polynomials in $\mathbf{f}$. By em-

ploying this transformation, Eq. (4.26f) becomes

$$\frac{d}{d\mathfrak{t}}\begin{pmatrix} t \\ Z_1 \\ \vdots \\ Z_{k-1} \\ Z_k \\ Z_{k+1} \\ \vdots \\ Z_R \end{pmatrix} = \begin{pmatrix} Z_k^{\mathfrak{q}-1} \\ Z_k^{\mathfrak{q}} \cdot \left(f_1\left(Z_1,\ldots,Z_R\right) - Z_1 f_k\left(Z_1,\ldots,Z_R\right)\right) \\ \vdots \\ Z_k^{\mathfrak{q}} \cdot \left(f_{k-1}\left(Z_1,\ldots,Z_R\right) - Z_{k-1} f_k\left(Z_1,\ldots,Z_R\right)\right) \\ -Z_k^{\mathfrak{q}+1} \cdot f_k\left(Z_1,\ldots,Z_R\right) \\ Z_k^{\mathfrak{q}} \cdot \left(f_{k+1}\left(Z_1,\ldots,Z_R\right) - Z_{k+1} f_k\left(Z_1,\ldots,Z_R\right)\right) \\ \vdots \\ Z_k^{\mathfrak{q}} \cdot \left(f_R\left(Z_1,\ldots,Z_R\right) - Z_R f_k\left(Z_1,\ldots,Z_R\right)\right) \end{pmatrix}, \tag{4.28}$$

The finite equilibria of the resulting dynamical system, Eq. (4.28), represent the infinite equilibria of the original dynamical system, Eq. (4.14). We note here that $\mathbf{Z} \in \mathbb{R}^{R+1}$, though the value of Z_0^e is irrelevant; $Z_0^e = 0$.

Now, following the same presented procedure to obtain Eq. (4.28), one can show that the original dynamical system described by Eq. (4.14) is recast in the projective space, defined by Eqs. (4.22), in the following compact form:

$$\frac{d\mathbf{Z}}{d\mathfrak{t}} = \mathbf{F}\left(\mathbf{Z}\right), \tag{4.29a}$$

where

$$\mathbf{Z} = \begin{pmatrix} Z_0 \\ Z_1 \\ \vdots \\ Z_{k-1} \\ Z_k \\ Z_{k+1} \\ \vdots \\ Z_R \end{pmatrix}, \quad \mathbf{F}(\mathbf{Z}) = \begin{pmatrix} Z_k^{\mathfrak{q}-1} \\ Z_k^{\mathfrak{q}} \cdot \left(f_1(\mathbf{Z}) - Z_1 \sum_{j=1}^{R} a_j f_j(\mathbf{Z}) \right) \\ \vdots \\ Z_k^{\mathfrak{q}} \cdot \left(f_{k-1}(\mathbf{Z}) - Z_{k-1} \sum_{j=1}^{R} a_j f_j(\mathbf{Z}) \right) \\ -Z_k^{\mathfrak{q}+1} \sum_{j=1}^{R} a_j f_j(\mathbf{Z}) \\ Z_k^{\mathfrak{q}} \cdot \left(f_{k+1}(\mathbf{Z}) - Z_{k+1} \sum_{j=1}^{R} a_j f_j(\mathbf{Z}) \right) \\ \vdots \\ Z_k^{\mathfrak{q}} \cdot \left(f_R(\mathbf{Z}) - Z_R \sum_{j=1}^{R} a_j f_j(\mathbf{Z}) \right) \end{pmatrix}, \quad (4.29b)$$

and we denote $Z_0 = t$.

4.2.4 Equilibria's dynamical character

After identifying all the system's, Eq. (4.14), equilibria, the local dynamic behavior of the system within the neighborhood of each equilibrium is investigated by employing standard linearization techniques. The stability of each equilibrium is determined by examining the eigenvalue spectrum λ_i and the corresponding eigenvectors υ_i of the constant Jacobian matrix evaluated at the equilibrium $\mathbf{J}^e$. Further details regarding linearization technique are provided in Appendix C.

The physical equilibrium point must be a stable node [164]; *i.e.* all the eigenvalues of its $\mathbf{J}^e$ are real and negative. Furthermore, the ratio between the largest and smallest time scales identifies the system's temporal stiffness $\mathcal{S}_t$. In addition, the eigenvector associated with the least negative eigenvalue represents the system's slowest mode or direction in composition space along which the trajectories approach the physical equilibrium. Similarly, the eigenvector associated with the

largest eigenvalue in magnitude represents the system's fastest mode.

Physically, since all its eigenvalues are negative, a spatially homogeneous closed reactive system is a dissipative system [102]. Such a system, has to reach in infinite time its physical equilibrium point as a final state. From a geometrical viewpoint, this final state is a 0-D attractor. Since every attractor has its own basin of attraction [165], the reactive system's unique physical equilibrium point has a basin of attraction, which all the trajectories inside of it approach.

4.2.5 Construction method

Here, the procedure for constructing the closed spatially homogeneous reactive system's 1-D SIM is presented. In this, the following conjecture has been found to be useful, although there is no formal proof for it.

Conjecture:

> *Only the system's isolated non-physical real finite and infinite equilibria are relevant to the construction of a 1-D SIM connecting to the physical equilibrium. Furthermore, among these non-physical equilibria, only those with one unstable eigenvector direction can be candidate members of the 1-D SIM.*

As a consequence of the first part of the conjecture, the high-dimensional equilibria and the complex equilibria are not relevant. Furthermore, as a consequence of the second part of the conjecture, the real critical points with the following dynamical character are excluded: sinks, sources, saddles with more than one positive eigenvalue, and non-hyperbolic equilibria with more than one positive eigenvalue.

The system's finite and infinite equilibria that satisfy our conjecture will be called candidate equilibria. Starting from each one of these equilibria, a heteroclinic orbit is generated tangent to the equilibria unstable direction, *i.e.* the

eigenvector associated with the positive eigenvalue. Only heteroclinic orbits that connect to the physical equilibrium are relevant to the construction of the 1-D SIM. In general, the 1-D SIM consists of at most two branches. Among the heteroclinic orbits, two such orbits represent the branches of the system's 1-D SIM. These orbits can be identified since they are the only ones that approach the physical equilibrium point tangent to its slowest mode, and they are attractive.

First, the candidate points are categorized based on their location; the first category contains the finite candidate points, and the second category contains the candidate points located at infinity. Within each category the candidate points are ordered based on the magnitude of their positive eigenvalue. In each category, the first candidate point is taken as the one with the least positive eigenvalue among all the candidate points in that category. The second candidate point is taken as the one with the second least positive eigenvalue among all the candidate points in that category, and so on.

Next, we start the process of SIM construction by generating a heteroclinic orbit from the first candidate point in the first category; the finite candidate point with the least positive eigenvalue. To generate such an orbit, Eq. (4.14) is integrated in the direction of the eigenvector associated with the positive eigenvalue pointing towards the reactive system's physical equilibrium. Then, we check whether the generated orbit approaches the physical equilibrium point in the direction of its slowest mode, *i.e.* the eigenvector associated with the least negative eigenvalue at the physical equilibrium point. Subsequently, if the physical equilibrium is not located at the origin, another orbit is generated starting from the finite candidate point with the second lowest positive eigenvalue. If both of these orbits approach the physical equilibrium point in the direction of its slowest mode,

then these two orbits correspond to the SIM's two branches. Otherwise, we generate a new heteroclinic orbit from the finite candidate point with the third lowest eigenvalue, and so on. After using all finite candidate points, we follow the same procedure using the infinite candidate points. This procedure halts as soon as we construct two heteroclinic orbits that approach the physical equilibrium point in the direction of its slowest mode, see Fig. 4.2.

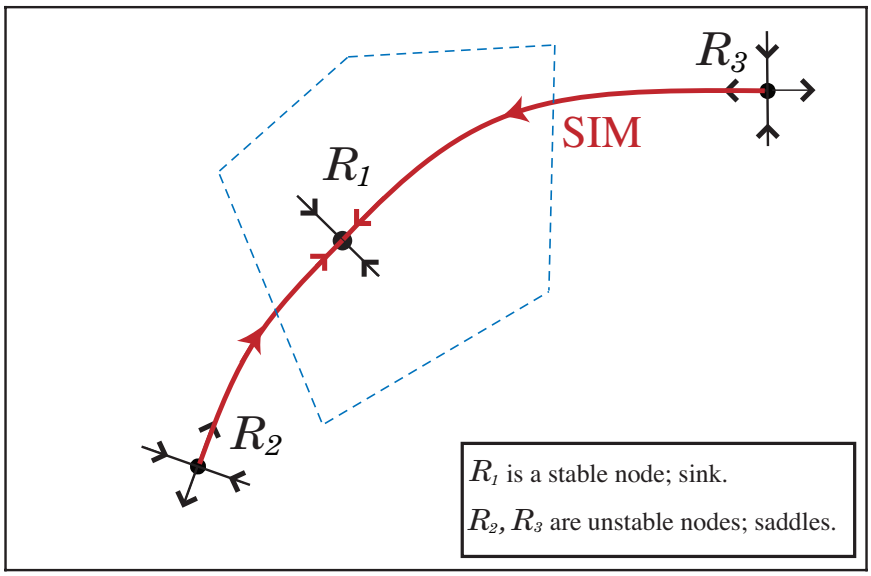

Figure 4.2. Sketch illustrating the construction method of a 1-D SIM. The thick line represents the constructed 1-D SIM. R_1 is the reactive system's unique physical equilibrium point. R_2 and R_3 are candidate points. The open arrows indicate the equilibria's local stability. The dashed simplex represents $\mathbb{S}$.

Finally, the attractiveness of the constructed 1-D SIM is examined locally along the complete manifold. Here, we pose the following criteria to hold along each branch of the 1-D SIM. The eigenvalues λ_i of $\mathbf{J}$ are computed locally along the heteroclinic orbit. Call λ_1 the largest eigenvalue. Then we require that for $i > 1$

$$\lambda_i < 0 \quad \text{and} \quad \mathsf{S} \equiv \frac{|\lambda_1|}{|\lambda_i|} < 1. \tag{4.30}$$

The constraints ensure that the composition field contracts along the 1-D SIM, and S is the contraction factor. Note that these criteria are more restrictive than the requirement for a contraction mapping, *i.e.* $\sum_{i=1}^{R} \lambda_i < 0$. Furthermore, the criteria preclude the SIM from emanating from a source. To summarize, we take the 1-D SIM to consist of at most two heteroclinic orbits that are locally attractive along their complete trajectories.

At this point, we note a fundamental question with regard to the existence of the actual SIM. Such a question has various interpretations in the literature [166–169]. The cause of such discussion is due to the difference in defining the SIM, in particular, whether it has to be locally invariant and slow or globally invariant and slow. Reference [169] states that for high dimensional dynamical systems:

> "A manifold that is locally invariant and locally slow exists but one that is globally invariant and globally slow does not."

This statement seems legitimate in the context of limit cycle type of character dynamical systems. However, our work is confined to closed reactive systems where limit cycles will not be exhibited. Moreover, the constructed 1-D SIM is a heteroclinic orbit, which implies that it is globally invariant.

4.3 Model problems

In this section, we illustrate our strategy for constructing a 1-D SIM using four problems. The first problem is a simple but realistic reactive system. The next two systems have been used in the literature as prototypes for illustrating alternate techniques of constructing SIMs. The last problem is a realistic reactive system, which has been used in Ref. [45] to construct a 1-D SIM using Poincaré sphere technique.

4.3.1 Zel'dovich mechanism

A common reaction kinetics model is the Zel'dovich mechanism of nitric oxide formation [67]. This mechanism consists of $N = 5$ species, $L = 2$ elements, and $J = 2$ reversible reactions. Kinetic data are adopted from Baulch *et al.* [170], see Table D.2. A special case in which the system is isochoric will be considered, and the assigned mixture temperature and volume are $T = 4000\ K$ and $V = 10^3\ cm^3$, respectively. For convenience, the assigned initial number of moles of each species is $\mathbf{n}^* = 10^{-3}\ mol$.

Here, $i = \{1, 2, 3, 4, 5\}$ correspond to the species $\{NO, N, O, O_2, N_2\}$, and $l = \{1, 2\}$ correspond to the elements $\{N, O\}$, respectively. For this system $\boldsymbol{\phi}$ has dimension 2×5:

$$\boldsymbol{\phi} = \begin{pmatrix} 1 & 1 & 0 & 0 & 2 \\ 1 & 0 & 1 & 2 & 0 \end{pmatrix},$$

and $\boldsymbol{\nu}$ has dimension 5×2:

$$\boldsymbol{\nu} = \begin{pmatrix} 1 & -1 \\ -1 & -1 \\ 1 & 1 \\ -1 & 0 \\ 0 & 1 \end{pmatrix}.$$

For the constraint of element conservation for each reaction, Eq. (2.3), we have

$$\boldsymbol{\phi} \cdot \boldsymbol{\nu} = \begin{pmatrix} 0 & 0 \\ 0 & 0 \end{pmatrix}.$$

Thus, there are two element constraints in this model.

We start by formulating the set of ODEs that describes this kinetic model. Following Eq. (4.2a), we get

$$\frac{d}{dt}\begin{pmatrix} n_1 \\ n_2 \\ n_3 \\ n_4 \\ n_5 \end{pmatrix} = V \begin{pmatrix} 1 & -1 \\ -1 & -1 \\ 1 & 1 \\ -1 & 0 \\ 0 & 1 \end{pmatrix} \begin{pmatrix} r_1 \\ r_2 \end{pmatrix}, \tag{4.31a}$$

where, from Eq. (2.12),

$$\begin{aligned} r_1 &= \frac{\mathcal{A}_1 T^{\beta_1}}{V^2} \exp\left(\frac{-\bar{\mathcal{E}}_1}{\bar{\Re} T}\right)\left(n_2 n_4 - \frac{n_1 n_3}{K_1^c}\right), \\ r_2 &= \frac{\mathcal{A}_2 T^{\beta_2}}{V^2} \exp\left(\frac{-\bar{\mathcal{E}}_2}{\bar{\Re} T}\right)\left(n_2 n_1 - \frac{n_5 n_3}{K_2^c}\right). \end{aligned}$$

Now, Eq. (4.31a) defines a real $\mathbb{R}^N$ composition space. To reduce the dimension of this composition space, we construct the matrix $\mathfrak{D}$, following one of the methods described in Appendix H. Here, method-I will be employed to construct $\mathfrak{D}$. First, we perform a series of row operations on Eq. (4.31a) to find all of the system's linear constraints; *i.e.* we generate the row-echelon form of $\boldsymbol{\nu}$. For that reason, we add the first row to the second and the fourth rows. Then, multiply the first row by -1 and add it to the third row. This gives

$$\frac{d}{dt}\begin{pmatrix} n_1 \\ n_2+n_1 \\ n_3-n_1 \\ n_4+n_1 \\ n_5 \end{pmatrix} = V \begin{pmatrix} 1 & -1 \\ 0 & -2 \\ 0 & 2 \\ 0 & -1 \\ 0 & 1 \end{pmatrix} \begin{pmatrix} r_1 \\ r_2 \end{pmatrix}. \tag{4.31b}$$

Next, add the second row to the third row, multiply the second row by $-\frac{1}{2}$ and add it to the fourth row, and multiply the second row by $\frac{1}{2}$ and add it to the fifth row. This gives

$$\frac{d}{dt}\begin{pmatrix} n_1 \\ n_2+n_1 \\ n_2+n_3 \\ \frac{1}{2}n_1-\frac{1}{2}n_2+n_4 \\ \frac{1}{2}n_1+\frac{1}{2}n_2+n_5 \end{pmatrix} = V \begin{pmatrix} 1 & -1 \\ 0 & -2 \\ 0 & 0 \\ 0 & 0 \\ 0 & 0 \end{pmatrix} \begin{pmatrix} r_1 \\ r_2 \end{pmatrix}, \tag{4.31c}$$

which is rewritten as

$$\begin{pmatrix} 1 & 0 & 0 & 0 & 0 \\ 1 & 1 & 0 & 0 & 0 \\ 0 & 1 & 1 & 0 & 0 \\ \frac{1}{2} & -\frac{1}{2} & 0 & 1 & 0 \\ \frac{1}{2} & \frac{1}{2} & 0 & 0 & 1 \end{pmatrix} \frac{d}{dt} \begin{pmatrix} n_1 \\ n_2 \\ n_3 \\ n_4 \\ n_5 \end{pmatrix} = V \begin{pmatrix} 1 & -1 \\ 0 & -2 \\ 0 & 0 \\ 0 & 0 \\ 0 & 0 \end{pmatrix} \begin{pmatrix} r_1 \\ r_2 \end{pmatrix}, \tag{4.31d}$$

or in Gibbs notation,

$$\mathbf{L} \cdot \frac{d\mathbf{n}}{dt} = V \left(\mathbf{U} \cdot \mathbf{r} \right).$$

We note that the rank of $\boldsymbol{\nu}$ is $R = 2$ which corresponds to the number of the non-zero rows of $\mathbf{U} = \mathbf{L} \cdot \boldsymbol{\nu}$.

In Eq. (4.31d) the last three equations are homogeneous, so this model contains three linear constraints. Moreover, it implies that the behavior of $\mathbf{n}$ as a function of time is described by the evolution of only two variables: n_1 and n_2. The remaining variables, $\{n_3, n_4, n_5\}$, can be expressed in terms of n_1 and n_2. These expressions are obtained by integrating the three homogeneous equations in the system to obtain

$$n_2 + n_3 = c_1, \tag{4.32a}$$

$$\frac{1}{2} n_1 - \frac{1}{2} n_2 + n_4 = c_2, \tag{4.32b}$$

$$\frac{1}{2} n_1 + \frac{1}{2} n_2 + n_5 = c_3, \tag{4.32c}$$

where c_1, c_2 and c_3 are constants that are determined from $\mathbf{n}^*$. Further elementary

row operations on Eqs. (4.32) reveal the following set:

$$n_1 + n_3 + 2n_4 = \quad c_1 + 2c_2 \quad = n_1^* + n_3^* + 2n_4^*, \tag{4.33a}$$

$$n_1 + n_2 + 2n_5 = \quad 2c_3 \quad = n_1^* + n_2^* + 2n_5^*, \tag{4.33b}$$

$$\sum_{i=1}^{N} n_i = \quad c_1 + c_2 + c_3 \quad = \sum_{i=1}^{N} n_i^*. \tag{4.33c}$$

Equations (4.33a) and (4.33b) indicate that the total number of moles of elemental oxygen and nitrogen are conserved. Equation (4.33c) states that the total number of molecules is constant. This last constraint is a consequence of including only bimolecular reactions in this kinetic model, which is not the case in general.

Now, by including the dependent variables, Eqs. (4.32) can be rearranged to obtain

$$\begin{pmatrix} n_1 \\ n_2 \\ n_3 \\ n_4 \\ n_5 \end{pmatrix} = \begin{pmatrix} 0 \\ 0 \\ c_1 \\ c_2 \\ c_3 \end{pmatrix} + \begin{pmatrix} 1 & 0 \\ 0 & 1 \\ 0 & -1 \\ -\frac{1}{2} & \frac{1}{2} \\ -\frac{1}{2} & -\frac{1}{2} \end{pmatrix} \begin{pmatrix} n_1 \\ n_2 \end{pmatrix}, \tag{4.34a}$$

and by introducing the reduced composition space variables as $z_k = (n_k - n_k^*)/m$, $k = 1, 2$, we get

$$\begin{pmatrix} n_1 \\ n_2 \\ n_3 \\ n_4 \\ n_5 \end{pmatrix} = \begin{pmatrix} n_1^* \\ n_2^* \\ c_1 - n_2^* \\ c_2 - \frac{1}{2}n_1^* + \frac{1}{2}n_2^* \\ c_3 - \frac{1}{2}n_1^* - \frac{1}{2}n_2^* \end{pmatrix} + m \begin{pmatrix} 1 & 0 \\ 0 & 1 \\ 0 & -1 \\ -\frac{1}{2} & \frac{1}{2} \\ -\frac{1}{2} & -\frac{1}{2} \end{pmatrix} \begin{pmatrix} z_1 \\ z_2 \end{pmatrix}. \tag{4.34b}$$

Using Eqs. (4.33), this system can be rewritten as

$$\mathbf{n} = \begin{pmatrix} n_1 \\ n_2 \\ n_3 \\ n_4 \\ n_5 \end{pmatrix} = \begin{pmatrix} n_1^* \\ n_2^* \\ n_3^* \\ n_4^* \\ n_5^* \end{pmatrix} + m \begin{pmatrix} 1 & 0 \\ 0 & 1 \\ 0 & -1 \\ -\frac{1}{2} & \frac{1}{2} \\ -\frac{1}{2} & -\frac{1}{2} \end{pmatrix} \begin{pmatrix} z_1 \\ z_2 \end{pmatrix} = \mathbf{n}^* + m\boldsymbol{\mathcal{D}} \cdot \mathbf{z}. \tag{4.34c}$$

As we can see, this model problem is now described in the $R = 2$ dimensional reactive composition space. Using Eqs. (4.10a) and (4.11), the non-linear ODE that describes the reactive system evolution is:

$$\frac{d\mathbf{z}}{dt} = \dot{\mathbf{w}} = \mathbf{f}(\mathbf{z}), \tag{4.35a}$$

where

$$\dot{\mathbf{w}} = \frac{-1}{\rho} \begin{pmatrix} r_2 - r_1 \\ r_1 + r_2 \end{pmatrix}. \tag{4.35b}$$

The mixture total mass is obtained by summing Eq. (2.2c) from $i = 1$ to N, $m = 1.20024 \times 10^{-1}\ g$. So, the mixture mass density is $\rho = 1.20024 \times 10^{-4}\ g/cm^3$. Explicitly, the evolution of the system is

$$\begin{aligned} \frac{dz_1}{dt} &= 2.50545 \times 10^2 + 1.16148 \times 10^7 z_2 + 6.98833 \times 10^8 z_2^2 - 9.97639 \times 10^4 z_1 \\ &\quad -3.22221 \times 10^9 z_2 z_1, \end{aligned} \tag{4.36a}$$

$$\begin{aligned} \frac{dz_2}{dt} &= 2.50545 \times 10^2 - 1.16599 \times 10^7 z_2 - 6.97930 \times 10^8 z_2^2 + 8.47281 \times 10^4 z_1 \\ &\quad -1.83651 \times 10^9 z_2 z_1, \end{aligned} \tag{4.36b}$$

where we note that the maximum degree of Eq. (4.36) is $\mathfrak{q} = 2$.

4.3.1.1 Finite equilibria

The procedure described in Sec. 4.2.2 is used to find the finite equilibria of the autonomous dynamical system, Eq. (4.35a), which describes the evolution of $\mathbf{z}$. By equilibrating the left hand side of Eqs. (4.36) and using `BERTINI` to find all the $\mathbf{z}^e$ that satisfy $\mathbf{f}(\mathbf{z}^e) = \mathbf{0}$, we find the following finite equilibria,

$$\begin{aligned} R_1 &\equiv (\mathbf{z}^e) = \left(-1.78335 \times 10^{-5}, -1.66808 \times 10^{-2}\right) mol/g, \\ R_2 &\equiv (\mathbf{z}^e) = \left(-4.19501 \times 10^{-3}, -2.66414 \times 10^{-5}\right) mol/g, \\ R_3 &\equiv (\mathbf{z}^e) = \left(3.04740 \times 10^{-3}, 2.94464 \times 10^{-5}\right) mol/g. \end{aligned}$$

Here, all the finite equilibria are real isolated critical points. The rest of the species are obtained from Eq. (4.34c):

$$\begin{aligned} R_1 \equiv (\mathbf{n}^e) = \big(&-2.14046 \times 10^{-6}, -2.00211 \times 10^{-3}, 4.00217 \times 10^{-3}, \\ &1.69579 \times 10^{-8}, 3.00212 \times 10^{-3}\big)\ mol, \\ R_2 \equiv (\mathbf{n}^e) = \big(&-5.03503 \times 10^{-4}, -3.19762 \times 10^{-6}, 2.00320 \times 10^{-3}, \\ &1.25015 \times 10^{-3}, 2.25335 \times 10^{-3}\big)\ mol, \\ R_3 \equiv (\mathbf{n}^e) = \big(&3.65762 \times 10^{-4}, 3.53428 \times 10^{-6}, 1.99647 \times 10^{-3}, \\ &8.18886 \times 10^{-4}, 1.81535 \times 10^{-3}\big)\ mol. \end{aligned}$$

It is clear that R_1 and R_2 are non-physical equilibria, while R_3 is a physical root that satisfies Eq. (4.18); R_3 is the reactive system's unique physical equilibrium point.

To investigate the dynamical character of each critical point, first Eqs. (4.36)

are linearized to find $\mathbf{J}^e$. Following Eq. (C.2) we obtain

$$\mathbf{J}^e = 10^9 \times \begin{pmatrix} -9.97639 \times 10^{-5} - 3.22221 z_2^e & 1.16148 \times 10^{-2} + 1.39767 z_2^e - 3.22221 z_1^e \\ 8.47281 \times 10^{-5} - 1.83651 z_2^e & -1.16599 \times 10^{-2} - 1.39586 z_2^e - 1.83651 z_1^e \end{pmatrix}. \tag{4.37}$$

By substituting R_1, R_2, and R_3 into $\mathbf{J}^e$, linear analysis in the neighborhood of each critical point reveals that R_1 is a source, R_2 is a saddle, and R_3 is a sink. The system's eigenvalues and the corresponding eigenvectors associated with each finite critical point are:

$$\begin{aligned} R_1 : (\lambda, \boldsymbol{\upsilon}) &= \left(4.17748 \times 10^7, 2.35315 \times 10^7\right), \\ &\quad \left([7.00082 \times 10^{-1}, 7.14063 \times 10^{-1}]^T, [3.60549 \times 10^{-1}, 9.32740 \times 10^{-1}]^T\right), \\ R_2 : (\lambda, \boldsymbol{\upsilon}) &= \left(7.10632 \times 10^5, -4.64305 \times 10^6\right), \\ &\quad \left([9.99583 \times 10^{-1}, 2.88607 \times 10^{-2}]^T, [-9.83408 \times 10^{-1}, 1.81406 \times 10^{-1}]^T\right), \\ R_3 : (\lambda, \boldsymbol{\upsilon}) &= \left(-1.91355 \times 10^5, -1.73009 \times 10^7\right), \\ &\quad \left([9.99998 \times 10^{-1}, 1.79171 \times 10^{-3}]^T, [-1.06750 \times 10^{-1}, 9.94286 \times 10^{-1}]^T\right). \end{aligned}$$

The eigenvalues' and eigenvectors' units are $1/s$ and mol/g, respectively.

Since the finite root R_2 has only one unstable mode, it is a candidate point for the 1-D SIM construction. Moreover, the system's physical fast and slow time scales are the ones associated with its physical equilibrium; R_3. These are, respectively, 5.78006×10^{-8} s and 5.22588×10^{-6} s, which give rise to a $\mathcal{S}_t = \mathcal{O}(10^2)$. So, even the two-step Zel'dovich mechanism retains temporal stiffness at $T = 4000$ K. The multiscale nature of this system is clearly shown in Fig. 4.3,

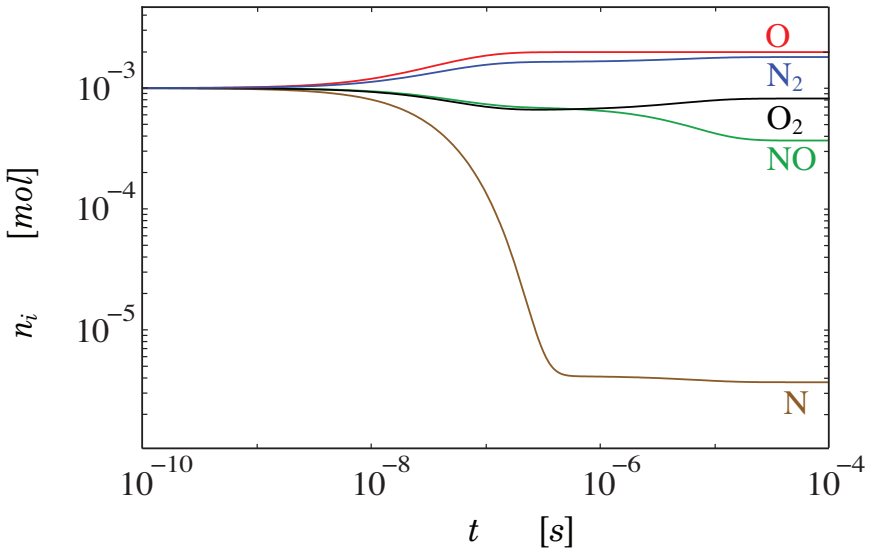

Figure 4.3. The time evolution of number of moles of each species for the Zel'dovich model problem.

where the full dynamics of the evolution of the species are presented. Here, the first reaction commences at $t \sim 10^{-8}$ s, and the system enters its last relaxation toward the physical equilibrium state after $t \sim 10^{-5}$ s.

4.3.1.2 Infinite equilibria

In addition to its three finite critical points, this system has equilibria at infinity. They can be identified using the projective space technique described in Sec. 4.2.3.2. For simplicity, the simple form of the transformation is employed, Eqs. (4.23).

Arbitrarily, we select $k = 1$, so the Zel'dovich reactive system in the projective space is realized by the following transformation: $Z_0 = t, Z_1 = 1/z_1,\ Z_2 = z_2/z_1$.

Subsequently, following Eq. (4.28), we have

$$\frac{dZ_0}{d\mathfrak{t}} = Z_1, \tag{4.38a}$$

$$\frac{dZ_1}{d\mathfrak{t}} = 9.97639 \times 10^4 Z_1^2 - 2.50545 \times 10^2 Z_1^3 + 3.22221 \times 10^9 Z_1 Z_2 - 1.16148 \times 10^7 Z_1^2 Z_2 - 6.98833 \times 10^8 Z_1 Z_2^2, \tag{4.38b}$$

$$\frac{dZ_2}{d\mathfrak{t}} = 8.47281 \times 10^4 Z_1 + 2.50545 \times 10^2 Z_1^2 (1 - Z_2) - 1.83651 \times 10^9 Z_2 - 1.16148 \times 10^7 Z_1 Z_2 + 2.52428 \times 10^9 Z_2^2 - 1.16148 \times 10^7 Z_1 Z_2^2 - 6.98833 \times 10^8 Z_2^3. \tag{4.38c}$$

By using `BERTINI` to find all the $\mathbf{Z}^e$ that satisfy $\mathbf{F}(\mathbf{Z}^e) = \mathbf{0}$, equilibrating the right hand side of Eqs. (4.38), we find three equilibria:

$$\begin{aligned} I_1 &\equiv (\mathbf{Z}^e) = (0, 0), \\ I_2 &\equiv (\mathbf{Z}^e) = (0, 1.00989), \\ I_3 &\equiv (\mathbf{Z}^e) = (0, 2.60224), \end{aligned}$$

and they represent the infinite equilibria of the original system, Eqs. (4.36). Here, all the infinite equilibria are real isolated critical points.

To investigate the dynamical character of each critical point, Eqs. (4.38b) and (4.38c) are linearized to find $\mathbf{J}^e$, and the eigenvalues and corresponding eigenvec-

tors are calculated:

$$
\begin{aligned}
I_1 : (\lambda, \boldsymbol{v}) &= \left(0, -1.83651 \times 10^9\right), \left([1.00000, 4.61353 \times 10^{-5}]^T, [0,1]^T\right), \\
I_2 : (\lambda, \boldsymbol{v}) &= \left(2.54135 \times 10^9, 1.12379 \times 10^9\right), \\
&\quad \left([9.99863 \times 10^{-1}, -1.65300 \times 10^{-2}]^T, [0,1]^T\right), \\
I_3 : (\lambda, \boldsymbol{v}) &= \left(3.65270 \times 10^9, -2.89575 \times 10^9\right), \\
&\quad \left([9.99862 \times 10^{-1}, -1.65893 \times 10^{-2}]^T, [0,1]^T\right),
\end{aligned}
$$

where the eigenvalues' units are $g/(mol\ s^2)$, the units of the first component of each eigenvector are g/mol, and the second component is dimensionless.

It is clear that I_2 is a source, I_3 is a saddle with one positive eigenvalue, and I_1 is a non-hyperbolic critical point. Consequently, the Hartman-Grobman theorem is not applicable at I_1. The normal form theory [171] is utilized to investigate the dynamical character of I_1, for further details see Appendix C. It is found that I_1 is a saddle-node [172], which consists of two hyperbolic sectors, one parabolic sector, and three separatrices, in the nomenclature of Ref. [157]. Only one of these separatrices is unstable. Thus, I_1 and I_3 are candidate points for constructing the system's 1-D SIM.

4.3.1.3 The construction of the SIM

Following our 1-D SIM construction procedure, the candidate points are segregated into two categories. The first category contains only one candidate point; R_2. The second category contains two candidate points: I_1 and I_3. So, the candidate points are ordered as follows: first R_2, second I_1, and third I_3, since R_2 is the only point in the first category, I_1 is infinite and it has the least positive

eigenvalue among the infinite candidate points.

Now, starting from the unstable direction of the candidate point R_2 that points toward the reactive system's physical equilibrium, Eqs. (4.36) are numerically integrated to generate a heteroclinic orbit. This orbit approaches R_3, the reactive system's physical equilibrium point, along its slowest mode. So, the generated orbit represents the first branch of the 1-D SIM. Then, starting from the unstable direction of the candidate point I_1 pointing towards the reactive system's physical equilibrium, Eqs. (4.38) are numerically integrated to generate another heteroclinic orbit. Also, this orbit approaches R_3 along its slowest mode, So, it represents the second and last branch of the reactive system's 1-D SIM, see Fig. 4.4. Subsequently, there is no need to check the third candidate point, I_3. However, to examine the described methodology, Eqs. (4.38) are numerically integrated starting from the unstable direction of the third candidate point I_3 pointing towards R_3 to generate a third heteroclinic orbit, illustrated in Fig. 4.4 as a dotted line. It is clearly shown that the heteroclinic orbit emanating from I_3 is attracted to the heteroclinic orbit that emanating from I_1.

In Fig. 4.5, part of the system's composition space and the SIM are shown. Upon visual examination of the attractiveness of the constructed SIM, it is clearly seen that all trajectories inside $\mathbb{S}$, and some outside of it, are attracted to the constructed 1-D SIM. Moreover, along the SIM's two branches, including the three equilibria R_3, R_2, and I_1, the criteria defined by Eq. (4.30) are satisfied, and S decreases monotonically along the 1-D SIM; its maximum value is $\mathsf{S} = 0.153053$ at R_2.

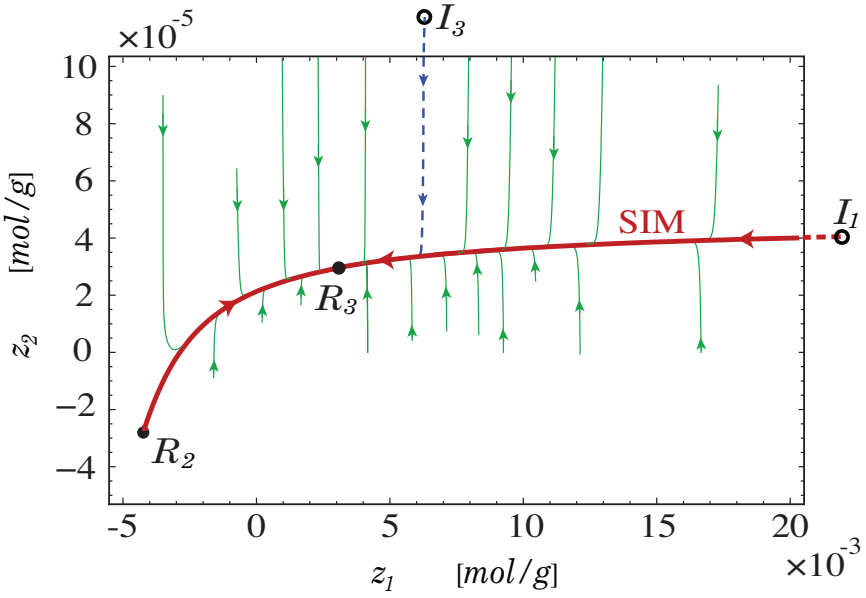

Figure 4.4. The constructed 1-D SIM for the Zel'dovich model problem. The SIM is illustrated as a thick line. The thin lines represent trajectories. The solid dots represent finite critical points. The open circles represent infinite critical points. The arrows indicate the flow directions. R_3 represents the system's physical equilibrium state.

4.3.2 Lebiedz's pedagogical mechanism

The second example here is identical to the second example presented by Lebiedz [41]. A simple closed reactive system contains three species given by the following kinetics model:

$$A + A \rightleftharpoons B \rightleftharpoons C.$$

Using the same argument, described in the original work [41], that the total mass is conserved, the dimension of the composition space of this model problem is reduced from $N = 3$ to $N - 1 = 2$. Also, for convenience, the dimensionless variables c_A and c_B in the original work [41] are denoted here by z_1 and z_2,

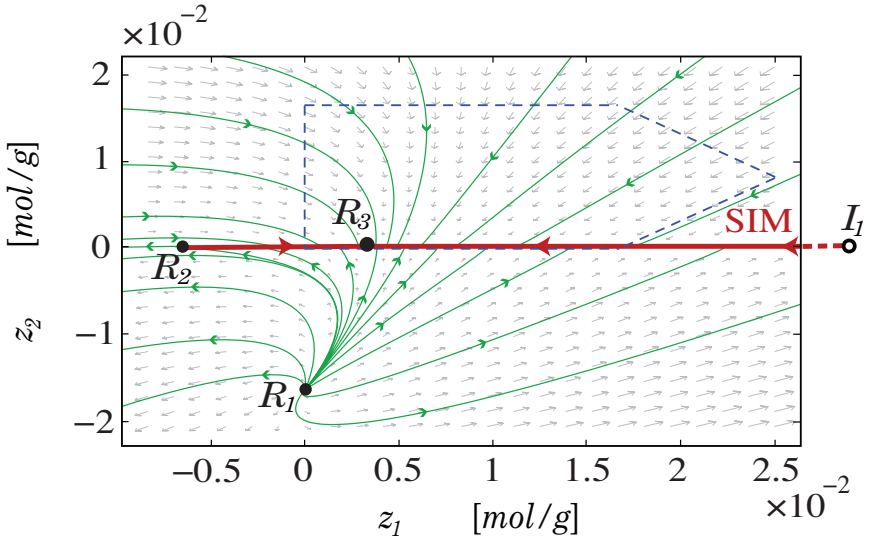

Figure 4.5. A region of the finite composition space for the Zel'dovich mechanism. The solid dots represent finite critical points. The open circle represents an infinite critical point. The arrows indicate the flow directions. The dashed simplex represents $\mathbb{S}$. The SIM is illustrated as a thick line. The thin lines represent trajectories. R_3 represents the system's physical equilibrium state.

respectively. The evolution of the reactive system is described by [41]

$$\frac{dz_1}{dt} = 10^{-5} z_2 - z_1^2, \tag{4.39a}$$

$$\frac{dz_2}{dt} = z_1^2 + (1 - 1002 z_2 - z_1) \times 10^{-5}, \tag{4.39b}$$

which is in the form of Eq. (4.14), and it is clear that $\mathfrak{q} = 2$.

To construct the actual SIM for this system, we use the procedure of Sec. 4.2. For this system, two finite equilibria are found,

$$R_1 \equiv (\mathbf{z}^e) = \left(9.99450 \times 10^{-5}, 9.98901 \times 10^{-4}\right),$$

$$R_2 \equiv (\mathbf{z}^e) = \left(-9.99550 \times 10^{-5}, 9.99101 \times 10^{-4}\right).$$

The two finite equilibria are isolated points with real coordinates. Also, linear analysis in the neighborhood of each equilibrium reveals that R_1 is a sink and R_2 is a saddle. The eigenvalues and the associated eigenvectors at the equilibria are:

$$
\begin{aligned}
R_1 : (\lambda, \boldsymbol{\upsilon}) &= \left(-1.99697 \times 10^{-4}, -1.00198 \times 10^{-2}\right), \\
&\left([9.99813 \times 10^{-1}, 1.93329 \times 10^{-2}]^T, [-1.01830 \times 10^{-3}, 9.99999 \times 10^{-1}]^T\right), \\
R_2 : (\lambda, \boldsymbol{\upsilon}) &= \left(1.99705 \times 10^{-4}, -9.78501 \times 10^{-3}\right), \\
&\left([9.99789 \times 10^{-1}, -2.05354 \times 10^{-2}]^T, [-9.78501 \times 10^{-4}, 1.00000]^T\right).
\end{aligned}
$$

It is clear that R_1 is the system's unique equilibrium point, and R_2 is a candidate saddle; its eigenvalue spectrum contains only one positive eigenvalue.

To investigate the existence of an equilibrium at infinity, the simple form of the projective space technique is employed. By choosing $k = 2$, the projective space is realized by the following transformation: $Z_0 = t, Z_1 = z_1/z_2,\ Z_2 = 1/z_2$. Thus, the reactive system's behavior at infinity is described by the following set of ODEs,

$$
\begin{aligned}
\frac{dZ_0}{d\mathfrak{t}} &= Z_2, && \text{(4.40a)} \\
\frac{dZ_1}{d\mathfrak{t}} &= 10^{-5} Z_2 - Z_1^2 + 10^{-5} Z_1 Z_2 \left(1002 + Z_1 - Z_2\right) - Z_1^3, && \text{(4.40b)} \\
\frac{dZ_2}{d\mathfrak{t}} &= -Z_1^2 Z_2 + 10^{-5} Z_2^2 \left(1002 + Z_1 - Z_2\right). && \text{(4.40c)}
\end{aligned}
$$

For this system there are two equilibria,

$$
\begin{aligned}
I_1 &\equiv (\mathbf{Z}^e) = (0, 0), \\
I_2 &\equiv (\mathbf{Z}^e) = (-1, 0).
\end{aligned}
$$

Stability analysis in the neighborhood of these equilibria reveals that I_2 is a stable proper node [157], with $\lambda_1 = \lambda_2 = -1$, while I_1 is a non-hyperbolic critical point with $\lambda_1 = \lambda_2 = 0$. Using the normal form theory [171], we find that I_1 is a non-hyperbolic node which consists of two hyperbolic sectors and two parabolic sectors, in the nomenclature of Ref. [157], for further details see Appendix C.

Since R_2 is the only critical point with one unstable direction, it is the only candidate point for this system. Consequently, the system's SIM has only one branch. In Fig. 4.6(a), the system's 1-D SIM is presented and several trajectories have been generated away from it to examine the attractiveness of the SIM. Also, along the SIM's branches, including R_1 and R_2, criteria (4.30) hold, and the maximum value of $\mathsf{S} = 1.99310 \times 10^{-2}$ occurs at R_2.

Figure 4.6(a) shows what might be considered as a second branch for the system's 1-D SIM, although our criteria indicate that this system's 1-D SIM has only one branch. A wider range of the system's composition space is shown in Fig. 4.6(b). It is apparent that there is an attractive small region that extends horizontally to the right of R_1. However, this apparent "attractive manifold," does not satisfy our global criteria (4.30) and it is not unique.

To obtain a better understanding of the dynamics of this system, sketches of the global phase portrait are illustrated in Fig. 4.7. Because of scaling effects, it is difficult to graphically illustrate the global dynamical behavior. First, in Fig. 4.7(a), the view of the projective space in the transformed coordinates is shown. Since there are two sinks for this system, R_1 and I_2, there are two basins of attraction [165]. Each basin contains only one sink, which all the trajectories inside of it approach. The shaded area represents part of the basin of attraction for R_1. Also, illustrated in dashed lines, the fast invariant manifolds of R_2 and

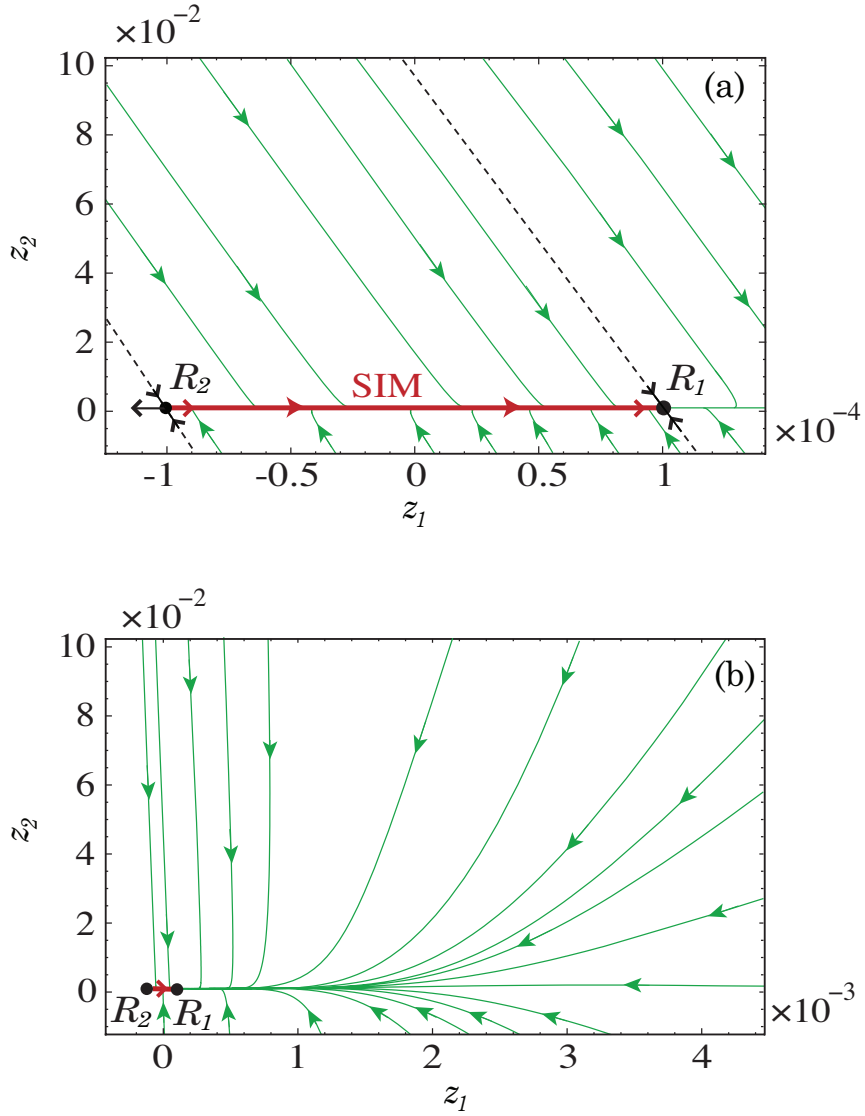

Figure 4.6. Part of the finite composition space for the Lebiedz system. The thick line is the system's 1-D SIM. The thin lines represent trajectories. The dashed lines represent the fast invariant manifolds. The arrows indicate the flow directions. R_2 is a non-physical finite critical point, and R_1 represents the system's physical equilibrium point. Figure (a) is a blow-up near the system's SIM, and (b) is a wider range of the system's composition space.

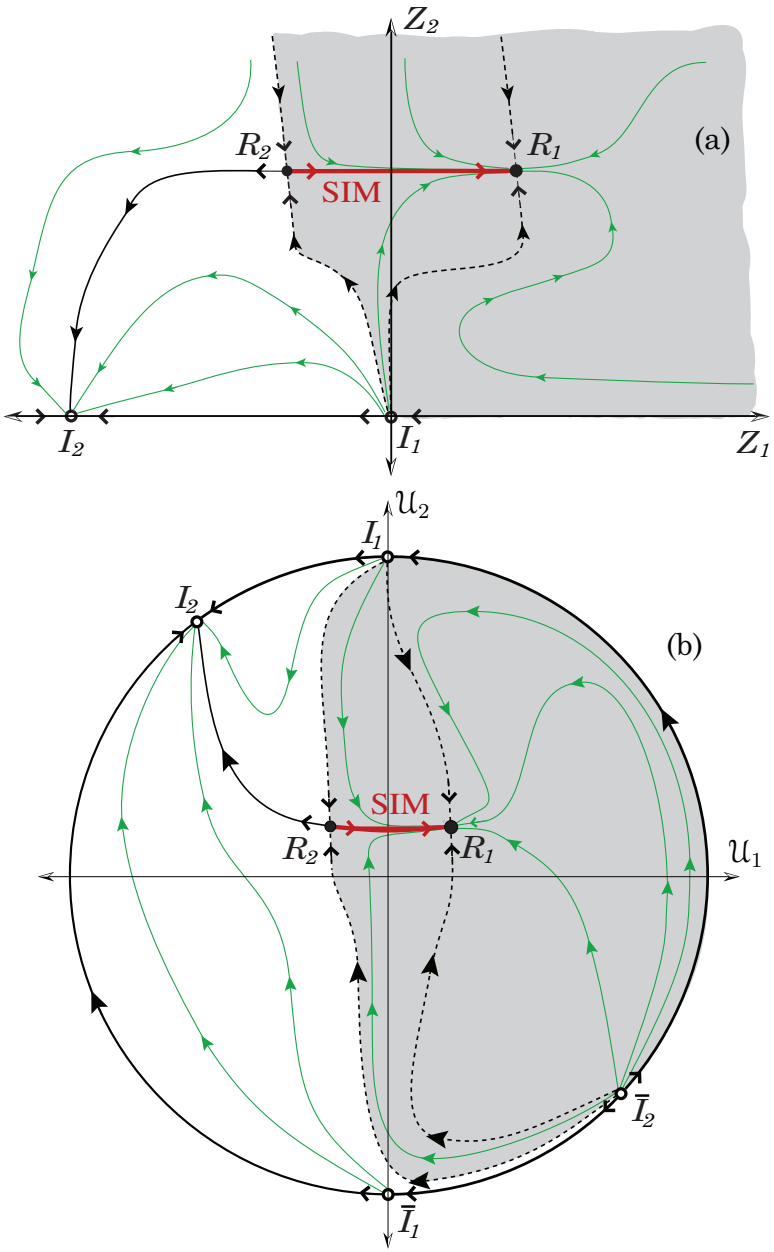

Figure 4.7. Sketches of (a) the projective space portrait and (b) the global phase portrait for the Lebiedz system. Solid dots represent finite critical points. The shaded area represents the basin of attraction of R_1. The thick line represents the SIM. The dashed lines represent the fast invariant manifolds. The thin lines are trajectories. Open circles denote critical points at infinity and their images ($\bar{I}_i$).

R_1 define the boundary between the two basins and the two parts of the basin of attraction for R_1, respectively.

Next, a projection of the system's Poincaré sphere onto a 2-D plane is presented in Fig. 4.7(b). Here, the circle's boundary represents infinity in the untransformed space and the shaded area is the basin of attraction for R_1. Also, $\overline{I}_1$ and $\overline{I}_2$ are antipodal points to the infinite critical points I_1 and I_2 [157].

Figure 4.7 clearly shows that the constructed 1-D SIM gives an accurate description of the asymptotic behavior of the system's trajectories, though it consists of only one branch. Moreover, it shows that the horizontal attractive submanifold near R_1, which might appear to be a second branch of the system's 1-D SIM, is not unique. This apparent attractive manifold consists of heteroclinic orbits that initiate from $\overline{I}_2$. However, none of these orbits are attractive along their complete trajectories; near $\overline{I}_2$ all orbits have $\mathsf{S} \geq 1$, since $\overline{I}_2$ is a source.

4.3.3 Simple hydrogen–air reactive system

This example is adopted from Sec. II of Ren *et al.* [37], where it serves as a model problem for illustrating how to construct the invariant constrained equilibrium edge preimage curve (ICE-PIC) manifold. Here, it is used to demonstrate the simplicity of extending our proposed technique to higher-dimensional reactive systems.

The reaction mechanism contains $N = 6$ species, $L = 3$ elements, and $J = 6$ reversible reactions, see Table D.3. A special case in which the system is isobaric, identical to Ren *et al.* [37], will be considered. The assigned mixture temperature and pressure are $T = 3000\ K$ and $p = 1\ atm$, respectively. The initial conditions are $(n_1^* = 3.02827 \times 10^{-4}, n_2^* = 1.00942 \times 10^{-4}, n_3^* = 3.02827 \times 10^{-4}, n_4^* = 2.32167 \times$

$10^{-5}, n_5^* = 1.11037 \times 10^{-4}, n_6^* = 3.32151 \times 10^{-3})\ mol$. Here, $i = \{1, 2, 3, 4, 5, 6\}$ corresponds to the species $\{H_2, O, H_2O, H, OH, N_2\}$, respectively. This gives rise to $m = 1.00942 \times 10^{-1}\ g$.

The reactive system in this model problem is described in the $R = N - L = 3$ dimensional reactive composition space. The system's only constraints are the conservation of elements; thus, the ODEs that describe the system evolution are of the form

$$\frac{d\mathbf{z}}{dt} = \mathbf{f}(\mathbf{z}), \quad \mathbf{z} \in \mathbb{R}^3. \tag{4.41}$$

The dynamics are fully described by $\{H_2, O, H_2O\}$, and the rest of the species, $\{H, OH, N_2\}$, are given by the system's constraints, Eq. (4.5),

$$2n_1 + 2n_3 + n_4 + n_5 = 1.24563 \times 10^{-3}\ mol, \tag{4.42a}$$

$$n_2 + n_3 + n_5 = 4.14873 \times 10^{-4}\ mol, \tag{4.42b}$$

$$2n_6 = 6.64302 \times 10^{-3}\ mol, \tag{4.42c}$$

which are identical to those given by Ren *et al.* [37].

The time evolution of the species is shown in Fig. 4.8. The multiscale nature of this system is clearly seen. Also, it can be noted that the times at which the first reaction event commences and that at which the system relaxes onto its equilibrium are approximately $t = 10^{-9}\ s$ and $t \sim 10^{-3}\ s$, respectively.

We use the method described in Sec. 4.2 to construct the SIM for this system. First, all the system's finite equilibria are identified. There are fifteen isolated

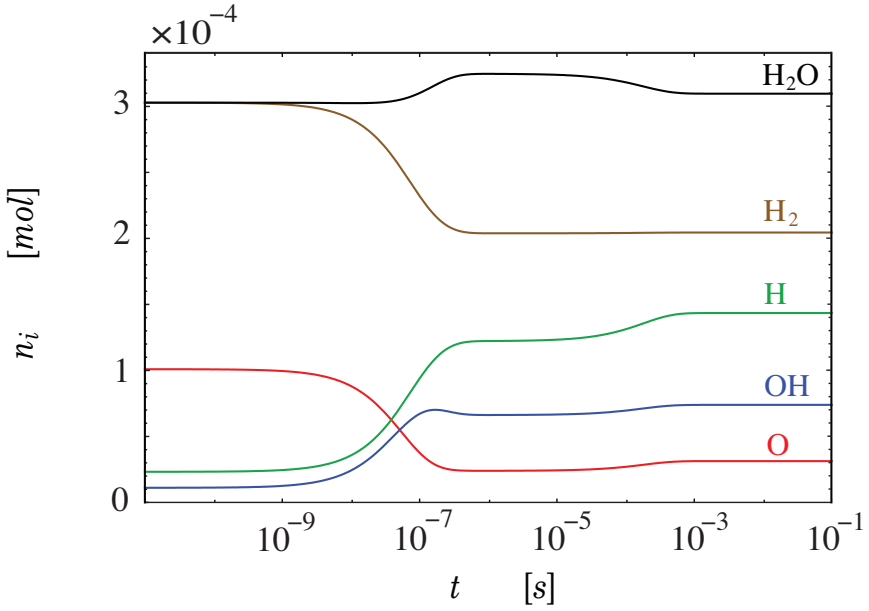

Figure 4.8. The time evolution of number of moles of each species for the simple hydrogen–oxygen reactive system, identical to that of Ren *et al.*

critical points; eight of them are complex and seven are real. The real ones are:

$$R_1 \equiv (\mathbf{z}^e) = \left(-1.67204 \times 10^{-1}, 3.03617 \times 10^{-3}, 3.53209 \times 10^{-3}\right)\ mol/g,$$

$$R_2 \equiv (\mathbf{z}^e) = \left(6.44204 \times 10^{-2}, 1.20566 \times 10^{-2}, -7.12337 \times 10^{-3}\right)\ mol/g,$$

$$R_3 \equiv (\mathbf{z}^e) = \left(-6.47244 \times 10^{-3}, -2.00868 \times 10^{-2}, -2.19220 \times 10^{-3}\right)\ mol/g,$$

$$R_4 \equiv (\mathbf{z}^e) = \left(1.97888 \times 10^{-3}, 5.03888 \times 10^{-3}, 9.41881 \times 10^{-3}\right)\ mol/g,$$

$$R_5 \equiv (\mathbf{z}^e) = \left(-1.21290 \times 10^{-3}, -4.44837 \times 10^{-3}, 5.03482 \times 10^{-3}\right)\ mol/g,$$

$$R_6 \equiv (\mathbf{z}^e) = \left(2.72293 \times 10^{-3}, 3.34454 \times 10^{-4}, 4.71857 \times 10^{-3}\right)\ mol/g,$$

$$R_7 \equiv (\mathbf{z}^e) = \left(2.02552 \times 10^{-3}, 3.10118 \times 10^{-4}, 3.06770 \times 10^{-3}\right)\ mol/g.$$

It is clear that R_1, R_2, R_3, and R_5 are non-physical equilibria. Moreover, R_4 and R_6 are also non-physical critical points; this can be shown by computing the

values of other species using the system's constraints, Eqs. (4.42). Thus, R_7 is the system's unique physical equilibrium point, consistent with the results in Fig. 4.8.

Figure 4.9 shows part of the system's finite composition space, all the finite equilibria, and the system's $\mathbb{S}$ within the dashed simplex. The dynamical analysis within the neighborhood of each critical point reveals that R_3 and R_7 are sinks, and R_1, R_2, R_4, R_5 and R_6 are saddles. The eigenvalue spectrum associated with each finite critical point is:

$$
\begin{aligned}
R_1 &: (\lambda) = \left(2.92495 \times 10^3, -6.66878 \times 10^6 \pm \mathtt{i}1.00392 \times 10^8\right)\ s^{-1},\\
R_2 &: (\lambda) = \left(1.84203 \times 10^{14}, -1.27257 \times 10^{12}, -1.69944 \times 10^{14}\right)\ s^{-1},\\
R_3 &: (\lambda) = \left(-1.02554 \times 10^5, -2.97288 \times 10^7 \pm \mathtt{i}2.63895 \times 10^7\right)\ s^{-1},\\
R_4 &: (\lambda) = \left(1.61839 \times 10^7, 8.94446 \times 10^6, -4.64945 \times 10^4\right)\ s^{-1},\\
R_5 &: (\lambda) = \left(3.22464 \times 10^4, -2.12785 \times 10^6 \pm \mathtt{i}6.70905 \times 10^6\right)\ s^{-1},\\
R_6 &: (\lambda) = \left(1.57132 \times 10^4, -6.27795 \times 10^6 \pm \mathtt{i}4.37013 \times 10^6\right)\ s^{-1},\\
R_7 &: (\lambda) = \left(-5.59456 \times 10^3, -9.08383 \times 10^6, -1.77047 \times 10^7\right)\ s^{-1}.
\end{aligned}
$$

The fastest and slowest time scales associated with the physical equilibrium R_7 are $5.64822 \times 10^{-8}\ s$ and $1.78745 \times 10^{-4}\ s$, respectively. This will give rise to $\mathcal{S}_t = \mathcal{O}(10^3)$, which indicates that the system's trajectories, inside the physical domain, will relax onto the SIM at a steep angle; the fast modes will be exhausted rapidly.

To explore the existence of equilibria at infinity, the projective space technique is employed. We select $k = 2$, though other choices would work as well. So, the reactive system in the projective space is realized by the following transformation: $Z_0 = t, Z_1 = z_1/z_2, Z_2 = 1/z_2$, and $Z_3 = z_3/z_2$. For this system there are two

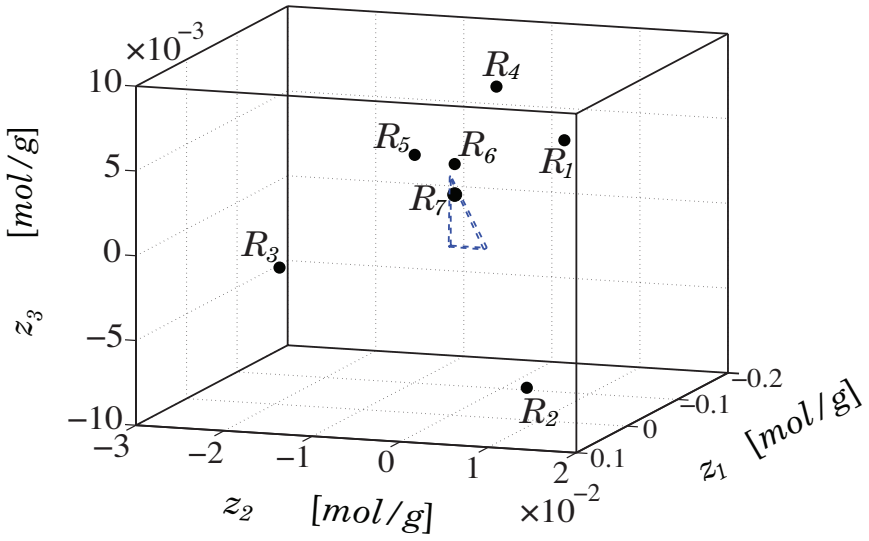

Figure 4.9. A region of the finite composition space for the simple hydrogen–oxygen reactive system. The dashed simplex represents $\mathbb{S}$. The solid dots represent finite equilibria. The unique critical point inside the polygon, R_7, represents the physical equilibrium point.

equilibria located at infinity, but neither of them are isolated. One is a 1-D equilibrium, and the other is a 2-D equilibrium. Consequently, R_1, R_2, R_5 and R_6 are the only candidate points, since the eigenvalue spectra of the corresponding Jacobians each contain only one unstable mode.

To construct the SIM, the dynamical system, Eq. (4.41), is numerically integrated, starting from the candidate points, in the direction of the unstable mode pointing towards R_7. First, we generate a heteroclinic orbit starting from R_1, since it has the slowest unstable mode among the candidate points. The generated orbit connects with R_7 along its slowest mode. Thus, it represents the first branch of the system's 1-D SIM. Then, we generate another heteroclinic orbit starting from R_6. This orbit also approaches R_7 along its slowest mode to form the second branch of the 1-D SIM. Subsequently, there is no need to generate trajectories starting

from the other candidate points R_2 and R_5. However, to check the methodology, Eq. (4.41) is numerically integrated starting from the unstable direction of the candidate points R_2 and R_5 to generate two more heteroclinic orbits. These two heteroclinic orbits approaches R_3, which is another unphysical sink for the system; $R_3 \notin \mathbb{S}$.

The system's 1-D SIM is presented in Fig. 4.10. Although the SIM has been constructed and it can be illustrated, the right branch of the SIM is not presented entirely due to scaling effects. Some trajectories in Fig. 4.10 have been generated from inside $\mathbb{S}$, while others have been initiated from its boundary. The attractiveness of the SIM is revealed by visually examining the relaxation of several trajectories rapidly onto it. This observation is consistent with our previous prediction that has been obtained based on the temporal stiffness of the system. In addition, it has been verified that along the SIM's two branches the criteria (4.30) hold, and the maximum value of S along the 1-D SIM is approximately 2.50292×10^{-3} at R_6. Thus, the SIM is highly attractive; this is consistent with observation and our previous prediction.

4.3.4 Hydrogen oxidation mechanism

As a fourth example, the Michael mechanism [173] for the oxidation of hydrogen is employed to illustrate the 1-D SIM construction method presented in Sec. 4.2. This mechanism contains $N = 6$ species, $L = 2$ elements, and $J = 8$ elementary reactions; see Table D.4. A special case in which the system is isochoric is considered. The chosen mixture temperature and volume are $T = 1200\ K$ and $V = 10^3\ cm^3$. The initial number of moles of all species are taken to be $n_i^* = 10^{-3}\ mol, i = 1, \ldots, N$. Thus, the mixture mass is $m = 8.60448 \times 10^{-2}\ g$,

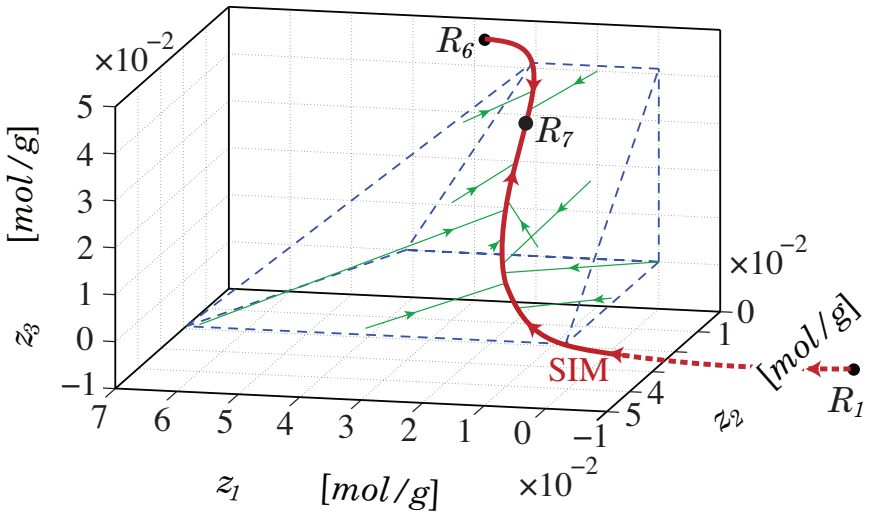

Figure 4.10. The SIM for the simple hydrogen–oxygen reactive system given by a thick line. The solid dots represent finite critical points. R_7 represents the system's physical equilibrium state. The dashed simplex represents $\mathbb{S}$. The thin lines illustrate several trajectories.

and using Eq. (2.4), the initial mixture pressure is $p^* = 5.90816 \times 10^{-1}\ atm$. Here, $i = \{1, 2, 3, 4, 5, 6\}$ corresponds to the species $\{H_2, O, O_2, H, OH, H_2O\}$, respectively.

In this system, the total number of moles remain constant, as a consequence of the fact that the kinetics mechanism includes only bimolecular reactions. Consequently, one algebraic constraint, in addition to element conservation, is provided to the system. Thus, the reactive system is described in the $R = N - L - 1 = 3$ dimensional reactive composition space,

$$\frac{d\mathbf{z}}{dt} = \mathbf{f}(\mathbf{z}), \quad \mathbf{z} \in \mathbb{R}^3. \tag{4.43}$$

Subsequently, the dynamics are fully described by $\{H_2, O, O_2\}$, and the rest of the

species, $\{H, OH, H_2O\}$, are given by the systems constraints, Eq. (4.5),

$$n_1 - n_3 + n_4 = 1 \times 10^{-3}\ mol, \tag{4.44a}$$

$$n_1 - n_2 - n_3 + n_6 = 5 \times 10^{-3}\ mol, \tag{4.44b}$$

$$2n_2 + 3n_3 - n_1 + n_5 = 0\ mol. \tag{4.44c}$$

The full time evolution of species is shown in Fig. 4.11. The multiscale nature of this system is clearly shown. Also, it can be visually noted that the times at which the first reaction event commences and that at which the system relaxes onto its equilibrium are approximately $t = 10^{-9}\ s$ and $t = 10^{-5}\ s$, respectively.

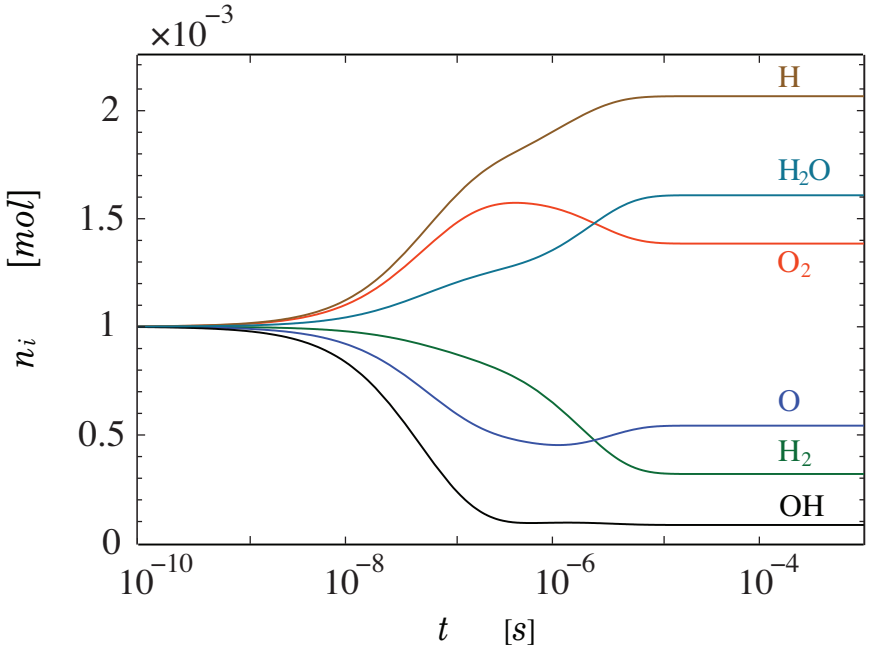

Figure 4.11. The time evolution of number of moles of each species for the oxidation of hydrogen reactive system.

The dynamical system, Eq. (4.43), has eight finite critical isolated points; six of them are real. The real ones are:

$$
\begin{aligned}
R_1 &\equiv (\mathbf{z}^e) = \left(-5.84827 \times 10^{-2}, 6.84851 \times 10^{-4}, -3.52417 \times 10^{-4}\right)\ mol/g, \\
R_2 &\equiv (\mathbf{z}^e) = \left(4.64874 \times 10^{-2}, 0, 3.48656 \times 10^{-2}\right)\ mol/g, \\
R_3 &\equiv (\mathbf{z}^e) = \left(3.72687 \times 10^{-3}, 6.31637 \times 10^{-3}, 1.60689 \times 10^{-2}\right)\ mol/g, \\
R_4 &\equiv (\mathbf{z}^e) = \left(6.32982 \times 10^{-3}, -1.85982 \times 10^{-3}, 2.49265 \times 10^{-2}\right)\ mol/g, \\
R_5 &\equiv (\mathbf{z}^e) = \left(1.27629 \times 10^{-3}, -5.97920 \times 10^{-2}, 6.00416 \times 10^{-2}\right)\ mol/g, \\
R_6 &\equiv (\mathbf{z}^e) = \left(1.43296 \times 10^{-3}, -7.58236 \times 10^{-2}, 7.08086 \times 10^{-2}\right)\ mol/g.
\end{aligned}
$$

It is clear that R_1, R_4, R_5 and R_6 are non-physical equilibria. Moreover, R_2 is also a non-physical critical point; this can be shown by computing the other species using Eqs. (4.44). Thus, R_3 is the system's unique physical equilibrium point, consistent with the results in Fig. 4.11. Figure 4.12 shows part of the system's finite composition space, the finite equilibria, and $\mathbb{S}$ within the dashed simplex, where it is clear that R_3 is the only critical point inside it.

The dynamical behavior analysis within the neighborhood of each critical point reveals that R_1, R_2, and R_5 are saddles, R_4 and R_6 are sources, and R_3 is a sink.

The system's eigenvalues associated with each finite critical point are:

$$
\begin{aligned}
R_1 &: (\lambda) = (5.92648 \times 10^6 \pm \mathtt{i}5.13071 \times 10^5, -1.17997 \times 10^6)\ 1/s, \\
R_2 &: (\lambda) = (7.92868 \times 10^5, -3.35464 \times 10^6, -1.00600 \times 10^7)\ 1/s, \\
R_3 &: (\lambda) = (-4.29725 \times 10^5, -1.22549 \times 10^6, -1.01802 \times 10^7)\ 1/s, \\
R_4 &: (\lambda) = (6.87704 \times 10^6, 3.51397 \times 10^6, 1.56608 \times 10^6)\ 1/s, \\
R_5 &: (\lambda) = (5.65080 \times 10^7, 3.56085 \times 10^6, -1.05552 \times 10^4)\ 1/s, \\
R_6 &: (\lambda) = (7.19214 \times 10^7, 4.46684 \times 10^6, 1.05214 \times 10^4)\ 1/s.
\end{aligned}
$$

The slowest and fastest time scales associated with the physical equilibrium R_3 are $2.32707 \times 10^{-6}\ s$ and $9.82303 \times 10^{-8}\ s$ respectively. Thus, $\mathcal{S}_t = 23.6899$.

In addition to the system's finite equilibria, this reactive system has seven isolated infinite equilibria. They are obtained using the projective space method, in which we select $k = 2$ arbitrarily. The real ones are:

$$
\begin{aligned}
I_1 \equiv (\mathbf{Z}^e) &= (-9.77396, 0, -4.58666)\,, \\
I_2 \equiv (\mathbf{Z}^e) &= (0.60213, 0, -0.47874)\,, \\
I_3 \equiv (\mathbf{Z}^e) &= (-0.01228, 0, -0.67333)\,.
\end{aligned}
$$

The eigenvalue spectra of these critical points are:

$$
\begin{aligned}
I_1 &: (\lambda) = (6.09587 \times 10^{12}, -5.74260 \times 10^{12} \pm \mathtt{i}7.82642 \times 10^{12})\ g/(mol\ s), \\
I_2 &: (\lambda) = (7.34957 \times 10^{11}, 6.32121 \times 10^{11}, -1.18980 \times 10^{13})\ g/(mol\ s), \\
I_3 &: (\lambda) = (7.61722 \times 10^{9}, -6.50356 \times 10^{11}, -1.12237 \times 10^{13})\ g/(mol\ s).
\end{aligned}
$$

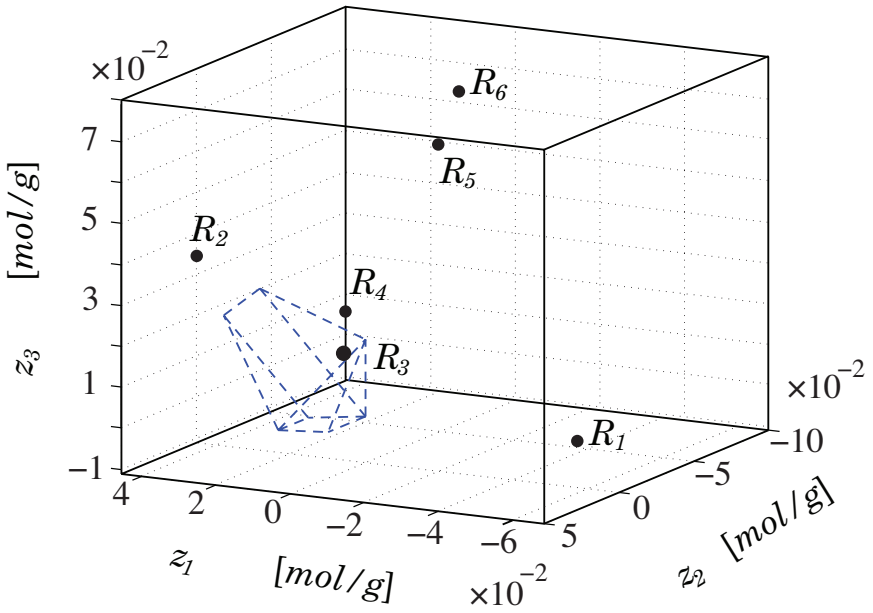

Figure 4.12. A region of the finite composition space for the hydrogen oxidation reactive system. The dashed simplex represents $\mathbb{S}$. The solid dots represent finite equilibria. The unique critical point inside the polygon, R_3, represents the physical equilibrium point.

All of the dynamical system's infinite equilibria are saddles.

Now, among the system's equilibria, the eigenvalue spectra of three critical points contain only one positive eigenvalue. These equilibria, ordered as described in Sec. 4.2.5, are R_2, I_1 and I_3. To construct the SIM, the dynamical system is numerically integrated, starting from these three critical points, in the direction of the unstable mode pointing toward R_3. Subsequently, three heteroclinic orbits are generated. Although all of them reach R_3, two of these orbits connect to R_3 along its slowest mode. Thus, they represent the two branches of the 1-D SIM. These two heteroclinic orbits are the ones that have been initiated from R_2 and I_3. In Fig. 4.13, the 1-D SIM for the reactive system is shown.

The attractiveness of the SIM is revealed by visually examining the relaxation

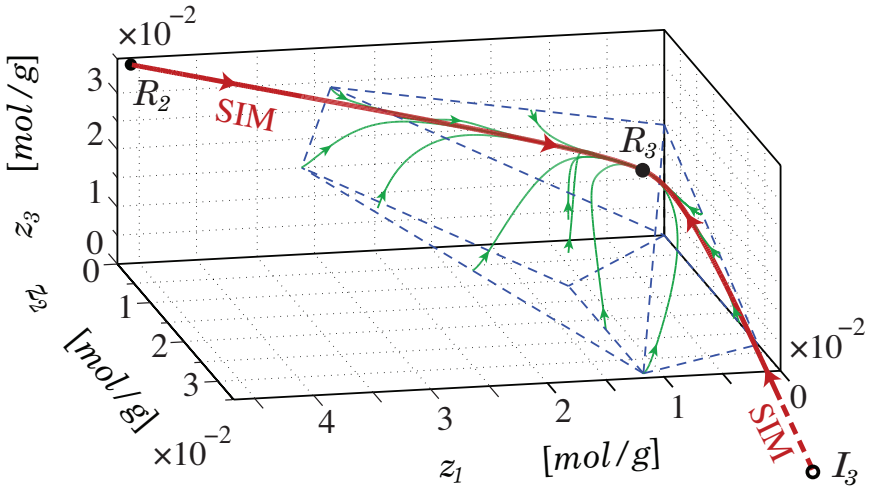

Figure 4.13. The 1-D SIM for the hydrogen oxidation reactive system is illustrated as a thick line. The solid dots represent finite critical points. R_3 represents the system's physical equilibrium state. The open circle represents infinite equilibrium. The dashed simplex represents $\mathbb{S}$. The thin lines illustrate several trajectories.

of several trajectories onto it. In addition, it has been verified that along the SIMs two branches the criteria (4.30) hold, and the maximum value of S along the 1-D SIM is 3.50656×10^{-1} at R_3. Thus, the SIM is not highly attractive; this is consistent with observation from Fig. 4.13, and the value of $\mathcal{S}_t = \mathcal{O}(10^1)$.

4.4 1-D SIM for detailed hydrogen–air mechanism

In this section, the 1-D SIM for a detailed hydrogen–air kinetic system is constructed. The reactive system is based on the detailed kinetic mechanism listed in Table D.1. The system is an isochoric stoichiometric hydrogen–air mixture, where the molar ratio is given by $2H_2 + (O_2 + 3.76N_2)$, and initially it is at $p^* = 10^7\ dyne/cm^2$ and $T = 1500\ K$.

Utilizing the conservation of the three elements $\{H, O, N\}$, the $H_2 - Air$ re-

active system can be described by the following autonomous dynamical system,

$$\frac{d\mathbf{z}}{dt} = \mathbf{f}(\mathbf{z}), \quad \mathbf{z} \in \mathbb{R}^6. \tag{4.45}$$

Here, $i = \{1, 2, 3, 4, 5, 6\}$ correspond to the species $\{H_2, O_2, H, O, OH, H_2O\}$, respectively. The rest of the species, $\{HO_2, H_2O_2, N_2\}$, are recast using Eq. (4.5).

The full dynamics of species evolution are obtained by integrating Eq. (4.45), see Fig. 4.14. At $t \approx 10^{-8}$ s, the species growth rates change slightly, which indicates that significant dissociation reactions are induced. For $10^{-7} < t < 10^{-6}$ s, the minor species continue to increase rapidly with different growth rates. On the other hand, the major species H_2, O_2, and N_2 have essentially constant specific moles. Just past $t \approx 10^{-6}$ s all the species undergo significant change, and the radicals' specific moles reach their maximum values. At $t \approx 10^{-5}$ s, an exothermic recombination of radicals commences forming the predominant product H_2O, which continues up to $t \approx 5$ s, after which the system approaches the equilibrium state. Figure 4.14 clearly illustrates the multiscale nature of this system.

The first step in constructing the SIM, following the methodology presented in Sec. 4.2, is to find all of the system's real isolated equilibria, finite and infinite. For this system 284 finite equilibria and 42 infinite equilibria are found. Of the finite equilibria, one is 3-D, one is 2-D, six are 1-D, and 276 are 0-D. Of the 276 0-D equilibria, 90 are real, and 186 are complex. Of the 42 infinite equilibria, six are 1-D, and 36 are 0-D. Of the latter 0-D equilibria, 18 are complex, and 18 are real. One of the 90 real finite critical points represents the unique physical

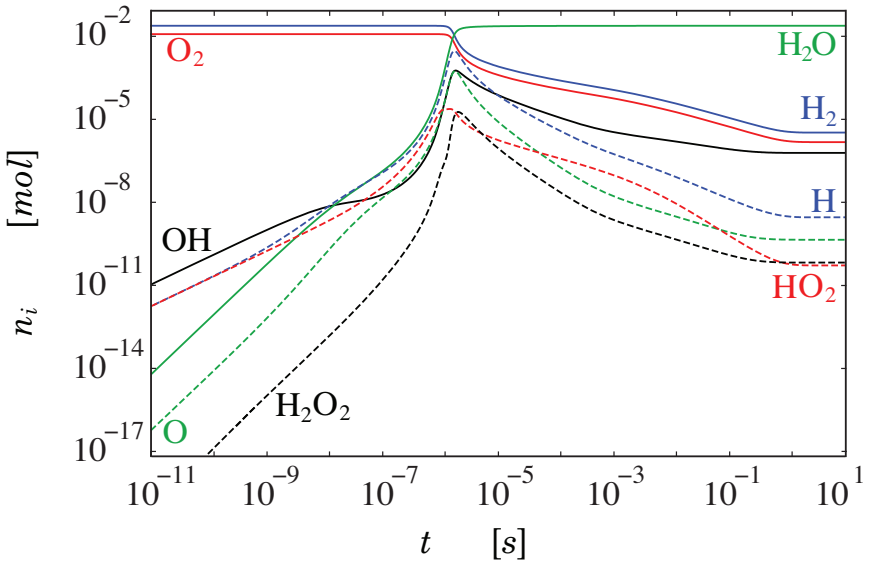

Figure 4.14. The time evolution of number of moles of each species for the detailed hydrogen–air reactive system.

equilibrium state of the system. This corresponds to

$$R_{19} \equiv (\mathbf{z}^e) = \big(1.98329 \times 10^{-6}, 9.00337 \times 10^{-7}, 1.72092 \times 10^{-9}, \\ 2.66737 \times 10^{-10}, 3.66249 \times 10^{-7}, 1.44126 \times 10^{-2}\big)\ mol/g.$$

Then, the dynamical character of each of the 108 isolated real finite and infinite critical points is determined. It is found that among them there are only 14 candidate points for constructing the SIM; all of them are finite. The other critical points are either sources, sinks, or saddles with more than one unstable direction. By examining the trajectories that emanate from the candidate points, only two are connected with R_{19} tangent to its slowest mode via heteroclinic orbits. These

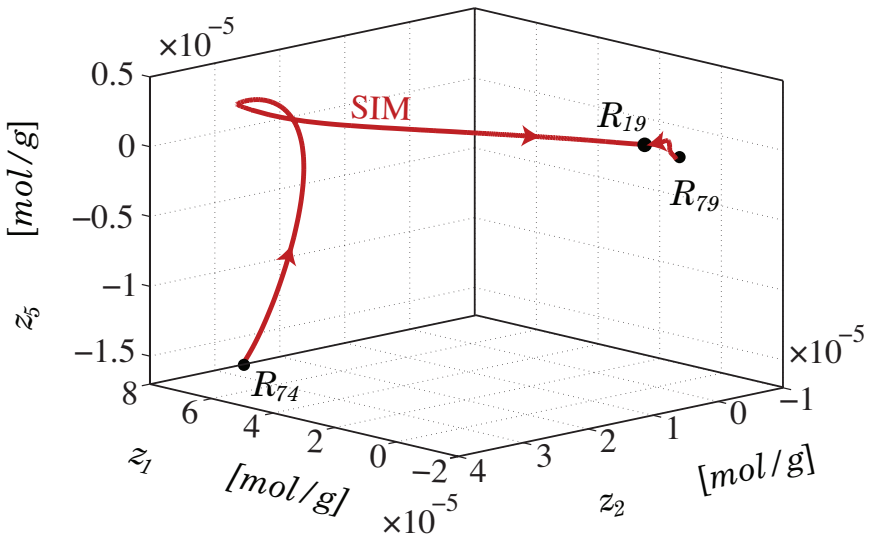

Figure 4.15. The 1-D SIM for the detailed hydrogen–air mechanism. The solid dots represent finite critical points. R_{19} represents the system's physical equilibrium state.

two candidate points are:

$$R_{74} \equiv (\mathbf{z}^e) = \big(6.26283 \times 10^{-5}, 3.42557 \times 10^{-5}, -2.29776 \times 10^{-6},$$
$$4.80374 \times 10^{-7}, -1.54421 \times 10^{-5}, 1.43609 \times 10^{-2}\big)\ mol/g,$$
$$R_{79} \equiv (\mathbf{z}^e) = \big(-3.34038 \times 10^{-6}, -1.50262 \times 10^{-6}, 5.26822 \times 10^{-9},$$
$$8.81723 \times 10^{-10}, -6.65954 \times 10^{-7}, 1.44185 \times 10^{-2}\big)\ mol/g,$$

and these two heteroclinic orbits combine to provide the two branches of the 1-D SIM. Figure 4.15 shows a 3-dimensional projection of the 1-D SIM embedded inside the 6-dimensional composition space. The 1-D SIM is attractive along the complete trajectories; criteria (4.30) hold along the SIM's branches. Subsequently, it provides the best description of the system's slow dynamics.

CHAPTER 5

THERMODYNAMICS OF CLOSED REACTIVE SYSTEMS

In this chapter, the relation between the isothermal reactive systems' slow dynamics, described by the actual SIMs, and notions from thermodynamics is addressed. In addition to a mathematical proof, a realistic reactive system is utilized to show that other than identifying the physical equilibrium point, traditional thermodynamic potentials provide no guidance in determining a system's actual SIM. Finally, a comparison between several published classical thermodynamics-based manifolds and the actual SIMs is presented.

5.1 Background

Recently, several methods employing equilibrium thermodynamics to construct attractive manifolds have been developed [33, 37, 40, 41]. These methods employ classical thermodynamics far from the equilibrium state to explore reactive systems' dynamics. While results from this class of methods may seem intuitive, they have not been fully compared to the exact SIM. Moreover, some of these methods relies on the concept of minimum entropy production [74]. The validity of this principle has been called into question in other fields [75]. In Ref. [75], Müller and Weiss employ an expression for the dissipative entropy source in a heat-conducting fluid to disprove the principle of minimum entropy production.

By considering one-dimensional stationary heat conduction in a fluid at rest, they show that this principle contradicts the first law of thermodynamics as long as Fourier's law holds.

In Chapter 4, a procedure to construct the actual one-dimensional SIMs for reactive systems has been provided. Such manifolds are defined as heteroclinic orbits that are locally attractive along their complete trajectories, and they describe the asymptotic structures of the invariant attracting reactive systems' trajectories during their relaxation toward equilibrium. Utilizing this procedure to construct reactive systems' actual 1-D SIMs makes it possible to examine the relation between thermodynamics and reactive systems' slow dynamics.

5.2 Analysis

Similar to Chapter 4, we confine our attention to closed, isothermal, spatially homogeneous reactive mixtures of calorically imperfect ideal gases described by detailed mass-action kinetics. For such reactive systems, it shown that the systems' dynamics are govern by

$$\frac{d\mathbf{z}}{dt} = \dot{\mathbf{w}}(\mathbf{z}), \quad \{\mathbf{z}, \dot{\mathbf{w}}\} \in \mathbb{R}^R, \quad \mathbb{R}^R \subset \mathbb{R}^N. \qquad ((4.10a))$$

All the mixture thermodynamic properties are scaler functions that are only defined in $\mathbb{S}$. In this chapter, the entropy S, the Helmholtz free energy A, and the Gibbs free energy G are of special interest. Each one of them is a convex function with a unique global extremum inside $\mathbb{S}$ [156]; maximum for S and minima for G and A. For an isolated system, *i.e.* closed and adiabatic, the maximum of S corresponds to the reactive system's unique physical equilibrium state $\mathbf{z}^e$. While, in the case of isothermal-isobaric and isothermal-isochoric systems, the minimum

of G and A correspond to $\mathbf{z}^e$, respectively.

The mixture entropy is given by

$$S = \sum_{i=1}^{N} n_i \bar{s}_i. \qquad ((2.10c))$$

The differential change of S is postulated by the second law of thermodynamics [161]. This changes occur as a results of heat transfer between the system and its surrounding, as well as irreversible processes within the system. However, this change is stated differently in non-equilibrium thermodynamics and classical thermodynamics [140].

In classical thermodynamics, the second law of thermodynamics states that the change of S, for a closed system, is constrained by [103, 161, 174]

$$dS \geq \frac{\delta Q}{T}, \tag{5.1a}$$

where δQ is the sum of the heat supplied to the system at temperature T by its surroundings. Equation (5.1a) can be rewritten using the first law of thermodynamics,

$$dE = \delta Q - \delta W, \tag{5.1b}$$

as

$$dS \geq \frac{1}{T}\left(dE + \delta W\right), \tag{5.1c}$$

$$TdS \geq dE + pdV, \tag{5.1d}$$

$$dE - TdS + pdV \leq 0, \tag{5.1e}$$

where $\delta W = pdV$ is the reversible work done by the system. Now, for a multi-

component system, the Gibbs' equation states that [140]

$$dE = TdS - pdV + \sum_{i=1}^{N} \bar{\mu}_i dn_i. \tag{5.1f}$$

By substituting Eq. (5.1f) into Eq. (5.1e), one finds that the second law of thermodynamics implies

$$\sum_{i=1}^{N} \bar{\mu}_i dn_i \leq 0. \tag{5.1g}$$

So, for closed reactive mixture of ideal gases, the only source of irreversibility is the chemical reaction. At equilibrium state, the equality in Eq. (5.1g) applies.

In non-equilibrium thermodynamics, the differential change of S consists of two parts [74, 99, 175],

$$dS = d_e S + d_i S, \tag{5.2a}$$

where

$$d_e S = \frac{\delta Q}{T}, \tag{5.2b}$$

is the change in S due to the system's exchange of matter and energy with its surroundings, and

$$d_i S = -\frac{1}{T} \sum_{i=1}^{N} \bar{\mu}_i dn_i, \tag{5.2c}$$

is the irreversibility, which is the change in entropy due to irreversible processes within the system boundary. Contrary to classical equilibrium thermodynamics, the second law, as it stated in Eqs. (5.2), can be applied to systems not at their equilibrium state [140]. Furthermore, by introducing time into both sides of Eq. (5.2c), we get an expression for the irreversibility production rate σ, also

known as the entropy production rate [176],

$$\sigma \equiv \frac{d_i S}{dt} = -\frac{1}{T}\sum_{i=1}^{N} \bar{\mu}_i \frac{dn_i}{dt}. \tag{5.3}$$

Similar to all other thermodynamic functions, σ is a scalar convex function defined only within $\mathbb{S}$. Furthermore, it has a global minimum that corresponds to $\mathbf{z}^e$, whether the system is an isothermal, isochoric, isobaric, adiabatic, or any combination of these conditions [177].

5.3 Thermodynamics and SIM

All the reactive system's, Eq. (4.10a), trajectories within the physically accessible domain $\mathbb{S}$ approach the unique equilibrium point $\mathbf{z}^e$ in infinite time. Near equilibrium, the system's dynamics relax onto the eigenvector associated with the slowest time scale. At the equilibrium point, the eigenvector associated with the smallest eigenvalue in magnitude of the Jacobian,

$$\mathbf{J}^e = \left.\frac{\partial \dot{\mathbf{w}}}{\partial \mathbf{z}}\right|_{\mathbf{z}=\mathbf{z}^e}, \tag{(C.2b)}$$

defines the direction of the system's slowest mode.

Only in this paragraph and for simplicity, the argument will be presented for a 2-D reactive system. However, it can be easily extended to a higher dimensional reactive system. In a 2-D composition space, σ and the appropriate thermodynamic scalar field can be represented by iso-contours. The major/minor axes of these thermodynamics quantities' contours identify the thermodynamically preferred paths toward $\mathbf{z}^e$. Near equilibrium these contours approach ellipses. For each of these functions, the major axes of these ellipses are aligned with the

eigenvector associated with the largest eigenvalue of that function's local Hessian matrix, *e.g.*

$$\mathbf{H}_{\sigma}^{e} = \left.\frac{\partial^2 \sigma}{\partial z_i \partial z_j}\right|_{\mathbf{z}=\mathbf{z}^e}. \qquad ((C.2c))$$

Similarly, the minor axes are aligned with the eigenvector associated with the smallest eigenvalue of $\mathbf{H}^e$. Note that $\mathbf{H}^e$ is symmetric and real.

Thus, by investigating the relation between the principal direction of the reactive system's $\mathbf{J}^e$ and the ultimate paths to $\mathbf{z}^e$ assigned by σ and the system's appropriate thermodynamic potential, the relation between reactive system's slow dynamics and thermodynamics is revealed.

5.3.1 Isothermal-isobaric reactive mixtures

To analyze a reactive system under isothermal-isobaric conditions, the appropriate thermodynamic potential is the Gibbs free energy [161], defined as

$$G = E + pV - TS. \tag{5.4a}$$

The differential change of G is given by

$$dG = dE + Vdp + pdV - SdT - TdS. \tag{5.4b}$$

Thus, for an isothermal-isobaric system, the second law of thermodynamics (5.1e) can be written as

$$dG \leq \underbrace{Vdp - SdT}_{=0,\ \text{isothermal-isobaric}}. \tag{5.4c}$$

Furthermore, using Gibbs' relation (5.1f), we get

$$dG = \underbrace{Vdp}_{=0,\ \text{isobaric}} - \underbrace{SdT}_{=0,\ \text{isothermal}} + \sum_{i=1}^{N} \bar{\mu}_i dn_i, \tag{5.4d}$$

Thus, at the equilibrium state we have

$$dG = \sum_{i=1}^{N} \bar{\mu}_i dn_i = 0. \tag{5.4e}$$

Now, in the vicinity of $\mathbf{z}^e$, the deviations of G and σ from their equilibrium values are described by

$$G = G|_{\mathbf{z}^e} + \left.\frac{\partial G}{\partial \mathbf{z}}\right|_{\mathbf{z}=\mathbf{z}^e} \cdot \mathbf{z}' + \frac{1}{2}\mathbf{z}'^T \cdot \mathbf{H}_G^e \cdot \mathbf{z}' + \ldots, \tag{5.5a}$$

$$\sigma = \sigma|_{\mathbf{z}^e} + \left.\frac{\partial \sigma}{\partial \mathbf{z}}\right|_{\mathbf{z}=\mathbf{z}^e} \cdot \mathbf{z}' + \frac{1}{2}\mathbf{z}'^T \cdot \mathbf{H}_\sigma^e \cdot \mathbf{z}' + \ldots, \tag{5.5b}$$

Here, $\mathbf{z}' = \mathbf{z} - \mathbf{z}^e$ is the perturbation from equilibrium, further details about this standard lineariztion are given in Appendix C. However, the gradients of G and σ vanish at the physical equilibrium; G and σ have minima at $\mathbf{z}^e$. Moreover, at the equilibrium $\sigma = 0$ [177]. So, the deviations from equilibrium values are described by

$$G - G|_{\mathbf{z}=\mathbf{z}^e} = \frac{1}{2}\mathbf{z}'^T \cdot \mathbf{H}_G^e \cdot \mathbf{z}' + \ldots, \tag{5.6a}$$

$$\sigma = \frac{1}{2}\mathbf{z}'^T \cdot \mathbf{H}_\sigma^e \cdot \mathbf{z}' + \ldots. \tag{5.6b}$$

Now, let focus on Eq. (5.6b), though the following argument is also valid for Eq. (5.6a). Since $\mathbf{H}_\sigma^e$ is symmetric and real, it can be diagonalized to take the

following simple form:

$$\mathbf{H}^e_\sigma = \mathbf{\Omega}^T \cdot \mathbf{\Pi} \cdot \mathbf{\Omega}, \tag{5.7}$$

where $\mathbf{\Omega}$ is an orthogonal matrix. Its column vectors are orthonormal, and each of them represents an eigenvector of $\mathbf{H}^e_\sigma$. Also, $\mathbf{\Pi}$ is a real and diagonal matrix that has the eigenvalues of $\mathbf{H}^e_\sigma$ on its diagonal. Subsequently, Eq. (5.6b) can be rewritten as

$$\sigma \approx \frac{1}{2}\mathbf{z}'^T \cdot \mathbf{\Omega}^T \cdot \mathbf{\Pi} \cdot \mathbf{\Omega} \cdot \mathbf{z}'. \tag{5.8}$$

From a geometric perspective, $\mathbf{\Omega}$ is a rotation matrix. Now, by defining the new dependent variables as $\mathfrak{Z} = \mathbf{\Omega} \cdot \mathbf{z}'$, Eq. (5.8) can be rewritten as a quadratic forms in $\mathbb{R}^R$,

$$\sigma = \frac{1}{2}\mathfrak{Z}^T \cdot \mathbf{\Pi} \cdot \mathfrak{Z}, \qquad \mathfrak{Z} \in \mathbb{R}^R. \tag{5.9}$$

From a geometric perspective, Eq. (5.9) is that of an ellipsoid, since it is the sum of R squares. In the composition space, the principal axes of Eq. (5.9) are aligned with the $\mathfrak{Z}$ axes, and they are spanned by the column vectors of $\mathbf{\Omega}$.

Now, the eigenvectors of $\mathbf{H}^e_G$ and $\mathbf{H}^e_\sigma$ define, respectively, the directions of the major/minor axes of the convex functions G and σ; the eigenvector associated with the largest eigenvalue assigns the direction of greatest curvature [178]. However, it is easy to show that at equilibrium there is a relationship between these three matrices, $\mathbf{H}^e_G, \mathbf{H}^e_\sigma$, and $\mathbf{J}^e$. To find this relation, we start by recalling the definition of G,

$$G = \sum_{i=1}^{N} \bar{\mu}_i n_i. \tag{(2.10d)}$$

However, $\mathbf{n}$ are not linearly independent as described in Sec. 4.1. To represent G by the dependent reduced variables $\mathbf{z}$, we substitute Eq. (4.5) into Eq. (2.10d) to

obtain

$$G = \sum_{i=1}^{N} \bar{\mu}_i \left(n_i^* + m \sum_{k=1}^{R} \mathcal{D}_{ik} z_k \right), \tag{5.10a}$$

$$= \underbrace{\sum_{i=1}^{N} \bar{\mu}_i n_i^*}_{G^*} + m \sum_{k=1}^{R} z_k \sum_{i=1}^{N} \bar{\mu}_i \mathcal{D}_{ik}. \tag{5.10b}$$

So, the gradient of G with respect to the reduced composition variables $\mathbf{z}$ is given by

$$\frac{\partial G}{\partial z_k} = m \sum_{i=1}^{N} \bar{\mu}_i \mathcal{D}_{ik}, \quad k = 1, \ldots, R. \tag{5.11}$$

Also, by substituting Eq. (4.9a) into Eq. (5.3), we get

$$\sigma = -\frac{m}{T} \sum_{i=1}^{N} \sum_{k=1}^{R} \bar{\mu}_i \mathcal{D}_{ik} \frac{dz_k}{dt}, \tag{5.12a}$$

which can be rearranged as

$$\sigma = -\frac{1}{T} \sum_{k=1}^{R} \frac{dz_k}{dt} m \sum_{i=1}^{N} \bar{\mu}_i \mathcal{D}_{ik}. \tag{5.12b}$$

Now, by substituting Eqs. (4.10a) and (5.11) into Eq. (5.12b), the irreversibility production rate can be written as

$$\sigma = -\frac{1}{T} \sum_{k=1}^{R} \dot{w}_k \frac{\partial G}{\partial z_k}. \tag{5.12c}$$

Subsequently, the gradient of σ with respect to $\mathbf{z}$ is given by

$$\frac{\partial \sigma}{\partial z_j} = -\frac{1}{T} \sum_{k=1}^{R} \frac{\partial G}{\partial z_k} \frac{\partial \dot{w}_k}{\partial z_j} + \frac{\partial^2 G}{\partial z_j \partial z_k} \dot{w}_k, \tag{5.13}$$

and $\mathbf{H}_\sigma$ is

$$\frac{\partial^2\sigma}{\partial z_i \partial z_j} = -\frac{1}{T}\sum_{k=1}^{R}\left(\frac{\partial G}{\partial z_k}\frac{\partial^2 \dot{w}_k}{\partial z_i \partial z_j} + \frac{\partial^2 G}{\partial z_i \partial z_k}\frac{\partial \dot{w}_k}{\partial z_j} + \frac{\partial^2 G}{\partial z_j \partial z_k}\frac{\partial \dot{w}_k}{\partial z_i} + \frac{\partial^3 G}{\partial z_i \partial z_j \partial z_k}\dot{w}_k\right). \tag{5.14}$$

At equilibrium, G is minimized, and thus

$$\dot{w}_k\big|_{\mathbf{z}=\mathbf{z}^\mathbf{e}} = 0, \quad k = 1, \ldots, R, \tag{5.15a}$$

$$\left.\frac{\partial G}{\partial z_k}\right|_{\mathbf{z}=\mathbf{z}^e} = 0, \quad k = 1, \ldots, R. \tag{5.15b}$$

Subsequently,

$$\left.\frac{\partial^2\sigma}{\partial z_i \partial z_j}\right|_{\mathbf{z}=\mathbf{z}^\mathbf{e}} = -\frac{1}{T}\sum_{k=1}^{R}\left(\frac{\partial^2 G}{\partial z_i \partial z_k}\frac{\partial \dot{w}_k}{\partial z_j} + \frac{\partial^2 G}{\partial z_j \partial z_k}\frac{\partial \dot{w}_k}{\partial z_i}\right)_{\mathbf{z}=\mathbf{z}^\mathbf{e}}, \tag{5.16a}$$

or in Gibbs notation, and using Eq. (C.2b),

$$\mathbf{H}^e_\sigma = -\frac{1}{T}\left[(\mathbf{H}^e_G \cdot \mathbf{J}^e) + (\mathbf{H}^e_G \cdot \mathbf{J}^e)^T\right]. \tag{5.16b}$$

In the highly unusual case in which $\mathbf{H}^e_G$ is diagonal with identical eigenvalues, the SIM can be identified by consideration of the eigenvectors of $\mathbf{H}^e_\sigma$. In that case, the eigenvectors of $\mathbf{J}^e$ are aligned with those of $\mathbf{H}^e_\sigma$. However, essentially all practical reactive systems have $\mathbf{H}^e_G$ which is not diagonal and does not have identical eigenvalues. Thus, $\mathbf{H}^e_G$ operates on $\mathbf{J}^e$ in a non-uniform way, such that the eigenvalues and the eigenvectors of $\mathbf{H}^e_\sigma$ are not the same as those of $\mathbf{J}^e$. So, the system's dynamics cannot be deduced from σ or G. In conclusion, we can state that any approach that employes equilibrium thermodynamic potentials alone to deduce a reactive system's slow dynamics has inherent flaws.

5.3.2 Isothermal-isochoric reactive mixtures

To analyze a reactive system under isothermal-isochoric conditions, the appropriate thermodynamic potential is the Helmholtz free energy [161], defined as

$$A = E - TS. \tag{5.17a}$$

Similar to the analysis presented in Sec. 5.3.1, it is easy to show that for an isothermal-isochoric system, the second law of thermodynamics (5.1e) can be written as

$$dA \leq 0. \tag{5.17b}$$

Thus, at the equilibrium state we have

$$dA = \sum_{i=1}^{N} \bar{\mu}_i dn_i = 0. \tag{5.17c}$$

Now, using

$$n_i = n_i^* + m\left(\sum_{k=1}^{R} \mathcal{D}_{ik} z_k\right), \quad i = 1, \ldots, N, \tag{(4.5)}$$

the differential change of n_i can be written as

$$dn_i = m \sum_{k=1}^{R} \mathcal{D}_{ik} z_k, \quad i = 1, \ldots, N. \tag{5.18}$$

By substituting Eq. (5.18) into Eq. (5.17c), we get

$$dA = m \sum_{i=1}^{N} \bar{\mu}_i \sum_{k=1}^{R} \mathcal{D}_{ik} z_k. \tag{5.19}$$

Consequently, the gradient of A with respect to $\mathbf{z}$ is given by

$$\frac{\partial A}{\partial z_k} = m \sum_{i=1}^{N} \bar{\mu}_i \mathcal{D}_{ik}, \quad k = 1, \ldots, R. \tag{5.20}$$

Then, following the same procedure presented in Sec. 5.3.1, one can easily verify the following relation,

$$\mathbf{H}_{\sigma}^{e} = -\frac{1}{T}\left[(\mathbf{H}_{A}^{e} \cdot \mathbf{J}^{e}) + (\mathbf{H}_{A}^{e} \cdot \mathbf{J}^{e})^{T}\right], \tag{5.21}$$

where $\mathbf{H}_{A}^{e}$ is the local Hessian matrix of the Helmholtz free energy at the equilibrium state.

In the highly unusual case in which $\mathbf{H}_{A}^{e}$ is diagonal with identical eigenvalues, the SIM can be identified by consideration of the eigenvectors of $\mathbf{H}_{\sigma}^{e}$. In that case, the eigenvectors of $\mathbf{J}^{e}$ are aligned with those of $\mathbf{H}_{\sigma}^{e}$. However, essentially all practical reactive systems have $\mathbf{H}_{A}^{e}$ which is not diagonal and does not have identical eigenvalues. Thus, $\mathbf{H}_{A}^{e}$ operates on $\mathbf{J}^{e}$ in a non-uniform way, such that the eigenvalues and the eigenvectors of $\mathbf{H}_{\sigma}^{e}$ are not the same as those of $\mathbf{J}^{e}$. So, the system's dynamics cannot be deduced from σ or A. Consequently, our conclusion from Sec. 5.3.1 holds for isothermal-isochoric systems; employing equilibrium thermodynamic potentials to elucidate reactive systems' dynamic behavior is incorrect.

5.4 Model problem: Zel'dovich mechanism

Here, the Zeldovich mechanism employed in Sec. 4.3.1 will be used as a model problem to examine the relation between slow dynamics and thermodynamics. Although, this reactive system is taken to be isothermal-isochoric, the pressure

remains constant throughout the reaction process as a consequence of including only bimolecular reactions in the kinetic model. This can be easily verified; from the thermal equation of state,

$$pV = n\bar{\Re}T, \qquad ((2.4))$$

and the third constraint for this system,

$$n = \sum_{i=1}^{N} n_i = \sum_{i=1}^{N} n_i^*, \qquad ((4.33c))$$

it is clear that this system is isobaric, too. Thus, in addition to the irreversibility production rate, the Gibbs free energy is the appropriate thermodynamic function to analyze this reactive system.

From Chapter 4, this system's slow dynamics is described by the system's one-dimensional SIM, which was constructed using the procedure described in Sec. 4.2. Figures 4.4–4.5, show the system's 1-D SIM.

Now, to examine the relationship between system's slow dynamics and thermodynamics, σ and G are calculated within $\mathbb{S}$ and are illustrated in Figs. 5.1.

Figure 5.2 shows several contours of the system's Gibbs free energy and irreversibility production rate along with the constructed 1-D SIM for the Zel'dovich mechanism. Figure 5.2(a) is far from R_3, while Fig. 5.2(b) is an expansion in the vicinity of R_3. In Fig. 5.2(b) stretching has been employed to expose the difference between the contours' major/minor axes and the SIM. Even within the close neighborhood of R_3 the contours' axes are not aligned with the 1-D SIM. So, here equilibrium thermodynamic quantities cannot explain the 1-D SIM, which describes the system's preferred path toward equilibrium. Subsequently, the gradients of these thermodynamic scalar functions do not drive the system's

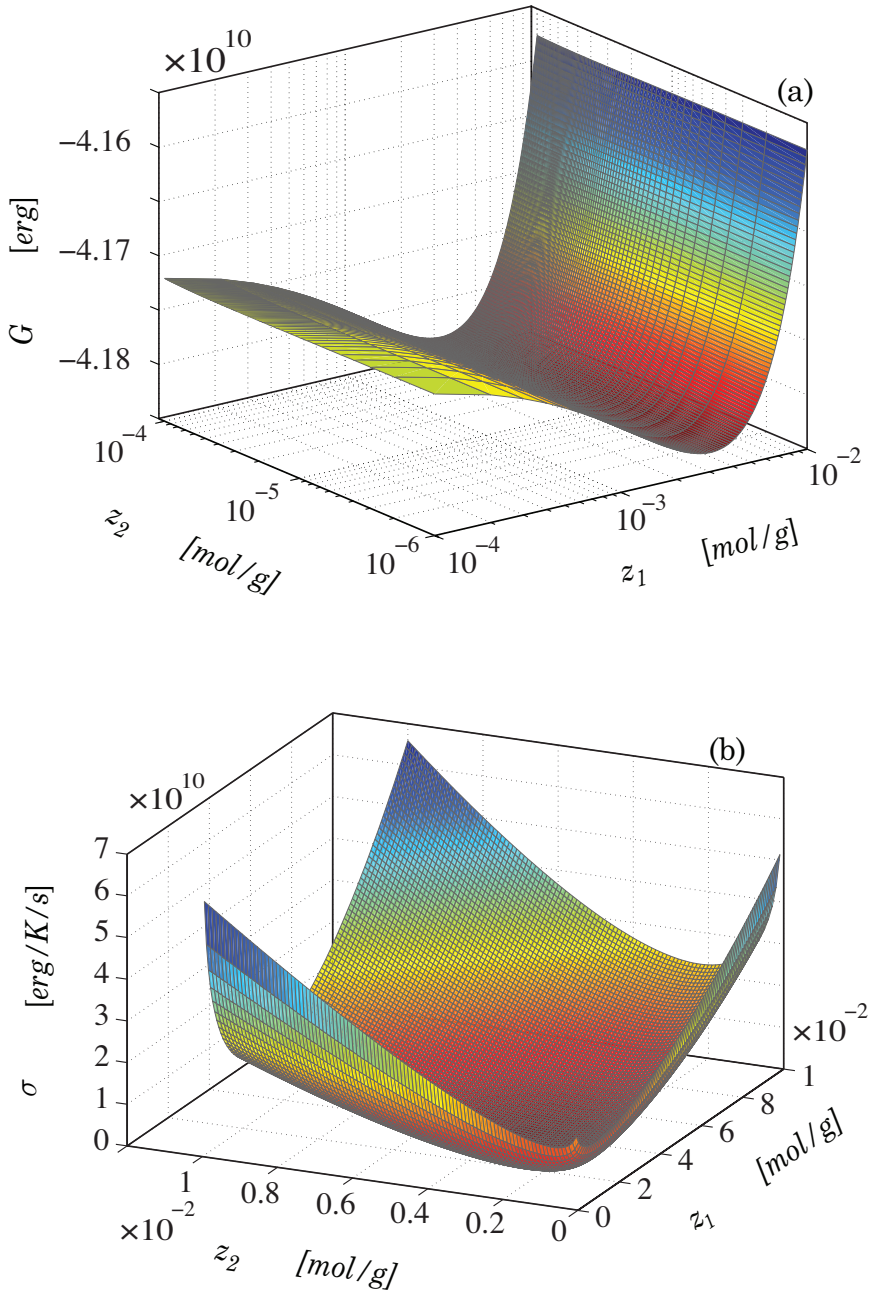

Figure 5.1. Surfaces illustrating (a) the Gibbs free energy, (b) the irreversibility production rate for the Zel'dovich mechanism in the neighborhood of the equilibrium point.

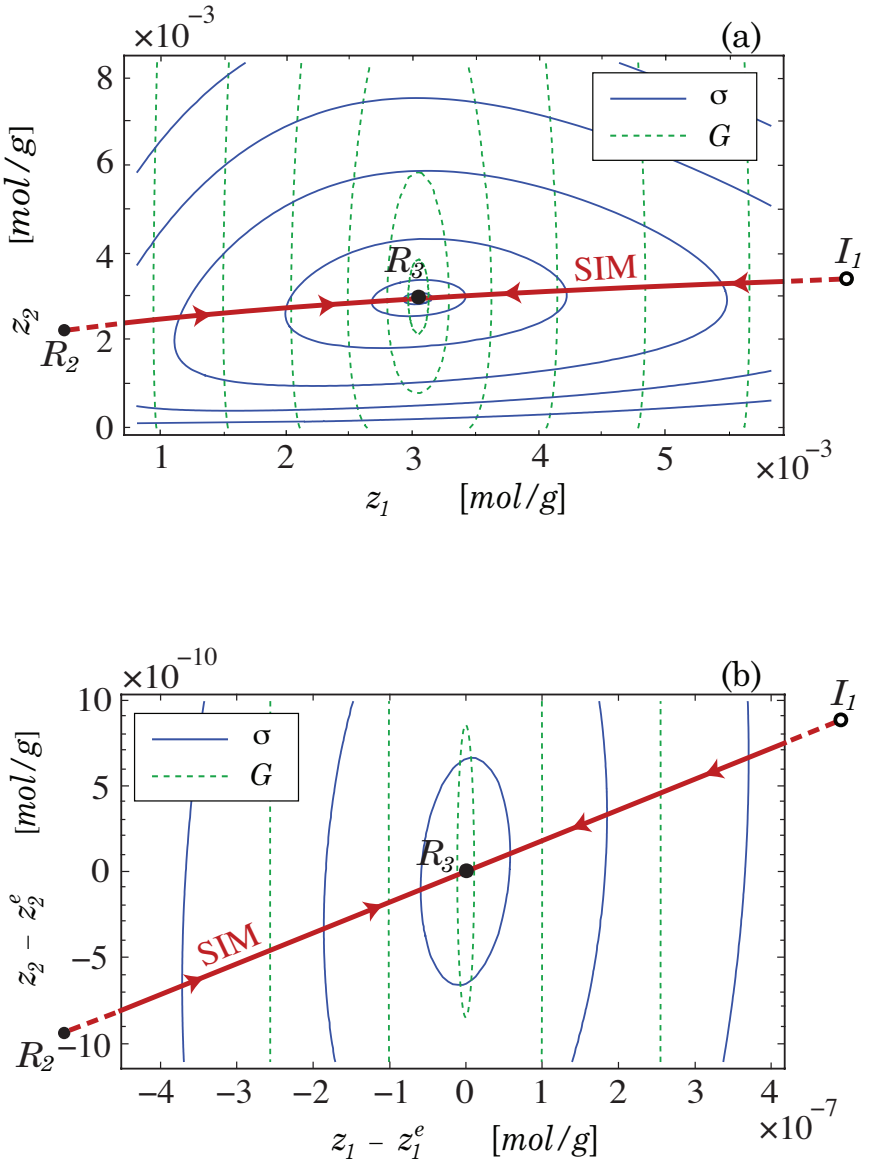

Figure 5.2. (a) The SIM for the Zel'dovich mechanism near the physical equilibrium state R_3, (b) a blow-up of the top panel in the vicinity of R_3. The solid lines and the dashed lines represent different levels of the system's irreversibility production rate and Gibbs free energy, respectively. The solid dots represent finite critical points, and the open circle represents an infinite critical point.

dynamics. Explicitly,

$$\mathbf{H}_{\sigma}^{e} = \begin{pmatrix} 1.49361 \times 10^{15} & -2.09205 \times 10^{16} \\ -2.09205 \times 10^{16} & 1.17635 \times 10^{19} \end{pmatrix}, \tag{5.22a}$$

$$\mathbf{H}_{G}^{e} = \begin{pmatrix} 1.52205 \times 10^{13} & -8.02837 \times 10^{11} \\ -8.02837 \times 10^{11} & 1.36005 \times 10^{15} \end{pmatrix}, \tag{5.22b}$$

$$\mathbf{J}^{e} = \begin{pmatrix} -1.94646 \times 10^{5} & 1.83659 \times 10^{6} \\ 3.06494 \times 10^{4} & -1.72976 \times 10^{7} \end{pmatrix}. \tag{5.22c}$$

So, it can be easily verified that Eq. (5.16) holds for this model problem;

$$\mathbf{H}_{\sigma}^{e} = -\frac{1}{T}\left[(\mathbf{H}_{G}^{e} \cdot \mathbf{J}^{e}) + (\mathbf{H}_{G}^{e} \cdot \mathbf{J}^{e})^{T}\right]. \tag{(5.16b)}$$

Moreover, the two terms on the right side of Eq. (5.16) are identical. Thus, Eq. (5.16) can be rewritten as

$$\mathbf{H}_{\sigma}^{e} = -\frac{2}{T}\left(\mathbf{H}_{G}^{e} \cdot \mathbf{J}^{e}\right). \tag{5.23}$$

Now, the eigenvalues λ_i and the associated eigenvectors $\boldsymbol{\upsilon}$ of $\mathbf{H}_{\sigma}^{e}, \mathbf{H}_{G}^{e}$, and $\mathbf{J}^{e}$,

Eqs. (5.22), are given by

$$\begin{aligned}
\mathbf{H}^e_\sigma : (\lambda, \boldsymbol{\upsilon}) &= \left(1.17635 \times 10^{19}, 1.45640 \times 10^{15}\right), \\
&\left([1.77864 \times 10^{-3}, -9.99998 \times 10^{-1}]^T, [-9.99998 \times 10^{-1}, -1.77864 \times 10^{-3}]^T\right), \\
\mathbf{H}^e_G : (\lambda, \boldsymbol{\upsilon}) &= \left(1.36005 \times 10^{15}, 1.52201 \times 10^{13}\right), \\
&\left([5.96981 \times 10^{-4}, -1.00000]^T, [-1.00000, -5.96981 \times 10^{-4}]^T\right), \\
\mathbf{J}^e : (\lambda, \boldsymbol{\upsilon}) &= \left(-1.73009 \times 10^{7}, -1.91355 \times 10^{5}\right), \\
&\left([-1.06750 \times 10^{-1}, 9.94286 \times 10^{-1}]^T, [-9.99998 \times 10^{-1}, 1.79171 \times 10^{-3}]^T\right),
\end{aligned}$$

where for each matrix the second eigenvector yields the direction of the slow mode. It is clear that these eigenvectors are not aligned with each other. For $\mathbf{J}^e$, the arctangent of the ratio between the second component and the first component of υ_2 defines the angle θ^e_{SIM} at which the 1-D SIM approaches R_3. Similarly, the same ratio between the second component and the first component of υ_2 of $\mathbf{H}^e_G$ and $\mathbf{H}^e_\sigma$ defines, respectively, the angles θ^e_G and θ^e_σ at which each scalar field approaches R_3. These angles are

$$\begin{aligned}
\theta^e_\sigma &= \tan^{-1}\left(\frac{1.77864 \times 10^{-3}}{-9.99998 \times 10^{-1}}\right) = 1.77864 \times 10^{-3}\ rad, \\
\theta^e_G &= \tan^{-1}\left(\frac{-5.96981 \times 10^{-4}}{-1.00000}\right) = 5.96981 \times 10^{-4}\ rad, \\
\theta^e_{SIM} &= \tan^{-1}\left(\frac{1.79171 \times 10^{-3}}{-9.99998 \times 10^{-1}}\right) = 1.79171 \times 10^{-3}\ rad.
\end{aligned}$$

Thus, even at R_3, the reactive system's SIM cannot be identified using G or σ. Indeed, at R_3 the error in σ is small; the difference between θ^e_{SIM} and θ^e_σ is $\mathcal{O}\left(10^{-5}\ rad\right)$. But, this error grows as we move away from R_3.

Moreover, other choices of dependent variables would lead to larger differences,

e.g. in the chemical potential composition space, $(\bar{\mu}_1, \bar{\mu}_2)$, the difference between θ^e_{SIM} and θ^e_σ is $\mathcal{O}\left(10^0\ rad\right)$. Furthermore, as is shown in Table 5.1, the difference between θ^e_{SIM} and θ^e_σ increases monotonically as the system temperature increases, *i.e.* stiffness decreases.

TABLE 5.1

THE RELATIVE DIFFERENCE BETWEEN THE ANGLE AT WHICH THE 1-D SIM APPROACHES THE PHYSICAL EQUILIBRIUM POINT AND THE ANGLES AT WHICH σ AND G APPROACH THAT POINT FOR ZEL'DOVICH MECHANISM.

$T\ \ [K]$	$\lvert\theta^e_{SIM} - \theta^e_\sigma/\theta^e_{SIM}\rvert$	$\lvert\theta^e_{SIM} - \theta^e_G/\theta^e_{SIM}\rvert$
1000	1.60×10^{-9}	1.00×10^{0}
1500	2.60×10^{-6}	9.99×10^{-1}
2000	8.26×10^{-5}	9.94×10^{-1}
2500	5.77×10^{-4}	9.76×10^{-1}
3000	1.98×10^{-3}	9.30×10^{-1}
3500	4.47×10^{-3}	8.33×10^{-1}
4000	7.29×10^{-3}	6.67×10^{-1}
7000	3.00×10^{-2}	2.92×10^{-1}
10000	5.44×10^{-2}	2.45×10^{-1}

5.5 Comparison with published results

Here, a comparison between previously published reactive systems' low dimensional manifolds and their actual 1-D SIMs is performed.

5.5.1 The invariant constrained equilibrium manifold

Here, the system described in Sec. 4.3.3 has been employed by Ren *et al.* [37] to present the ICE-PIC method. This system's 1-D SIM was constructed using the procedure described in Sec. 4.2, and illustrated in Fig. 4.10.

In this section, we compare the constructed SIM with the previously published [37] invariant constrained equilibrium (ICE) manifold. Calculations are first performed to reproduce the ICE manifold for the considered reactive system. Generation of the ICE manifold is based on minimizing a classical thermodynamics potential. First, the constrained equilibrium manifold (CEM) is developed by varying one dependent variable to minimize the system's Gibbs potential for each combination of the rest of the dependent variables. The intersection between the CEM and $\mathbb{S}$ defines a closed curve. Then, starting from several points located on the closed curve, trajectories are generated. The collection of all these trajectories represents the ICE manifold. Figure 5.3 shows the 1-D SIM and the 2-D ICE manifold. The computed ICE manifold is identical to that illustrated in Fig. 4 of Ren *et al.* [37].

From Fig. 5.3, it is clear that there are trajectories within $\mathbb{S}$ which are not attracted to the 2-D ICE manifold. However, all the trajectories are attracted to the 1-D SIM. Although it is difficult to visualize in Fig. 5.3, the 2-D ICE manifold does not contain the system's SIM: the 1-D SIM is not a subset of the 2-D ICE manifold. The error of the ICE manifold grows as we move away from

R_7. Consequently, the 2-D ICE manifold cannot fully identify the system's SIM.

Furthermore, for this reactive system Eq. (5.16) holds, where

$$\mathbf{H}_{\sigma}^{e} = \begin{pmatrix} 3.45619 \times 10^{17} & 1.41689 \times 10^{17} & 8.64077 \times 10^{16} \\ 1.41689 \times 10^{17} & 1.06515 \times 10^{18} & 5.52281 \times 10^{17} \\ 8.64077 \times 10^{16} & 5.52281 \times 10^{17} & 2.87142 \times 10^{17} \end{pmatrix},$$

$$\mathbf{H}_{G}^{e} = \begin{pmatrix} 8.26606 \times 10^{13} & -3.48042 \times 10^{13} & 3.48042 \times 10^{13} \\ -3.48042 \times 10^{13} & 1.32663 \times 10^{14} & 1.72953 \times 10^{13} \\ 3.48042 \times 10^{13} & 1.72953 \times 10^{13} & 5.96845 \times 10^{13} \end{pmatrix},$$

$$\mathbf{J}^{e} = \begin{pmatrix} -1.08285 \times 10^{7} & -4.44165 \times 10^{6} & -2.70247 \times 10^{6} \\ -5.17866 \times 10^{6} & -1.21977 \times 10^{7} & -6.46233 \times 10^{6} \\ 5.64353 \times 10^{6} & -7.75527 \times 10^{6} & -3.76793 \times 10^{6} \end{pmatrix}.$$

Moreover, similar to our model problem, the Zel'dovich mechanism for nitric oxide formation,

$$\mathbf{H}_{\sigma}^{e} = -\frac{2}{T}\left(\mathbf{H}_{G}^{e} \cdot \mathbf{J}^{e}\right), \qquad ((5.23))$$

which implies that $\mathbf{H}_{G}^{e}$ operates on $\mathbf{J}^{e}$ in a non-uniform way, such that the eigenvalues and the eigenvectors of $\mathbf{H}_{\sigma}^{e}$ are not the same as those of $\mathbf{J}^{e}$. Thus, neither σ nor G can elucidate the reactive system's dynamics.

5.5.2 The minimal entropy production trajectory method

The system described in Sec. 4.3.2 by Eqs. (4.39) has been employed by Lebiedz [41] to present the MEPT method. This system's 1-D SIM was constructed using the procedure described in Sec. 4.2, and illustrated in Fig. 4.6. However, the system's 1-D SIM has only one branch.

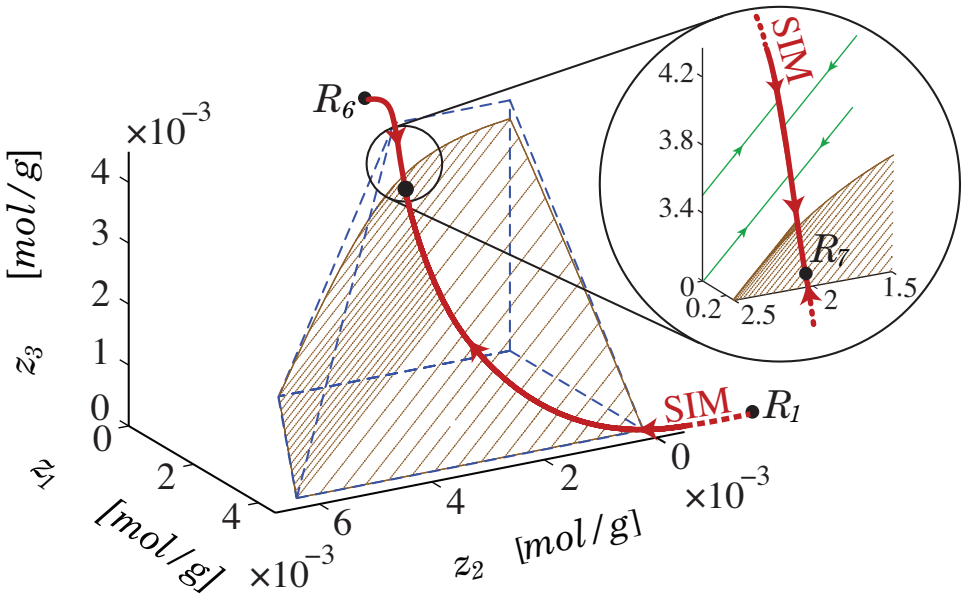

Figure 5.3. A comparison between the actual 1-D SIM, illustrated as thick line, and the 2-D ICE manifold for the simple hydrogen-oxygen reactive system. The solid dots represent finite critical points. R_7 represents the system's physical equilibrium state. The dashed simplex represents $\mathbb{S}$. Thin lines represent trajectories inside $\mathbb{S}$. The ICE manifold is identical to the one presented in Ren *et al.*

The MEPT method is based on minimizing a classical thermodynamic quantity, which is in this case σ. To compare the system's actual 1-D SIM to its MEPT, a series of calculations was performed to reproduce the MEPT. By following the same procedure described in the original work [41], we were able to reconstruct the MEPT for this system. This is given by the dashed line in Fig. 5.4, and is identical to the one presented in Ref. [41]. Further details regarding the construction of the MEPT for this problem are given in Appendix K.

Figure 5.4(a) is identical to Fig. 4 of Ref. [41]; Fig 5.4(b) shows a wider range of the system's finite composition space, and Fig. 5.4(c) is a closer look at the system's dynamical behavior near the physical equilibrium point R_1. Figure 5.4

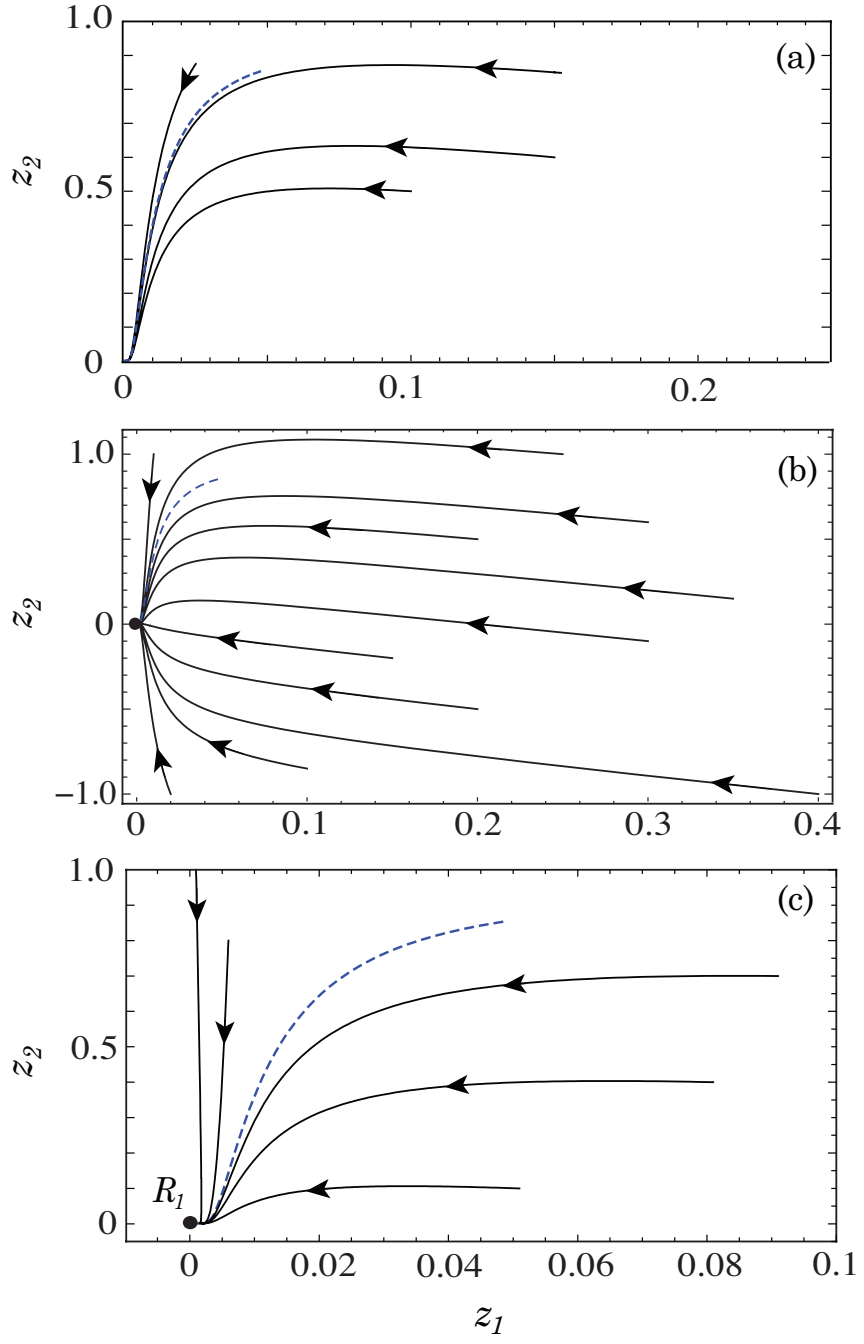

Figure 5.4. Part of the finite composition space of the Lebiedz system. Figure (a) is identical to Fig. (4) in the original work of Lebiedz, (b) is a wider range of its finite composition space, and (c) is a blow-up near its equilibrium, R_1. Different sets of trajectories are illustrated in each figure.

clearly shows that the MEPT is not an attractive manifold, though near R_1 it seems attractive. However, any trajectory approaching R_1 from the right side is as attractive as the MEPT near R_1. Moreover, by recalling Fig. 4.6, the MEPT is a subset of a heteroclinic orbit that connects $\overline{I}_2$ with R_1, where $\overline{I}_2$ is the antipodal point of I_2. From Sec. 4.3.2, I_2 is a stable node with $\lambda_1 = \lambda_2 = -1$, which implies that $\overline{I}_2$ is a source with $\lambda_1 = \lambda_2 = 1$. Thus, near $\overline{I}_2$ the $\mathsf{S} \geq 1$. Subsequently, the MEPT is not attractive along its complete trajectory, and thus does not correspond to the actual SIM of the system.

CHAPTER 6

CONCLUSIONS AND FUTURE WORK

A dynamical system approach based on standard/generalized eigenvalue analysis was presented and implemented to identify all the physical, temporal and spatial, scales inherent in a reactive flow model. The coupling between the scales and the implications for the very fine scales necessary to claim a resolved simulation of a combustion process were illustrated. To this end, a robust method of constructing the SIMs of reactive systems was developed to rationally reduce the computational cost of their modeling.

Chemically reacting systems are multiscale problems that admit wide spectra of temporal and spatial scales. A standard eigenvalue analysis was employed to determine the smallest time scale over which an unsteady spatially homogeneous reacting system modeled by detailed mass–action kinetics evolves in time. For accurate simulation of a reactive system, this scale serves as a lower bound for the employed time step. To determine the finest length scale in a reactive flow structure, a rigorous method based on generalized eigenvalue analysis was developed. This method accurately calculates the required spatial discretization to formally capture all the detailed continuum physics in the reaction zone. This result was verified by performing a formal grid convergence study. The length scale predictions are fully reflective of the underlying physics of advection and diffusion coupled with detailed kinetics and not the particular numerical method chosen.

This has been verified by showing that the finest length scale is well–correlated with the mean free path cutoff length scale estimated from kinetic theory. Thus, it is possible to use a simple mean free path calculation as *a priori* estimate of the lower bound for grid discretization. This finest length scale for a laminar premixed flame is nearly identical to the finest length scale for a Chapman–Jouguet detonation in a comparable mixture. Furthermore, it was shown that when the reaction zone structure is resolved, the small wavelength modes critical in the thin reaction zone structures induced by fast reaction have associated with them time scales which are dictated by a balance between chemistry and transport. Moreover, it was revealed that short wavelength modes have very fast time scales which are dominated by diffusion, modes which have wavelengths ranging from the finest combustion length scale to the coarsest combustion length scale have time scales which are dictated by a combination of reaction and diffusion effects, and modes which have coarse wavelengths have time scales which are reaction dominated. These results have been achieved by conducting a spectral analysis of one–dimensional premixed reactive mixtures of calorically imperfect ideal gases.

The slow invariant manifold provides an effective way to overcome the presence of a wide range spectrum when modeling a closed reactive system. It corresponds to the exact description of the slow dynamics in the composition space of the reacting system. The presented method for constructing a slow invariant manifold is based on a geometrical approach that relies upon finding and examining the dynamical behavior of all of the system's critical points. It has been shown that the construction method is algorithmically easy and computationally efficient. The resulting procedure provides a useful tool to significantly reduce the computational cost associated with modeling reactive systems. Furthermore, it has been demon-

strated that a reactive system's one–dimensional slow invariant manifold cannot be identified by consideration of the topology of a classical thermodynamic function, such as entropy, Gibbs free energy, or irreversibility production rate, even near the equilibrium state. This point has been confirmed by a mathematical proof that shows that equilibrium thermodynamic potentials do not alone determine reactive systems' dynamics during their approach towards the equilibrium.

This work provides a potential for several possibilities of future work, some of them are straightforward extensions of the work presented here. For example, we can work on obtaining and analyzing the eigenvalue spectrum for a fully resolved laminar flame structure. Although it is an overwhelming computational task, it might be performed by employing parallel computational resources. Exploring this issue and getting a better understanding of it will provide us with a good tool to develop an efficient algorithm that predicts all scales of reactive flow modeling with a detailed chemical kinetics. Moreover, this approach might be extended to other problems such as combustion instability and pollutant formation. Slow invariant manifold for non-isothermal reactive system are yet to be constructed; modeling the exponential term in the Arrhenius kinetic rates, Eq. (2.13a), as a polynomial would allow for the temperature evolution equation, Eq. (B.6) or (B.12), to be augmented with species evolution equation in the construction procedure for a slow invariant manifold. Finally, constructing two–dimensional slow invariant manifolds should be considered by extending the presented conjecture in Sec. 4.2.5 to account for equilibria with two unstable eigenvector directions as candidate members of the two–dimensional slow invariant manifold.

APPENDIX A

MULTICOMPONENT GAS PHASE SPECIES TRANSPORT PROPERTIES

Here, a description of the calculation of the transport properties of a N species gaseous mixture is presented. For such a multicomponent mixture, the mass diffusion coefficients, the thermal diffusion coefficients, and the thermal conductivity are given by [104, 106, 129]

$$\mathfrak{D}_{ij} = \frac{16\ T\ \bar{m}\ X_i}{25\ p\ \bar{m}_j}\left(\mathsf{P}_{ij} - \mathsf{P}_{ii}\right), \quad i,j = 1,\ldots,N, \tag{A.1}$$

$$D_i^T = \frac{8\ \bar{m}_i X_i}{5\ \bar{\Re}}\mathsf{c}_{i00}, \quad i = 1,\ldots,N, \tag{A.2}$$

$$k = -\sum_{i=1}^{N}\left(X_i \mathsf{c}_{i10} + X_i \mathsf{c}_{i01}\right), \tag{A.3}$$

where $\mathbf{c}_{00}$, $\mathbf{c}_{10}$, and $\mathbf{c}_{01}$ are vectors of dimensions N that represent the solution of the L-matrix system, and $\mathbf{P}$ is an $N \times N$ matrix defined as the inverse of the first sub-matrix in the L-matrix system; $\mathbf{P} = \left(\mathbf{L}^{00,00}\right)^{-1}$. Following Ref. [106], the linear system known as the detailed L-matrix system is given by

$$\begin{bmatrix} \mathbf{L}^{00,00} & \mathbf{L}^{00,10} & \mathbf{L}^{00,01} \\ \mathbf{L}^{10,00} & \mathbf{L}^{10,10} & \mathbf{L}^{10,01} \\ \mathbf{L}^{01,00} & \mathbf{L}^{01,10} & \mathbf{L}^{01,01} \end{bmatrix} \cdot \begin{bmatrix} \mathbf{c}_{00} \\ \mathbf{c}_{10} \\ \mathbf{c}_{01} \end{bmatrix} = \begin{bmatrix} \mathbf{0} \\ \boldsymbol{X} \\ \boldsymbol{X} \end{bmatrix}, \tag{A.4}$$

where the sub-matrices $\mathbf{L}^{\mathtt{M},\mathtt{N}}$, $\{\mathtt{M},\mathtt{N}\} = 00, 10,$ or 01, are constant matrices of size $N \times N$ defined as

$$\mathsf{L}_{ij}^{00,00} = \sum_{k=1}^{N} \frac{16\ T\ X_k}{25\ p\ \bar{m}_i\ \mathscr{D}_{ik}} \left(\bar{m}_j\ X_j \left(1-\delta_{ik}\right) - \bar{m}_i\ X_j \left(\delta_{ij}-\delta_{jk}\right)\right), \tag{A.5}$$

$$\mathsf{L}_{ij}^{00,10} = \sum_{k=1}^{N} \frac{8\ T\ \bar{m}_k\ X_k\ X_j}{5\ p \left(\bar{m}_j + \bar{m}_k\right) \mathscr{D}_{jk}} \left(\delta_{ij}-\delta_{ik}\right) \left(1.2\ \mathscr{C}_{jk} - 1\right), \tag{A.6}$$

$$\mathsf{L}_{ij}^{00,01} = 0, \tag{A.7}$$

$$\mathsf{L}_{ij}^{10,00} = \sum_{k=1}^{N} \frac{8\ T\ \bar{m}_k\ X_k\ X_j}{5\ p \left(\bar{m}_j + \bar{m}_k\right) \mathscr{D}_{jk}} \left(\delta_{ij}-\delta_{ik}\right) \left(1.2\ \mathscr{C}_{jk} - 1\right), \tag{A.8}$$

$$\begin{aligned}\mathsf{L}_{ii}^{10,10} = &-\frac{16\bar{m}_i X_i^2}{\bar{\Re}\eta_i}\left(1+\frac{10c_{pi}^{rot}}{\mathsf{K}\xi_{ii}}\right) - \frac{16T}{25p}\sum_{\substack{k=1\\k\neq i}}^{N}\frac{X_k X_i}{\left(\bar{m}_i+\bar{m}_k\right)^2 \mathscr{D}_{ik}}\Bigg(7.5\bar{m}_i^2 + 6.25\bar{m}_k^2 \\ &- 3\ \bar{m}_k^2\ \mathscr{B}_{ik} + 4\ \bar{m}_i\ \bar{m}_k\ \mathscr{A}_{ik}\ \left(1+\frac{5}{3\pi}\left(\frac{c_{pi}^{rot}}{\xi_{ik}\mathsf{K}}+\frac{c_{pk}^{rot}}{\xi_{ki}\mathsf{K}}\right)\right)\Bigg),\end{aligned} \tag{A.9}$$

$$\begin{aligned}\mathsf{L}_{ij}^{10,10} = &\sum_{k=1}^{N}\frac{16\ T\ \bar{m}_i\ X_k\ X_i}{25\ p\ \bar{m}_j\ \left(\bar{m}_i+\bar{m}_k\right)^2 \mathscr{D}_{ik}}\Bigg(\left(\delta_{jk}-\delta_{ij}\right)\left(7.5\ \bar{m}_j^2 + 6.25\ \bar{m}_k^2 - 3\ \bar{m}_k^2\ \mathscr{B}_{ik}\right) \\ &- 4\ \bar{m}_j\ \bar{m}_k\ \mathscr{A}_{ik}\left(\delta_{jk}+\delta_{ij}\right)\left(1+\frac{5}{3\pi}\left(\frac{c_{pi}^{rot}}{\xi_{ik}\mathsf{K}}+\frac{c_{pk}^{rot}}{\xi_{ki}\mathsf{K}}\right)\right)\Bigg), \quad i\neq j,\end{aligned} \tag{A.10}$$

$$\mathsf{L}_{ii}^{10,01} = \frac{16\ \bar{m}_i\ X_i^2\ c_{pi}^{rot}}{3\ \pi\ \bar{\Re}\ \eta_i\ \xi_{ii}\ c_{pi}^{int}} + \sum_{\substack{k=1\\k\neq i}}^{N}\frac{32\ T\ \bar{m}_i\ X_k\ X_i\ \mathscr{A}_{ik}\ c_{pi}^{rot}}{5\ \pi\ p\left(\bar{m}_i+\bar{m}_k\right)\mathscr{D}_{ik}\ \xi_{ik}\ c_{pi}^{int}}, \tag{A.11}$$

$$\mathsf{L}_{ij}^{10,01} = \sum_{k=1}^{N}\frac{32\ T\ \bar{m}_j\ X_k\ X_j\ \mathscr{A}_{jk}\ c_{pj}^{rot}}{5\ \pi\ p\left(\bar{m}_j+\bar{m}_k\right)\mathscr{D}_{jk}\ \xi_{jk}\ \mathsf{K}\ c_{pj}^{int}}\left(\delta_{ik}+\delta_{ij}\right), \quad i\neq j, \tag{A.12}$$

$$\mathsf{L}_{ij}^{01,00} = 0, \tag{A.13}$$

$$\mathsf{L}_{ij}^{01,10} = \mathsf{L}_{ji}^{10,01}, \tag{A.14}$$

$$\mathsf{L}_{ij}^{01,01} = 0, \quad i\neq j, \tag{A.15}$$

$$\mathsf{L}_{ii}^{01,01} = -\frac{8\ \mathsf{K}\ \bar{m}_i\ X_i^2\ c_{pi}^{rot}}{\pi\ \bar{\Re}\ \eta_i\ \xi_{ii}\ c_{pi}^{int\,2}} - \frac{4\ T\ \mathsf{K}}{p\ c_{pi}^{int}}\left(\sum_{k=1}^{N}\frac{X_i\ X_k}{\mathscr{D}_{ik}^{int}} + \sum_{\substack{k=1\\k\neq i}}^{N}\frac{12\ X_i\ X_k\ \bar{m}_i\ \mathscr{A}_{ik}\ c_{pi}^{rot}}{5\ \pi\ \mathscr{D}_{ik}\ \bar{m}_k\ \xi_{ik}\ c_{pi}^{int}}\right). \tag{A.16}$$

Here, δ_{ij} is Kronecker delta, $\mathsf{K} = 1.381 \times 10^{-16}\ erg/K$ is Boltzman's constant, ξ_{ij} are the relaxation collision numbers, and $c_{pi}^{rot} = 2/3$ and $c_{pi}^{int} = c_{pi} - c_{pi}^{rot}$ are the rotational and internal parts of the i^{th} species molecular specific heats, respectively. Also, $\mathscr{D}_{ij}^{int}$ are the internal energy binary diffusion coefficients, $\mathscr{D}_{ij}$ are the binary diffusion coefficients, η_i is the viscosity of species i, $\mathscr{A}_{ij}, \mathscr{B}_{ij}$, and $\mathscr{C}_{ij}$ are three ratios of the collision integrals. These variables are calculated using the following relations:

$$\eta_i = \frac{5\sqrt{\pi\ \bar{m}_i\ \mathsf{K}\ T}}{16\ \pi\ \varsigma_i^2\ \Omega^{2,2}}, \quad i = 1, \ldots, N, \tag{A.17}$$

$$\mathscr{D}_{ij}^{int} = \frac{\mathscr{D}_{ij}}{1 + 2985\ T^{-3/2}}, \quad i, j = 1, \ldots N, \tag{A.18}$$

$$\mathscr{D}_{ij} = \frac{3\sqrt{2\ \pi\ \mathsf{K}^3\ T^3\ (\bar{m}_i + \bar{m}_j)\ /\ (\bar{m}_i \bar{m}_j)}}{4\ p\ \pi\ \ (\varsigma_i + \varsigma_j)^2\ \Omega_{ij}^{1,1}}, \quad i, j = 1, \ldots N, \tag{A.19}$$

$$\mathscr{A}_{ij} = \frac{\Omega_{ij}^{2,2}}{2\Omega_{ij}^{1,1}}, \quad i, j = 1, \ldots N, \tag{A.20}$$

$$\mathscr{B}_{ij} = \frac{5\Omega_{ij}^{1,2} - \Omega_{ij}^{1,3}}{3\Omega_{ij}^{1,1}}, \quad i, j = 1, \ldots N, \tag{A.21}$$

$$\mathscr{C}_{ij} = \frac{\Omega_{ij}^{1,2}}{3\Omega_{ij}^{1,1}}, \quad i, j = 1, \ldots N, \tag{A.22}$$

where ς_i is the Lennard-Jones collision diameter and $\mathbf{\Omega}^{\mathrm{I,J}}$ are the collision integrals [104, 105, 140].

The transport data, the collision integrals, and the relaxation collision numbers for the i^{th} species are adopted from `TRANSPORT` [129].

APPENDIX B

MODELING SPATIALLY HOMOGENEOUS REACTIVE SYSTEMS

Here, the set of equations that describe the time evolution of a spatially homogeneous closed reactive system is provided. Consistent with the rest of this dissertation, we restrict the analysis in this appendix to mixtures of calorically imperfect ideal gases that obey Dalton's law, and a detailed mass-action kinetics model describes the chemical interaction between the species.

In general, the equation that governs the evolution of species in a reactive mixture can be derived from the definition of $\dot{\omega}_i$, the molar production rate per unit volume [99],

$$\frac{dn_i}{dt} = V\dot{\omega}_i, \quad i = 1, \ldots, N. \tag{B.1}$$

By multiplying this equation, Eq. (B.1), with $\bar{m}_i/m$, and employing Eq. (2.2c) and the definitions of ρ and Y_i from Sec. 2.1.3, one gets [100, 103]

$$\frac{dY_i}{dt} = \frac{\dot{\omega}_i \bar{m}_i}{\rho}, \qquad i = 1, \ldots, N. \tag{B.2}$$

Furthermore, by multiplying Eq. (B.2) with $\bar{\mathsf{m}}_l \phi_{li}/\bar{m}_i$, summing from $i = 1$ to N,

and employing Eqs. (2.3), (2.16a), (2.16b), and (2.11), one recovers

$$\frac{dy_l}{dt} = 0, \qquad l = 1, \ldots, L, \tag{(3.14b)}$$

$$\frac{dY_i}{dt} = \frac{\dot{\omega}_i \bar{m}_i}{\rho}, \qquad i = 1, \ldots, N - L. \tag{(3.14c)}$$

For isothermal, *i.e.* constant temperature, reactive systems, solving for the reaction dynamics is performed by integrating the time evolution of species ODEs, Eq. (3.14c), constrained by Eq. (3.14b) and $T = T^*$. However, for non-isothermal systems the conservation of energy is need to be augmented.

B.1 Adiabatic isobaric systems

For an adiabatic isobaric system, the first law of thermodynamics states that the total enthalpy is a conserved quantity [161, 179],

$$\frac{dH}{dt} = 0. \tag{B.3}$$

Using Eq. (2.10b), recalling that the system is closed, one gets

$$\frac{dh}{dt} = 0. \tag{(3.14a)}$$

This equation in addition to the species evolutions can be employed to solve for the reaction dynamics. However, an iterative scheme needs to be used at each time step in order to solve Eq. (3.14a) and find the mixture temperature.

As an alternative and more convenient way to solve for the reactive system evolution, an explicit equation in temperature is derived from Eq. (3.14a). By

using Eq. (2.9c), one can get

$$\sum_{i=1}^{N}\left(h_i\frac{dY_i}{dt}+Y_i\frac{dh_i}{dt}\right)=0, \tag{B.4}$$

which can be rewritten, by employing Eqs. (2.5b) and (3.14c), as

$$\sum_{i=1}^{N}\left(\frac{h_i\dot{\omega}_i\bar{m}_i}{\rho}\right)+\sum_{i=1}^{N}\left(Y_ic_{pi}\frac{dT}{dt}\right)=0. \tag{B.5}$$

After rearrangements, and employing Eq. (2.9a), the following ODE which represents the evolution of temperature for an adiabatic isobaric reactive system is derived,

$$\frac{dT}{dt}=-\frac{1}{\rho c_p}\sum_{i=1}^{N}h_i\bar{m}_i\dot{\omega}_i. \tag{B.6}$$

B.2 Adiabatic isochoric systems

Similarly, for an adiabatic isochoric system, *i.e.* fixed volume, the first law of thermodynamics states that the total internal energy is a conserved quantity [161, 179],

$$\frac{dE}{dt}=0. \tag{B.7}$$

Using Eq. (2.9b), recalling that the system is closed, one gets

$$\frac{de}{dt}=0. \tag{B.8}$$

Similar to adiabatic isobaric systems, this equation in addition to the species evolutions can be employed to solve for the reaction dynamics. However, an iterative scheme needs to be used at each time step in order to solve Eq. (B.8) and find the mixture temperature. To derive an explicit equation in temperature

for the adiabatic isochoric reactive mixture, Eq. (2.9b) is substituted in Eq. (B.8) to get

$$\sum_{i=1}^{N}\left(e_i\frac{dY_i}{dt}+Y_i\frac{de_i}{dt}\right)=0. \tag{B.9}$$

By employing Eqs. (2.5a), (2.5b), and (3.14c), one gets

$$\sum_{i=1}^{N}\left(\frac{e_i\dot{\omega}_i\bar{m}_i}{\rho}\right)+\sum_{i=1}^{N}Y_i\frac{dT}{dt}\left(c_{pi}-\frac{\bar{\Re}}{\bar{m}_i}\right)=0. \tag{B.10}$$

which can be rewritten, after rearrangements and employing Eq. (2.9a), as

$$\frac{dT}{dt}=-\frac{\sum_{i=1}^{N}e_i\bar{m}_i\dot{\omega}_i}{\rho\left(c_p-\bar{\Re}\sum_{i=1}^{N}\frac{Y_i}{\bar{m}_i}\right)}. \tag{B.11}$$

Furthermore, by employing the definition of the mass-based mixture-average specific heat at constant volume [161, 180], $c_v=c_p-\bar{\Re}/\bar{m}$, the following equation is derived,

$$\frac{dT}{dt}=-\frac{1}{\rho c_v}\sum_{i=1}^{N}e_i\bar{m}_i\dot{\omega}_i. \tag{B.12}$$

APPENDIX C

PARTIAL REVIEW OF DYNAMICAL SYSTEMS THEORY

In this appendix, we briefly review several elements from dynamical systems theory that are essential for this work. This include description of the standard linerazation technique, the linear stability analysis of a critical point, the Hartman-Grobman theorem, the normal form theory, and definitions of the following terms: hyperbolic/non-hyperbolic critical points, a dynamical system separatrix, and parabolic/elleptic/hyperbolic sectors. Further details can be found in Refs. [157, 171, 172, 181].

C.1 Standard linearization

Consider a standard nonlinear dynamical system described by

$$\frac{d\mathbf{z}}{dt} = \mathbf{f}(\mathbf{z}), \quad \mathbf{z} \in \mathbb{R}^R, \quad t \in \mathbb{R}^1, \quad \mathbf{f} : \mathbb{R}^R \to \mathbb{R}^R. \tag{C.1}$$

This system is called an autonomous dynamical system [181] since $\mathbf{f}(\mathbf{z})$ is a not an explicit function of t. The dynamic behavior of $\mathbf{f}(\mathbf{z})$ is revealed by analyzing the stability of its equilibria. A point $\mathbf{z}^e$ is called an equilibrium point, *i.e.* critical point, of the system if $\mathbf{f}(\mathbf{z}^e) = \mathbf{0}$. The dynamical behavior of $\mathbf{z}^e$ is explored by conducting a standard linear analysis. Using Taylor series, the nonlinear functions

$\mathbf{f}$ can be approximated near $\mathbf{z}^e$ by

$$\mathbf{f}(\mathbf{z}) = \underbrace{\mathbf{f}(\mathbf{z}^e)}_{=0} + \mathbf{J}^e \cdot (\mathbf{z} - \mathbf{z}^e) + \frac{1}{2}(\mathbf{z} - \mathbf{z}^e)^T \cdot \mathbf{H}^e \cdot (\mathbf{z} - \mathbf{z}^e) + \ldots, \tag{C.2a}$$

where

$$\mathbf{J}^e = \left.\frac{\partial \mathbf{f}}{\partial \mathbf{z}}\right|_{\mathbf{z}=\mathbf{z}^e} \tag{C.2b}$$

and

$$\mathbf{H}^e = \left.\frac{\partial}{\partial \mathbf{z}}\left(\frac{\partial \mathbf{f}}{\partial \mathbf{z}}\right)\right|_{\mathbf{z}=\mathbf{z}^e} \tag{C.2c}$$

are the local Jacobian and Hessian matrices, respectively, evaluated at $\mathbf{z}^e$. By defining the perturbation from the equilibrium as $\mathbf{z}' = \mathbf{z} - \mathbf{z}^e, \quad \mathbf{z} \in \mathbb{R}^R$, the system's dynamics is described locally, in the neighborhood of $\mathbf{z}^e$, as

$$\frac{d\mathbf{z}'}{dt} = \mathbf{J}^e \cdot \mathbf{z}' + \frac{1}{2}(\mathbf{z}')^T \cdot \mathbf{H}^e \cdot \mathbf{z}' + \mathcal{O}\left(\mathbf{z}'^3\right). \tag{C.3}$$

Consequently,

1. The point $\mathbf{z}^e$ is a hyperbolic equilibrium point of the system, if none of the eigenvalues of $\mathbf{J}^e$ evaluated at $\mathbf{z}^e$ has zero real part. Otherwise, $\mathbf{z}^e$ is a non-hyperbolic equilibrium point of the system $\mathbf{f}$ [171].

2. A sector in the composition space of this system is an open region in the neighborhood of any $\mathbf{z}^e$. Any sector is one of three types: elliptic, parabolic, or hyperbolic, see Fig. C.1. If the trajectories within the sector are homoclinic orbits, it is an elliptic sector. If the trajectories within the sector are heteroclinic orbits that connect $\mathbf{z}^e$ with another equilibrium point, it is a parabolic sector. Otherwise, it is a hyperbolic sector [157].

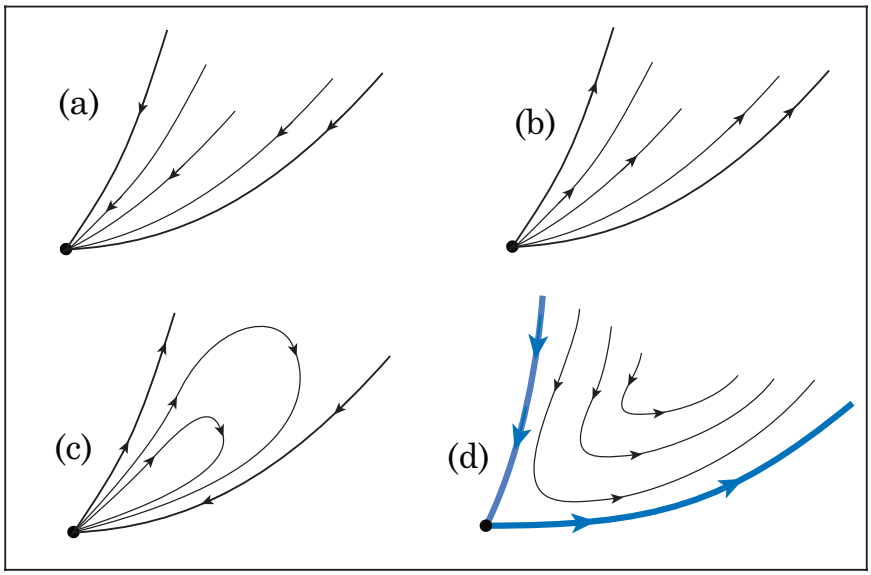

Figure C.1. A sketch illustrating sectors in a dynamical system composition space, where (a) and (b) are parabolic sectors, (c) is an elliptic sector, and (d) is a hyperbolic sector. Here, the separatrices are represented as thick lines.

3. The trajectories that represent the boundaries of a hyperbolic sector are called separatrices. These separatrices approach $\mathbf{z}^e$ as $t \to \pm\infty$.

C.2 Hartman-Grobman theorem

For a hyperbolic equilibrium [157], the Hartman-Grobman theorem is used to reveal its dynamical character. If Eq. (C.1) has a hyperbolic equilibrium point $\mathbf{z}^e$, then the theorem states that the local behavior of the dynamical system in the vicinity of $\mathbf{z}^e$ is qualitatively the same as the behavior of the following linear system

$$\frac{d\mathbf{z}}{dt} = \mathbf{J}^e \cdot (\mathbf{z} - \mathbf{z}^e)\,. \tag{C.4}$$

In other words, the local behavior of the dynamical system in the vicinity of $\mathbf{z}^e$ is approximated by the leading term of its Taylor series. Moreover, the real parts of the eigenvalues (λ) of $\mathbf{J}^e$ determine the dynamical character of $\mathbf{z}^e$, where

1. $\mathbf{z}^e$ called a sink, if all the eigenvalues of $\mathbf{J}^e$ have negative real parts.

2. $\mathbf{z}^e$ called a source, if all eigenvalues have positive real parts.

3. If at least one of the eigenvalues has negative real part and another has positive real part, $\mathbf{z}^e$ called a saddle.

The only stable critical point among these equilibria is the sink; the saddle and the source are unstable equilibria. Thus, for dissipative systems, every sink is a 0-D attractor. However, there is no globally accepted definition for the term attractor, and from a geometrical viewpoint, an attractor can be a point, a curve, or a manifold. Lichtenberg and Liberman [165] state that for a dissipative system,

> "The stable, steady state motion for an N-dimensional system must lie on a surface of dimension less than N. Loosely speaking, this surface is called an attractor."

But, it is globally accepted that every attractor has its own basin of attraction [162, 165]. So, every sink has its own basin of attraction, which all the trajectories inside of it has to approach the sink in infinite time.

C.3 Non-hyperbolic equilibria

For a non-hyperbolic equilibrium, the Hartman-Grobman theorem is not applicable, so the normal form theory has to be employed to reveal the dynamical character of the non-hyperbolic equilibrium, see Fig. C.2. This theory is used

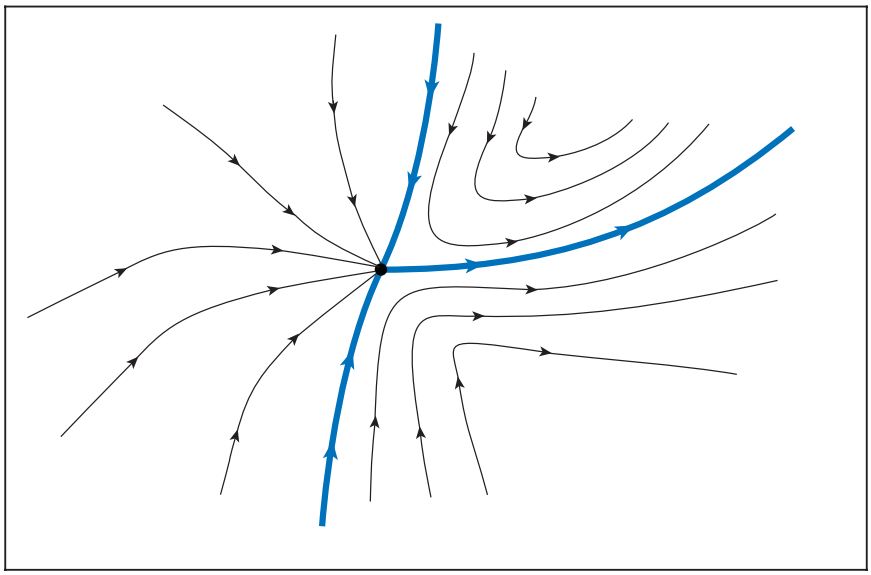

Figure C.2. A sketch illustrating the non-hyperbolic saddle-node. The thick lines are the separatrices.

to identify the local behavior of a standard dynamical system in the neighborhood of a non-hyperbolic equilibrium point based on the center manifold theorem [157, 171, 172].

Now, if Eq. (C.1) has a non-hyperbolic equilibrium point $\mathbf{z}^e$, then the local behavior of the dynamical system in the vicinity of $\mathbf{z}^e$ is qualitatively the same as the behavior of the following non-linear system

$$\frac{d\mathbf{z}'}{dt} = \mathbf{J}^e \cdot \mathbf{z}' + \frac{1}{2}\left(\mathbf{z}'\right)^T \cdot \mathbf{H}^e \cdot \mathbf{z}'. \tag{C.5}$$

In order to analyze this system, the normal form theory states that a local non-linear coordinate transformation, in the following form

$$\mathfrak{Z} = \mathbf{z}' + \mathfrak{F}\left(\mathfrak{Z}\right), \quad \{\mathfrak{Z}, \mathbf{z}'\} \in \mathbb{R}^R, \quad \mathfrak{F} : \mathbb{R}^R \to \mathbb{R}^R, \tag{C.6}$$

has to be made, where $\mathfrak{F}$ are non-linear functions and $\mathfrak{Z}$ are the new dependent variables. Such that, the non-linear part of the original dynamical system, Eq. (C.5), is brought to a canonical form.

Reference [172], provides a detailed list contains several non-hyperbolic equilibria that have been analyzed, *e.g.* saddle-node.

APPENDIX D

CHEMICAL REACTION MECHANISMS

In this appendix, all the utilized chemical reaction mechanisms in this work are listed. The elements, species, and reaction steps in the reaction mechanisms are presented in the tables. The third bodies are denoted by M, and their collision efficiencies coefficients α_{ji} with respect to all the species are unity unless otherwise specified.

TABLE D.1

HYDROGEN–AIR REACTION MECHANISM.

Elements: H, O, and N.				
Species: $H_2, O_2, H, O, OH, HO_2, H_2O_2, H_2O$, and N_2.				
j	Reaction	$\mathcal{A}_j$ $\left[\frac{(mol/cm^3)^{\left(1-\sum_{i=1}^{N}\nu'_{ij}\right)}}{s\ K^{\beta_j}}\right]$	β_j	$\bar{\mathcal{E}}_j$ $\left[\frac{cal}{mol}\right]$
1	$H_2 + O_2 \rightleftharpoons OH + OH$	1.70×10^{13}	0.0	47780
2	$OH + H_2 \rightleftharpoons H_2O + H$	1.17×10^{9}	1.3	3626
3	$H + O_2 \rightleftharpoons OH + O$	5.13×10^{16}	−0.816	16507
4	$O + H_2 \rightleftharpoons OH + H$	1.80×10^{10}	1.0	8826
5	$H + O_2 + \mathsf{M} \rightleftharpoons HO_2 + \mathsf{M}^1$	2.10×10^{18}	−1.0	0
6	$H + O_2 + O_2 \rightleftharpoons HO_2 + O_2$	6.70×10^{19}	−1.42	0
7	$H + O_2 + N_2 \rightleftharpoons HO_2 + N_2$	6.70×10^{19}	−1.42	0
8	$OH + HO_2 \rightleftharpoons H_2O + O_2$	5.00×10^{13}	0.0	1000
9	$H + HO_2 \rightleftharpoons OH + OH$	2.50×10^{14}	0.0	1900
10	$O + HO_2 \rightleftharpoons O_2 + OH$	4.80×10^{13}	0.0	1000
11	$OH + OH \rightleftharpoons O + H_2O$	6.00×10^{8}	1.3	0
12	$H_2 + \mathsf{M} \rightleftharpoons H + H + \mathsf{M}^2$	2.23×10^{12}	0.5	92600
13	$O_2 + \mathsf{M} \rightleftharpoons O + O + \mathsf{M}$	1.85×10^{11}	0.5	95560
14	$H + OH + \mathsf{M} \rightleftharpoons H_2O + \mathsf{M}^3$	7.50×10^{23}	−2.6	0
15	$H + HO_2 \rightleftharpoons H_2 + O_2$	2.50×10^{13}	0.0	700

Continued on next page

TABLE D.1

Continued

j	Reaction	$\mathcal{A}_j$ $\left[\frac{\left(mol/cm^3\right)^{\left(1-\sum_{i=1}^{N}\nu'_{ij}\right)}}{s\ K^{\beta_j}}\right]$	β_j	$\bar{\mathcal{E}}_j$ $\left[\frac{cal}{mol}\right]$
16	$HO_2 + HO_2 \rightleftharpoons H_2O_2 + O_2$	2.00×10^{12}	0.0	0
17	$H_2O_2 + \mathsf{M} \rightleftharpoons OH + OH + \mathsf{M}$	1.30×10^{17}	0.0	45500
18	$H_2O_2 + H \rightleftharpoons HO_2 + H_2$	1.60×10^{12}	0.0	3800
19	$H_2O_2 + OH \rightleftharpoons H_2O + HO_2$	1.00×10^{13}	0.0	1800

The non-unity third body collision efficiency coefficients α_{ji} are:

[1] for reaction 5, $\alpha_{5,H_2} = 3.3, \alpha_{5,H_2O} = 21$.

[2] for reaction 12, $\alpha_{12,H_2} = 3, \alpha_{12,H_2O} = 6, \alpha_{12,H} = 2$.

[3] for reaction 14, $\alpha_{14,H_2O} = 20$.

TABLE D.2

ZEL'DOVICH MECHANISM OF NITRIC ACID FORMATION.

Elements: N and O.				
Species: NO, N, O, O_2, and N_2.				
j	Reaction	$\mathcal{A}_j$ $\left[\frac{\left(mol/cm^3\right)^{\left(1-\sum_{i=1}^{N}\nu'_{ij}\right)}}{s\ K^{\beta j}}\right]$	β_j	$\bar{\mathcal{E}}_j$ $\left[\frac{cal}{mol}\right]$
1	$N + O_2 \rightleftharpoons NO + O$	5.841×10^9	1.01	6195.6
2	$N + NO \rightleftharpoons N_2 + O$	21.077×10^{12}	0.00	0.0

TABLE D.3

SIMPLE HYDROGEN–AIR KINETICS MECHANISM.

Elements: H, O, and N.				
Species: H_2, H, O, OH, H_2O, and N_2.				
j	Reaction	$\mathcal{A}_j$ $\left[\frac{\left(mol/cm^3\right)^{\left(1-\sum_{i=1}^{N}\nu'_{ij}\right)}}{s\ K^{\beta_j}}\right]$	β_j	$\bar{\mathcal{E}}_j$ $\left[\frac{cal}{mol}\right]$
1	$O + H_2 \rightleftharpoons H + OH$	5.08×10^4	2.7	6290
2	$H_2 + OH \rightleftharpoons H_2O + H$	2.16×10^8	1.5	3430
3	$O + H_2O \rightleftharpoons OH + OH$	2.97×10^6	2.0	13400
4	$H_2 + \mathsf{M} \rightleftharpoons H + H + \mathsf{M}$[1]	4.58×10^{19}	-1.4	104380
5	$O + H + \mathsf{M} \rightleftharpoons OH + \mathsf{M}$[1]	4.71×10^{18}	-1.0	0
6	$H + OH + \mathsf{M} \rightleftharpoons H_2O + \mathsf{M}$[1]	3.80×10^{22}	-2.0	0

[1]The non-unity third body collision efficiency coefficients are:

$\alpha_{j,H_2} = 2.5, \alpha_{j,H_2O} = 12, \quad j = 4, 5, 6.$

TABLE D.4

MICHAEL'S MECHANISM FOR HYDROGEN OXIDATION.

Elements: H and O.				
Species: H_2, O_2, H, O, OH, and H_2O.				
j	Reaction[1]	$\mathcal{A}_j$ $\left[\frac{\left(mol/cm^3\right)^{\left(1-\sum_{i=1}^{N}\nu'_{ij}\right)}}{s\ K^{\beta_j}}\right]$	β_j	$\bar{\mathcal{E}}_j$ $\left[\frac{cal}{mol}\right]$
1	$H + O_2 \longrightarrow O + OH$	9.76×10^3	0.0	14842.5
2	$O + OH \longrightarrow O_2 + H$	3.26×10^{11}	0.375	−2208.4
3	$O + H_2 \longrightarrow OH + H$	5.08×10^4	2.67	6289.3
4	$OH + H \longrightarrow H_2 + O$	2.28×10^4	2.67	4420.6
5	$H + H_2O \longrightarrow OH + H_2$	9.39×10^8	1.52	18367.5
6	$H_2 + OH \longrightarrow H_2O + H$	2.14×10^8	1.52	3447.5
7	$O + H_2 \longrightarrow OH + OH$	4.50×10^4	2.70	14542.7
8	$OH + OH \longrightarrow O + H_2O$	4.33×10^3	2.70	−2484.3

[1]A reduced version of this mechanism is obtained by eliminating the first two elementary reactions.

TABLE D.5

OZONE DECOMPOSITION REACTION MECHANISM.

Elements: O.				
Species: O, O_2, and O_3.				
j	Reaction	$\mathcal{A}_j$ $\left[\frac{\left(mol/cm^3\right)^{\left(1-\sum_{i=1}^{N}\nu'_{ij}\right)}}{s\ K^{\beta_j}}\right]$	β_j	$\bar{\mathcal{E}}_j$ $\left[\frac{cal}{mol}\right]$
1	$O_3 + \mathsf{M} \rightleftharpoons O + O_2 + \mathsf{M}$	6.76×10^6	2.50	24123
2	$O + O_3 \rightleftharpoons O_2 + O_2$	4.58×10^6	2.50	6000
3	$O_2 + \mathsf{M} \rightleftharpoons O + O + \mathsf{M}$	5.71×10^6	2.50	117350

APPENDIX E

DETONATION LENGTH SCLAES

Here, the robust method developed by Powers and Paolucci [122] to calculate the length scales for a gas phase Chapman–Jouguet (CJ) detonation [143] is used. Detailed kinetic models identical to the ones that have been employed in Sec. 3.3: the GRI 3.0 mechanism [141] for hydrocarbon–air reactive mixtures, and the hydrogen–air mechanism extracted from Ref. [120], are adopted. At the unshocked state, the initial pressure is $p^* = 1\ atm$, and the temperature is $T^* = 800\ K$ for hydrogen–air mixtures, and $T^* = 298\ K$ for hydrocarbon–air mixtures. The standard code `DLSODE` [119], which utilizes an implicit Adams scheme, is used to obtain a resolved reaction zone structure. The spatial step sizes are adapted to achieve the absolute error tolerance of 10^{-14}; the minimum utilized grid sizes are listed in Table E.1.

First, a comparison between $\ell_{finest}, \ell_{induction}$, and ℓ_{mfp} for the hydrogen–air mixture has been conducted for a wide range of Φ and pressures, see Figs. E.1–E.2. The results are consistent with Figs. 3.14–3.16 for laminar premixed flames, and clearly show that the finest length scale is not a function of the fuel–air ratio. Then, for each hydrocarbon–air reactive mixture, the calculated finest length scale ℓ_{finest}, induction zone length $\ell_{induction}$, and the estimated mean free path ℓ_{mfp} over a wide range of pressures are presented, Figs. E.3–E.7.

TABLE E.1

THE MINIMUM GRID SIZE EMPLOYED FOR DETONATION PROBLEMS.

$p \quad [atm]$	$\Delta x \quad [cm]$	
	$H_2 - air$	$C_xH_y - air$
5×10^{-1}	9×10^{-5}	1×10^{-5}
1×10^{0}	6×10^{-5}	6×10^{-6}
2×10^{0}	1×10^{-5}	3×10^{-6}
5×10^{0}	6×10^{-5}	1×10^{-6}
1×10^{1}	3×10^{-6}	6×10^{-7}

It is clearly shown that the predicted ℓ_{finest} is well correlated with the mean free path for all the calculations performed; in all cases ℓ_{finest} is slightly above ℓ_{mfp}, fully consistent with the continuum assumption. So, similar as laminar premixed flames, ℓ_{finest} for CJ detonations can be easily estimated *a priori* using Eq. (3.34).

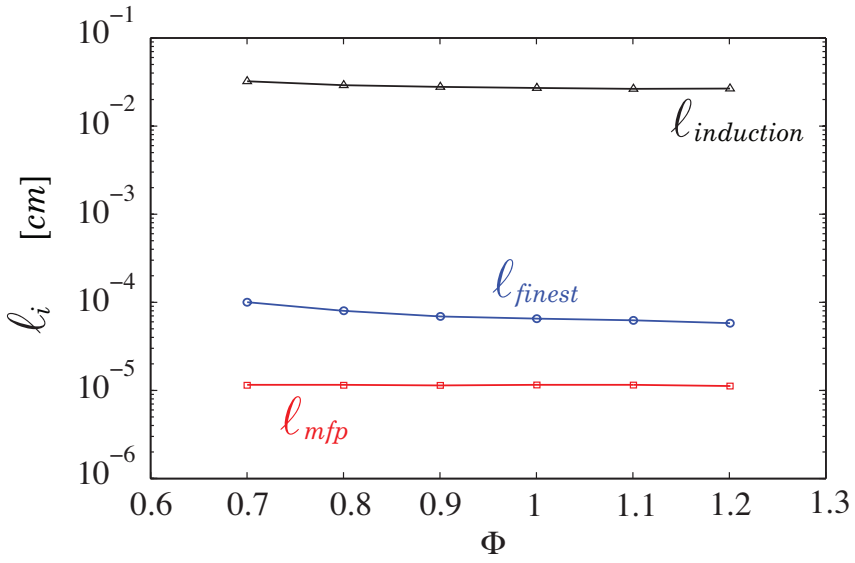

Figure E.1. The induction zone length, the predicted finest length scale, and the mean free path versus the equivalence ratio for a CJ detonation in a hydrogen–air mixture, $T^* = 800\ K$ and $p^* = 1\ atm$.

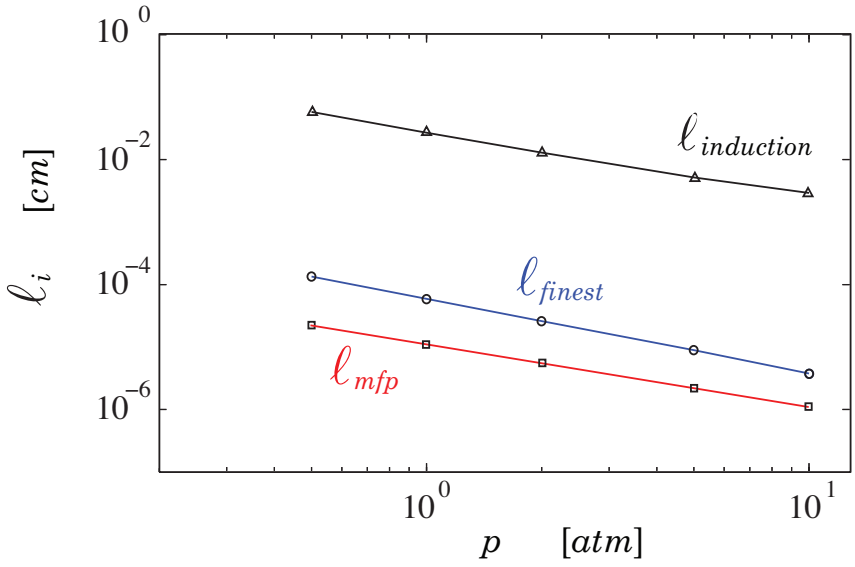

Figure E.2. The induction zone length, the finest length scale, and the mean free path versus pressure for a CJ detonation in a stoichiometric hydrogen–air mixture, $T^* = 800\ K$.

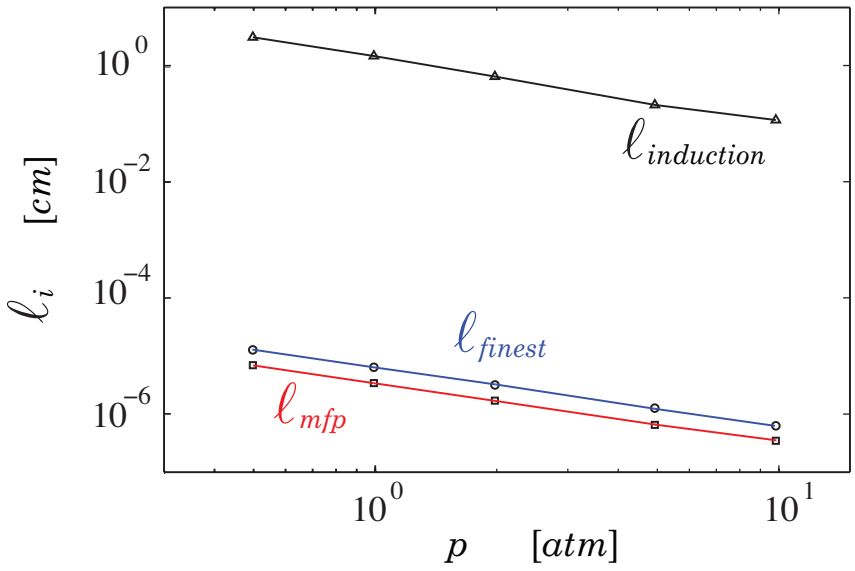

Figure E.3. The induction zone length, the finest length scale, and the mean free path versus pressure for a CJ detonation in a stoichiometric methane–air mixture, $T^* = 298\ K$.

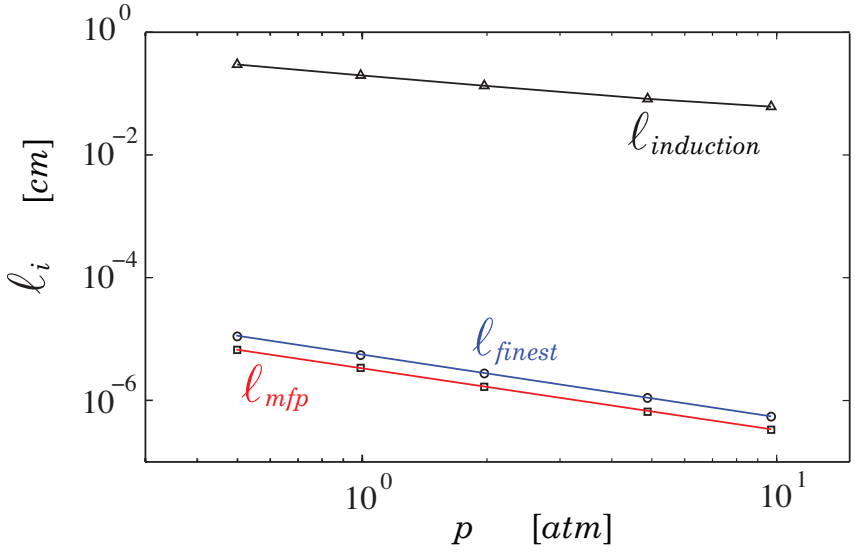

Figure E.4. The induction zone length, the finest length scale, and the mean free path versus pressure for a CJ detonation in a stoichiometric ethane–air mixture, $T^* = 298\ K$.

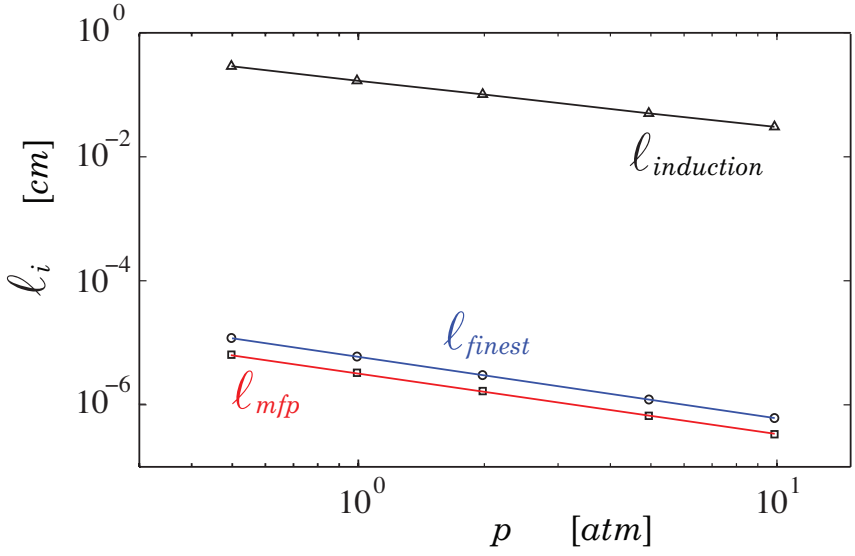

Figure E.5. The induction zone length, the finest length scale, and the mean free path versus pressure for a CJ detonation in a stoichiometric propane–air mixture, $T^* = 298\ K$.

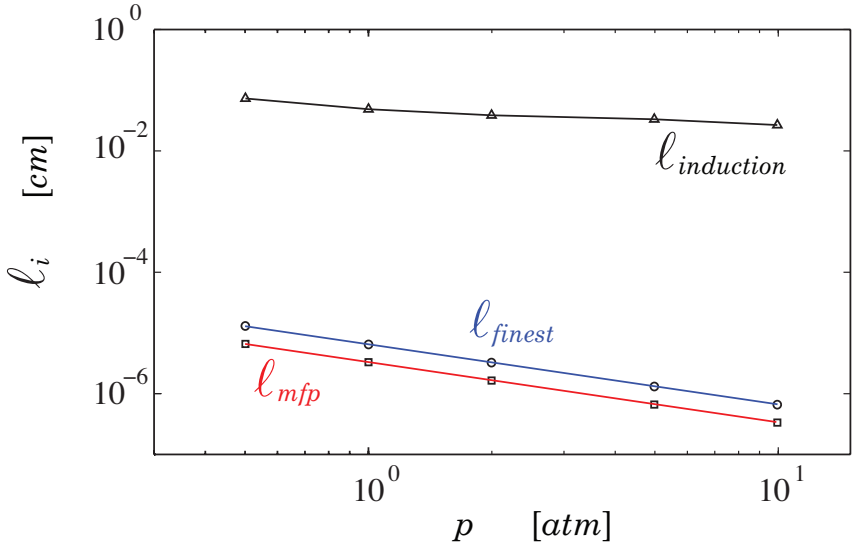

Figure E.6. The induction zone length, the finest length scale, and the mean free path versus pressure for a CJ detonation in a stoichiometric ethylene–air mixture, $T^* = 298\ K$.

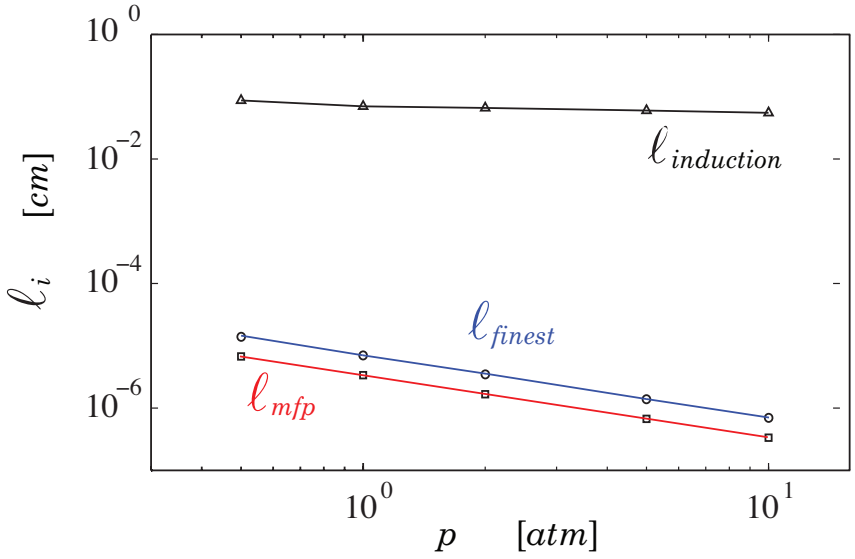

Figure E.7. The induction zone length, the finest length scale, and the mean free path versus pressure for a CJ detonation in a stoichiometric acetylene–air mixture, $T^* = 298\ K$.

APPENDIX F

SCALE ANALYSIS FOR OXYGEN DISSOCIATION

Here, the possibility of the existence of a direct connection between the finest length scale predicted by the eigenvalue analysis and that predicted by a simple collision theory estimate is further explored. Such an analysis is analytically tractable for a simple kinetic system in conjunction with a small number of assumptions.

Consider an isothermal dissociation-recombination oxygen system with no diffusion at $T = 5000\ K$. The reaction mechanism for this system is given by

$$O_2 + \mathsf{M} \rightleftharpoons 2O + \mathsf{M}, \tag{F.1}$$

where from Table D.1 the reaction rate coefficients are $\beta = 0.5$, $\mathcal{A} = 1.85 \times 10^{11}\ cm^3/\left(mol\ K^{1/2}\right)$, and $\bar{\mathcal{E}} = 95560.0\ cal/mol$. For this simple problem, the initial conditions are set to $\bar{\rho}^*_{O_2} = \bar{\rho}^*_O = 10^{-3}\ mol/cm^3$, and a constant advection velocity $u = 10\ cm/s$ is considered. Consequently, the species evolution equations are

$$\frac{\partial \bar{\rho}_O}{\partial t} + u\frac{\partial \bar{\rho}_O}{\partial x} = \dot{\omega}_O, \tag{F.2a}$$

$$\frac{\partial \bar{\rho}_{O_2}}{\partial t} + u\frac{\partial \bar{\rho}_{O_2}}{\partial x} = \dot{\omega}_{O_2}. \tag{F.2b}$$

Let us further restrict attention to a steady wave so that all time derivatives are zero. Thus, the system of PDEs (F.2) is reduced to a system of ODEs:

$$u\frac{d\bar{\rho}_O}{dx} = \dot{\omega}_O = 2\mathcal{A}T^\beta \exp\left(\frac{-\bar{\mathcal{E}}}{\bar{\Re}T}\right)\left(\bar{\rho}_{O_2}\left(\bar{\rho}_{O_2}+\bar{\rho}_O\right) - \frac{\bar{\rho}_O^2\left(\bar{\rho}_{O_2}+\bar{\rho}_O\right)}{K^c}\right), \tag{F.3a}$$

$$u\frac{d\bar{\rho}_{O_2}}{dx} = \dot{\omega}_{O_2} = -\mathcal{A}T^\beta \exp\left(\frac{-\bar{\mathcal{E}}}{\bar{\Re}T}\right)\left(\bar{\rho}_{O_2}\left(\bar{\rho}_{O_2}+\bar{\rho}_O\right) - \frac{\bar{\rho}_O^2\left(\bar{\rho}_{O_2}+\bar{\rho}_O\right)}{K^c}\right). \tag{F.3b}$$

By summing two times (F.3b) with (F.3a) and integrating, an algebraic relation representing the conservation of element O is obtained:

$$\bar{\rho}_{O_2} = \bar{\rho}^*_{O_2} + \frac{1}{2}\bar{\rho}^*_O - \frac{1}{2}\bar{\rho}_O. \tag{F.4}$$

The system can then be recast as a single ODE by using (F.4) to eliminate $\bar{\rho}_{O_2}$ in (F.3a) to form,

$$\begin{aligned}\frac{d\bar{\rho}_O}{dx} &= f\left(\bar{\rho}_O\right)\\ &= \frac{2\mathcal{A}T^\beta \exp\left(\frac{-\bar{\mathcal{E}}}{\bar{\Re}T}\right)}{u}\left(\bar{\rho}^*_{O_2}+\frac{1}{2}\bar{\rho}^*_O+\frac{1}{2}\bar{\rho}_O\right)\left(\bar{\rho}^*_{O_2}+\frac{1}{2}\bar{\rho}^*_O-\frac{1}{2}\bar{\rho}_O-\frac{\bar{\rho}_O^2}{K^c}\right).\end{aligned} \tag{F.5}$$

The equilibrium point is found by setting the right hand side of (F.5) equal to zero, which yields

$$\bar{\rho}^e_O = \frac{\sqrt{K^c\left(16\bar{\rho}^*_{O_2}+8\bar{\rho}^*_O+K^c\right)}-K^c}{4}. \tag{F.6}$$

To determine the length scale ℓ_{finest} over which this particular system evolves, standard eigenvalue analysis is applied to Eq. (F.5). The eigenvalue for this system is the derivative of the right hand side of Eq. (F.5), $df/d\bar{\rho}_O$, and ℓ_{finest} is given

by the reciprocal of this eigenvalue, see Eq. (3.30). For this particular system,

$$\ell_{finest} = \frac{\mathcal{C}}{\mathcal{A}}, \tag{F.7a}$$

where

$$\mathcal{C} \equiv \frac{u\ T^{-\beta}\ \exp\left(\frac{\bar{E}}{\Re T}\right) K^c}{\bar{\rho}_O \left(4\bar{\rho}^*_{O_2} + 2\bar{\rho}^*_O + K^c + 3\bar{\rho}_O\right)} \tag{F.7b}$$

and at the equilibrium point,

$$\ell_{finest} = \frac{-16\ u\ T^{-\beta}\ \exp\left(\frac{\bar{\mathcal{E}}}{\Re T}\right) \sqrt{K^c} \left(\sqrt{K^c} - \sqrt{16\bar{\rho}^*_{O_2} + 8\bar{\rho}^*_O + K^c}\ \right)^{-1}}{\mathcal{A}\left(16\bar{\rho}^*_{O_2} + 8\bar{\rho}^*_O + K^c + \sqrt{9\ K^c \left(16\bar{\rho}^*_{O_2} + 8\bar{\rho}^*_O + K^c\right)}\ \right)} \tag{F.8}$$

Now, the collision frequency factor $\mathcal{A}$ can be related to molecular collision parameters. A simple relation is given by [140] in p. 223, which can be easily reduced to the following form

$$\mathcal{A} \approx 2\mathcal{N}d^2\sqrt{\frac{2\pi\bar{\Re}}{\bar{m}}} \tag{F.9a}$$

where [140]'s P and s have been approximated as unity, following the same assumption made by [103]. As a result, $\mathcal{A}$ can be related directly to ℓ_{mfp} by substituting (3.34) into (F.9a),

$$\mathcal{A} \approx \frac{2}{\rho\ell_{mfp}}\sqrt{\frac{\bar{\Re}\bar{m}}{\pi}} \tag{F.9b}$$

and ℓ_{finest} can be related to ℓ_{mfp} by substituting (F.9b) into (F.7a), which yields

$$\ell_{finest} \approx \ell_{mfp}\ \left(\frac{\rho\mathcal{C}}{2}\sqrt{\frac{\pi}{\bar{\Re}\bar{m}}}\ \right) \tag{F.10}$$

where it is found by substitution of numerical parameters for oxygen dissociation

that $\frac{\rho^{\mathcal{C}}}{2}\sqrt{\frac{\pi}{\Re\bar{m}}} \sim \mathcal{O}(1)$, with a maximum value of approximately 4.82114. This simple analysis, which is not dependent on any discrete numerical method, provides a proof of a direct connection between ℓ_{finest} and ℓ_{mfp} for this simple example. We believe it is reasonable to speculate that this result extends to systems with more complex kinetics, based on our earlier numerical analysis.

The spatial distribution of this system's species concentrations is shown in Fig. F.1(a). This fully resolved structure, consistent with our previous methodology, has been calculated by integrating Eq. (F.5) and employing Eq. (F.4). In addition, the length scale over which the system evolves, found from Eq. (F.7a), is shown in Fig. F.1(b). It is clearly seen that ℓ_{finest} is of the same order of magnitude, albeit slightly larger, as ℓ_{mfp} through the entire domain. Thus, ℓ_{mfp} can be considered as a lower bound for ℓ_{finest}, although they are calculated independently.

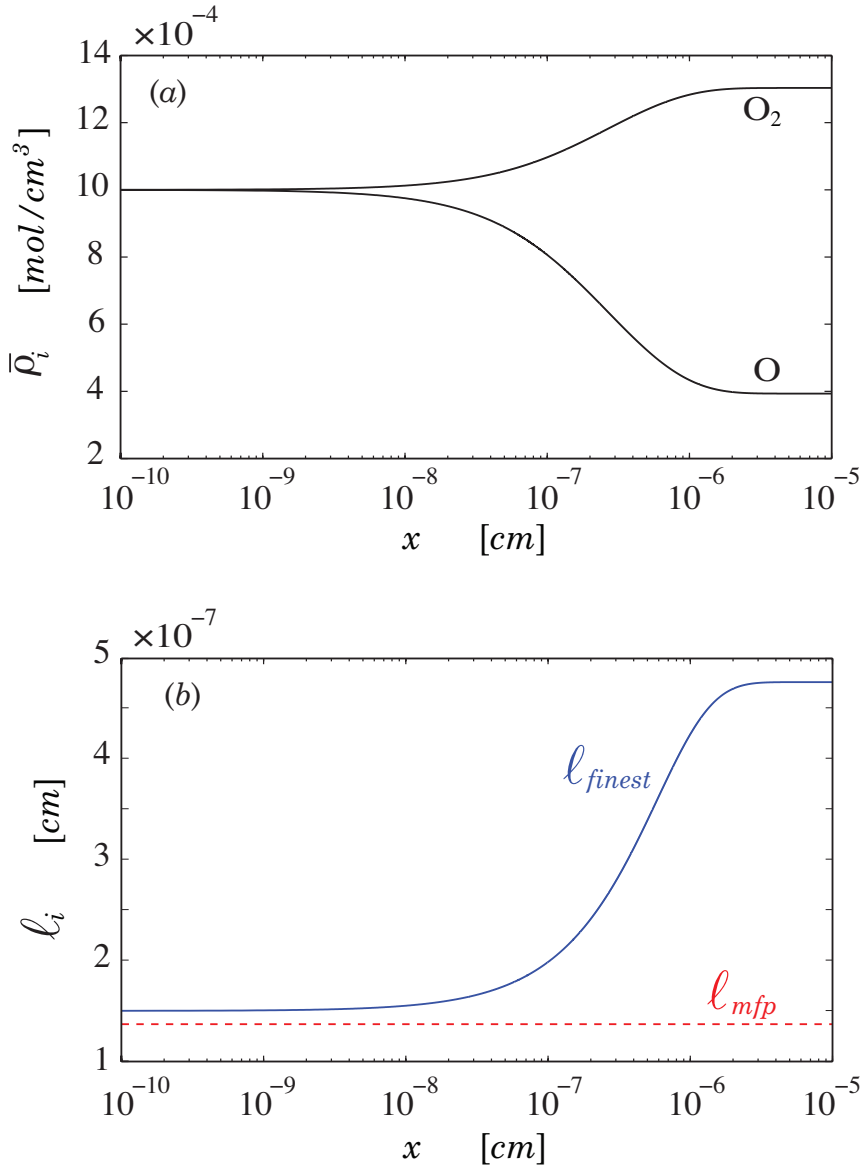

Figure F.1. Isothermal oxygen dissociation at $T = 5000\ K$, (a) species concentration versus distance, (b) finest length scale obtained analytically and mean free path versus distance.

APPENDIX G

FINE SCALE ANALYSIS OF LAMINAR PREMIXED OZONE FLAME

Here, the ozone decomposition in a one-dimensional unsteady laminar premixed flame, which is governed by Eqs. (2.20), is considered. The employed kinetic mechanism is consists of $J = 3$ reversible reactions involving $N = 3$ species; an irreversible version of the employed kinetic model has been widely used in the literature [72, 91, 116], see Table D.5.

G.1 Time scale spectrum

For the unsteady spatially homogeneous version, the considered system is adiabatic, isobaric, and initially at $T^* = 1200\ K$ with an initial mass fraction composition of $Y_O = 0, Y_{O_2} = 2/3$, and $Y_{O_3} = 1/3$, at $p = 0.821\ atm$. Using the methodology described in Sec. 3.2, the time evolution of species mass fractions and the time scale spectrum over which the unsteady spatially homogeneous reactive system evolves are determined, see Figs. G.1–G.2.

In Fig. G.1, a power law growth of the O species is clearly noted for $t < 10^{-8}\ s$. This growth modulates at $t \sim 2 \times 10^{-8}\ s$, which indicates that significant dissociation reactions are induced. At $t = 5 \times 10^{-7}\ s$, the species undergo significant change that indicates a vigorous reaction has commenced. Just past $t = 1 \times 10^{-6}\ s$ the system relaxes to a metastable state for two decades. Finally, at $t = 1 \times 10^{-4}\ s$,

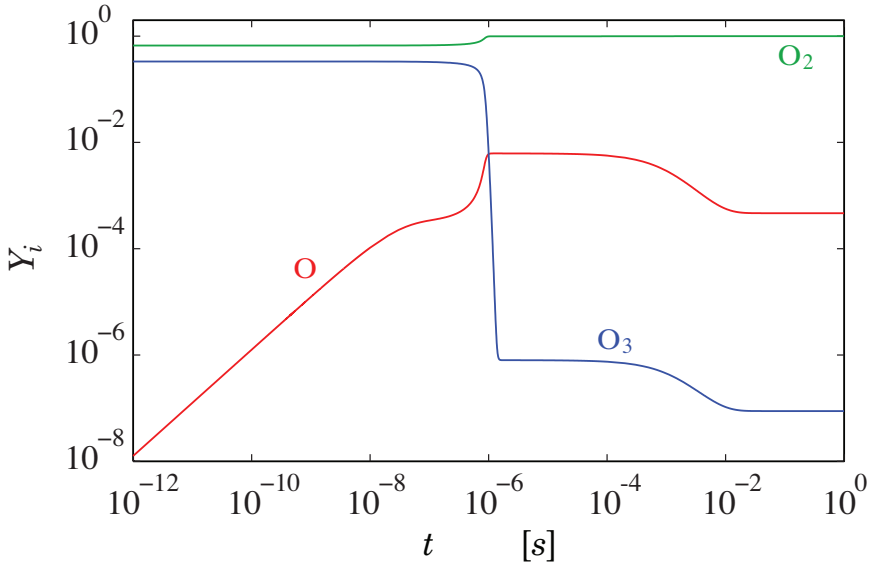

Figure G.1. Time evolution of species mass fractions for the ozone decomposition reactive system, $T^* = 1200\ K$, $p = 0.821\ atm$.

recombination of O and dissociation of O_3 commences forming more of the predominant product O_2 before the system relaxes to equilibrium near $t = 10^{-2}\ s$.

In Fig. G.2, two time scales are seen in the spectrum. Because our reaction mechanism has $N = 3$ species with $L = 1$ elements being conserved, we find $N - L = 2$ independent modes. The multiscale nature of this problem is clearly seen. Initially, the fast time scale and the slow time scale are $2.43 \times 10^{-8}\ s$ and $6.17 \times 10^{-7}\ s$, respectively. The fast time scale correlates well with the time at which the first significant reaction commences. Near equilibrium the slowest time scale is $4.16 \times 10^{-3}\ s$, and the fastest time scale is $5.42 \times 10^{-8}\ s$, giving rise to $\mathcal{S}_t \sim \mathcal{O}(10^5)$.

In Table G.1, values of various properties at the initial state and the equilibrium state are listed.

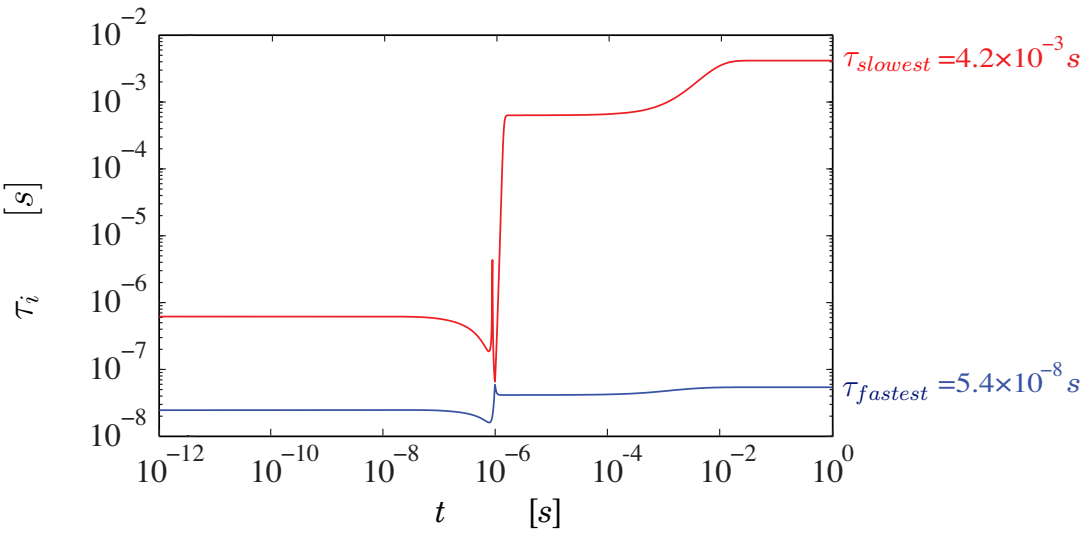

Figure G.2. Time scales over which the ozone decomposition reactive system evolves, $T^* = 1200\ K$, $p = 0.821\ atm$.

TABLE G.1

THERMOCHEMICAL AND DYNAMIC PROPERTIES FOR THE OZONE DECOMPOSITION REACTIVE SYSTEM.

Property	Initial state	Equilibrium
$p \quad [dyne/cm^2]$	8.31878×10^5	8.31878×10^5
$T \quad [K]$	1.20000×10^3	2.06145×10^3
$\rho \quad [g/cm^3]$	3.00161×10^{-4}	1.55242×10^{-4}
Y_O	0.00000×10^0	4.66188×10^{-4}
Y_{O_2}	6.66667×10^{-1}	9.99534×10^{-1}
Y_{O_3}	3.33333×10^{-1}	8.81467×10^{-8}
$\tau_{fastest} \quad [s]$	2.43865×10^{-8}	5.41894×10^{-8}
$\tau_{slowest} \quad [s]$	6.17324×10^{-7}	4.16430×10^{-3}

G.2 Length scale spectrum

For the one-dimensional steady planar flame, the methodology presented in Sec. 3.3 is employed to calculate the spatial distribution of the dependent variables, and to determine the system's length scales.

Here, an adiabatic steady one-dimensional laminar premixed flame freely propagating in a $O - O_2 - O_3$ mixture at $p = 0.821\ atm$ is considered. The unburned mixture's mass fractions are $Y_O = 0, Y_{O_2} = 2/3$, and $Y_{O_3} = 1/3$, temperature is $T_u = 300\ K$, and the specified temperature is assigned at $x_f = 2.30\ cm$ as $T_f = 400\ K$. These working conditions, $T_u, p, \boldsymbol{Y}$, are similar to that of [72, 91]. However, the multicomponent transport model is employed in this work, while in Refs. [72, 91] the calculations have been performed using constant transport coefficients and Lewis number $Le = k/(\rho c_p D)$.

Using a grid that has been adaptively refined to control the error and capture regions of steep gradient, a fully resolved steady species profile is obtained and presented in Fig. G.3. Note that the cold boundary temperature here is lower than the initial condition temperature of the unsteady spatially homogeneous ozone mixture in Sec. G.1; we were unable to obtain a laminar premixed flame in an ozone mixture at $T_u = 1200\ K$.

The local length scales ℓ_i are predicted throughout the domain, Fig. G.4. The multiscale nature of the problem and the length scales over which the species evolve are shown. Since there are $2N - L = 5$ independent variables, there are $2N - L = 5$ length scales in the spectrum. The length scale analysis reveals that the fine length scale and the coarse scale for this system vary from $1.38 \times 10^{8}\ cm$ and $1.32 \times 10^{-3}\ cm$ in the preheat zone to $8.69 \times 10^{-1}\ cm$ and $1.12 \times 10^{-8}\ cm$ in the hot far-field region, respectively. Thus, the spatial stiffness in the hot region

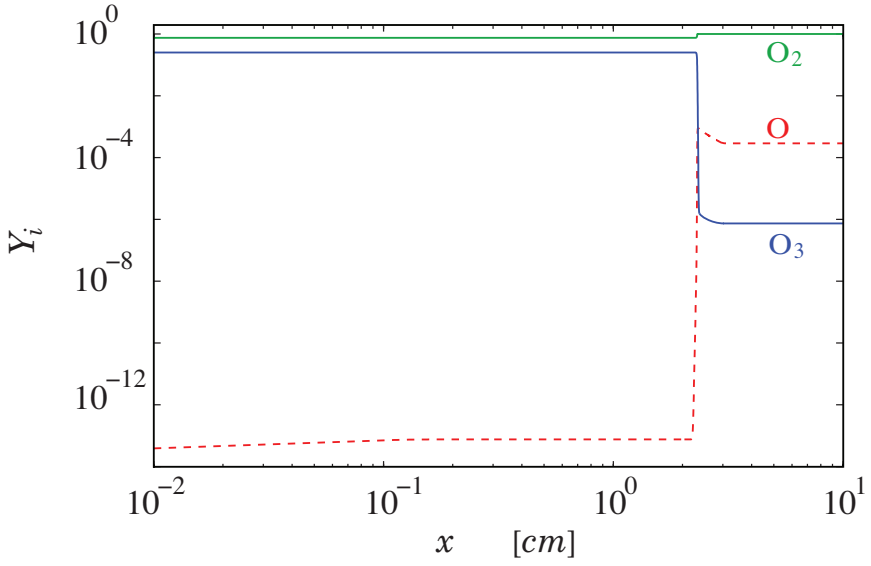

Figure G.3. Species mass fraction versus distance for the steady laminar premixed ozone flame, $T_u = 300\ K$, $p = 0.821\ atm$.

is $\mathcal{S}_x \sim \mathcal{O}(10^8)$.

The important finest length scale is $\ell_{finest} = 1.12{\times}10^{-8}\ cm$, which occurs at the system's chemical equilibrium. This scale is close in magnitude to the analogous finest length scale in an inviscid CJ detonation in a comparable mixture [182], $\ell_{finest} = 6.4 \times 10^{-8}\ cm$.

Now, to estimate the mixture ℓ_{mfp}, Eq. (3.34) is employed. Here, similar to Sec. 3.3.5.4, the molecular cross-section diameter is adopted from Ref. [140], $d = 3.70 \times 10^{-8}\ cm$. Although this estimate of d is for air, it is close in magnitude to the mixture average collision diameter $d_{mix} = 3.43600 \times 10^{-8}\ cm$, which can be calculated using Eq. (3.35). Here, a problem can be easily noted; the predicted ℓ_{finest} is smaller than the mixture molecular cross-section diameter and the average collision diameter. Now, using Eq. (3.34), it reveals that $\ell_{mfp} = 3.40947{\times}10^{-5}\ cm$, which is three orders of magnitudes larger than the predicted ℓ_{finest} for the laminar

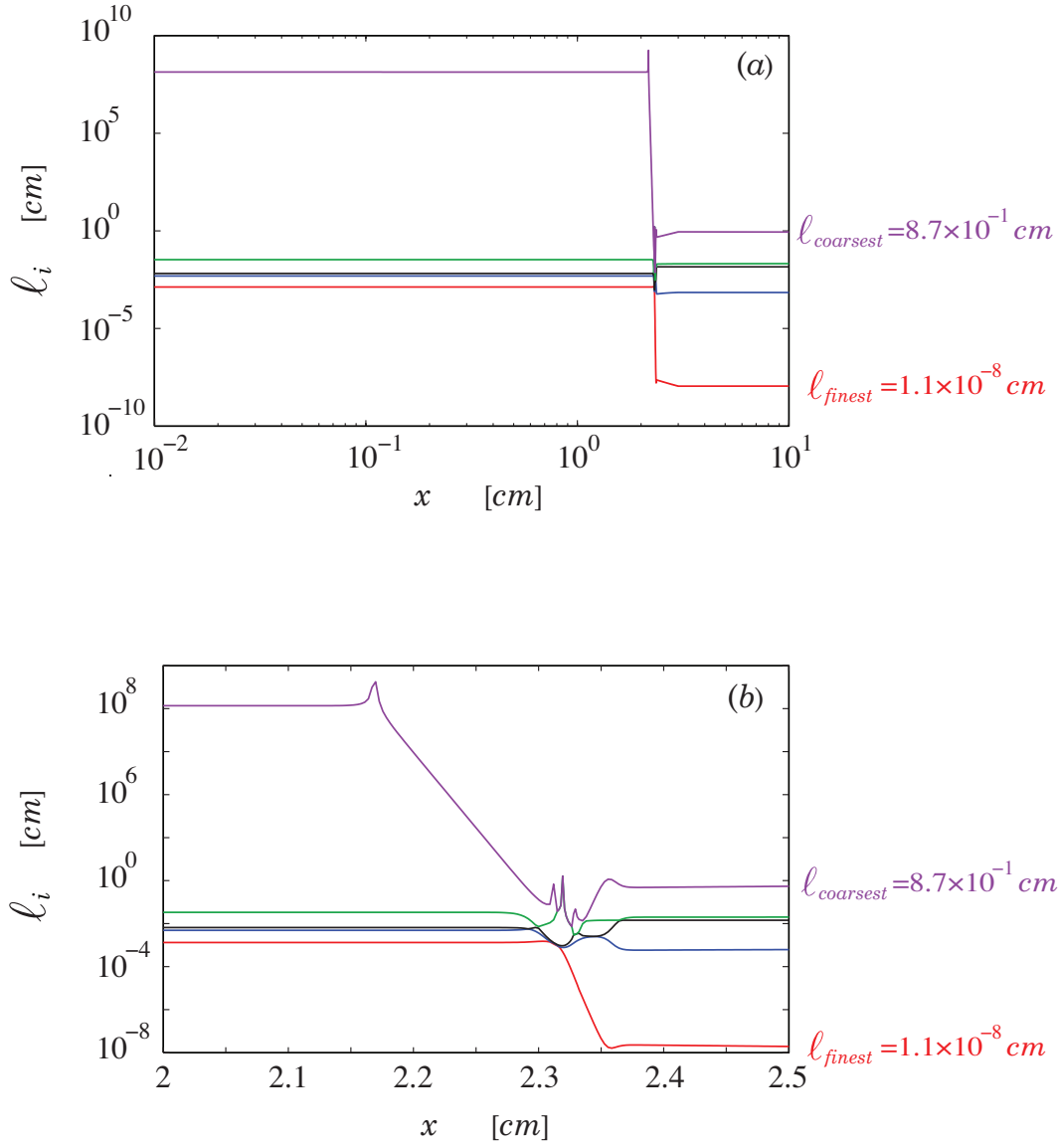

Figure G.4. Length scales versus distance for the steady laminar premixed ozone dissociation flame, $T_u = 300\ K$, $p = 0.821\ atm$. Figure (a) is the full reaction zone, and (b) is a blow-up near the ignition point $x \approx 2.3\ cm$.

TABLE G.2

THERMOCHEMICAL AND DYNAMIC PROPERTIES FOR THE ONE-DIMENSIONAL LAMINAR PREMIXED OZONE FLAME.

Property	Cold boundary	Hot boundary
$p \quad [dyne/cm^2]$	8.31878×10^5	8.31878×10^5
$T \quad [K]$	3.00000×10^2	1.24963×10^3
$u \quad [cm/s]$	4.53500×10^1	2.12546×10^2
$\rho \quad [g/cm^3]$	1.20065×10^{-3}	2.56177×10^{-4}
Y_O	1.75055×10^{-14}	1.43724×10^{-4}
Y_{O_2}	6.66667×10^{-1}	9.99855×10^{-1}
Y_{O_3}	3.33333×10^{-1}	1.10602×10^{-6}
$\ell_{coarsest} \quad [cm]$	1.37602×10^8	8.68965×10^{-1}
$\ell_{finest} \quad [cm]$	1.32227×10^{-3}	1.11729×10^{-8}

premixed ozone decomposition flame! Such a result implies that there is a contradiction with the continuum model. Further investigation is needed to elucidate this inconsistency.

A precise list of several properties' values at the cold boundary and at the hot boundary is given in Table G.2.

G.3 Spatially discretized spatio-temporal spectrum

Following the procedure presented in Sec. 3.4, the time scale spectrum, for the system resulting from perturbing the chemical equilibrium state of the spatially

homogeneous ozone decomposition reactive system, is presented in Fig. G.5, where the modified wavelength is defined by Eq. (3.39). Here, the unperturbed state is identical to the equilibrium state of Sec. G.1.

Figure G.5 is generated from combining four small windows of the system's Fourier modes. Each window contains about three decades of wavelength and has been calculated for a specific spatial length, $\mathtt{L} = \{10^2, 10^0, 10^{-3}, 10^{-6}\}\ cm$. Also, a plot of the system's times scales associated with the fundamental modes versus $2\mathtt{L}/\pi$ is given in Fig. G.6.

Figures G.5–G.6 clearly show that the time scales associated with long wavelength modes match with the chemical time scales shown in Fig G.2; they are dictated by reaction. However, at $\widehat{\Lambda}/2\pi = 2\mathtt{L}/\pi \sim 10^{-1}\ cm$ the diffusion effect starts to appear through the slowest time scales associated with moderate wavelength modes. Also, the balance between reaction and diffusion is clear: short wavelength modes, $\widehat{\Lambda}/2\pi = 2\mathtt{L}/\pi < 10^{-7}\ cm$, are dominated by diffusion, and large wavelength modes, $\widehat{\Lambda}/2\pi = 2\mathtt{L}/\pi > 10^{0}\ cm$, are dominated by reaction. Furthermore, the effect of adopting non-uniform diffusion coefficients, the multicomponent diffusion coefficients $\mathfrak{D}_{ij}$ in Eqs. (2.21a), is noted in the diffusion dominated region, $\Lambda/2\pi = 2\mathtt{L}/\pi \leq 10^{-7}\ cm$. Similar to the hydrogen–air mixture, one would expect $\tau \sim \mathtt{L}^2/\mathfrak{D}_{ij}$, so that the slope of each should be the same, but the intercept is different for each $\mathfrak{D}_{ij}$. It is obvious that in the diffusion-dominated region, there is a two decade drop in τ for every one decade drop in $\mathtt{L}$, consistent with our prediction.

It is clear from Figs. G.5–G.6 that the branch associated with the slowest chemical time scales starts to become influenced by diffusion before branches associated with the faster chemical time scales; the turning point for the fastest chemical time

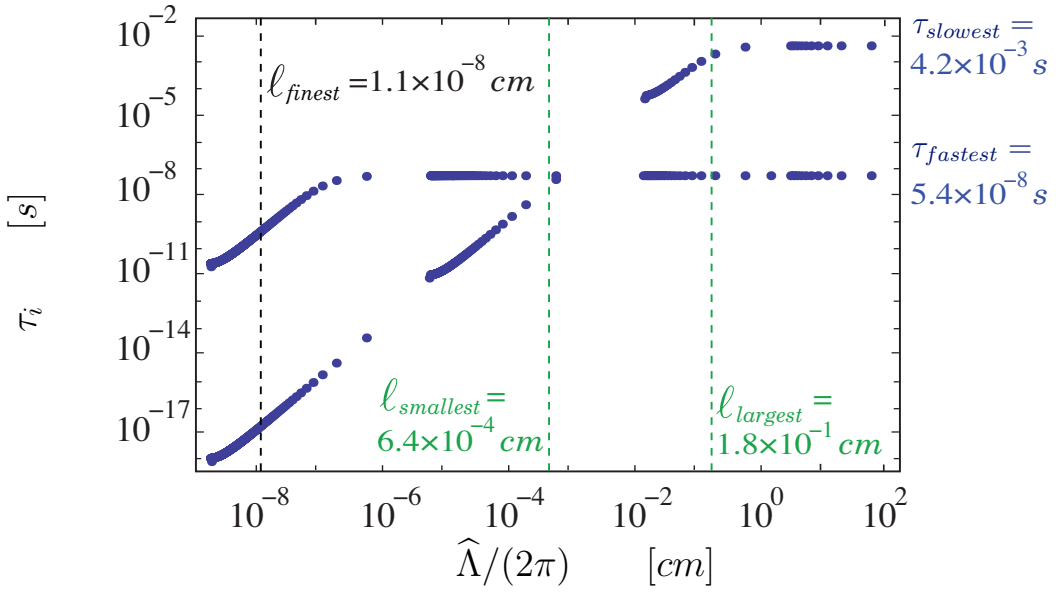

Figure G.5. Time scale spectrum versus the modified wavelength for the ozone reaction-advection-diffusion system.

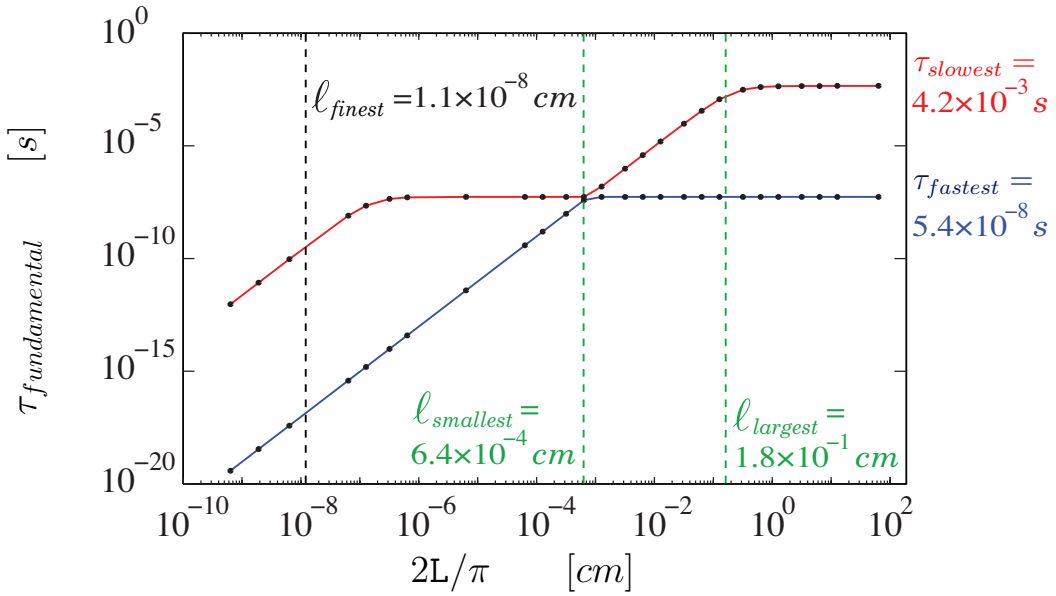

Figure G.6. Time scales associated with the fundamental modes for the ozone reaction-advection-diffusion system versus the length 2L/π.

scale branch is $2\mathrm{L}/\pi \sim 10^{-3}\ cm$ and for the slowest chemical time scale branch is $2\mathrm{L}/\pi \sim 10^{-1}\ cm$. Furthermore, another turning point for the fastest time scale is located at $\Lambda/2\pi = 2\mathrm{L}/\pi = 10^{-7}\ cm$. This turning point represents the system's shortest wavelength where a balance between reaction and diffusion exist; for a resolved structure this length length scale need to be captured.

From Fig. G.6, it is clear that the first two turning points are predicted well by a formula similar to Eq. (3.40),

$$\ell_{smallest} = \sqrt{D_{mix}\tau_{fastest}} = 6.38 \times 10^{-4}\ cm, \tag{G.1a}$$

$$\ell_{largest} = \sqrt{D_{mix}\tau_{slowest}} = 1.77 \times 10^{-1}\ cm. \tag{G.1b}$$

Here, the mixture average diffusion coefficient, given by Eq. (3.41), is $D_{mix} \approx 7.5\ cm^2/s$, and the reaction-only fast and slow time scales, from Sec. G.1, are $\tau_{fastest} = 5.42 \times 10^{-8}\ s$ and $\tau_{slowest} = 4.16 \times 10^{-3}\ s$, respectively. Moreover, the finest length scale calculated, in Sec. G.2, by spatial eigenvalue analysis under-predicts the second turning point of the fastest reaction-advection-diffusion time scale by one order of magnitude.

Reasons for the discrepancies are unclear, but could be related to the difference in temperatures; the unperturbed state in this section is at $T^e = 2061.45\ K$, while ℓ_{finest} is calculated in Sec. G.2 at $T^e = 1249.63\ K$. However, the location of the turning point for the slowest time scale, where the reaction-diffusion balance exists, is higher than our prediction in Sec. G.2 for the ozone decomposition flame. This may be due to the full laminar flame being composed of Fourier modes of smaller wavelengths which have more demanding time constants.

APPENDIX H

CONSTRUCTION OF PROJECTION MATRICES

Here, two different ways to construct the $\mathfrak{D}$ matrix will be provided. As it has been mentioned in Sec. 4.1, the $\mathfrak{D}$ matrix is not unique.

H.1 Method–I

First, a row-echelon form of the ν_{ij} matrix is obtained by performing a series of row operations on Eq. (4.2a). The number of non-zero rows in the row-echelon form of ν_{ij} is the rank of ν_{ij} and $\mathcal{D}_{ik}$, since ν_{ij} and $\mathcal{D}_{ik}$ span the same column space. Then, we use elementary row operations to identify the $N \times N$ lower triangular matrix $\mathbf{L}$ which, when matrix multiplied with Eq. (4.2a) yields $\mathbf{L} \cdot d\mathbf{n}/dt = V\mathbf{U} \cdot \mathbf{r}$, where $\mathbf{U} = \mathbf{L} \cdot \boldsymbol{\nu}$ is an upper triangular matrix of dimension $N \times R$.

This non-unique matrix describes the system's linear constraints, which are obtained by integrating the $N - R$ homogeneous ODEs that are obtained as a result of reduction to the row-echelon form. Finally, the $\mathfrak{D}$ matrix is constructed such that the first R row vectors of it are set in the reduced row-echelon form, while the other row vectors are obtained using $\mathbf{L}$ to reflect the system's constraints.

H.2 Method–II

First, the **LUP**-decomposition of the $\boldsymbol{\nu}^T$ matrix is obtained, [126] such that

$$\mathbf{P} \cdot \boldsymbol{\nu}^T = \mathbf{L} \cdot \mathbf{U}, \tag{H.1a}$$

where the lower triangular matrix $\mathbf{L}$ and the permutation matrix $\mathbf{P}$ are square matrices of dimension $N \times N$, but the upper triangular matrix $\mathbf{U}$ is non-square and has the same dimension and rank as $\boldsymbol{\nu}$; $N \times R$. Consequently, $\boldsymbol{\nu}$ is decomposed as the product of three matrices,

$$\begin{aligned} \left(\mathbf{P} \cdot \boldsymbol{\nu}^T\right)^T &= \left(\mathbf{L} \cdot \mathbf{U}\right)^T, && \text{(H.1b)} \\ \boldsymbol{\nu} \cdot \mathbf{P}^T &= \mathbf{U}^T \cdot \mathbf{L}^T, && \text{(H.1c)} \\ \boldsymbol{\nu} &= \mathbf{U}^T \cdot \mathbf{L}^T \cdot \left(\mathbf{P}^T\right)^{-1}. && \text{(H.1d)} \end{aligned}$$

Now, all the independent row vectors of $\boldsymbol{\nu}$ are the non-zero column vectors of $\mathbf{U}^T$; the $\mathfrak{D}$ is the first R column vectors of $\mathbf{U}^T$,

$$\mathbf{U}^T = \left[\mathfrak{D} \quad \vdots \quad \mathbf{0}\right]. \tag{H.2}$$

Although method II is simpler than method I in constructing the $\mathfrak{D}$ matrix, the resulting R dependent variables using method II are linear combinations of the original N dependent variables. However, in the case of using method I to constructing the $\mathfrak{D}$ matrix, the resulting R dependent variables are a subset of the original N dependent variables. Thus, in this work, method I will be employed to construct the $\mathfrak{D}$ matrix. A detailed example is given in Sec. 4.3.1 to illustrate the construction of $\mathfrak{D}$ for a realistic reactive system.

APPENDIX I

ELEMENTS OF ALGEBRAIC GEOMETRY

I.1 Homotopy continuation

Homotopy continuation is a mathematical approach for solving a system of equations by tracking the solutions of another systems of equations. In other words, define a system of equations $\mathbf{g}$ whose equilibria can be easily calculated. Then, track those equilibria as one deforms $\mathbf{g}$ into the system $\mathbf{f}$ that one wants to solve [183].

Basically, a homotopy is a mapping given by the following relation,

$$\mathcal{H}(\mathbf{z};\mathtt{t}) = (1-\mathtt{t})\mathbf{f}(\mathbf{z}) + \mathtt{t}\mathbf{g}, \quad \mathbf{z} \in \mathbb{R}^R, \quad \{\mathbf{f},\mathbf{g}\} : \mathbb{R}^R \to \mathbb{R}^R, \quad 0 \leq \mathtt{t} \leq 1, \quad \text{(I.1)}$$

where $\mathtt{t}$ is a parameter. Start with $\mathtt{t} = 1$ and find the equilibria of $\mathcal{H}_1$ that satisfies $\mathcal{H} = 0$. Then, decrease $\mathtt{t}$ by a small step size and find the new $\mathcal{H}_{\Delta\mathtt{t}}$ that satisfies $\mathcal{H} = 0$. As $\mathtt{t}$ runs from 1 to 0, the homotopy mapping $\mathcal{H}$ ends at $\mathbf{f}(\mathbf{z})$, and the equilibria of $\mathcal{H}_0$ that satisfies $\mathcal{H} = 0$ are the desired solutions.

In `BERTINI`, the path $\mathbf{z}^e(\mathtt{t})$ is tracked using a predictor/corrector scheme; the Euler prediction with Newton correction. Reference [158] provides a detailed description of using homotopy continuation to describe all solutions to a given polynomial system, see Fig. I.1.

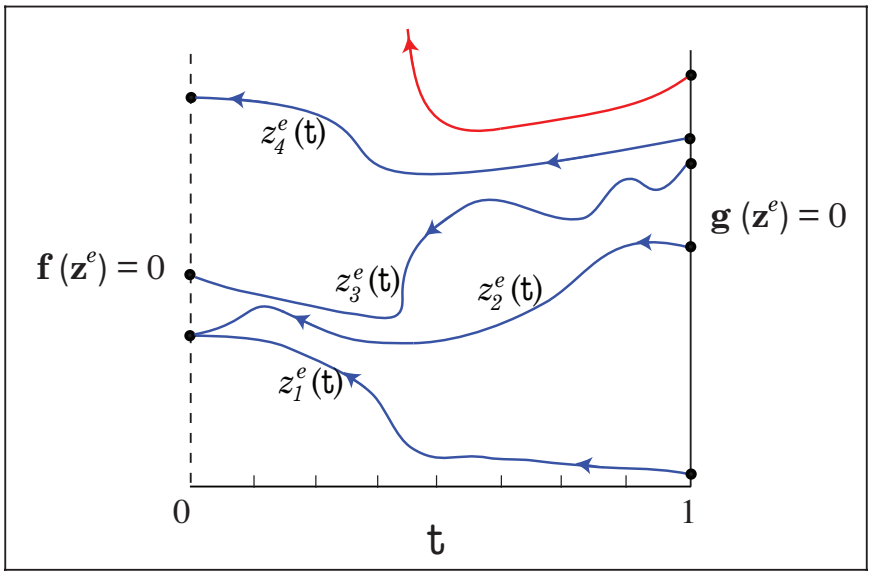

Figure I.1. A sketch illustrating the homotopy continuation.

I.2 Polynomial scaling

Scaling is an essential requirement for the robust behavior of numerical methods to find nonlinear systems' equilibria. The basic idea of polynomial scaling algorithms is to use both a change of variables and equation scaling to rescale the original polynomials into a new system of polynomials that has coefficients centered about unity [163]. In other words, if $f_1(z_1, \ldots, z_R), \ldots, f_R(z_1, \ldots, z_R)$ are polynomials, and the differences between the coefficients of $\mathbf{f}$ are several orders of magnitude, one can computes real constants $a_1, \ldots, a_R$ and $b_1, \ldots, b_R$ to define a new scaled system of polynomials $\Gamma_1(\zeta_1, \ldots, \zeta_R), \ldots, \Gamma_R(\zeta_1, \ldots, \zeta_R)$ by

$$\mathbf{\Gamma}(\boldsymbol{\zeta}) = \mathbf{b} \cdot \mathbf{f}(\mathbf{a} \cdot \mathbf{z}), \quad \{\boldsymbol{\zeta}, \mathbf{z}, \mathbf{a}, \mathbf{b}\} \in \mathbb{R}^R. \tag{I.2}$$

To demonstrate the scaling method, a simple example will be presented. Con-

sider the following polynomials:

$$\begin{aligned} f_1(\mathbf{z}) &= 1 \times 10^{12} z_1^2 - 1 \times 10^{-6} z_2, \\ f_2(\mathbf{z}) &= 1 \times 10^{9} z_2^2 - 1 \times 10^{-3} z_1. \end{aligned}$$

To rescale this system, define $\boldsymbol{\Gamma}$ and $\boldsymbol{\zeta}$ as

$$\begin{aligned} z_1 &= 1 \times 10^{-16} \zeta_1, \\ z_2 &= 1 \times 10^{-14} \zeta_2, \\ \Gamma_1 &= 1 \times 10^{20} f_1, \\ \Gamma_2 &= 1 \times 10^{19} f_2. \end{aligned}$$

By substituting $\boldsymbol{\Gamma}$ and $\boldsymbol{\zeta}$ in the original system of polynomials, $\mathbf{f}(\mathbf{z})$, a new scaled system is obtained. This system is given by

$$\begin{aligned} \Gamma_1 &= \zeta_1^2 - \zeta_2, \\ \Gamma_2 &= \zeta_2^2 - \zeta_1, \end{aligned}$$

which can be solved easily, and numerically it is very stable.

In realistic reactive system, computing the real constants $\mathbf{a}$ and $\mathbf{b}$ to define a new scaled set of polynomials is a major task. In this work, the scaling algorithm `SCLGEN` [163] is used to calculate $\mathbf{a}$ and $\mathbf{b}$. Reference [163] provides a detailed description of the polynomial system algorithm `SCLGEN`.

APPENDIX J

REACTIVE SYSTEM'S EQUILIBRIUM CONDITION

It is clear, from Eqs. (4.2a) and (2.12), that in order for a closed spatially homogenous reactive system to come onto an equilibrium state the following condition has to be satisfy,

$$r_j = 0 \quad \Rightarrow \quad K_j^c = \frac{\prod_{i=1}^{N} \bar{\rho}_i^{\,\nu''_{ij}}}{\prod_{i=1}^{N} \bar{\rho}_i^{\,\nu'_{ij}}} = \prod_{i=1}^{N} \bar{\rho}_i^{\,\nu_{ij}}, \qquad j = 1, \ldots, J. \tag{J.1}$$

This equation implies that at equilibrium all the reaction steps in the mechanism have to come onto a state at which reactant and product molar concentrations are in balance and no further reactions are commence.

Let start from Eq. (2.13b),

$$K_j^c = \left(\frac{p^o}{\bar{\Re} T}\right)^{\sum_{i=1}^{N} \nu_{ij}} \exp\left(-\frac{\sum_{i=1}^{N} \bar{\mu}_i^o \nu_{ij}}{\bar{\Re} T}\right), \quad j = 1, \ldots, J. \qquad ((2.13b))$$

By substituting the definition of $\bar{\mu}_i^o$, from Eq. (2.6a), into Eq. (2.13b), one gets

$$K_j^c = \left(\frac{p^o}{\bar{\Re} T}\right)^{\sum_{i=1}^{N} \nu_{ij}} \exp\left(\sum_{i=1}^{N} \nu_{ij} \ln\left(\frac{p_i}{p^o}\right) - \frac{\sum_{i=1}^{N} \nu_{ij} \bar{\mu}_i}{\bar{\Re} T}\right), \quad j = 1, \ldots, J, \tag{J.2}$$

which can be written, after rearrangement and employing Eq. (2.4), as

$$K_j^c = \left(\frac{p^o}{\bar{\Re}T}\right)^{\sum_{i=1}^N \nu_{ij}} \exp\left(-\frac{\sum_{i=1}^N \nu_{ij}\bar{\mu}_i}{\bar{\Re}T}\right) \exp\left(\sum_{i=1}^N \ln\left(\frac{\bar{\Re}T\bar{\rho}_i}{p^o}\right)^{\nu_{ij}}\right), \quad j = 1, \ldots, J. \tag{J.3}$$

Furthermore, by a standard mathematical manipulations, interchanging the summation and the logarithm in the last term in the right hand side of Eq. (J.3), one gets

$$K_j^c = \left(\frac{p^o}{\bar{\Re}T}\right)^{\sum_{i=1}^N \nu_{ij}} \exp\left(-\frac{\sum_{i=1}^N \nu_{ij}\bar{\mu}_i}{\bar{\Re}T}\right) \exp\left(\ln\prod_{i=1}^N \left(\frac{\bar{\Re}T\bar{\rho}_i}{p^o}\right)^{\nu_{ij}}\right), \quad j = 1, \ldots, J, \tag{J.4}$$

which can be rewritten, after further mathematical manipulations, as

$$K_j^c = \left(\frac{p^o}{\bar{\Re}T}\right)^{\sum_{i=1}^N \nu_{ij}} \exp\left(-\frac{\sum_{i=1}^N \nu_{ij}\bar{\mu}_i}{\bar{\Re}T}\right) \left(\frac{\bar{\Re}T}{p^o}\right)^{\sum_{i=1}^N \nu_{ij}} \prod_{i=1}^N \bar{\rho}_i^{\nu_{ij}}, \quad j = 1, \ldots, J. \tag{J.5}$$

Now, it is clear that the equilibrium constant for the j^{th} reaction is given by

$$K_j^c = \prod_{i=1}^N \bar{\rho}_i^{\nu_{ij}} \exp\left(-\frac{\sum_{i=1}^N \nu_{ij}\bar{\mu}_i}{\bar{\Re}T}\right), \quad j = 1, \ldots, J. \tag{J.6}$$

By comparing Eq. (J.6) and Eq. (J.1), we have

$$\exp\left(-\frac{\sum_{i=1}^N \nu_{ij}\bar{\mu}_i}{\bar{\Re}T}\right) = 1, \tag{J.7}$$

at the system's physical equilibrium point. Thus, the equilibrium condition for a closed spatially homogeneous reactive system is

$$\sum_{i=1}^N \nu_{ij}\bar{\mu}_i = 0. \tag{J.8}$$

APPENDIX K

CONSTRUCTING THE MINIMAL ENTROPY PRODUCTION TRAJECTORIES

Here, additional details on the construction of the MEPT of the following reactive system,

$$\begin{aligned} A + A &\rightleftharpoons B, \qquad \mathsf{k}_1^F = 1, \quad \mathsf{k}_1^B = 10^{-5}, \\ B &\rightleftharpoons C, \qquad \mathsf{k}_2^F = 10^{-2}, \quad \mathsf{k}_2^B = 10^{-5}, \end{aligned}$$

are presented. This system is identical to the second example presented by Lebiedz [41], where k_j^F and k_j^B represent the forward and the backward Arrhenius kinetic rate for the j^{th} reaction, respectively. This mechanism contains $N = 3$ species that undergo $J = 2$ reversible reactions.

First, following Lebiedz [41], we define the entropy production due to irreversibility processes, *i.e.* the irreversibility production rate, within the system for the j^{th} reaction as

$$\sigma_j \equiv \frac{d_i S_j}{dt} = \bar{\Re}\left(r_j^F - r_j^B\right) \ln\left(\frac{r_j^F}{r_j^B}\right), \quad j = 1, 2, \tag{K.1}$$

where r^F and r^B are the reaction rate of the forward and backward reaction,

respectively. Next, a variational problem is set, such that the following functional,

$$\mathscr{F} = \int_0^{\mathsf{T}} \sum_{j=1}^{J} \left(\frac{d_i S}{dt} \right)^2 dt, \tag{K.2}$$

is minimized, under the following constraints,

$$\begin{aligned}
\frac{dz_A}{dt} &= \mathsf{k}_1^B z_B - \mathsf{k}_1^F z_A^2, \\
\frac{dz_B}{dt} &= \mathsf{k}_1^F z_A^2 - z_B \left(\mathsf{k}_1^B + \mathsf{k}_2^F \right) + \mathsf{k}_2^B z_C. \\
\frac{dz_C}{dt} &= \mathsf{k}_2^F z_B - \mathsf{k}_2^B z_C, \\
z_C \left(t = 0 \right) &= constant, \\
\left| z_C \left(\mathsf{T} \right) - z_C^e \right| &\leq \epsilon = 0.1,
\end{aligned}$$

where T is a free parameter that represent the final time of integration.

Using the same argument, described in the original work, that the total mass is conserved; $z_A + z_B + z_C = 1$, the evolution of the reactive system is described by

$$\frac{dz_A}{dt} = 10^{-5} z_B - z_A^2, \tag{K.3a}$$

$$\frac{dz_B}{dt} = z_A^2 + (1 - 1001 z_B - z_A) \times 10^{-5}. \tag{K.3b}$$

Then, to accelerate the MEPT construction process, we adopted two numbers from the original work [41]: the final time $\mathsf{T} = 260$, and the initial concentration $z_C(t = 0) = 0.1$. Thus, the functional subject to minimization become

$$\mathscr{F} = \int_0^{260} \left(\sigma_1^2 + \sigma_2^2 \right) dt. \tag{K.4}$$

Explicitly, the minimization process commences by calculating Eq. (K.4) over a wide range of z_B and z_C values. Then, the loci of the minimum values of $\mathscr{F}$ associated with the adopted initial condition $z_C(0) = 0.1$ is identified. It is found that at $z_C(0) = 0.1$, the minimum value of $\mathscr{F}$ is located at $z_B(0) = 8.53 \times 10^{-1}$. Consequently, the initial value of z_A is 4.73×10^{-2}. The computed MEPT is presented in Fig. K.1, which is identical to Figs. 2 and 4 in Lebiedz [41].

Here, it is noted that there was a typographical error in the original work of Lebiedz [41]. On page 6895, the last line in the second paragraph states that $z_A(0) \equiv$"$c_A(0) = 0.0395$", although Fig. 2 on the same page in the original work is consistent with our results, $z_A(0) \equiv c_A(0) = 0.0473$.

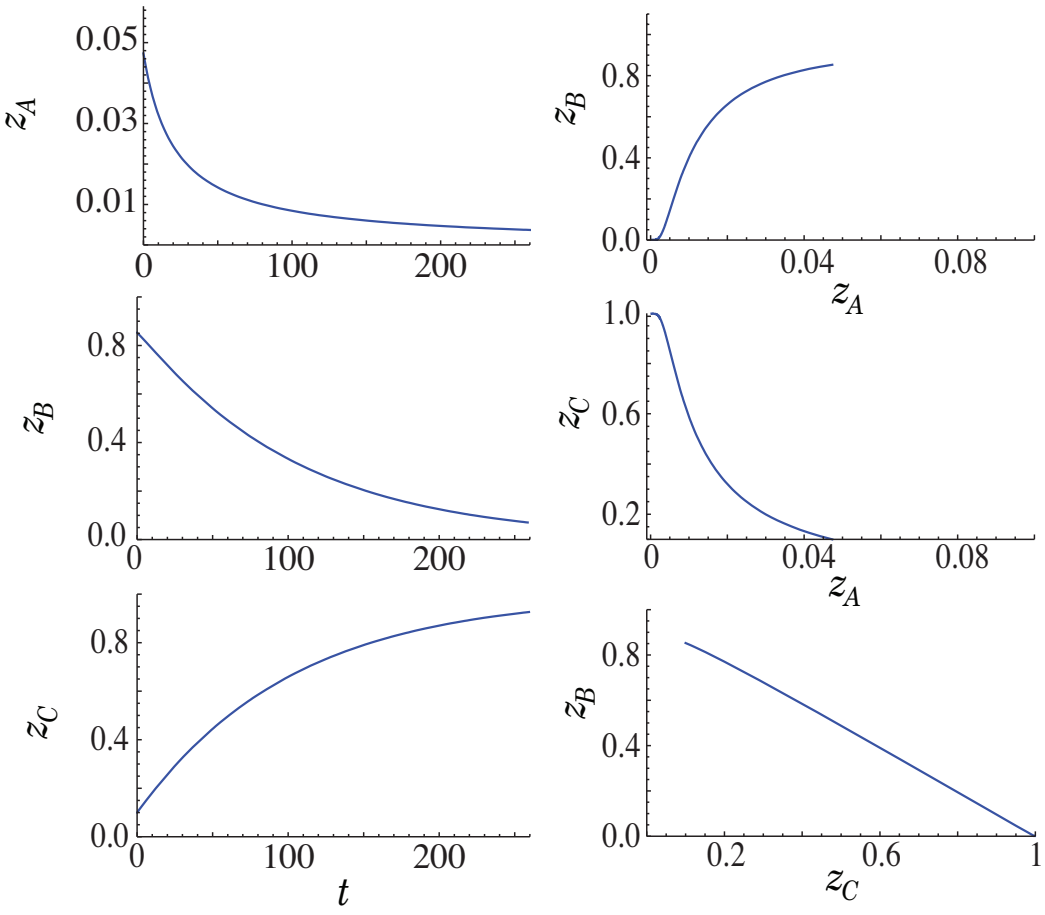

Figure K.1. The MEPT for the system described by Eq. (K.3) with the following initial condition: $z_A(0) = 4.732 \times 10^{-2}$, $z_B(0) = 8.5268 \times 10^{-1}$, and $z_C(0) = 1.0 \times 10^{-1}$.

BIBLIOGRAPHY

[1] J. F. Griffiths. Reduced kinetics models and their application to practical combustion systems. *Progress in Energy and Combustion Science*, 21(1): 25–107, 1995.

[2] R. Hilbert, F. Tap, H. El-Rabii, and D. Thevénin. Impact of detailed chemistry and transport models on turbulent combustion simulations. *Progress in Energy and Combustion Science*, 30(1):61–117, 2004.

[3] A. L. Kuharsky and A. L. Fogelson. Surface-mediated control of blood coagulation: The role of binding site densities and platelet deposition. *Biophysical Journal*, 80(3):1050–1074, 2001.

[4] S. R. Taylor, F. J. Doyle III, and L. R. Petzold. Oscillator model reduction preserving the phase response: Application to the circadian clock. *Biophysical Journal*, 95(5):1658–1673, 2008.

[5] R. E. Zeebe and D. Wolf-Gladrow. *CO_2 in Seawater: Equilibrium, Kinetics, Isotopes*. Elsevier, Amsterdam, Netherlands, 2001.

[6] J. H. Seinfeld and S. N. Pandis. *Atmospheric Chemistry and Physics: From Air Pollution to Climate Change*. John Wiley & Sons, New York, NY, 1998.

[7] J. M. Powers. Review of multiscale modeling of detonation. *Journal of Propulsion and Power*, 22(6):1217–1229, 2006.

[8] W. L. Oberkampf and T. G. Trucano. Verification and validation in computational fluid dynamics. *Progress in Aerospace Science*, 38:209–272, 2002.

[9] P. J. Roache. Quantification of uncertainty in computational fluid dynamics. *Annual Review of Fluid Mechanics*, 29, 1997.

[10] J. Stoer and R. Bulirsch. *Introduction to Numerical Analysis*. Springer-Verlag, Berlin, German, 2004.

[11] R. D. Richtmyer and K. W. Morton. *Difference Methods for Initial-Value Problems*. Krieger, Malabar, FL, 1994.

[12] R. J. LeVeque. *Finite Volume Methods for Hyperbolic Problems*. Cambridge University Press, Cambridge, UK, 2002.

[13] A Iserles. *A First Course in the Numerical Analysis of Differential Equations*. Cambridge University Press, Cambridge, UK, 2002.

[14] C. J. Roy. Review of code and solution verification procedures for computational simulation. *Journal of Computational Physics*, 205(1):131–156, 2005.

[15] A. Ern and V. Giovangigli. Impact of detailed multicomponent transport on planar and counterflow hydrogen/air and methane/air flames. *Combustion Science and Technology*, 149(1-6):157–181, 1999.

[16] J. Charentenay and A. Ern. Multicomponent transport impact on turbulent premixed H_2/ O_2 flames. *Combustion Theory and Modelling*, 6(3):439–462, 2002.

[17] Y. Wang and A. Trouvé. Direct numerical simulation of nonpremixed flame-wall interactions. *Combustion and Flame*, 144(3):461–475, 2006.

[18] H. J. Curran, P. Gaffuri, W. J. Pitz, and C. K. Westbrook. A comprehensive modeling study of iso-octane oxidation. *Combustion and Flame*, 129:253280, 2002.

[19] L. Petzold and W. Zhu. Model reduction for chemical kinetics: An optimization approach. *AIChE Journal*, 45(4):869–886, 1999.

[20] I. P. Androulakis. Kinetic mechanism reduction based on an integer programming approach. *AIChE Journal*, 46(2):361–371, 2000.

[21] T. Lu and C. K. Law. A directed relation graph method for mechanism reduction. In *Proceedings of the Combustion Institute*, volume 30, pages 1333–1341, 2005.

[22] T. Lu and C. K. Law. On the applicability of directed relation graphs to the reduction of reaction mechanisms. *Combustion and Flame*, 146(3):472–483, 2006.

[23] J. Wei and J. C. W. Kuo. A lumping analysis in monomolecular reaction systems; analysis of the exactly lumpable system. *Industrial and Engineering Chemistry Fundamentals*, 8(1):114–123, 1969.

[24] G. Li and H. Rabitz. A general analysis of exact lumping in chemical kinetics. *Chemical Engineering Science*, 44(6):1413–1430, 1989.

[25] G. Li, A. S. Tomlin, H. Rabitz, and J. Toth. A general analysis of approximate nonlinear lumping in chemical kinetics. I. Unconstrained lumping. *Journal of Chemical Physics*, 101(2):1172–1187, 1994.

[26] G. Li, A. S. Tomlin, H. Rabitz, and J. Toth. A general analysis of approximate nonlinear lumping in chemical kinetics. II. Constrained lumping. *Journal of Chemical Physics*, 101(2):1188–1201, 1994.

[27] U. Maas and S. B. Pope. Simplifying chemical kinetics: Intrinsic low-dimensional manifolds in composition space. *Combustion and Flame*, 88 (3-4):239–264, 1992.

[28] V. Bykov, V. Gol'dshtein, and U. Maas. Simple global reduction technique based on decomposition approach. *Combustion Theory and Modelling*, 12 (2):389–405, 2008.

[29] S. H. Lam and D. A. Goussis. Understanding complex chemical kinetics with computational singular perturbation. In *Proceedings of the Combustion Institute*, volume 22, pages 931–941, 1988.

[30] S. H. Lam. Using CSP to understand complex chemical kinetics. *Combustion Science and Technology*, 89(5-6):375–404, 1993.

[31] S. H. Lam and D. A. Goussis. The CSP method for simplifying kinetics. *International Journal of Chemical Kinetecs*, 26(4):461–486, 1994.

[32] M. Valorani and S. Paolucci. The *G-Scheme*: A framework for multi-scale adaptive model reduction. *Journal of Computational Physics*, 228(13):4665–4701, 2009.

[33] J. C. Keck and D. Gillespie. Rate-controlled partial-equilibrium method for treating reacting gas-mixtures. *Combustion and Flame*, 17(2):237–248, 1971.

[34] J. C. Keck. Rate-controlled constrained-equilibrium theory of chemical-reactions in complex-systems. *Progress in Energy and Combustion Science*, 16(2):125–154, 1990.

[35] J. C. Keck and D. Gillespie. Rate-controlled constrained-equilibrium method using constraint potentials. *Combustion Theory and Modelling*, 2(1):81–94, 1998.

[36] Q. Tang and S. B. Pope. A more accurate projection in the rate-controlled constrained-equilibrium method for dimension reduction of combustion chemistry. *Combustion Theory and Modelling*, 8(2):255–279, 2004.

[37] Z. Ren, S. B. Pope, A. Vladimirsky, and J. M. Guckenheimer. The invariant constrained equilibrium edge preimage curve method for the dimension reduction of chemical kinetics. *Journal of Chemical Physics*, 124(11):114111, 2006.

[38] Z. Ren, S. B. Pope, A. Vladimirsky, and J. M. Guckenheimer. Application of the ICE-PIC method for the dimension reduction of chemical kinetics coupled with transport. In *Proceedings of the Combustion Institute*, volume 31, pages 473–481, 2007.

[39] A. N. Gorban and I. V. Karlin. Method of invariant manifold for chemical kinetics. *Chemical Engineering Science*, 58(21):4751–4768, 2003.

[40] A. N. Gorban, I. V. Karlin, and A. Yu. Zinovyev. Constructive methods of invariant manifolds for kinetic problems. *Physics Reports*, 396(4-6):197–403, 2004.

[41] D. Lebiedz. Computing minimal entropy production trajectories: An approach to model reduction in chemical kinetics. *Journal of Chemical Physics*, 120(15):6890, 2004.

[42] V. Reonhardt, M. Winckler, and D. Lebiedz. Approximation of slow attracting manifolds in chemical kinetics by trajectory-based optimization approaches. *Journal of Physical Chemistry A*, 112(8):1712–1718, 2008.

[43] M. R. Roussel and S. J. Fraser. Geometry of the steady-state approximation: Perturbation and acceleration convergence method. *Journal of Chemical Physics*, 93(11):1072–1081, 1990.

[44] M. R. Roussel and S. J. Fraser. On the geometry of transient relaxation. *Journal of Chemical Physics*, 94(11):7106–7113, 1991.

[45] M. J. Davis and R. T. Skodje. Geometric investigation of low-dimensional manifolds in systems approaching equilibrium. *Journal of Chemical Physics*, 111(3):859–874, 1999.

[46] R. T. Skodje and M. J. Davis. Geometric simplification of complex kinetic systems. *Journal of Physical Chemistry A*, 105(45):10356–10365, 2001.

[47] H. G. Kaper and T. J. Kaper. Asymptotic analysis of two reduction methods for systems of chemical reactions. *Physica D*, 165(1-2):66–93, 2002.

[48] A. N. Yannacopoulos, A. S. Tomlin, J. Brindley, J. H. Merkin, and M. J. Pilling. The use of algebraic sets in the approximation of inertial manifolds and lumping in chemical kinetic systems. *Physica D*, 83(4):421–449, 1995.

[49] M. Feinberg. Mathematical aspects of mass action kinetics. In L. Lapidus and N. R. Amundson, editors, *Chemical Reactor Theory: A Review*, chapter 1, pages 1–78. Prentice-Hall, Englewood Cliffs, NJ, 1977.

[50] F. Creta, A. Adrover, S. Cerbelli, M. Valorani, and M. Giona. Slow manifold structure in explosive kinetics. 1. bifurcations of points-at-infinity in prototypical models. *Journal of Physical Chemistry A*, 110(50):13447–13462, 2006.

[51] F. Creta, A. Adrover, S. Cerbelli, M. Valorani, and M. Giona. Slow manifold structure in explosive kinetics. 2. extension to higher dimensional systems. *Journal of Physical Chemistry A*, 110(50):13463–13474, 2006.

[52] M. S. Okino and M. L. Mavrovouniotis. Simplification of mathematical models of chemical reaction systems. *Chemical Reviews*, 98(2):391–408, 1998.

[53] A. M. Khokhlov, E. S. Oran, A. Y. Chtchelkanova, and J. C. Wheeler. Interaction of a shock with a sinusoidally perturbed flame. *Combustion and Flame*, 117(1-2):99–116, 1999.

[54] J. Mantzaras and P. Benz. An asymptotic and numerical investigation of homogeneous ignition in catalytically stabilized channel flow combustion. *Combustion and Flame*, 117(4):455–472, 1999.

[55] J. D. Buckmaster and G. S. S. Ludford. *Theory of Laminar Flames*. Cambridge University Press, Cambridge, UK, 1982.

[56] J. D. Buckmaster. The structure and stability of laminar flames. *Annual Review of Fluid Mechanics*, 25:21–53, 1993.

[57] N. Peters. Reducing mechanisms. In M. D. Smooke, editor, *Reduced Kinetic Mechanisms and Asymptotic Approximations for Methane-Air Flames : A Topical Volume*, chapter 3, pages 48–67. Springer-Verlag, Berlin, Germany, 1991.

[58] R. W. Bilger, M. B. Esler, and S. H. Starner. On reduced mechanisms for methane-air combustion. In M. D. Smooke, editor, *Reduced Kinetic Mechanisms and Asymptotic Approximations for Methane-Air Flames : A Topical Volume*, chapter 5, pages 86–110. Springer-Verlag, Berlin, Germany, 1991.

[59] J. Y. Chen and R. W. Dibble. Application of reduced chemical mechanisms for prediction of turbulent nonpremixed methane jet flames. In M. D. Smooke, editor, *Reduced Kinetic Mechanisms and Asymptotic Approximations for Methane-Air Flames : A Topical Volume*, chapter 9, pages 193–226. Springer-Verlag, Berlin, Germany, 1991.

[60] G. J. Sharpe. Linear stability of planar premixed flames: reactive Navier-Stokes equations with finite activation energy and arbitrary lewis number. *Combustion Theory and Modelling*, 7(1):45–65, 2003.

[61] J. Yuan, Y. Ju, and C. K. Law. Pulsating and hydrodynamic instabilities at large Lewis numbers. *Combustion and Flame*, 144(1-2):386–397, 2006.

[62] T. Turanyi, T. Berces, and S. Vajda. Reaction rate analysis of complex kinetic systems. *International Journal of Chemical Kinetics*, 21(2):83–99, 1989.

[63] B. Rogg. Sensitivity analysis of laminar premixed $ch_4 - air$ flames using full and reduced kinetic mechanisms. In M. D. Smooke, editor, *Reduced Kinetic Mechanisms and Asymptotic Approximations for Methane-Air Flames : A Topical Volume*, chapter 8, pages 159–192. Springer-Verlag, Berlin, Germany, 1991.

[64] A. S. Tomlin, T. Turanyi, and M. J. Pilling. Mathematical tools for the construction, investigation and reduction of combustion mechanisms. In M. J. Pilling, editor, *Low-temperature Combustion and Autoignition*, chapter 4, pages 293–437. Elsevier, Amsterdam, Netherlands, 1997.

[65] W. Liu, C. K. Law, and T. F. Lu. Multiple criticality and staged ignition of methane in the counterflow. *International Journal of Chemical Kinetics*, 41(12):764–776, 2009.

[66] M. A. Kramer, H. Rabitz, J. M. Calo, and R. J. Kee. Sensitivity analysis in chemical kinetics: Recent developments and computational comparisons. *International Journal of Chemical Kinetics*, 16(5):559–578, 1983.

[67] J. Warnatz, U. Maas, and R. W. Dibble. *Combustion: Physical and Chemical Fundamentals, Modeling and Simulation, Experiments, Pollutant Formation*. Springer-Verlag, Berlin, Germany, 1996.

[68] H. K. Chelliah, C. Trevino, and F. A. Williams. Asymptotic analysis of methane-air diffusion flames. In M. D. Smooke, editor, *Reduced Kinetic Mechanisms and Asymptotic Approximations for Methane-Air Flames : A Topical Volume*, chapter 7, pages 1–28. Springer-Verlag, Berlin, Germany, 1991.

[69] J. Y. Chen. A general procedure for constructing reduced reaction-mechanisms with given independent relations. *Combustion Science and Technology*, 57(1):89–94, 1998.

[70] T. Turanyi, A. S. Tomlin, and M. J. Pilling. On the error of the quasi-steady-state approximation. *Journal of Physical Chemistry*, 97(1):163–172, 1993.

[71] A. Zagaris, H. G. Kaper, and T. J. Kaper. Analysis of the computational singular perturbation reduction method for chemical kinetics. *Journal of Nonlinear Science*, 14(1):59–91, 2004.

[72] S. Singh, J. M. Powers, and S. Paolucci. On slow manifolds of chemically reactive systems. *Journal of Chemical Physics*, 117(4):1482–1496, 2002.

[73] Sandeep Singh. *Rational Reduction of Reactive Flow Models and Efficient Computation of their Solutions*. PhD thesis, University of Notre Dame, Notre Dame, IN. 46556, February 2003.

[74] S. R. de Groot and P. Mazur. *Non-Equilibrium Thermodynamics*. Dover Publications, Mineola, NY, 1984.

[75] I. Müller and W. Weiss. *Entropy and Energy: A Universal Competition*. Springer-Verlag, Berlin, Germany, 2005.

[76] A. N. Al-Khateeb, J. M. Powers, S. Paolucci, A. J. Sommese, J. A. Diller, J. D. Hauenstein, and J. D. Mengers. One-dimensional slow invariant manifolds for spatially homogenous reactive systems. *Journal of Chemical Physics*, 131(2):024118, 2009.

[77] U. Maas and S. B. Pope. Implementation of simplified chemical kinetics based on intrinsic low-dimensional manifolds. In *Proceedings of the Combustion Institute*, volume 24, pages 103–112, 1992.

[78] U. Maas and S. B. Pope. Laminar flame calculations using simplified chemical kinetics based on intrinsic low-dimensional manifolds. In *Proceedings of the Combustion Institute*, volume 25, pages 1349–1359, 1994.

[79] S. B. Pope. Gibbs function continuation for the stable computation of chemical equilibrium. *Combustion and Flame*, 139(3):222–226, 2004.

[80] R. L. G. M. Eggels and L. P. H. DeGoey. Comparison of conventional and low-dimensional manifold methods to reduce reaction mechanisms. *Combustion and Flame*, 100(4):559–570, 1995.

[81] H. Bongers, J. A. Van Oijen, and L. P. H. DeGoey. Intrinsic low-dimensional manifold method extended with diffusion. In *Proceedings of the Combustion Institute*, volume 29, pages 1371–1378, 2002.

[82] D. A. Goussis, M. Valorani, F. Creta, and H. N. Najm. Reactive and reactive-diffusive time scales in stiff reaction-diffusion systems. *Progress in Computational Fluid Dynamics*, 5(6):316–326, 2005.

[83] M. Valorani, F. Creta, D. A. Goussis, J. C. Lee, and H. N. Najm. An automatic procedure for the simplification of chemical kinetic mechanisms based on CSP. *Combustion and Flame*, 146(1-2):29–51, 2006.

[84] A. Adrover, F. Creta, M. Giona, and M. Valorani. Stretching-based diagnostics and reduction of chemical kinetic models with diffusion. *Journal of Computational Physics*, on press, 2007.

[85] M. Valorani, H. N. Najm, and D. A. Goussis. CSP analysis of a transient flame-vortex interaction: time scales and manifolds. *Combustion and Flame*, 134(1-2):35–53, 2003.

[86] M. Valorani, D. A. Goussis, F. Creta, and H. N. Najm. Higher order corrections in the approximation of low-dimensional manifolds and the construction of simplified problems with the csp method. *Journal of Computational Physics*, 209(2):754–786, 2005.

[87] S. H. Lam. Reduced chemistry-diffusion coupling. *Combustion Science and Technology*, 179(4):767–786, 2007.

[88] M. J. Davis. Low-dimensional manifolds in reaction-diffusion equations. 1. Fundamental aspects. *Journal of Physicsal Chemistry A*, 110(16):5235–5256, 2006.

[89] M. J. Davis. Low-dimensional manifolds in reaction-diffusion equations. 2. Numerical analysis and method development. *Journal of Physicsal Chemistry A*, 110(16):5257–5272, 2006.

[90] S. Singh, Y. Rastigejev, S. Paolucci, and J. M. Powers. Viscous detonation in H_2–O_2–Ar using intrinsic low-dimensional manifolds and wavelet adaptive multilevel representation. *Combustion Theory and Modelling*, 5(2):163–184, 2001.

[91] S. B. Margolis. Time-dependent solution of a premixed laminar flame. *Journal of Computational Physics*, 27(3):410–427, 1978.

[92] T. Poinsot and D. Veynante. *Theoretical and Numerical Combustion*. R. T. Edwards, Philadelphia, PA, 2001.

[93] Y. C. Chen and J. Y. Chen. Fuel-dilution effect on differential molecular diffusion in laminar hydrogen diffusion flames. *Combustion Theory and Modelling*, 2(4):497–514, 1998.

[94] A. Ern and V. Giovangigli. *Multicomponent Transport Algorithms*. Springer-Verlag, Berlin, Germany, 1994.

[95] T. F. Lu and C. K. Law. Diffusion coefficient reduction through species bundling. *Combustion and Flame*, 148(3):117–126, 2007.

[96] A. Ern and V. Giovangigli. Thermal diffusion effects in hydrogen-air and methane-air flames. *Combustion Theory and Modelling*, 2(4):349–372, 1998.

[97] P. Popp and M. Baum. Analysis of wall heat fluxes, reaction mechanisms, and unburnt hydrocarbons during the head-on quenching of a laminar methane flame. *Combustion and Flame*, 108(3):327–348, 1997.

[98] H. Bongers and L. P. H. DeGoey. The effect of simplified transport modeling on the burning velocity of laminar premixed flames. *Combustion Science and Technology*, 175(10):1915–1928, 2003.

[99] I. Prigogine and R. Defay. *Chemical Thermodynamics*. Longmans, London, UK, 1954.

[100] R. Aris. *Vectors, Tensors, and the Basic Equations of Fluid Mechanics*. Dover Publications, Mineola, NY, 1989.

[101] I. Glassman. *Combustion*. Academic Press, New York, NY, 1977.

[102] J. Bebernes and D. Eberly. *Mathematical Problems from Combustion Theory*. Spriger-Verlag, New York, NY, 1989.

[103] C. K. Law. *Combustion Physics*. Cambridge University Press, New York, NY, 2006.

[104] H. J. Merk. The macroscopic equations for simultaneous heat and mass transfer in isotropic, continuous and closed systems. *Applied Scientific Research A*, 8(1):73–99, 1959.

[105] R. B. Bird, W. E. Stewart, and E. N. Lightfoot. *Transport Phenomena*. John Wiley & Sons, New York, NY, 1960.

[106] G. Dixon-Lewis. Flame structure and flame reaction kinetics. II. Transport phenomena in multicomponent systems. *Proceedings of the Royal Society of London A*, 307(1488):111–135, 1968.

[107] S. Paolucci. On the filtering of sound from the Navier-Stokes equations. Report: SAND82-8257, Sandia National Laboratories, Livermore, CA, 1982.

[108] F. A. Williams. *Combustion Theory*. Addison-Wesley, Redwood City, CA, 1985.

[109] A. Majda and J. Sethian. The derivation and numerical solution of the equations for zero Mach number combustion. *Combustion Science and Technology*, 42(3-4):185–205, 1985.

[110] B. Michaelis and B. Rogg. FEM-simulation of laminar flame propagation. I: Two-dimensional flames. *Journal of Computational Physics*, 196(2):417–447, 2004.

[111] M. D. Smooke, J. A. Miller, and R. J. Kee. Determination of adiabatic flame speeds by boundary value methods. *Combustion Science and Technology*, 34(1-6):79–90, 1983.

[112] J. O. Hirschfelder, C. F. Curtiss, and D. E. Campbell. The theory of flame propagation IV. *Journal of Physical Chemistry*, 57(4):403–414, 1953.

[113] D. B. Spalding. The theory of flame phenomena with a chain reaction. *Philosophical Transactions of the Royal Society of London, Series A*, 249 (957):1–25, 1956.

[114] D. B. Spalding, P. L. Stephenson, and R. G. Taylor. A calculation procedure for the prediction of laminar flame speeds. *Combustion and Flame*, 17(1): 55–64, 1971.

[115] G. Dixon-Lewis. Flame structure and flame reaction kinetics. I. Solution of conservation equations and application to rich hydrogen-oxygen flames. *Proceedings of the Royal Society of London A*, 298(1455):495–513, 1967.

[116] L. Bledjian. Computation of time-dependent laminar flame structure. *Combustion and Flame*, 20(1):5–17, 1973.

[117] J. A. Miller, R. J. Kee, and C. K. Westbrook. Chemical-kinetics and combustion modeling. *Annual Review of Physical Chemistry*, 41:345–387, 1990.

[118] R. J. Kee, M. E. Coltrin, and P. Glarborg. *Chemically Reacting Flow: Theory and Practice*. John Wiley & Sons, Hoboken, NJ, 2003.

[119] A. C. Hindmarsh. Odepack, a systematized collection of ODE solvers. In R. S. Stepleman *et al.*, editor, *Scientific computing*, pages 55–64. North-Holland, Amsterdam, Netherlands, 1983.

[120] J. A. Miller, R. E. Mitchell, M. D. Smooke, and R. J. Kee. Toward a comprehensive chemical kinetic mechanism for the oxidation of acetylene: Comparison of model predictions with results from flame and shock tube experiments. In *Proceedings of the Combustion Institute*, volume 19, pages 181–196, 1982.

[121] F. Dabireau, B. Cuenot, O. Vermorel, and T. Poinsot. Interactions of flames of H_2+O_2 with inert walls. *Combustion and Flame*, 135(1-2):123–133, 2003.

[122] J. M. Powers and S. Paolucci. Accurate spatial resolution estimates for reactive supersonic flow with detailed chemistry. *AIAA Journal*, 43(5):1088–1099, 2005.

[123] R. J. Kee, J. F. Grcar, M. D. Smooke, and J. A. Miller. A Fortran Program for Modeling Steady Laminar One Dimensional Premixed Flames. Report: SAND85-8240, Sandia National Laboratories, Albuquerque, NM, 1991.

[124] J. A. Miller, M. D. Smooke, R. M. Green, and R. J. Kee. Kinetic modeling of the oxidation of ammonia in flames. *Combustion Science and Technology*, 34(1-6):149–176, 1983.

[125] R. J. Kee and J. A. Miller. Computational modeling of flame structure. *Physica D*, 12(1-3):198–211, 1984.

[126] G. H. Golub and C. F. Van Loan. *Matrix Computations*. John Hopkins University Press, Baltimore, MD, 1983.

[127] R. J. Kee, F. M. Rupley, and J. A. Miller. Chemkin-II: A Fortran Chemical Kinetics Package for the Analysis of Gas Phase Chemical Kinetics. Report: SAND89-8009B, Sandia National Laboratories, Albuquerque, NM, 1992.

[128] R. J. Kee, F. M. Rupley, and J. A. Miller. The Chemkin Thermodynamic Data Base. Report: SAND87-8215B, Sandia National Laboratories, Albuquerque, NM, 1992.

[129] R. J. Kee, G. Dixon-Lewis, J. Warnatz, M. E. Coltrin, and J. A. Miller. A Fortran Computer Code Package for the Evaluation of Gas Phase, Multicomponent Transport Properties. Report: SAND86-8246B, Sandia National Laboratories, Albuquerque, NM, 1991.

[130] H. Burwasser and R. N. Pease. Burning velocities of hydrogen-air flames. *Journal of The American Chemical Society*, 77(22):5806–5808, 1955.

[131] G. J. Gibbs and H. F. Calcote. Effect of molecular structure on burning velocity. *Journal of Chemical and Engineering Data*, 4(3):226–237, 1959.

[132] D. A. Senior. Burning velocities of hydrogen-air and hydrogen-oxygen mixtures: Determination by burner method with schlieren photography. *Combustion and Flame*, 5(1):7–10, 1961.

[133] D. A. Miller, R. L. Evers, and G. B. Skinner. Effects of various inhibitors on hydrogen-air flame speeds. *Combustion and Flame*, 7(2):137–142, 1963.

[134] T. G. Scholte and P. B. Vaags. The burning velocity of hydrogen-air mixtures and mixtures of some hydrocarbons with air. *Combustion and Flame*, 3(4): 495–501, 1959.

[135] H. Edmondson and M. P. Heap. The burning velocity of hydrogen-air flames. *Combustion and Flame*, 16(2):161–165, 1971.

[136] R. Günther and G. Janisch. Meßwerte der flammengeschwindigkeit von gasen und gasgemischen. *Chemie Ingenieur Technik*, 43(17):975–978, 1971.

[137] R. Günther and G. Janisch. Measurements of burning velocity in a flat flame front. *Combustion and Flame*, 19(1):49–53, 1972.

[138] G. E. Andrews and D. Bradley. Determination of burning velocities: A critical review. *Combustion and Flame*, 18(1):133–153, 1972.

[139] G. Dixon-Lewis. Kinetic mechanism, structure and properties of premixed flames in hydrogen-oxygen-nitrogen mixtures. *Philosophical Transactions of the Royal Society of London A*, 292(1388):45–99, 1979.

[140] W. J. Vincenti and C. H. Kruger. *Introduction to Physical Gas Dynamics*. John Wiley & Sons, New York, NY, 1965.

[141] G. P. Smith, D. M. Golden, M. Frenklach, N. W. Moriarty, B. Eiteneer, M. Goldenberg, C. T. Bowman, R. K. Hanson, S. Song, W. C. Gardiner, V. V. Lissianski, and Z. Qin. GRI-Mech 3.0. Available at http://www.me.berkeley.edu/gri_mech/, 2006.

[142] R. S. Berry, S. A. Rice, and J. Ross. *Physical and Chemical Kinetics*. Oxford University Press, New York, NY, 2002.

[143] W. Fickett and W. C. Davis. *Detonation*. University of California Press, Berkley, CA, 1979.

[144] V. R. Katta and W. M. Roquemore. Numerical studies on the structure of two-dimensional H_2/Air premixed jet flame. *Combustion and Flame*, 102 (1-2):21–40, 1995.

[145] C. K. Westbrook. Hydrogen oxidation-kinetics in gaseous detonations. *Combustion Science and Technology*, 29(1-2):67–81, 1982.

[146] M. Thiele, J. Warnatz, A. Dreizler, S. Lindenmaier, U. Schieß l. R., Maas, A. Grant, and P. Ewart. Spark ignited hydrogen/air mixtures: two dimensional detailed modeling and laser based diagnostics. *Combustion and Flame*, 128(1-2):74–87, 2002.

[147] G. Patnaik and K. Kailasanath. Numerical simulations of burner-stabilized hydrogen–air flames in microgravity. *Combustion and Flame*, 99(2):247–253, 1994.

[148] T. L. Burks and E. S. Oran. A computational study of the chemical kinetics of hydrogen combustion. NRL Memorandum Report 4446, Naval Research Laboratory, Washington, DC, 1981.

[149] D. L. Baulch, D. D. Drysdale, D. G. Horne, and A. C. Lloyd. *Evaluated Kinetic Data for High Temperature Reactions. Volume I: Homogeneous Gas Phase Reactions of the H2-O2 Systems*. Butterworth, London, UK, 1972.

[150] R. F. Hampson (Editor), W. Braun, R. L. Brown, D. Garvin, J. T. Herron, R. E. Huie, M. J. Kurylo, A. H. Laufer, J. D. McKinley, H. Okabe, M. D. Scheer, W. Tsang, and D. H. Stedman. Survey of photochemical and rate data for twenty-eight reactions of interest in atmospheric chemistry. *Journal of Physical and Chemical Reference Data*, 2(2):268–312, 1973.

[151] O. M. Knio and H. N. Najm. Effect of stoichiometry and strain rate on transient flame response. In *Proceedings of the Combustion Institute*, volume 28, pages 1851–1857, 2000.

[152] H. N. Najm and P. S. Wyckoff. Premixed flame response to unsteady strain rate and curvature. *Combustion and Flame*, 110(1-2):92–112, 1997.

[153] M. Frenklach, H. Wang, C. L. Yu, M. Goldenberg, C. T. Bowman, R. K. Hanson, D. F. Davidson, E. J. Chang, G. P. Smith, D. M. Golden, W. C. Gardiner, and V. Lissianski. GRI-Mech 1.2. Available at http://www.me.berkeley.edu/gri_mech/, 2005.

[154] V. R. Katta, L. Brenez, and J. C. Rolon. Experimental and numerical investigation of structures of two-dimensional partially premixed methane/air flames. In *Proceedings of the Combustion Institute*, volume 28, pages 1909–1916, 2000.

[155] V. R. Katta and W. M. Roquemore. Simulation of dynamic methane jet diffusion flames using finite rate chemistry models. *AIAA Journal*, 36(11): 2044–2054, 1998.

[156] J. M. Powers and S. Paolucci. Uniqueness of chemical equilibria in ideal mixtures of ideal gases. *American Journal of Physics*, 76(9):848–855, 2008.

[157] L. Perko. *Differential Equations and Dynamical Systems*. Springer-Verlag, New York, NY, 2001.

[158] A. J. Sommese and C. W. Wampler. *The Numerical Solution of Systems of Polynomials Arising in Engineering and Science*. World Scientific, Hackensack, NJ, 2005.

[159] S. J. Fraser. Solvable model of kinetic control. *Journal of Chemical Physics*, 116(4):1277, 2002.

[160] D. J. Bates, J. D. Hauenstein, A. J. Sommese, and C. W. Wampler. Bertini: Software for numerical algebraic geometry. Available at http://www.nd.edu/~sommese/bertini, 2009.

[161] H. B. Callen. *Thermodynamics and an Introduction to Thermostatistics*. John Wiley & Sons, New York, NY, 1985.

[162] S. Lefschetz. *Differential Equations: Geometric Theory*. Interscience Publishers, New York, NY, 1963.

[163] A. Morgan. *Solving Polynomial Systems Using Continuation for Engineering and Scientific Problems*. Prentice Hall, Englewood Cliffs, NJ, 1987.

[164] D. B. Shear. Stability and uniqueness of the equilibrium point in chemical reaction systems. *Journal of Chemical Physics*, 48(9):4144–4147, 1968.

[165] A. J. Lichtenberg and M. A. Lieberman. *Regular and Chaotic Dynamics*. Springer-Verlag, New York, NY, 1992.

[166] E. N. Lorenz. On the existence of a slow manifold. *Journal of the Atmospheric Sciences*, 43(15):1547–1557, 1986.

[167] E. N. Lorenz and V. Krishnamurthy. On the nonexistence of a slow manifold. *Journal of the Atmospheric Sciences*, 44(20):2940–2950, 1987.

[168] S. J. Jacobs. Existence of a slow manifold in a model system of equations. *Journal of the Atmospheric Sciences*, 48(7):893–901, 1991.

[169] E. N. Lorenz. The slow manifold−what is it? *Journal of the Atmospheric Sciences*, 49(24):2449–2451, 1992.

[170] D. L. Baulch, C. T. Bowman, C. J. Cobos, R. A. Cox, T. Just, J. A. Kerr, M. J. Pilling, D. Stocker, J. Troe, W. Tsang, R. W. Walker, and J. Warnatz. Evaluated kinetic data for combustion modeling: Supplement II. *Journal of Physical and Chemical Reference Data*, 34(3):757–1357, 2005.

[171] J. Guckenheimer and P. Holmes. *Nonlinear Oscillation, Dynamical Systems, and Bifurcations of Vector Fields*. Springer-Verlag, New York, NY, 1983.

[172] A. A. Andronov. *Qualitative Theory of Second Order Dynamical Systems*. John Wiley & Sons, New York, NY, 1973.

[173] J. V. Michael. Measurement of thermal rate constants by flash or laser photolysis in shock tubes: Oxidations of H2 and D2. *Progress in Energy and Combustion Science*, 18(4):327–347, 1992.

[174] G. Van Wylen, R. Sonntag, and C. Borgnakke. *Fundamentals of Classical Thermodynamics*. John Wiley & Sons, New York, NY, 1996.

[175] I. Prigogine. *Introduction to Thermodynamics of Irreversible Processes*. Interscience Publishers, New York, NY, 1967.

[176] D. Kondepudi and I. Prigogine. *Modern Thermodynamics*. John Wiley & Sons, Chichester, UK, 1998.

[177] K. K. Kuo. *Principles of Combustion*. John Wiley & Sons, New York, NY, 1986.

[178] W. Kühnel. *Differential Geometry: Curves–Surfaces–Manifolds*. American Mathematical Society, Providence, RI, 2002.

[179] J. Kestin. *A Course in Thermodynamics*. Blaisdell, Waltham, MA, 1966.

[180] J. W. Tester and M. Modell. *Thermodynamics and its Applications*. Prentice Hall, Upper Saddle River, NJ, 1997.

[181] M. W. Hirsch and S. Smale. *Differential Equations, Dynamical Systems, and Linear Algebra*. Academic Press, New York, NY, 1974.

[182] T. D. Aslam and J. M. Powers. The dynamics of unsteady detonation in ozone. AIAA 2009-632. Orlando, FL, January 2009.

[183] Jonathan D. Hauenstein. *Regeneration, Local Dimension, and Applications in Numerical Algebraic Geometry*. PhD thesis, University of Notre Dame, Notre Dame, IN. 46556, April 2009.

This document was prepared & typeset with LaTeX 2ε*, and formatted with* NDdiss2ε *classfile (v3.0[2005/07/27]) provided by Sameer Vijay.*